Electronic Thesis and Dissertation Repository

12-12-2013 12:00 AM

Multinuclear Solid-State Nuclear Magnetic Resonance Spectroscopy of Microporous Materials

Jun Xu, *The University of Western Ontario*

Supervisor: Yining Huang, *The University of Western Ontario*
A thesis submitted in partial fulfillment of the requirements for the Doctor of Philosophy degree in Chemistry
© Jun Xu 2013

Follow this and additional works at: https://ir.lib.uwo.ca/etd

Part of the Inorganic Chemistry Commons

MULTINUCLEAR SOLID-STATE NUCLEAR MAGNETIC RESONANCE
SPECTROSCOPY OF MICROPOROUS MATERIALS

(Thesis format: Integrated Article)

by

Jun Xu

Graduate Program in Chemistry

A thesis submitted in partial fulfillment
of the requirements for the degree of
Doctor of Philosophy

The School of Graduate and Postdoctoral Studies
The University of Western Ontario
London, Ontario, Canada

© Jun Xu 2013

Abstract

Microporous materials have attracted tremendous attention since the 18th century due to their industrial importance in the broad areas of ion exchange, catalysis, adsorption, *etc*. It is essential to understand the relationships between the properties of microporous materials and their structures. However, the structures of many microporous materials are determined from the more limited powder X-ray diffraction (XRD) data due to the lack of suitable single-crystals for XRD. In such cases, an unambiguous structure solution of microporous materials requires additional information from other techniques such as solid-state NMR (SSNMR) spectroscopy. SSNMR spectroscopy can provide short-range information around the NMR-active nucleus of interest and it can also confirm the long-range ordering of the structure such as crystal symmetry. This thesis is focused on the study of two types of microporous materials, metal–organic frameworks (MOFs) and titanosilicates, by multinuclear SSNMR spectroscopy in combination with quantum chemical calculations for computational modeling.

A brief introduction is first given in *Chapter 1*. In *Chapter 2–6*, multinuclear SSNMR investigations of two prototypical MOFs with potential industrial applications, CPO-27-M (M = Mg, Zn, Co, Ni), and α-Mg$_3$(HCOO)$_6$, are carried out. MOFs are novel inorganic-organic hybrid microporous materials, constructed by the interconnection of metal ions by various organic linkers. MOFs have many promising properties compared to classical microporous materials such as rich structural diversity, high thermal stability, tunable porosity, selective adsorption, *etc.* The results presented in these chapters demonstrate that SSNMR spectroscopy is very suitable for the characterization of MOFs: The local Mg environments and the rehydration/adsorption processes of CPO-27-Mg were examined by natural abundance ^{25}Mg SSNMR spectroscopy at an ultrahigh magnetic field of 21.1 T. The dynamics of several guest molecules inside of CPO-27-M were monitored by variable-temperature ^{2}H SSNMR spectroscopy. The structures of another MOF, α-Mg$_3$(HCOO)$_6$, before and after guest adsorption, were thoroughly investigated by ^{1}H, ^{2}H, ^{13}C, ^{17}O, and ^{25}Mg SSNMR spectroscopy. Moreover, the existence of weak C–H···O and C–H···N hydrogen bonding were confirmed by ultrahigh-resolution ^{1}H SSNMR spectroscopy.

The last chapter consists of a comprehensive study of titanosilicates by ^{29}Si, ^{23}Na, ^{39}K, and $^{47/49}$Ti SSNMR spectroscopy. Microporous titanosilicates are novel inorganic materials with many unique structural features. This work is highlighted by the acquisition of natural abundance SSNMR spectra for three unreceptive quadrupolar nuclei, $^{47/49}$Ti and ^{39}K, at 21.1 T. $^{47/49}$Ti SSNMR experiments provides insights into the coordination environments of Ti inside the framework, whereas ^{39}K SSNMR experiments allow one to directly probe the local environment of extra-framework counter cations in titanosilicates.

Keywords

Metal–organic frameworks, titanosilicates, structure characterization, solid-state NMR, unreceptive quadrupolar nuclei, ultrahigh field, adsorption, guest dynamics.

Co-Authorship Statement

This thesis contains materials from previously published manuscripts. Dr. Yining Huang was the corresponding author on all the presented papers and was responsible for the supervision of Jun Xu over the course of his Ph.D. study. For copyright releases see the Appendix.

Chapter 2 is from the published letter co-authored by Jun Xu, Victor V. Terskikh and Yining Huang (*J. Phys. Chem. Lett.* **2013**, *4*, 7-11). The samples were prepared by J. Xu. Experiments were performed by J. Xu and V. V. Terskikh. J. Xu wrote the manuscript. V. V. Terskikh and Y. Huang revised the manuscript.

The majority of *Chapter 3* is from the published communication co-authored by Jun Xu, Victor V. Terskikh and Yining Huang (*Chem. Eur. J.* **2013**, *19*, 4432-4436). J. Xu prepared the samples. J. Xu and V. V. Terskikh performed experiments. The manuscript was written by J. Xu and it was revised by V. V. Terskikh and Y. Huang.

Dr. Victor V. Terskikh is credited for the acquisition of SSNMR spectra presented in *Chapter 4*. Theoretical calculations were also performed by V. V. Terskikh.

Regina Sinelnikov is thanked for making CPO-27-M samples used in *Chapter 5*.

Chapter 6 is a portion of the published article co-authored by Peng He, Jun Xu, Victor V. Terskikh, Andre Sutrisno, Heng-Yong Nie and Yining Huang (*J. Phys. Chem. C* **2013**, *117*, 16953-16960). The samples were provided by P. He and J. Xu. ^{17}O NMR spectra were collected by J. Xu and V. V. Terskikh. A. Sutrisno is credited and thanked for analyzing ^{17}O NMR spectra. ^{17}O contents of the samples were measured by H.-Y. Nie. Y. Huang was responsible for writing and editing the drafts. P. He, J. Xu, V. V. Terskikh and A. Sutrisno revised the manuscript.

Dr. Zhi Lin (University of Aveiro, Portugal) is credited for preparing the $TiSiO_4$ samples used in *Chapter 7*. Dr. Victor V. Terskikh is thanked for the acquisition of $^{47/49}$Ti and ^{39}K SSNMR spectra shown in *Chapter 7*. Theoretical calculations were also conducted by V. V. Terskikh.

Acknowledgments

Table of Contents

List of Tables

List of Figures

List of Abbreviations

1D	one-dimensional
2D	two-dimensional
3D	three-dimensional
3Q	triple-quantum
3QMAS	triple-quantum magic-angle spinning
B3LYP	**B**ecke's **3**-parameter hybrid density exchange functional with **L**ee, **Y**ang and **P**arr correlation functional
BABA	back-to-back
BDC	1, 4-benzenedicarboxylate
Cp	cyclopentadienyl
CP	cross-polarization
CPMAS	cross-polarization magic-angle spinning
CPO	Coordination Polymer of Oslo
CS	chemical shielding
CSA	chemical shielding anisotropy
CT	central transition
CW	continuous-wave
DAS	dynamic-angle spinning
DFS	double-frequency sweeps
DFT	density functional theory
DMF	*N,N*-dimethylformamide
DOBDC	2,5-dioxido-1,4-benzenedicarboxylate
DOR	double-rotation
DQ	double-quantum
EDS	energy dispersive X-ray spectroscopy
EFG	electric field gradient
ETS	Engelhard titanosilicate
FID	free induction decay
FSLG	frequency-switched Lee-Goldberg

FT	Fourier transformation
FWHH	full-width at half-height
GGA	Generalized Gradient Approximation
GIPAW	Gauge Including Projector Augmented Wave
GTO	Gaussian-type orbital
HB	Herzfeld-Berger
HETCOR	hetero-nuclear correlation
HTS	hydrothermal synthesis
IUPAC	International Union of Pure and Applied Chemistry
IRMOF	isoreticular metal–organic framework
MAS	magic-angle spinning
MAT	magic-angle turning
MOF	metal–organic framework
MP2	second-order Møller-Plesset perturbation theory
MQ	multiple-quantum
MQMAS	multiple-quantum magic-angle spinning
N.A.	natural abundance
NMR	nuclear magnetic resonance
NPD	neutron powder diffraction
o.d.	outer diameter
PAS	principle axis system
PBE	**P**erdew, **B**urke and **E**rnzerhof correlation functional
PHORMAT	phase-corrected magic-angle turning
ppm	parts per million
PXRD	powder X-ray diffraction
QCPMG	**q**uadrupolar **C**arr-**P**urcell-**M**eiboom-**G**ill pulse sequence
QE	quadrupolar echo
rf	radio frequency
S/N	signal-to-noise ratio
SEM	scanning electron microscopy
SPAM	soft-pulse-added-mixing
SQ	single-quantum

SSB	spinning sidebands
SSNMR	solid-state nuclear magnetic resonance
STS	solvothermal synthesis
SW	spectral width
THF	tetrahydrofuran
TGA	thermogravimetric analysis
$TiSiO_4$	titanosilicate-based materials
TMS	tetramethylsilane
TOF-SIMS	time-of-flight secondary ion mass spectrometry
TPPM	two-pulse phase-modulation
TTMSS	tetrakis(trimethylsilyl)silane
WURST	wideband uniform-rate smooth truncation
XRD	X-ray diffraction

List of Symbols

$A - F$	dipolar alphabets
B_0	strength of the external static magnetic field
B_1	strength of the radio frequency field during a pulse
C_2	two-fold rotation axis
C_3	three-fold rotation axis
C_6	six-fold rotation axis
C_Q	nuclear quadrupolar coupling constant
D^{IS}	direct dipolar coupling constant
e	elementary electron charge (1.602×10^{-19} C)
F_1, F_2	indirect and direct dimensions
h	Planck constant (6.626×10^{-34} J·s)
I	nuclear spin quantum number
$\mathbf{I}$	nuclear spin angular momentum vector
k	Boltzmann constant
mb	millibarn (10^{-31} m^2)
m_I	magnetic nuclear spin quantum number
$\mathbf{M}$	magnetization (bulk nuclear spin magnetic moment) vector
N_α, N_β	Boltzmann population of lower and higher energy levels
Q	nuclear electric quadrupole moment
D^{IS}	direct dipolar coupling constant between spins I and S
r_{IS}	internuclear distance between spins I and S
$\mathbf{r}_{IS}$	internuclear vector between spins I and S
S	spin quantum number
$\mathbf{S}$	spin angular momentum vector
t_1	evolution time of the indirect dimension
T	temperature
T_1	longitudinal (or spin-lattice) relaxation time
T_2	transverse (or spin-spin) relaxation time

$T_2{}^*$	transverse (or spin-spin) relaxation time including the effects of magnetic field inhomogeneity
V	electric field gradient tensor
V_{XX}, V_{YY}, V_{ZZ}	principle components of the electric field gradient tensor
α, β, γ	Euler angles relating the principle axis systems of the electric field gradient and chemical shift tensors
γ	gyromagnetic ratio
$\delta_{11}, \delta_{22}, \delta_{33}$	principle components of the chemical shift tensor
δ_{iso}	isotropic chemical shift
δ_{hyp}	hyperfine (paramagnetic) shift
δ_{con}	Fermi contact shift
δ_{dip}	dipolar shift
$\rho_{\alpha\beta}$	Fermi contact spin density
η_Q	EFG tensor asymmetry parameter
θ	angle between 2 axes
κ	chemical shift tensor skew parameter
λ	wavelength
μ	nuclear spin magnetic (dipole) moment
μ_0	magnetic moment constant ($4\pi \times 10^7$ N·Å^{-2})
ν_0	Larmor frequency
ν_Q	quadrupolar frequency
ν_{rot}	magic-angle spinning frequency of rotor
$\sigma_{11}, \sigma_{22}, \sigma_{33}$	principle components of the chemical shielding tensor
τ	interpulse delay
τ_{exc}	excitation time in DQ experiment
Ω	chemical shift tensor span parameter

Chapter 1

1   General Introduction

The materials studied in this thesis are microporous materials. According to the definition of International Union of Pure and Applied Chemistry (IUPAC),[1] they are porous materials containing channels and cavities with typical pore diameters larger than 2 nm. These molecular-scale pores block large molecules, but selectively allow small molecules to pass.[2] Numerous efforts have been devoted to the research of microporous materials due to their broad applications in industry and everyday life such as ion-exchangers, catalysts and sorbents.[3-6] One area that attracts much attention is to understand the structures of microporous materials including the topology of frameworks as well as the size, shape and connectivity of pore systems by a wide range of characterization techniques, since such structural features are of fundamental importance to their applications. Herein, solid-state nuclear magnetic resonance (NMR) spectroscopy, as one of the most powerful tools for the investigation of solid materials[7-11], is used to characterize various types of microporous materials.

1.1   Microporous Materials

1.1.1   Structures and Properties

The relationships between the structures of microporous materials and their properties are described as follows using several representative compounds as examples.

The most well-known group of microporous materials is crystalline microporous aluminosilicates (zeolites). The frameworks of zeolites are built from 4-connected AlO_4 and SiO_4 tetrahedra via oxygen bridges. The AlO_4 and SiO_4 tetrahedra of zeolites are connected in three dimensions in many ways, giving rise to very different properties. For example, zeolite Y can be most conveniently visualized as being formed from sodalite cages (truncated octahedra) joined through double 6-rings (Figure 1-1).[12] The pore structure is characterized by supercages with a diameter of approximately 12 Å and an accessible pore size of about 7.4 Å. The cages and pores allow adsorbing quite large molecules, making this structure useful in catalytic applications.
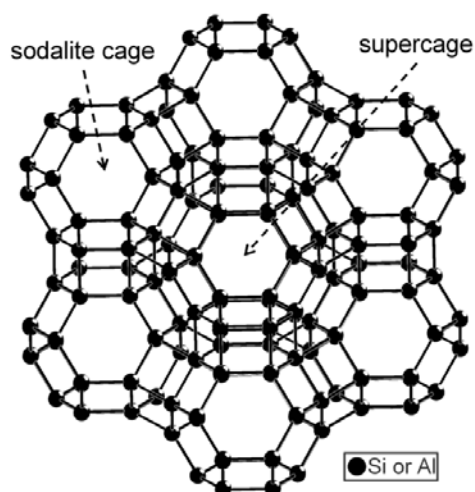
Figure 1-1: The structure of zeolite Y viewed down [110] direction. The bridge oxygens are omitted for clarity.
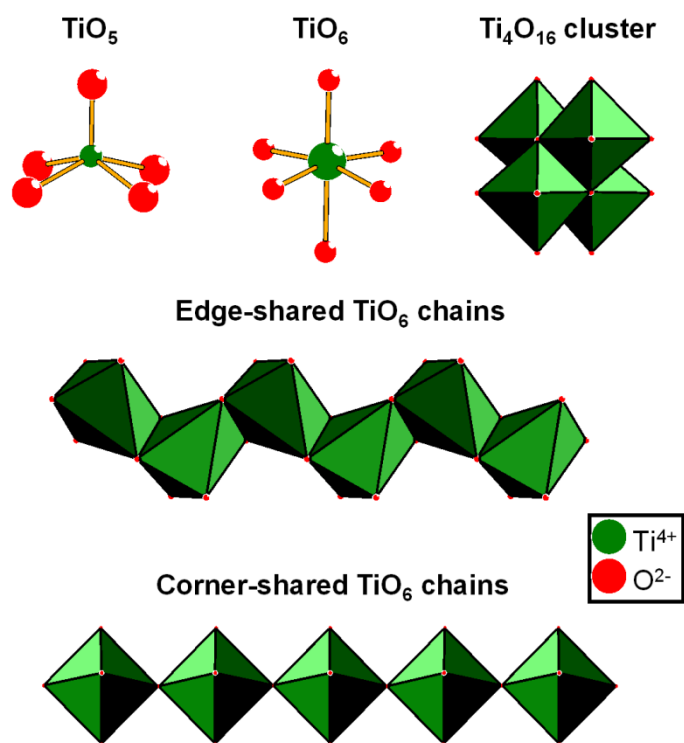
Figure 1-2: Some unique structural features of $TiSiO_4$ compared to zeolites.

In recent years, other types of inorganic microporous materials have received more and more attention including various titanosilicate-based materials, $TiSiO_4$. As Figure 1-2 shows, the structures of $TiSiO_4$ are distinct from zeolites in such a way that

they can posses 5- and/or 6-coordinated Ti^{4+} rather than the 4-coordinated Al^{3+} in zeolites.[13,14] In addition, such TiO_5 and TiO_6 units can interconnect with each other, forming one-dimensional edge- or corner-shared chains or clusters,[14-16] whereas such Al–O–Al connectivity is strictly forbidden in zeolites. These unique structure features of $TiSiO_4$ are considered to be responsible to their novel applications as nuclear waste treatment materials,[15] photocatalysts,[17] and quantum wires[18].
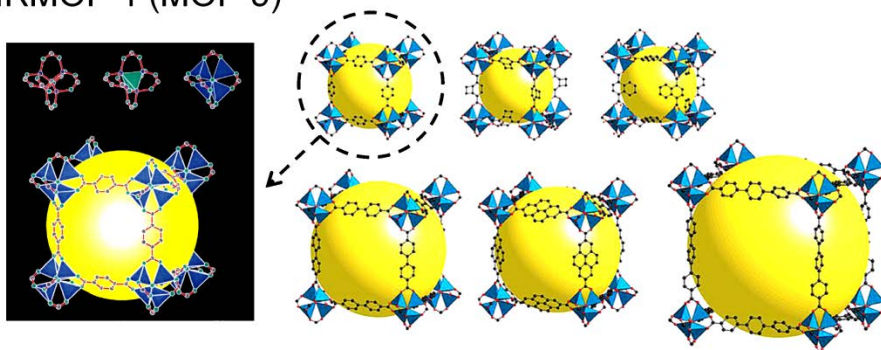
Figure 1-3: The structures of IRMOF series. (Ref. 19)

One of the most exciting advances in the field of microporous materials since 1990s is the emergence of a novel class of hybrid organic-inorganic porous materials, known as metal–organic frameworks (MOFs).[5,6] Unlike zeolites, where Al^{3+} are connected to Si^{4+} via bridge oxygens, metal cations of MOFs are linked by organic linkers. Therefore, MOFs could exhibit properties of both organic and inorganic compounds in a single material, such as rich structural diversity (similar to organic compounds) and high thermal stability (similar to inorganic compounds). In addition, promising properties that are not available in classical organic or inorganic materials could also be observed in MOFs including super large surface area, tunable porosity and high adsorption selectivity. As Figure 1-3 illustrates, the structure of MOF-5 (also known as IRMOF-1, which is the simplest member of the isoreticular MOF series) is derived from a cubic six-connected three-dimensional net.[19] The nodes of the net are built from four ZnO_4 tetrahedra which share a single O atom (μ^4-O^{2-}) in the center, forming a regular Zn_4O tetrahedron. The links of the net are 1,4-benzenedicarboxylate (BDC) ligands. Each –COO⁻ group of BDC connects to two neighboring ZnO_4 tetrahedra. The

pore sizes of IRMOFs can be facilely tuned by varying the length of organic linkers. The organic linkers can be further modified to combine various functional groups into the framework such as the –NH$_2$ group (IRMOF-3), which is a catalyst for Knoevenagel condensation.[20]

1.1.2   Syntheses

Although microporous materials (stilbite, a natural zeolite) were recognized and described by the Swedish mineralogist A. F. Cronstedt in 1756,[2] the effort to synthesize microporous materials did not start until St. Claire reported the first hydrothermal synthesis (HTS) of zeolite ievynite in 1862. The HTS of zeolites involves mixing the reagents with water and heating the mixture in a sealed vessel for a period of time, simulating the conditions under which natural zeolites were formed including high temperatures and pressures (*e.g.*, $T > 473$ K, $P > 10000$ kPa). HTS remains one of the most useful methods for the synthesis of microporous materials to date. The TiSiO$_4$-based materials studied in *Chapter 7* were prepared in this way.
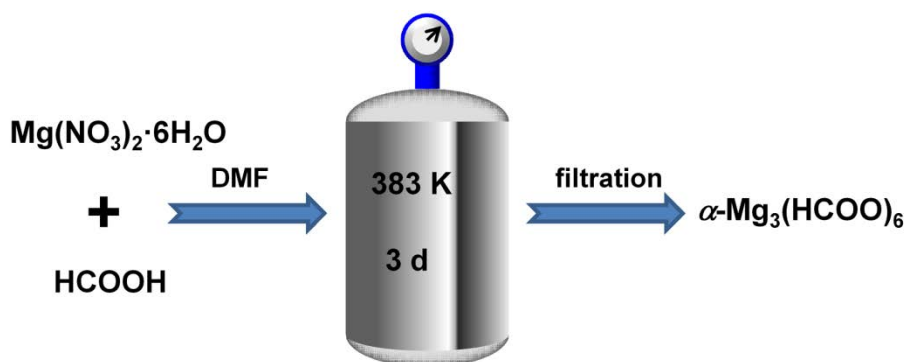
Figure 1-4: Schematic diagram of the solvothermal synthesis of α-Mg$_3$(HCOO)$_6$.

A different approach was used to synthesize MOF samples studied in *Chapters 2–6*. With the high polarity and solvability, water has the capacity of dissolving a wide variety of metal salts used in the synthesis of MOFs. However, it interacts too strongly with the metal ions. Interrupted and hydrated structures are often formed under the aqueous conditions rather than 3D frameworks.[21,22] In addition, many organic linkers are insoluble in water. Therefore, a large amount of MOFs (including those investigated in

this thesis) are prepared using solvothermal synthesis (STS, shown in Figure 1-4), which is very similar to HTS but uses non-aqueous, organic solvents instead of water. The most common solvents of STS are polar aprotic solvents such as *N,N*-dimethylformamide (DMF) and tetrahydrofuran (THF), which are good solvents for both metal salts and organic linkers.

1.1.3   Characterization

Thoroughly resolving the structure of microporous material is essential because it allows one to understand the relationships between the structures and their properties. Therefore, many characterization techniques[2-6] have been applied to microporous materials such as X-ray diffraction (XRD) and solid-state nuclear magnetic resonance (SSNMR) spectroscopy. The two types of techniques can provide structural information complementary to each other, making the combination of two methods valuable for the study of microporous materials. Only the principle of XRD is briefly introduced here since SSNMR spectroscopy will be discussed in detail in the next section.

XRD is the most frequently used tool to examine the phase identity and purity of crystalline solids.[23] Single-crystal XRD has been considered to be one of the most reliable structural determination methods to date. However, due to the micro-crystalline nature of many microporous materials, structural solutions of these materials are often based on the more limited powder XRD data. In such case, a powder sample can be conveniently regarded as an assembly of a large number of microcrystals with random orientations, if it is sufficiently ground.
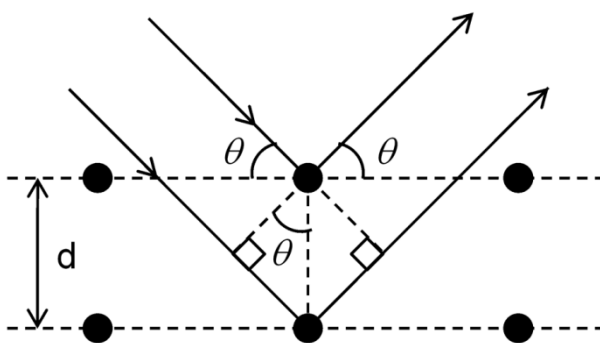
Figure 1-5: Schematic illustration of Bragg's Law.

Since the wavelength of an X-ray (*e.g.*, 1.7902 Å for Co Kα radiation, which is used in this thesis) has the same scale as the distance between periodic lattice planes, shining monochromic X-rays on a crystal generates a scattering pattern characteristic of the structure. As Figure 1-5 shows, the incident X-ray beam is partially reflected by the first layer of atoms. The remaining X-ray beam that is not reflected by this layer penetrates into the second layer of atoms and is reflected again. The reflected beams of many layers superimpose. Maximum intensity (diffraction peak) occurs if the difference in path length between reflected beams of two layers is an integer number of wavelength λ (Bragg's Law):

$$n\lambda = 2\,d_{(hkl)}\sin\theta \qquad\qquad (\textbf{Equation 1-1})$$

where θ is the angle of incidence, n is an integer, and $d_{(hkl)}$ is the distance between parallel lattice planes whose orientation is indicated by the Miller indices *hkl*. The overall effect is similar to how an optical grating diffracts a beam of light.

The peak positions and relative intensities of powder XRD patterns are determined by the long-range ordering characteristic of the structure such as the crystal symmetry, unit cell dimensions, and atomic parameters. Therefore, the structure of a microporous material can be conveniently identified by directly comparing its experimental powder XRD pattern with a reference pattern. However, lacking periodic properties, many structural features of microporous materials, such as the disordered extra-framework cations, stacking faults, disordered metal coordination spheres, and rapid tumbling guests, are not available from XRD experiments. In addition, it is very difficult to locate protons by XRD since X-rays are only weakly scattered by protons.

1.2 Solid-State NMR

Solid-state NMR spectroscopy has been extensively used as a powerful tool to obtain molecular-level information about both the structure of materials and dynamics occurring within these materials.[7-11] On the one hand, SSNMR experiment is capable of providing additional information to confirm the long-range periodicity obtained from the single-crystal and/or powder XRD data since the number of NMR peaks should equal to

the number of crystallographically non-equivalent sites.[24,25] On the other hand, the correlations between NMR parameters (*e.g.*, chemical shift) and chemical bond as well as local geometry (*e.g.*, bond length and bond angle) have shed light on the local environments of materials with unknown or poorly-described structures, in particular for glassy or amorphous materials. Recently, the increasing ability to relate these NMR parameters to the crystallographic coordinates of relevant atoms in the unit cell via theoretical calculations allows one to refine the data from diffraction experiments and, under favorable conditions, to solve crystal structures with little (or even no) diffraction data.[26,27] Moreover, ^{2}H SSNMR line shape is very sensitive to the guest motions.

The acquisition and interpretation of SSNMR spectra are challenging compared to those of solution NMR since the anisotropic (orientation-dependent) NMR interactions in solids are typically not averaged to their isotropic (orientation-independent) values due to the absence of rapid molecular tumbling. Therefore, the sensitivity and spectral resolution of SSNMR spectroscopy are severely limited by the line broadening induced by these anisotropic interactions. Nevertheless, the broad SSNMR spectra often contain valuable structural information about the local environment around the nucleus studied, which is unavailable from the solution NMR data.

1.2.1   Early History of Solid-State NMR

The history of nuclear magnetic resonance[28,29] goes back to the early twentieth century, when Pauli proposed that certain nuclei should possess spin angular momentum based on the observation of hyperfine splitting in the optical spectra of particular atoms. The idea that nuclei have magnetic moments was directly confirmed by the beam experiments of Gerlach and Stern. The phenomenon of NMR was first observed in gases by Rabi and co-workers (1937), using an extended version of the Stern-Gerlach apparatus to experimentally verify theoretical concepts in quantum mechanics by accurately measuring nuclear magnetic moments. Prior to Rabi's experiments, Gorter had attempted to observe an NMR signal in solid state (1936), although he was unsuccessful. A later attempt in 1942 by Gorter and Broer failed again. The crystals used were very pure in those experiments and the relaxation times were too long, resulting in a saturation effect and making resonance lines "invisible".

The first successful NMR experiments using bulk materials were carried out independently at the end of 1945 by Purcell *et al.* at Harvard University and by Bloch *et al.* at Stanford University (Purcell and Bloch were both awarded the 1952 Nobel Prize in Physics for the discovery of NMR in condensed matter). Purcell and co-workers studied the materials in the solid state, observing the proton signals in solid paraffin; whereas Bloch and co-workers conducted the first solution NMR experiments and found the proton signals of liquid H_2O. Both groups were aware of the importance of relaxation and efforts were made to avoid saturation.

Many fundamental concepts of NMR spectroscopy were discovered within its first seven years, including chemical shifts, dipolar coupling, spin-spin coupling, quadrupolar coupling, and relaxation. The power of NMR for measuring the dynamics of inter- and intra-molecular exchange process had also been established.

Commercial NMR spectrometers began to appear in 1952 with a 0.7 T magnet. Since then, a significant advance in solid-state NMR has been made in hardware technology by increasing the field strength, optimizing the probe design and improving the performance of electronics. For example, some SSNMR spectra shown in this thesis were acquired at a high magnetic field of 21.1 T. On the other hand, novel experimental techniques become more and more important for solid-state NMR. It was first realized in the 1960s that the spectral resolution in solids could be greatly enhanced by magic-angle spinning (MAS). Combined with other new experimental methods, including spin-echo (also referred to as Hahn-echo), cross-polarization (CP), time averaging, Fourier transformation and spin-decoupling, high-resolution one-dimensional spectra in solids were obtainable by the 1970s. After that, the advent of multi-dimensional NMR spectroscopy was another milestone, by which much more information could be extracted from solid-state NMR spectra. Spreading the information into a second (indirect) frequency dimension allows a wide variety of correlations (*e.g.*, the connectivity between two nuclei) to be observed and the behavior of normally forbidden NMR transitions to be studied. To date, solid-state NMR spectroscopy has been regarded as one of the most important techniques in the characterization of solid materials.

1.2.2 Physical Background

An NMR-active nucleus must have a nonzero nuclear spin angular momentum ($\mathbf{I}$), which is an intrinsic property of the nucleus. Most of the elements in the periodic table have magnetically active isotopes (isotopes are nuclei with the same number of protons but a different number of neutrons). Although there is no simple rule for predicting the nuclear spin, the following guideline applies (Table 1-1):

Table 1-1: The guideline to predict the nuclear spin.

Number of protons	Number of neutrons	Spin
Even	Even	Zero
Even	Odd	Half-integer
Odd	Even	Half-integer
Odd	Odd	Integer

The nuclear spin angular momentum ($\mathbf{I}$) is responsible for the appearance of nuclear magnetic moment μ via a linear relationship,[8]

$$\mu = \gamma \times \mathbf{I} \qquad (\textbf{Equation 1-2})$$

where the nuclear gyromagnetic ratio γ is one of the fundamental magnetic nuclear constants dependent on the nature of nuclei. γ can be either positive or negative, which could play an important role in some NMR experiments. However, the consequences of the sign can be ignored in this thesis. The nuclear magnetic moment μ is capable of responding to external magnetic fields (including a strong static magnetic field B_0 and a small oscillating field B_1), which (as well as the nuclear spin angular momentum $\mathbf{I}$) can be measured using an extended version of Stern-Gerlach experiments.[30]

The nuclear spin not only interacts with external magnetic fields (external interactions) but also interacts with other spins (internal interactions). These interactions are summarized in the general Hamiltonian of NMR[8]

$$\hat{H}_{\text{NMR}} = \hat{H}_{\text{Z}} + \hat{H}_{\text{CS}} + \hat{H}_{\text{D}} + \hat{H}_{\text{J}} + \hat{H}_{\text{Q}} \qquad (\textbf{Equation 1-3})$$

where $\hat{H}_Z$, $\hat{H}_{CS}$, $\hat{H}_D$, $\hat{H}_J$, and $\hat{H}_Q$ denote the Zeeman, chemical shielding, direct dipolar coupling, indirect (scalar, *J*-) spin-spin coupling, and quadrupolar interactions for nuclei with spin $I > 1/2$, respectively.

In most experiments, the static magnetic field B_0 is high enough that the Zeeman interaction dominates, and other interactions can be treated as perturbations on the former (the high-field approximation). The typical magnitudes of all the nuclear spin interactions are compared in Table 1-2. The dipolar coupling and quadrupolar interactions are averaged to zero in liquids while the chemical shielding interaction is averaged to its isotropic value σ_{iso} due to rapid tumbling of molecules. However, these anisotropic interactions are still present in solids, giving rise to much broader spectra compared to the spectra of liquids.

Table 1-2: Typical magnitudes of nuclear spin interactions (Ref. 8).

Nuclear spin interactions	Magnitude in liquids (Hz)	Magnitude in solids (Hz)
Zeeman	10^7–10^9	10^7–10^9
Chemical shielding	σ_{iso}	10^2–10^5
Dipolar	0	10^3–10^5
Scalar/J-coupling	10^0–10^3	10^0–10^3
Quadrupolar	0	10^3–10^7

1.2.2.1   Zeeman Interaction

The Zeeman interaction is the interaction between nuclear spins (*I*) and the static external magnetic field (B_0), which is typically much larger than other interactions. According to quantum mechanics, a nucleus with nuclear spin *I* have $2I + 1$ possible energy levels (distinguished by the magnetic nuclear spin quantum number m_I, $m_I = -I$, $-I +1$, …, $I - 1$, I). In the absence of external magnetic field, these energy levels are degenerate (*i.e.*, they have the same energy). However, when a strong magnetic field is applied, the nuclear spin energies become non-equivalent. As Figure 1-6 illustrates, the initially degenerate energy levels undergo splitting and this splitting energy ΔE expressed via Equation 1-4 is proportional to the gyromagnetic ratio γ, and the strength of the external magnetic field B_0:[8]

$$\Delta E = h\gamma B_0/2\pi \qquad (\textbf{Equation 1-4})$$

where h is the Planck's constant.
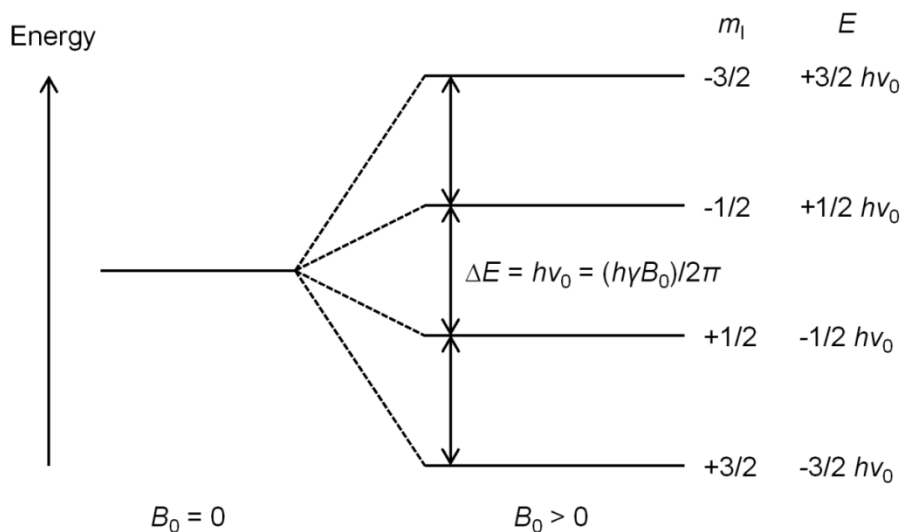
Figure 1-6: Schematic illustration of Zeeman's energy levels that appear for spin-3/2 nucleus placed into the external magnetic field B_0.

The fundamental conditions of the NMR phenomenon for an isolated nucleus (*i.e.*, all internal interactions are ignored), in the presence of the external magnetic field B_0, is that it undergoes single-quantum transitions (transitions between two adjacent energy levels, *e.g.*, $m = -1/2 \leftrightarrow 1/2$) from a low energy state to a high energy state at radio frequency irradiation with a frequency of v_0. The v_0 frequency, named the Larmor frequency, is determined by

$$v_0 = (h\gamma B_0/2\pi)/h = \gamma B_0/2\pi \qquad \textbf{(Equation 1-5)}$$

The magnitude of ΔE is responsible for the population differences between energy levels according to the Boltzmann distribution:

$$\frac{N_\beta}{N_\alpha} = e^{\frac{-\Delta E}{kT}} \qquad \textbf{(Equation 1-6)}$$

where N_β and N_α are the populations of the higher and lower energy levels, respectively, k is the Boltzmann constant and T is temperature in K. It is thus obvious that magnetic field strength, gyromagnetic ratio and temperature affect the population difference and

therefore the intrinsic sensitivity: larger population differences lead to higher intrinsic sensitivity.

1.2.2.2 Chemical Shielding Interaction

Chemical shielding originates from the secondary magnetic field of the electrons induced by the external magnetic field B_0.[7,8] When a molecule/atom is placed in the magnetic field, the circulation of electrons within their orbitals generates an additional local magnetic field. The total effective magnetic field experienced by the nucleus is the summation of this local magnetic field and the external magnetic field B_0. The extent of chemical shielding is therefore dependent on both the nature of nucleus and the structural features of the molecules. The chemical shielding is anisotropic since the electron distribution around a nucleus in a molecule is generally not spherically symmetric.

The chemical shielding Hamiltonian can be written as:[8]

$$\hat{H}_{CS} = -\gamma h \hat{I}_Z \sigma B_0 \qquad \text{(\textbf{Equation 1-7})}$$

where $\hat{I}_Z$ is the z-component of the spin operator, and σ is the chemical shielding tensor, which is described by a 3×3 second-rank matrix. Diagonalization of this matrix yields a tensor with three principle components in its principle axis system (PAS):

$$\sigma_{PAS} = \begin{pmatrix} \sigma_{11} & 0 & 0 \\ 0 & \sigma_{22} & 0 \\ 0 & 0 & \sigma_{33} \end{pmatrix} \qquad \text{(\textbf{Equation 1-8})}$$

The tensor components are ordered in a way that σ_{11} corresponds to the least shielded component and σ_{33} to the most shielded component, *i.e.*, $\sigma_{11} \leq \sigma_{22} \leq \sigma_{33}$. The chemical shielding tensor σ illustrates the orientation dependence of chemical shielding (referred to as chemical shielding anisotropy, CSA, shown in Figure 1-7). From Equation 1-7, the chemical shielding is proportional to the applied external magnetic field B_0, hence the line broadening due to the CSA effect is more significant at higher fields.

The chemical shielding interaction makes the nuclei with different local environments precess at different frequencies, and therefore have different chemical shift

values.[7-9] Chemical shift values are reported relative to a standard reference sample, using the following relationship between chemical shift and chemical shielding:

$$\delta(\text{sample}) = \frac{\sigma(\text{reference}) - \sigma(\text{sample})}{1 - \sigma(\text{reference})} \approx \sigma(\text{reference}) - \sigma(\text{sample})$$

(**Equation 1-9**)
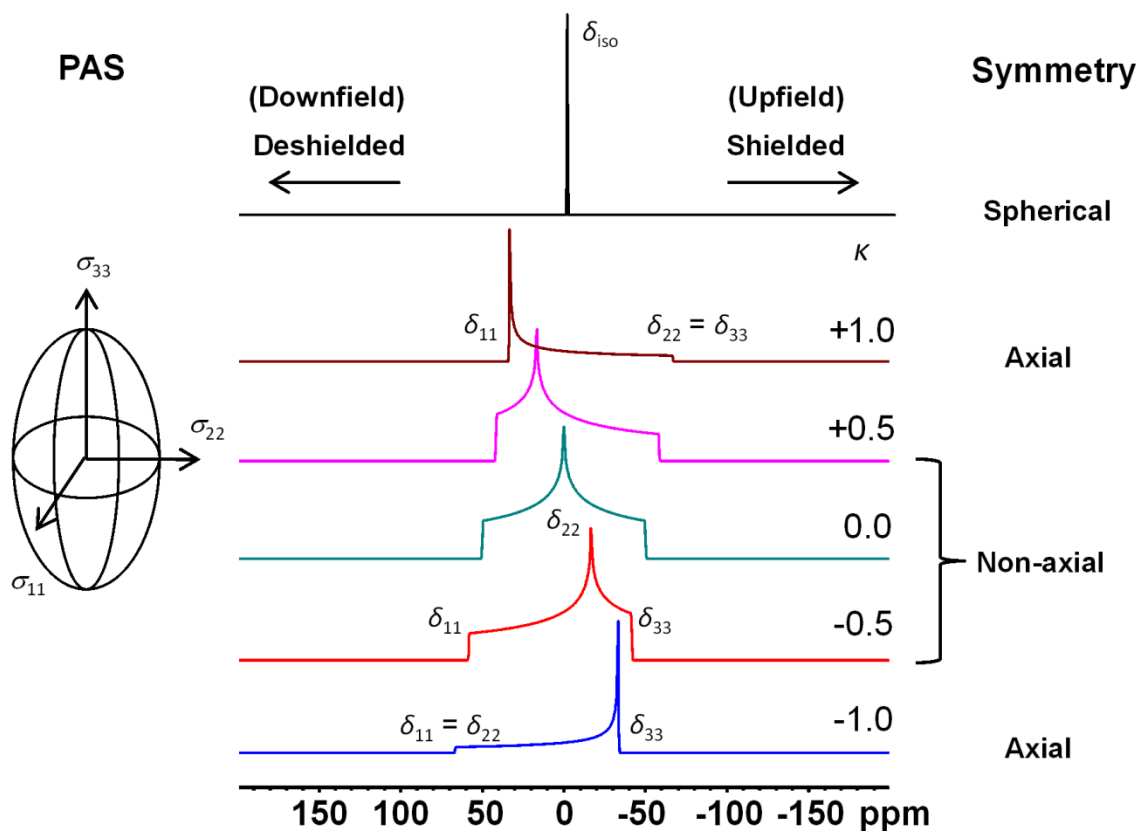
Figure 1-7: Left: ellipsoid representation of the chemical shielding tensor, whose principle axes coincide with the chemical shielding tensor principle axis system and the length of each principle axis of which is proportional to the principle value of the shielding tensor associated with that principle axis. Right: analytical simulations (performed using DMFIT software) of theoretical ^{13}C CSA powder patterns ($\delta_{\text{iso}} = 0$ ppm). Ω is set to 0 ppm for the top spectrum while it is 200 ppm for the other spectra.

The approximation in Equation 1-9 holds for all the nuclei studied in this thesis. Since chemical shielding interaction in Hz is field dependent, a field independent scale

(ppm, parts per million) is typically used. If the isotropic chemical shift $\delta_{iso} > 0$, the nucleus is deshielded relative to the reference; while if $\delta_{iso} < 0$, the nucleus is shielded.

In a solid powder sample, molecules are orientated randomly in an infinite number of possible orientations with respect to the external magnetic field. Therefore, the observed chemical shifts for each individual crystal are distinct, giving rise to a "CSA powder pattern" (Figure 1-7). The shape of the CSA pattern is determined by the three principle components of the chemical shielding tensor, which is sensitive to the local structure around the nucleus of the interest. The Herzfeld-Berger (HB) convention is used in this thesis to describe the chemical shift tensor which is derived from the three principle components of δ_{11}, δ_{22} and δ_{33} ($\delta_{11} \geq \delta_{22} \geq \delta_{33}$, corresponding to σ_{11}, σ_{22} and σ_{33} of the chemical shielding tensor):[31]

$$\delta_{iso} = (\delta_{11} + \delta_{22} + \delta_{33})/3 \qquad \textbf{(Equation 1-10)}$$

$$\Omega = \delta_{11} - \delta_{33} \ (\Omega \geq 0) \qquad \textbf{(Equation 1-11)}$$

$$\kappa = 3(\delta_{22} - \delta_{iso})/\Omega \ (-1 \leq \kappa \leq 1) \qquad \textbf{(Equation 1-12)}$$

where δ_{iso} is the isotropic chemical shift, Ω is the span and κ is the skew.

The isotropic chemical shift, which is the most frequently reported NMR parameter, is the average of the three principle chemical shift components, and equals to the chemical shift value observed in solution spectra. The span determines the width of the CSA powder pattern and the skew describes the shape of the powder pattern. When the nucleus observed is in an axially symmetric environment, two of the three principle components of chemical shift tensor become equivalent (Figure 1-7), yielding a skew value of ±1.

1.2.2.3   Dipolar Coupling Interaction

Direct dipolar coupling interaction, also known as direct dipole-dipole coupling, is a through-space interaction between the magnetic dipole moments of two spins, I and S. [7,8] The two spins involved in the dipolar interaction can be either the same (homonuclear)

or different (heteronuclear). The strength of dipolar coupling interaction is given by the dipolar coupling constant[32,33]

$$D^{IS} = (-\mu_0 \hbar \gamma_I \gamma_S)/4\pi r_{IS}^3 \qquad \textbf{(Equation 1-13)}$$

where μ_0 denotes the vacuum permittivity, $\hbar$ is the reduced Planck constant (h divided by 2π), $\gamma_{I,S}$ are the gyromagnetic ratios of the interacting spins I and S, and r_{IS} is their internuclear distance. It is therefore obvious that the dipolar coupling interaction is field independent. Transformation of the dipolar Hamiltonian into the laboratory frame with the z-direction defined by the external magnetic field, B_0, results the so-called "dipolar alphabet" A, B, C, D, E and F:[33]

$$A = (1 - 3 \, \cos^2 \theta)\hat{I}_Z^I \hat{I}_Z^S$$

$$B = \frac{1}{2}(1 - 3 \, \cos^2 \theta)\left(\hat{I}_Z^I \hat{I}_Z^S - \hat{I}^I \hat{I}^S\right)$$

$$C = -\frac{3}{2}\sin \theta \cos \theta \, e^{-i\phi}\left(\hat{I}_Z^I \hat{I}_+^S + \hat{I}_+^I \hat{I}_Z^S\right)$$

$$D = -\frac{3}{2}\sin \theta \cos \theta \, e^{-i\phi}\left(\hat{I}_Z^I \hat{I}_-^S + \hat{I}_-^I \hat{I}_Z^S\right)$$

$$E = -\frac{3}{4}\sin^2 \theta \, e^{-2i\phi}\hat{I}_+^I \hat{I}_+^S$$

$$F = -\frac{3}{4}\sin^2 \theta \, e^{2i\phi}\hat{I}_-^I \hat{I}_-^S \qquad \textbf{(Equation 1-14)}$$

where the vector $\mathbf{r}_{IS}$ connects the coupled spins I and S. In the dipolar alphabet, $\mathbf{r}_{IS}$ is expressed in terms of its polar coordinates (r_{IS}, θ, ϕ), describing the orientation of $\mathbf{r}_{IS}$ with respect to the laboratory frame. The raising and lowering operators $\hat{I}_\pm$ are defined as $\hat{I}_\pm = \frac{1}{\sqrt{2}}\left(\hat{I}_X \pm i\hat{I}_Y\right)$.

The shape of spectra is mainly determined by the first two secular (time-independent) terms A and B, since terms C to F do not commute with the Zeeman Hamiltonian and thus have negligible effects on the energy. If only the secular terms are counted, the dipolar interaction can be divided in to a static term and an exchange term

(detailed analyses are shown in the literature[33]). The static term can be viewed as the interaction of a spin I with the dipolar field of another spin S. Depending on the orientation, *i.e.*, parallel or anti-parallel, of the second spin, two energy levels can be distinguished, which means that the static term gives rise to a doublet splitting. The energy splitting is determined by the orientation dependence $\propto (1 - 3\cos^2\theta)$ (θ refers to the angle between the internuclear vector $\mathbf{r}^{IS}$ and B_0) of the terms A and B. Therefore, for a powder sample, doublet splitting arising from all of the different orientations of the internuclear vector is observed at the same time, yielding the famous "Pake doublet" (Figure 1-8).[32] The "horns" of the Pake doublet correspond to the spin pairs whose internuclear vector is perpendicular to the external magnetic field ($\theta = 90°$). The "feet" of the Pake doublet are due to the spin pairs whose internuclear vector is along the magnetic field ($\theta = 0°$). The former situation is most probable and has the highest intensity while the latter situation is statistically least favorable. The exchange term is negligible if the difference between Larmor frequencies of both nuclei is large compared to the dipolar coupling, *i.e.*, heteronuclear dipolar coupling.
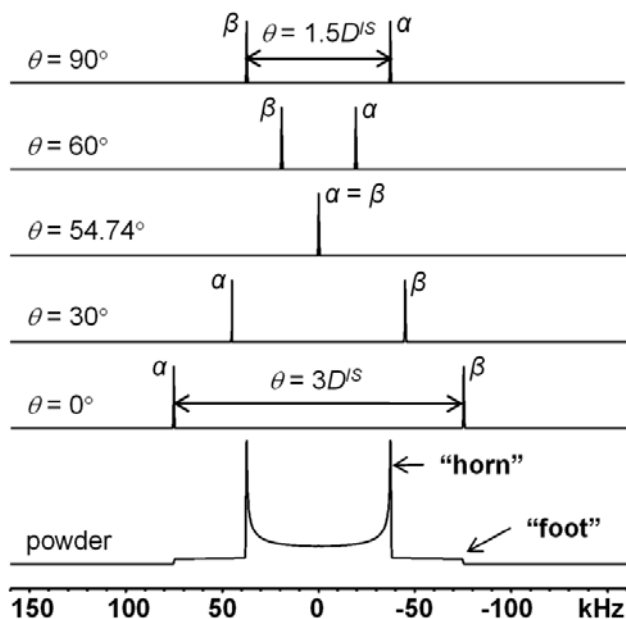
Figure 1-8: Analytical simulations (performed using DMFIT software) of theoretical ^{1}H–^{1}H homonuclear dipolar coupling powder patterns. D^{IS} is set to 50 kHz. For heteronuclear dipolar coupling, the doublet splitting is D^{IS} at 90° and $2D^{IS}$ at 0°.

1.2.2.4   J-Coupling Interaction

The J-coupling (also called scalar or indirect spin-spin coupling) is an indirect interaction of nuclear magnetic moments mediated via the electrons in the chemical bonds between the nuclei.[7,8] The perturbation of the surrounding electrons by the first spin, I, has an effect on the second spin, S. Therefore, J-coupling is a through-bond interaction in contrast to dipolar coupling, which is a through-space interaction. The J-coupling between I and S generates a splitting of the peaks in I and S spectra into $2S +1$ and $2I + 1$ evenly spaced peaks, respectively. Although J-coupling provides direct information on the nature of the chemical bonds, it is typically not observed in solids since the strength of J-coupling is much smaller than other interactions.

1.2.2.5   Quadrupolar Coupling Interaction

For a nucleus with $I > 1/2$ (quadrupolar nucleus), the quadrupolar coupling interaction occurs between the nuclear quadrupole moment (Q) and the local electric field gradient (EFG) at the nucleus.[7,8] It is known that the nuclear charge distribution of quadrupolar nucleus is non-spherical, giving rise to a quadrupole moment (Figure 1-9). In this way, the nucleus can be conveniently visualized as an ellipsoid, where the degree of distortion is determined by the magnitude of Q.[8] The quadrupole moment is therefore an internal property of a nucleus. The local electric field gradient is generated by the non-spherical charge distribution around the nucleus of interest.
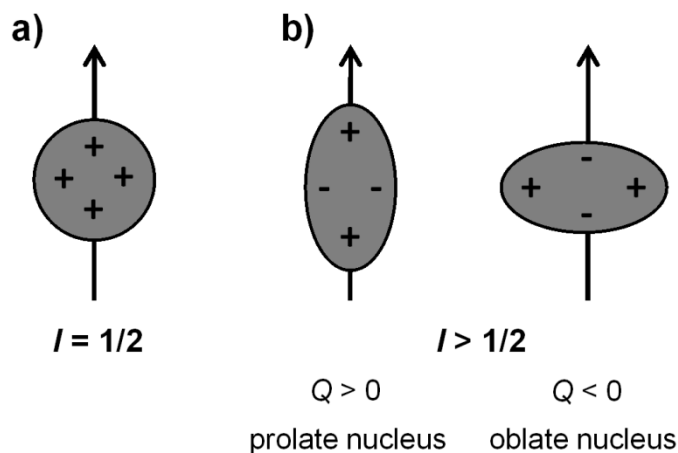
Figure 1-9: Charge distribution in (a) spin-1/2 nuclei and (b) quadrupolar nuclei.

Similar to chemical shielding, a second-rank EFG tensor is also used to describe the quadrupolar coupling interaction, which is diagonal in its principle axis system, with three nonzero components V_{XX}, V_{YY} and V_{ZZ}.[8] The three components are set such that $|V_{XX}| \leq |V_{YY}| \leq |V_{ZZ}|$, and they satisfy $V_{XX} + V_{YY} + V_{ZZ} = 0$. Two EFG parameters are typically reported, including nuclear quadrupolar coupling constant (C_Q) and asymmetry parameter (η_Q):

$$C_Q = (eQV_{ZZ})/h \qquad \textbf{(Equation 1-15)}$$

$$\eta_Q = (V_{XX} - V_{YY})/V_{ZZ} \ (0 \leq \eta_Q \leq 1) \qquad \textbf{(Equation 1-16)}$$

Although C_Q has a sign, NMR experiments can only measure its absolute value. The magnitude of C_Q indicates the strength of the quadrupolar interaction, which is determined by the spherical geometry around the nucleus of interest: a perfectly spherical symmetric coordination environment, including fourfold tetrahedral, sixfold octahedral, and eightfold cubic, gives rise to a zero C_Q. On the other hand, η_Q describes the axial symmetry at the nucleus. A zero η_Q corresponds to an axial symmetry with a C_3 or higher rotation axis.

When the quadrupolar interaction is small compared to the Zeeman interaction, it can be treated as a perturbation to the Zeeman energy levels. The condition is satisfied when the Larmor frequency ν_0 is much greater than the quadrupolar frequency[34]

$$\nu_Q = 3C_Q/2I(2I - 1) \qquad \textbf{(Equation 1-17)}$$

As Figure 1-10 illustrates, the $2I + 1$ Zeeman energy levels are perturbed to different extents by the quadrupolar interaction.[35] Within the first-order perturbation scheme, the central transition (CT, *i.e.*, $m = -1/2 \leftrightarrow 1/2$) of half-integer quadrupolar nuclei is unaffected; whereas all the satellite transitions (STs, *e.g.*, $m = -3/2 \leftrightarrow -1/2$) are significantly broadened. Therefore, the CT is favored in SSNMR experiments since it generates much narrower and more intense NMR pattern than the STs. Nevertheless, the CT is broadened by the second-order quadrupolar interaction. It was demonstrated that the total breadth for the CT in a static sample is given by[34]

$$\Delta\nu_{CT} = (25 + 22\eta_Q + \eta_Q^2)A/144 \qquad \textbf{(Equation 1-18)}$$

with parameter $A = [I(I+1) - 3/4]\nu_Q^2/\nu_0$. It is hence obvious that the line broadening of the CT, due to the second-order quadrupolar interaction, is inversely proportional to the strength of external magnetic field B_0, which is opposite to the broadening from CSA. The simulated powder patterns of the CT for a spin 5/2 nucleus (e.g., ^{25}Mg) are shown in Figure 1-11.
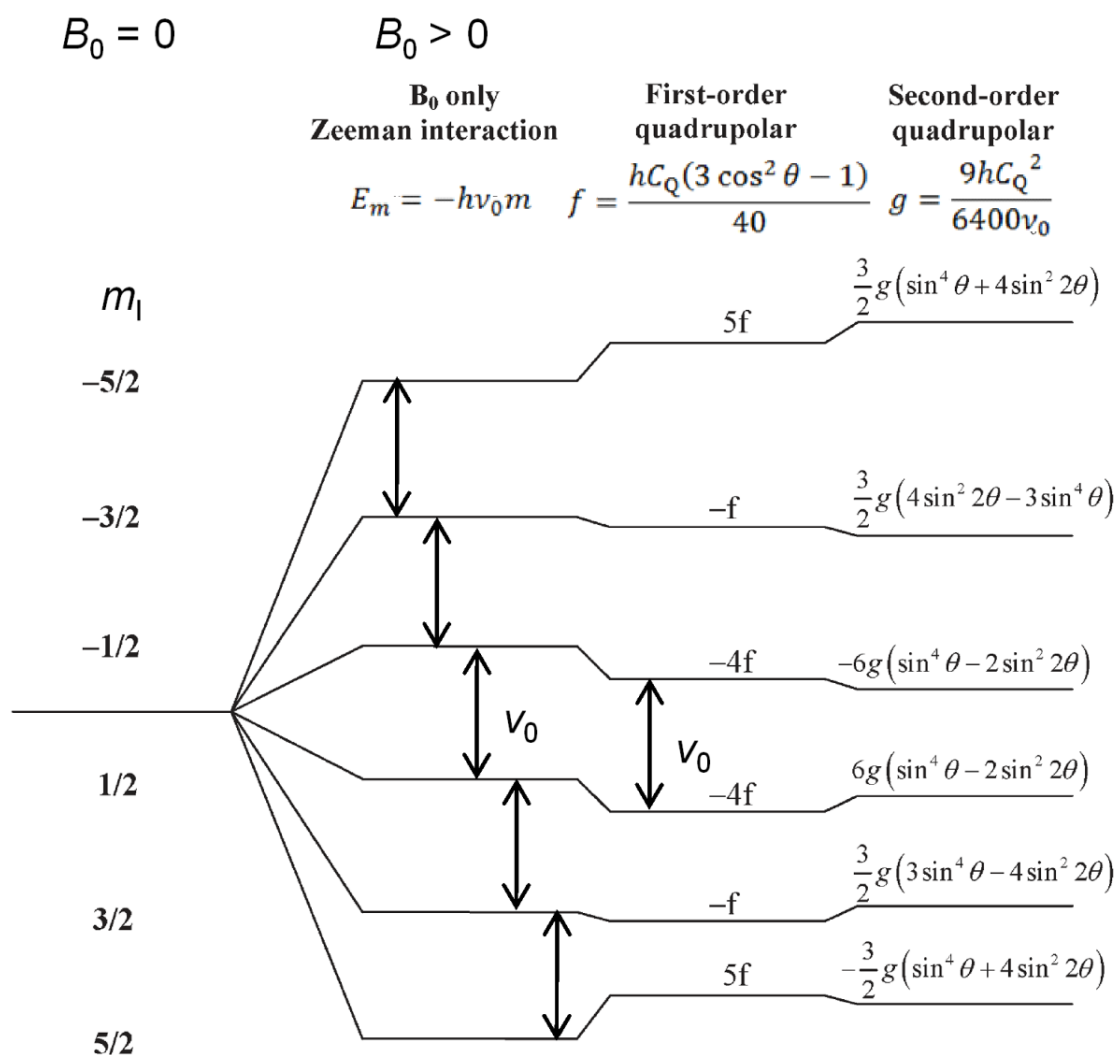
Figure 1-10: Energy level diagram of a spin-5/2 nucleus, showing how the splitting due to the Zeeman interaction is perturbed to first- and second-order by the quadrupolar interaction. (Ref. 34)
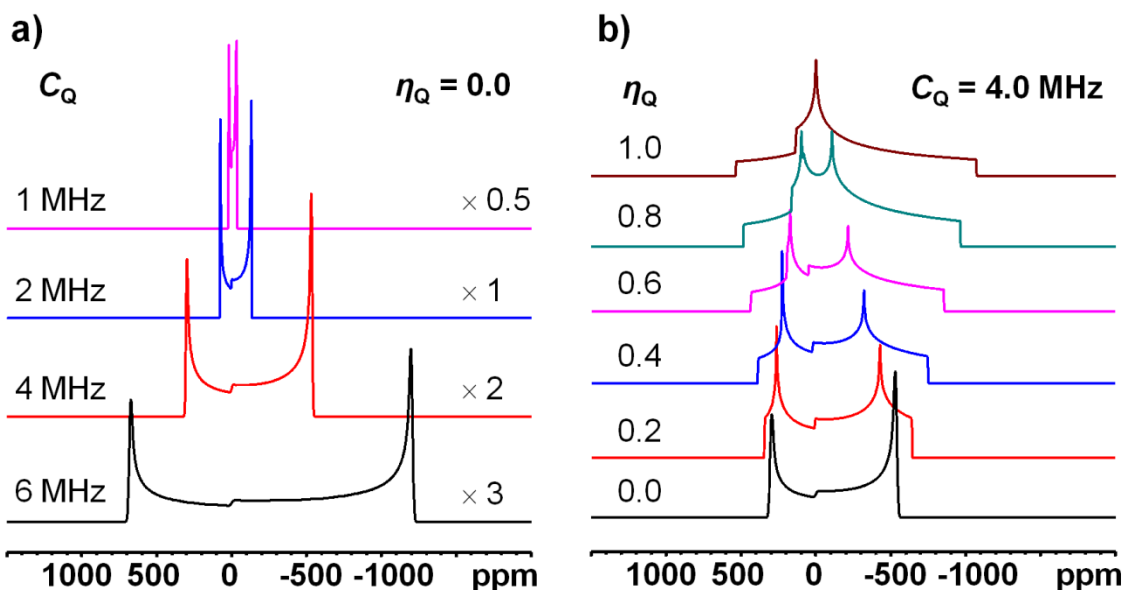
Figure 1-11: Analytical simulations (performed using DMFIT software) of theoretical ^{25}Mg (I = 5/2) powder patterns of the CT (v_0 = 24.5 MHz, δ_{iso} = 0 ppm) at 9.4 T, broadened by the second-order quadrupolar interaction. The effects of (a) C_Q and (b) η_Q towards the line width and shape are also illustrated.

The spectra of quadrupolar nuclei are sometimes broadened by both the CSA and the quadrupolar interactions, giving rise to very complicated line shapes. The CSA and EFG tensors typically do not have the same orientation. In such case, three Euler angles are used to define their relative orientations: α, β, and γ (0° $\leq \alpha \leq$ 360°; 0° $\leq \beta \leq$ 180°, β is the angle between δ_{33} and V_{ZZ}; 0° $\leq \gamma \leq$ 360°). These angles describe the rotations necessary to have the principle axis systems of two tensors coincide. The so-called "z–y–z" Rose convention[36] (also known as passive rotations[37]) for Euler angles is used in this thesis. All rotations are in a counter-clockwise fashion (right-handed, mathematically positive sense).

1.2.3   Experimental Background

A wide variety of NMR-active nuclei were studied in this thesis, including both spin-1/2 nuclei (*e.g.*, ^{1}H) and quadrupolar nuclei (*e.g.*, ^{2}H and ^{25}Mg). Their nuclear properties are shown in Table 1-3.[38,39]

Table 1-3: Nuclear properties of nuclei studied in this thesis.

Nuclei	Spin (I)	N.A. (%)	Q (millibarn)	γ ($\times 10^7$ rad·T^{-1}·s^{-1})	ν_0 (MHz) at 9.4 T	ν_0 (MHz) at 21.1 T
^{1}H	1/2	99.98	0	26.75	400.0	900.0
^{2}H	1	0.015	2.860	4.11	61.4	138.2
^{13}C	1/2	1.108	0	6.73	100.6	226.3
^{17}O	5/2	0.037	-25.58	-3.63	54.2	122.0
^{23}Na	3/2	100	104	7.08	105.8	238.1
^{25}Mg	5/2	10.0	199.4	-1.64	24.5	55.1
^{29}Si	1/2	4.7	0	-5.32	79.5	178.8
^{39}K	3/2	93.1	58.5	1.25	18.7	42.0
^{47}Ti	5/2	7.28	302	-1.51054	22.557	50.745
^{49}Ti	7/2	5.51	247	-1.51095	22.563	50.759

The challenges of studying these nuclei by solid-state NMR spectroscopy include: 1) a low intrinsic sensitivity associated with the low-γ nucleus (*e.g.*, ^{39}K), 2) a low natural abundance (*e.g.*, ^{17}O), 3) a large quadrupole moment (*e.g.*, ^{25}Mg and $^{47/49}$Ti), 4) two NMR-active isotopes with very similar Larmor frequencies ($^{47/49}$Ti), 5) the strong homonuclear dipolar coupling (^{1}H), and 6) a narrow chemical shift range (^{1}H and ^{25}Mg). Various approaches were used in this thesis to increase the sensitivity and improve the spectral resolution.

1.2.3.1   Isotopic Enrichment/Dilution

The signal intensity in an NMR experiment is proportional to the number of NMR-active nuclei in the sample tube. Therefore, large signal enhancement can be readily achieved by using isotopic-enriched samples. For example, increasing the ^{17}O percentage in a Mg-containing MOF, α-Mg$_3$(HCOO)$_6$, from 0.037% (natural abundance) to 8.9%, allowed the acquisition of high-quality ^{17}O spectrum in 4.3 h at 21.1 T (*Chapter 6*). However, the associated cost for isotopic enrichment is usually high.

Isotopic dilution, on the other hand, is a routine approach in ^{1}H solid-state NMR spectroscopy to improve the spectral resolution.[40,41] The line broadening of ^{1}H in solids is dominated by the strong ^{1}H-^{1}H homonuclear dipolar interaction. Substitution of ^{1}H by ^{2}H, whose gyromagnetic ratio is much smaller (~1/6) than that of ^{1}H, greatly weakens the dipolar coupling network in solids, giving rise to narrower ^{1}H resonance lines (*Chapter 4*).

1.2.3.2   High Magnetic Field

As Equation 1-6 shows, the population difference between adjacent Zeeman energy levels increases with the applied external magnetic field. The signal intensity is proportional to the population difference and therefore increases with applied magnetic field. The development of ultrahigh-field magnets has made the study of many nuclei in solids much more feasible in recent years.

The spectra obtained at different magnetic fields usually look distinct since although chemical shielding and quadrupolar interactions are field dependent, the effects are opposite: The chemical shielding interaction is proportional to the magnetic field strength while the second-order quadrupolar interaction is inversely proportional to B_0. In this thesis, some nuclei were studied at 21.1 T, benefitting from higher sensitivity, narrower second-order quadrupolar pattern, and stronger CSA effect.

1.2.3.3   Magic-Angle Spinning (MAS)

A simple, but very useful approach to obtain high-resolution solid-state NMR spectra is to rotate the sample at an angle of 54.74° (the so-called "magic-angle") with respect to the external magnetic field B_0 (Figure 1-12a).[42,43] Many NMR interactions, including chemical shielding, dipolar and first-order quadrupolar coupling interactions, are averaged under the magic-angle spinning (MAS) scheme. All of these interactions have essentially the same spatial orientational dependence of $(3\cos^2\theta - 1)$, where θ is the angle between B_0 and 1) the principle axis frame about which the chemical shielding tensor is defined (chemical shielding), 2) V_{ZZ} (quadrupolar coupling), or 3) the internuclear vector $\mathbf{r}_{IS}$ (dipolar coupling). When $\theta = 54.74°$, the term $(3\cos^2\theta - 1)$ is zero thus the spatial dependencies are removed. Actually, the anisotropic interactions can only be completely averaged out when the spinning speed of the sample, ν_{rot}, is sufficiently high (greater than the magnitude of these interactions in Hz). If not, these interactions will be modulated by the sample rotation, generating a series of peaks (*i.e.*, spinning sidebands, Figure 1-12b) which are evenly spaced with a separation equal to the spinning speed in Hz. The spinning sideband pattern at a low spinning frequency resembles the line shape of the static spectrum.
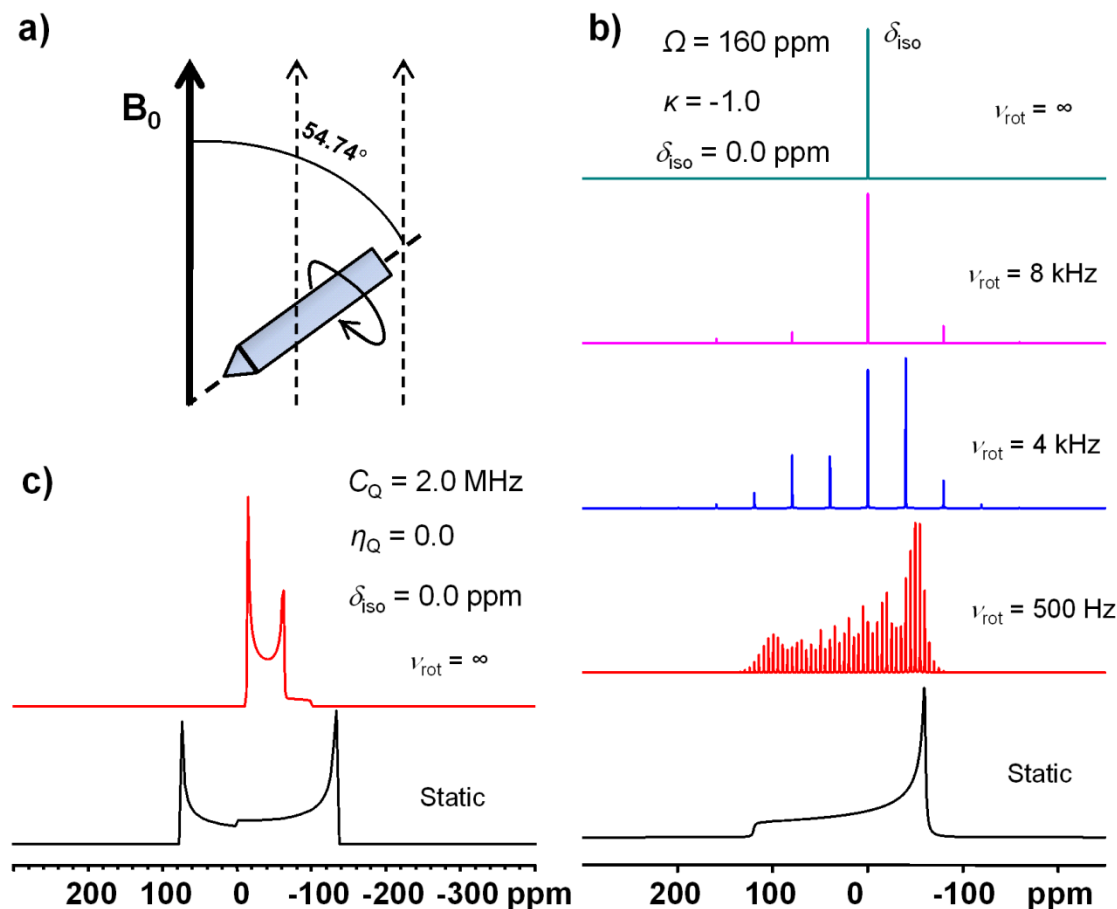
Figure 1-12: (a) Schematic diagram of the magic-angle spinning (MAS) experiment. Analytical simulations (performed using DMFIT software) of (b) theoretical ^{13}C ($I = 1/2$, $v_0 = 100.6$ MHz) CSA patterns and (c) ^{25}Mg ($I = 5/2$, $v_0 = 24.5$ MHz) quadrupolar patterns of the CT at 9.4 T, under MAS and static conditions.

The second-order quadrupolar interaction, however, has a more complicated spatial dependence term. Spinning the sample at a fixed angle will never completely average out the line broadening due to the second-order quadrupolar interaction. Nevertheless, MAS experiment is still extensively used to study quadrupolar nuclei. On the one hand, it produces NMR spectra that are not affected by the CSA. Furthermore, the line broadening induced by the residual second-order quadrupolar interaction is only 1/2–1/3 of the line broadening under the static condition (Figure 1-12c), giving rise to much better spectral resolution.[7,8] The signal intensity also increases simultaneously in the MAS experiment.

1.2.3.4　Cross-Polarization (CP)
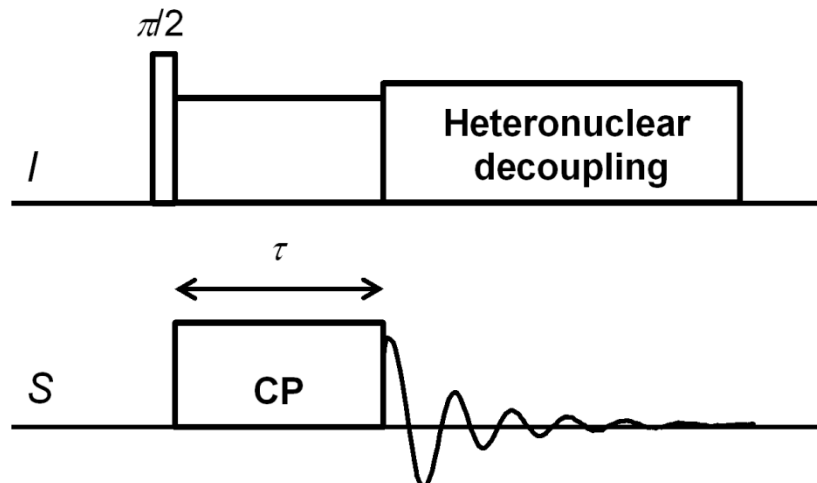
Figure 1-13: Pulse sequence for cross-polarization from abundant spin I to dilute spin S with detection of the S magnetization. τ is the contact time.

Cross-polarization (CP) is a routine technique to enhance the signal of a dilute and insensitive spin S by transferring the magnetization from an abundant spin I, which has a higher sensitivity, via the dipolar coupling between I and S. The most common nuclei involved in CP experiments are ^{1}H (the source of magnetization) and another spin-1/2 nucleus such as ^{13}C and ^{29}Si. The Hartmann-Hahn matching conditions are required for the observation of CP signal:[44]

Static condition $\qquad \gamma_I B_1(I) = \gamma_S B_1(S)$ $\qquad$ (**Equation 1-19**)

MAS condition $\qquad \gamma_I B_1(I) = \gamma_S B_1(S) \pm n\nu_{rot}$ $\qquad$ (**Equation 1-20**)

where B_1 is the strength of the radio frequency field, n is an interger, and ν_{rot} is the spinning speed. Under CP experiment, the transfer of magnetization occurs during the contact time τ (Figure 1-13). The intensity of CP signal hence varies with the contact time. The initial growth of CP signal is governed by the cross-polarization time constant (T_{CP}), which is determined by the heteronuclear dipolar coupling interaction. The decay of the magnetization at longer contact times is dictated by the proton (if I is ^{1}H) spin-lattice relaxation time in the rotating frame of the reference ($T_{1\rho}^H$). The CP dynamics[45]

(Figure 1-14) can be described by

$$S(\tau) = S_{max}(1 - \frac{T_{CP}}{T_{1\rho}^{H}})^{-1}[\exp\left(-\frac{\tau}{T_{1\rho}^{H}}\right) - \exp(-\frac{\tau}{T_{CP}})]$$

(**Equation 1-21**)

where $S(\tau)$ is the CP intensity at the contact time τ and S_{max} is the maximum CP intensity. Shorter internuclear distance corresponds to stronger dipolar coupling, and thus faster signal build-up speed. Therefore, CP is also broadly used as a spectral editing technique. Using a very short contact time, only the spins which are in close proximity in space can be detected since the dipolar coupling is strongly dependent on the internuclear distance r_{IS} ($\propto 1/r_{IS}^{3}$).
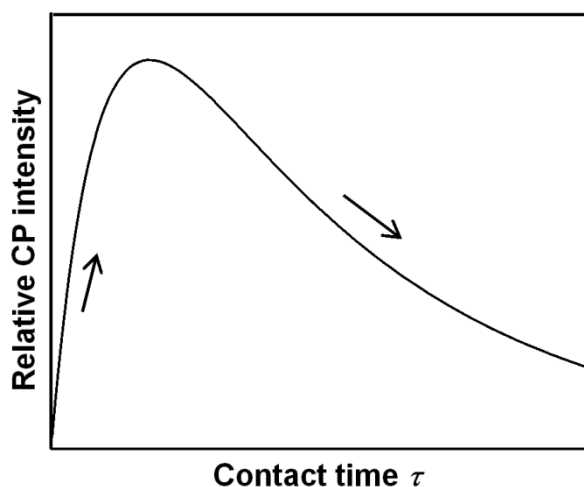
Figure 1-14: Plot of the CP signal intensity as a function of the contact time τ.

Heteronuclear correlation (HETCOR) experiment can be conveniently viewed as a two-dimensional version of CP experiments.[46-48] Herein, ^{1}H-^{13}C frequency-switched Lee-Goldberg (FSLG) HETCOR experiments (Figure 1-15) were performed to probe the connectivity between ^{1}H and ^{13}C (*Chapter 4*). FSLG is a homonuclear decoupling technique for ^{1}H, providing excellent resolution along the indirect (^{1}H) dimension.[49,50] The application of the magic-angle pulse (θ_{m}) produces an effective field in the rotating frame inclined at the magic-angle with respect to the static field B_{0}. FSLG irradiation between two magic-angle pulses makes the spin precess rapidly around this magic-angle

axis, resulting in an average of ^{1}H–^{1}H homonuclear dipolar coupling interaction. Two-pulse phase-modulation (TPPM) sequence[51] is used for the heteronuclear decoupling, which involves the fast alternation of the phase of the rf pulse with a length τ_p (*i.e.*, TPPM pulse length), between two values $+\phi/2$ and $-\phi/2$ (ϕ is called TPPM angle). TPPM has been demonstrated to greatly reduce the residual line broadening arising from insufficient proton decoupling power.
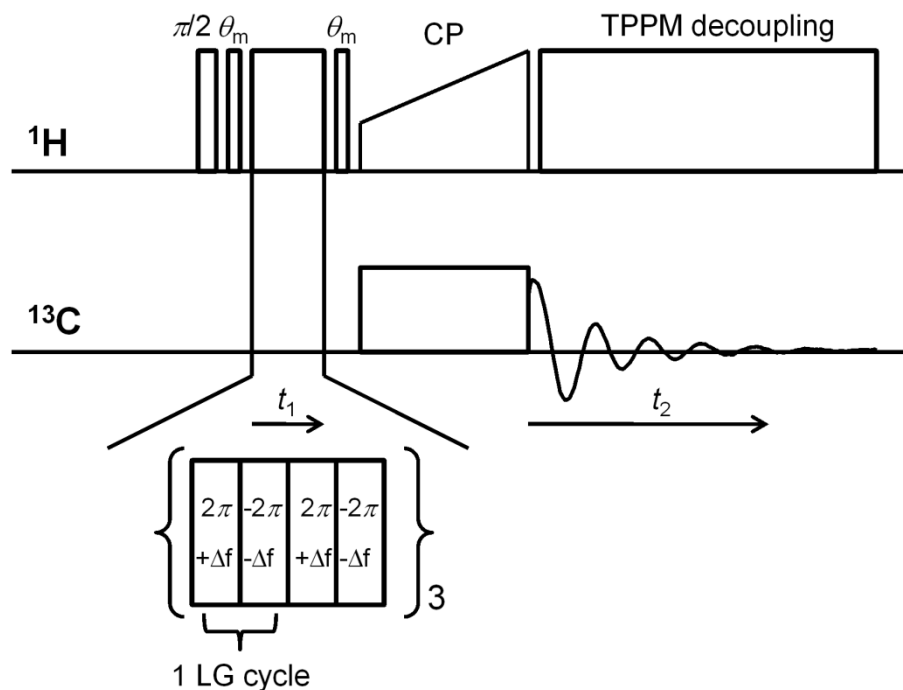
Figure 1-15: Pulse sequence for ^{1}H–^{13}C FSLG-HETCOR. θ_m is the magic-angle pulse (54.74°).

1.2.3.5   Quadrupolar Carr-Purcell-Meiboom-Gill (QCPMG)

Some nuclei studied in this thesis, such as $^{47/49}$Ti, have very low gyromagnetic ratios (γ), resulting in low intrinsic sensitivities and severe probe ringing effect (which distorts the line shape). In addition, these nuclei usually have low natural abundances and large quadrupole moments, giving rise to spectra extending several tens or hundreds kHz, or even a few MHz. A sensitivity enhancement technique, quadrupolar Carr-Purcell-Meiboom-Gill (QCPMG), was employed in this thesis to study these NMR-insensitive quadrupolar nuclei.[52]
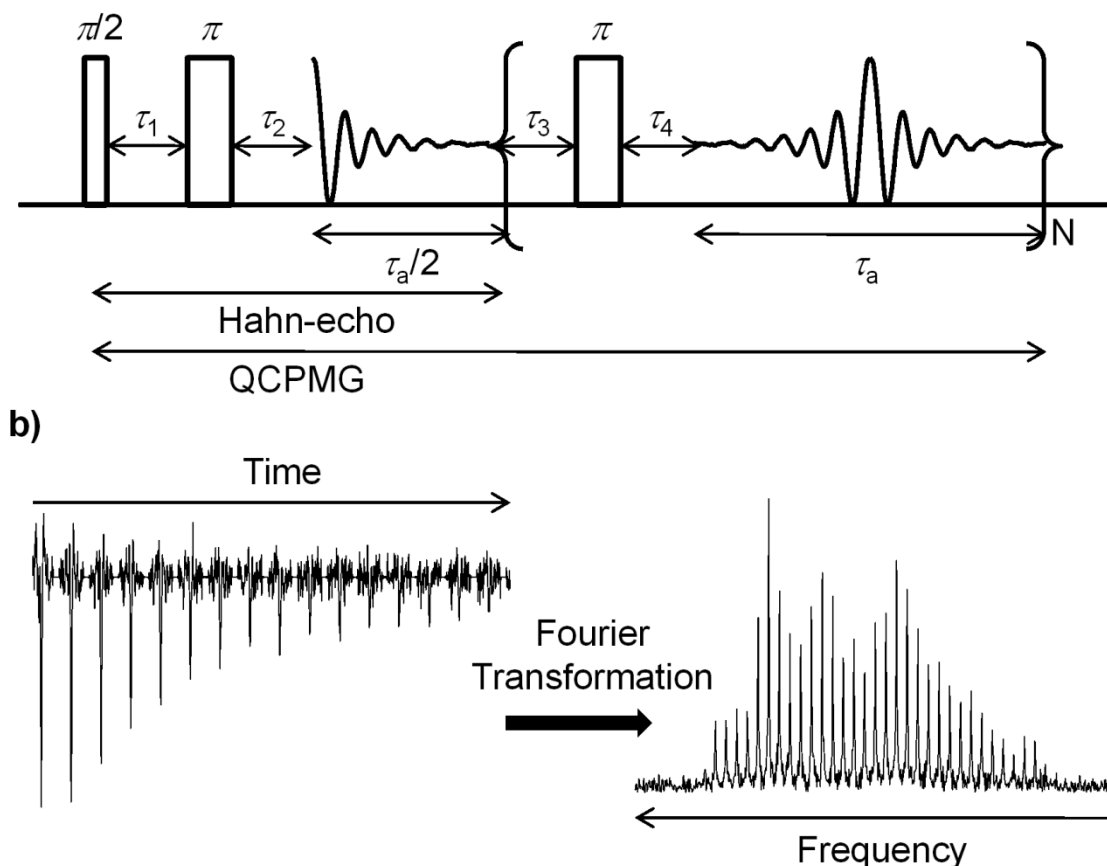
Figure 1-16: (a) The QCPMG pulse sequence. The block inside the brackets is called a Meiboom-Gill (MG) loop and it is repeated for N times. (b) An example of FID and spectrum of the QCPMG experiment.

As Figure 1-16 illustrates, the first part of the sequence is a regular Hahn-echo $(90°\text{-}\tau_1\text{-}180°)$[53] with the τ_2 (pre-acquisition delay) being adjusted so that the acquisition starts at the echo maximum. The second part is the N-repeated units consisting of a 180° refocusing pulse followed by sampling of the echo for a period of τ_a. Both τ_3 and τ_4 are delays to prevent breakthrough pulses. The FID acquired in QCPMG experiment is thus a train of several individual echoes. The spectrum after Fourier transformation shows many "spikelets" evenly separated by $1/\tau_a$, the envelope of which resembles the line shape of a regular Hahn-echo spectrum. Information about both "homogenous" (*e.g.*, dipolar coupling) and "inhomogenous" (*e.g.*, chemical shielding and quadrupolar coupling) interactions[54] may be extracted from the QCPMG spikelet spectrum. The homogeneous interactions affect the line shapes of the spikelets; whereas the envelope of the spikelet

manifold is determined by the inhomogenous interactions. A considerable increase in the overall sensitivity is achieved in the QCPMG experiment since the signal intensity is distributed among a limited number of spikelets, rather than a continuous broad profile. In addition, with the use of the QCPMG technique the total acquired signal is increased by collecting multiple echoes in a single scan.[55]

Another problem associated with broad NMR patterns is that they are often broader than the excitation bandwidth (typically a few tens of kHz). Two approaches were combined with QCPMG to solve this problem. The first approach is to acquire a series of spectra whose transmitter frequencies are varied in even increments and then added them together, generating the final spectrum.[56] The frequency step size (or offset) has to be chosen carefully to ensure it is uniformly excited across the whole line width. The second approach is to use the wideband uniform-rate smooth truncation (WURST) excitation sequence.[57,58] The WURST sequence exploits the usage of adiabatic pulses which can generate a much broader excitation profile bandwidth than standard rf pulses.

1.2.3.6   Multiple-Quantum MAS (MQMAS)

Multiple-quantum (MQ) NMR experiments are two-dimensional experiments that have four periods: excitation–evolution (t_1)–reconversion–detection (t_2).[59] During the excitation period, the MQ coherences are excited in different ways using a rf pulse. After the evolution time t_1, these MQ coherences are reconverted to the observable single-quantum coherences. Two types of conceptually distinct MQMAS experiments were performed in this thesis.

1.2.3.6.1   Double-Quantum (DQ) MAS

The nuclei studied in double-quantum (DQ) MAS experiments are typically spin-1/2 nuclei such as ^{1}H. Therefore, it is counter-intuitive that how these spin-1/2 nuclei can generate "double-quantum coherences", since spin-1/2 nuclei only have single-quantum transition. It is because the "double-quantum coherences" excited and observed in DQ MAS experiments are virtually not from the DQ transition of a single spin but from spin systems that are coupled by homonuclear dipolar interactions. The Hamiltonian for the dipolar interaction between spin I and S can be written as[33]

$$\widehat{H}_{\mathrm{D}}^{IS} = \widehat{I}^I \times \boldsymbol{D}^{IS} \times \widehat{I}^S \qquad \textbf{(Equation 1-22)}$$

using a coupling tensor $\boldsymbol{D}^{IS}$ which is, in the principle axis system of the interaction, always of symmetric form

$$\boldsymbol{D}^{IS} = -2D^{IS} \times \begin{pmatrix} -1/2 & 0 & 0 \\ 0 & -1/2 & 0 \\ 0 & 0 & 1 \end{pmatrix} \qquad \textbf{(Equation 1-23)}$$

where D^{IS} is the dipolar coupling constant defined in Equation 1-13.

In a similar way, the Hamiltonian for the quadrupolar interaction can also be written using the coupling tensor $\boldsymbol{Q}$ in the form

$$\widehat{H}_{\mathrm{Q}} = \widehat{I} \times \boldsymbol{Q} \times \widehat{I} \qquad \textbf{(Equation 1-24)}$$

where $\boldsymbol{Q}$, in the principle axis system of the interaction, is given by

$$\boldsymbol{Q} = \delta \times \begin{pmatrix} -\frac{1+\eta_Q}{2} & 0 & 0 \\ 0 & -\frac{1-\eta_Q}{2} & 0 \\ 0 & 0 & 1 \end{pmatrix} \qquad \textbf{(Equation 1-25)}$$

η_Q is the asymmetry parameter. δ is related to the quadrupolar frequency ν_Q by

$$\delta = \frac{2}{3}\nu_Q \qquad \textbf{(Equation 1-26)}$$

The formal analogy of the dipolar Hamiltonian and quadrupolar Hamiltonian (Equations 1-22 to 1-26) opens up the possibility of treating the dipolar-coupled systems as individual quadrupolar nucleus. In this way, *e.g.*, the three dipolar-coupled methyl protons become formally equivalent to a spin-3/2 nucleus such as ^{23}Na.

The pulse sequence of the back-to-back (BABA) DQ MAS experiments[60,61] is shown in Figure 1-17. The BABA pulse sequence was used during both excitation and reconversion periods. Other pulse sequences are also employed in DQ MAS experiments, but BABA is one of the most simple and robust schemes. Rotor-synchronization (*i.e.*, the increment in t_1 equals to the rotor period) is always required for BABA DQ MAS

experiments. The observed DQ coherence corresponds to two spins that are coupled by the dipolar interaction due to their close proximity in space. The DQ coherence between two equivalent spins AA (or BB) gives rise to a single peak (self-correlation peak) present on the diagonal of the spectrum. However, the DQ coherence between two non-equivalent spins AB yields two DQ cross peaks with equal intensity, which are symmetric with respect to their positions relative to the diagonal.
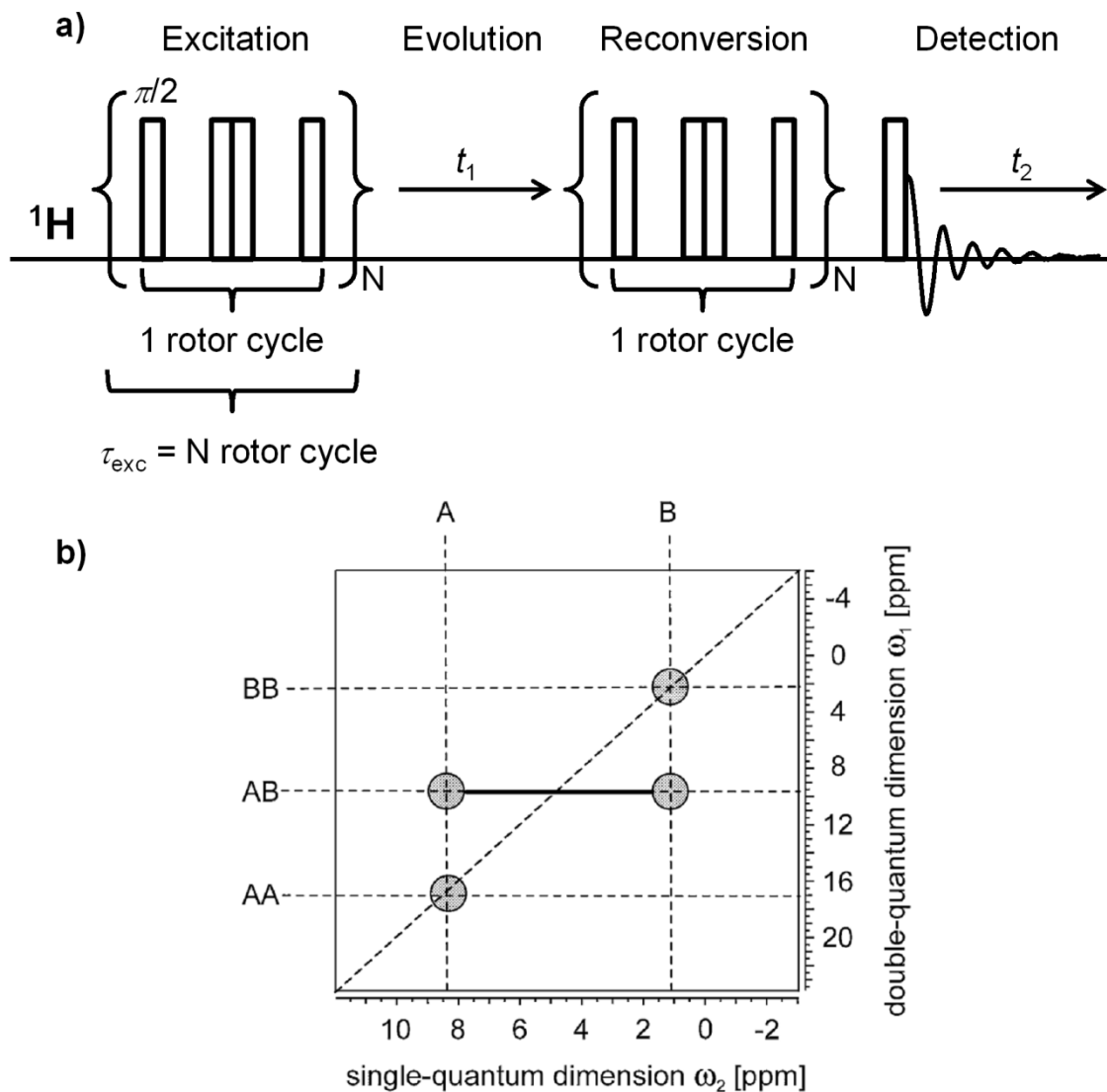
Figure 1-17: (a) Pulse sequence of BABA DQ MAS experiment. N is the number of rotor cycles used for excitation and reconversion. (b) Schematic representation of the typical pattern observed in 2D DQ MAS spectrum (Ref. 32). AA and BB are correlation peaks from two like spins while AB is from two unlike spins.
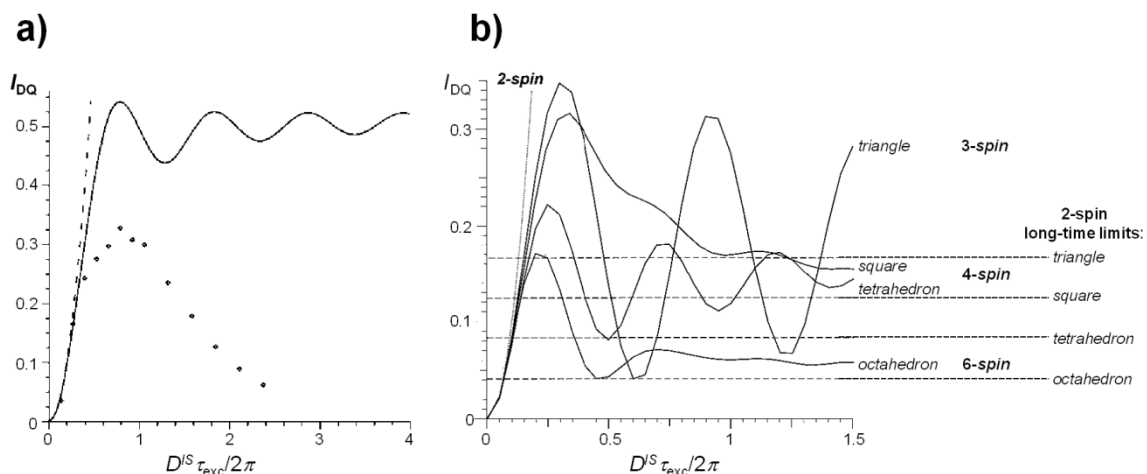
Figure 1-18: (a) Comparison of calculated (solid line) and experimentally (data points) observed DQ signal intensities. The experiments were performed on tribromoacetic acid, which is a ^{1}H–^{1}H spin pair model compound with a dipolar coupling of $D^{IS} = 2\pi \times 6.5$ kHz. I_{DQ} is normalized with respect to the signal of a one-pulse experiment. (b) Simulated DQ build-up curves for different spin systems (solid lines). The three, four, and six spins are localized at the vertices of an equilateral triangle, a square, a tetrahedron, and an octahedron, respectively. I_{DQ} is normalized to the number of coupled pairs in the respective system, and the dashed lines indicate the long-time limit for DQ intensities, provided that only two-spin DQ coherences are excited. The two figures are taken from Ref. 32. The dashed line in (a) or the dotted line in (b) is the leading two-spin term ($I_{DQ} \propto (D^{IS})^2 \tau_{exc}^2$) in the series expansion for multispin systems.

In recent years, DQ MAS experiments have been extensively used to probe the dipolar connectivity and, under favorable conditions, to measure the internuclear distance between two spins.[62,63] As Figure 1-18a shows, the growth of DQ signal (excited using the BABA scheme) is dependent on the strength of dipolar coupling. Although the linear approximation $I_{DQ} \propto (D^{IS})^2 \tau_{exc}^2$ is only valid for weak dipolar coupling or very short excitation times, $D^{IS} \tau_{exc}$ is a constant for maximum I_{DQ}, meaning that spin pairs with stronger dipolar coupling interactions always reach their maximum I_{DQ} faster. Herein I_{DQ} is the double-quantum intensity normalized with respect to the signal of a one-pulse experiment and τ_{exc} is the excitation time. However, the DQ build-up curves are also dependent on the geometry of dipolar-coupled spin systems (Figure 1-18b). Therefore,

unless the dipolar-coupled spins can be considered as an assembly of individual spin pairs (*i.e.*, the perturbation from other spins is weaker than 1/3 of the dominating coupling of interest or the distance to perturbing spins is larger than 3/2 of the considered pair distance),[33] it is extremely challenging to quantitatively measure the internuclear distance by DQ experiments.

1.2.3.6.2   Triple-Quantum MAS (3QMAS)
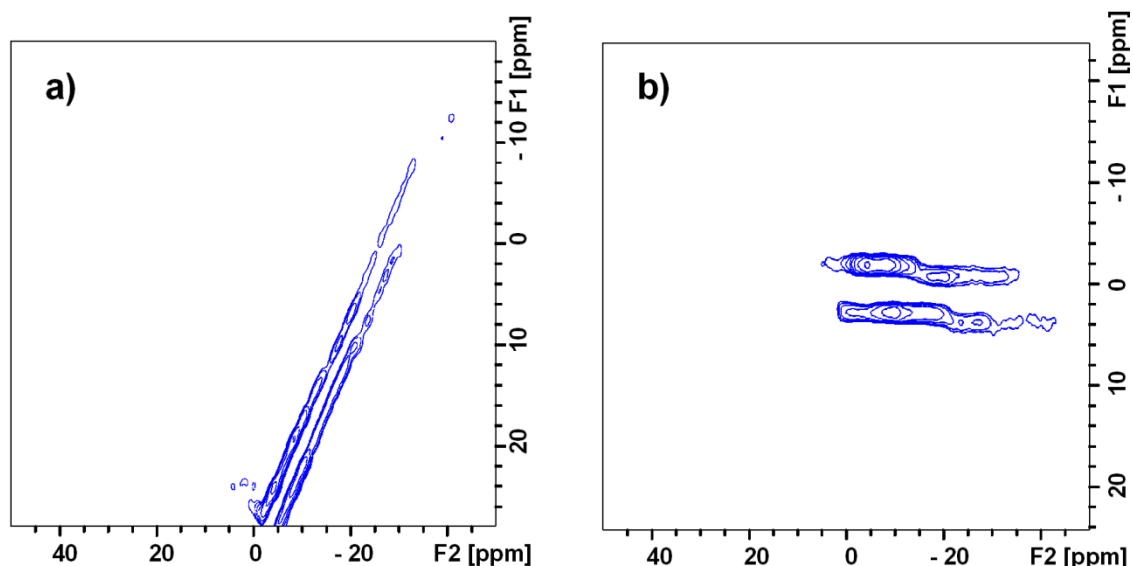
Figure 1-19: An example of 2D 3QMAS spectrum (a) before and (b) after shearing.

Triple-quantum MAS (3QMAS) is a two-dimensional MQMAS experiment initially developed by Frydman and co-workers for spin half-integer quadrupolar nuclei such as ^{23}Na ($I = 3/2$).[64] The principle of 3QMAS is that the second-order quadrupolar broadening of the symmetric triple-quantum transition (*i.e.*, $m = 3/2 \leftrightarrow -3/2$) of half-integer quadrupolar nuclei is related to the second-order quadrupolar broadening of the CT by a ratio. A 2D spectrum is acquired which directly correlates 3Q coherence with SQ coherence. As Figure 1-19 illustrates, this spectrum displays a ridge-like line shape for each site, whose slope equals to the above-mentioned ratio of second-order quadrupolar broadening of two transitions. A projection of the 2D spectrum perpendicular to this slope (which is called as "shearing") yields a spectrum free of quadrupolar broadening in the indirect (F1) dimension.
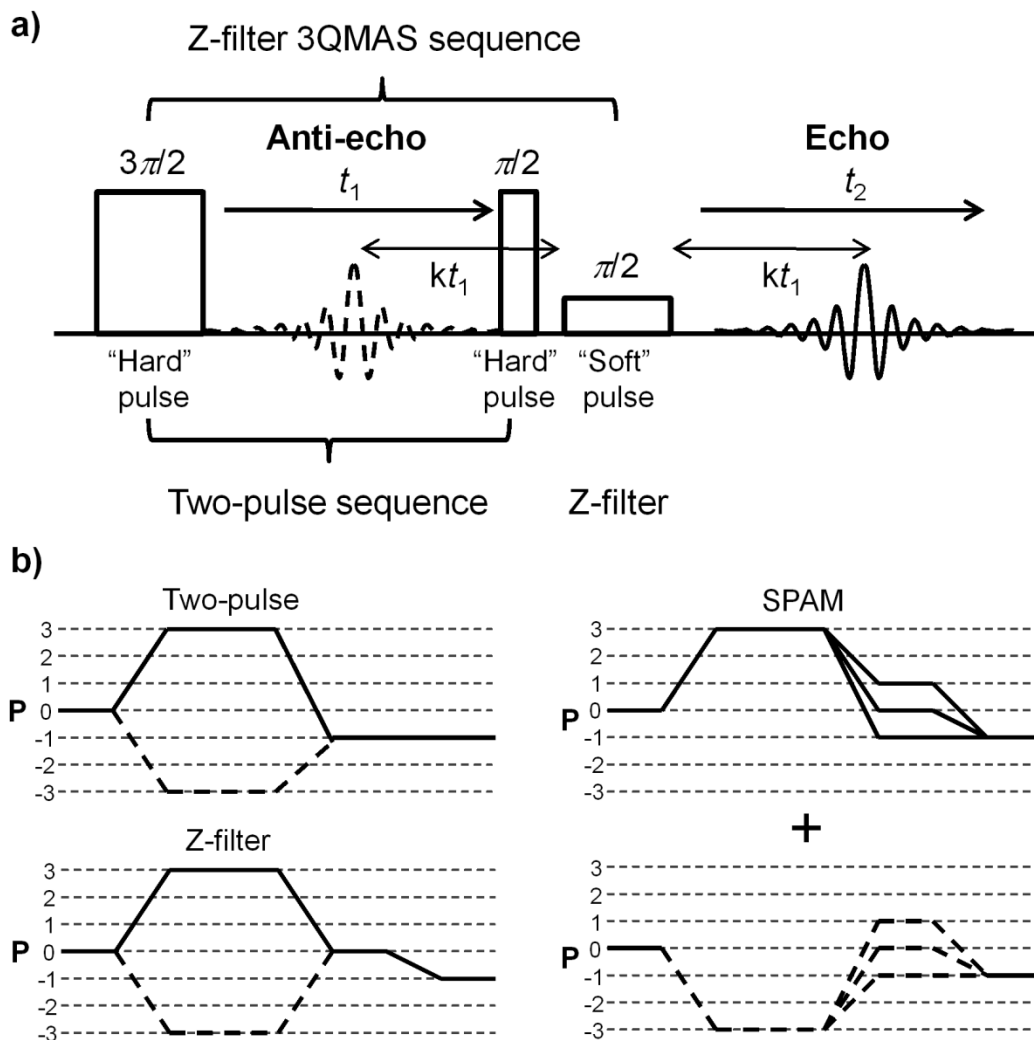
Figure 1-20: (a) The pulse sequence of 3QMAS experiment. (b) The coherence transfer pathway of the two-pulse, Z-filter, and SPAM-3QMAS. The solid line is the echo pathway while the dashed line is the anti-echo pathway. P is the coherence order.

2D 3QMAS spectra can be observed using the two-pulse sequence (Figure 1-20a).[65,66] The first "hard" pulse (at a high power level) excites the 3Q coherences. During the evolution time t_1, the 3Q coherences evolve under second-order quadrupolar interaction. The second "hard" pulse (at the same power level as the first pulse) converts the 3Q coherences to the directly observable $-1Q$ coherence. The coherence transfer pathway is hence $0Q \rightarrow \pm 3Q \rightarrow -1Q$ (Figure 1-20b). The drawback of such classical two-pulse approach is that the pure adsorption spectra can only be obtained if both $\pm 3Q$

are simultaneously selected and if their transfers to the observable signal (–1Q) have the same efficiencies. Unfortunately, the two coherence transfer pathways $0Q \rightarrow +3Q \rightarrow -1Q$ and $0Q \rightarrow -3Q \rightarrow -1Q$ in two-pulse 3QMAS experiment are not symmetric and thus generally do not have the same efficiencies. A solution to this problem is to make the coherence transfer pathway symmetric using the Z-filter principle,[67] which is done by adding a third $\pi/2$ "soft" pulse (at a low power level) following the second $\pi/2$ "hard" pulse. This soft pulse, also called Z-filter pulse if it is phase-cycled, makes the two symmetric coherence transfer pathways ($0Q \rightarrow \pm3Q \rightarrow 0Q \rightarrow -1Q$) possessing the same efficiencies, giving rise to pure adsorption 2D line shape.[68] In addition, the signal of Z-filter 3QMAS experiment is amplitude-modulated (cosine) as a function of t_1, opening up the possibility of using the first 1D spectrum to optimize independently the lengths of the three pulses. The optimized value is typically about $3\pi/2$ for the first pulse and about $\pi/2$ for the second pulse. Rotor synchronization of 3QMAS experiment has additional benefits that spinning sidebands are absent from the indirect dimension and the S/N ratio is also improved since all F1 spinning sidebands are folded back into the center bands.[68]

3QMAS experiments often suffer from a low sensitivity because the excitation of 3Q coherences is quite inefficient. The maximum 3Q signal is only approximately 55% of the CT signal for spin-3/2 nuclei and only 34% for spin-5/2 nuclei.[69] The radio frequency strength required for maximum 3Q intensity is typically ≥ 100 kHz,[69] which is not feasible for many nuclei. Therefore, 3QMAS is rarely used in the literatures to study the low-γ quadrupolar nuclei including ^{25}Mg. In this thesis, a simple but very effective approach, soft-pulse-added-mixing (SPAM),[70,71] was implemented to acquire high-quality 3QMAS spectra of ^{25}Mg. SPAM-3QMAS is derived from the Z-filter 3QMAS by eliminating the phase cycling of the Z-filter pulse. In this way, other coherence transfer pathways including $0Q \rightarrow 3Q \rightarrow \pm1Q \rightarrow -1Q$ and $0Q \rightarrow -3Q \rightarrow \pm1Q \rightarrow -1Q$ are also collected (Figure 1-20b), giving rise to twice or better signals. In 3QMAS experiment, the coherence transfer pathways like $0Q \rightarrow 3Q \rightarrow \pm1Q \rightarrow -1Q$ generates echo signal in the following expression

$$E(t_1, t_2) = \exp(-i\omega_1 t_1)\exp(i\omega_2 t_2) \qquad \textbf{(Equation 1-27)}$$

which has opposite signs in F1 and F2 frequencies; whereas the pathways like $0Q \rightarrow -3Q$ $\rightarrow \pm 1Q \rightarrow -1Q$ generates the anti-echo signal

$$A(t_1, t_2) = \exp(i\omega_1 t_1)\exp(i\omega_2 t_2) \qquad \textbf{(Equation 1-28)}$$

which has identical sign in F1 and F2 frequencies. In contrast with the amplitude-modulated data collected in the Z-filter 3QMAS experiment (*i.e.*, a linear combination of both echo and anti-echo signals), SPAM-3QMAS data are phase-modulated and consist of separated echo and anti-echo signals (echo/anti-echo acquisition mode). The echo/anti-echo data are processed in a way that the real part of the final spectrum is the sum of the anti-echo and complex conjugate echo, displaying pure absorption 2D line shape.[72]

1.2.3.7   Phase-Corrected Magic-Angle Turning (PHORMAT)
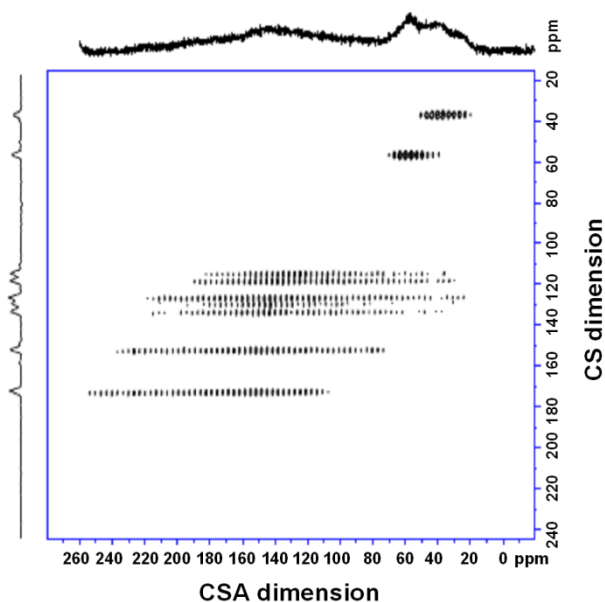
Figure 1-21: The ^{1}H-^{13}C PHORMAT 2D spectrum of tyrosine·HCl (Ref. 73).

Phase-corrected magic-angle turning (PHORMAT) technique[73,74] belongs to a large group of 2D NMR techniques that correlate the isotropic chemical shifts (along the indirect dimension) of spin-1/2 nuclei (*e.g.*, ^{13}C) with the CSA pattern along the direct dimension. One of the first sequences is the magic-angle hopping experiments,[75] which showed that an isotropic-shift spectrum can be obtained in the indirect dimension by

successively positioning a sample at 120° intervals about the magic-angle axis. The average of the three shifts at these positions is equal to the isotropic shift, independent of the orientation of the tensor. A more straightforward approach (magic-angle turning,[76] MAT) was then proposed by using continuous slow rotation of the sample and pulses spaced at 1/3 of the rotor period to obtain the isotropic-shift evolution instead of fast hopping of the sample. PHORMAT is the phase-corrected version of MAT experiments, which overcomes many limitations of previous MAT implementation. A spinning-sideband-free isotropic-shift spectrum is produced along the indirect dimension without the need of spectral shearing (Figure 1-21). PHORMAT data are also collected in the echo/anti-echo mode.

1.2.3.8 ^{2}H NMR
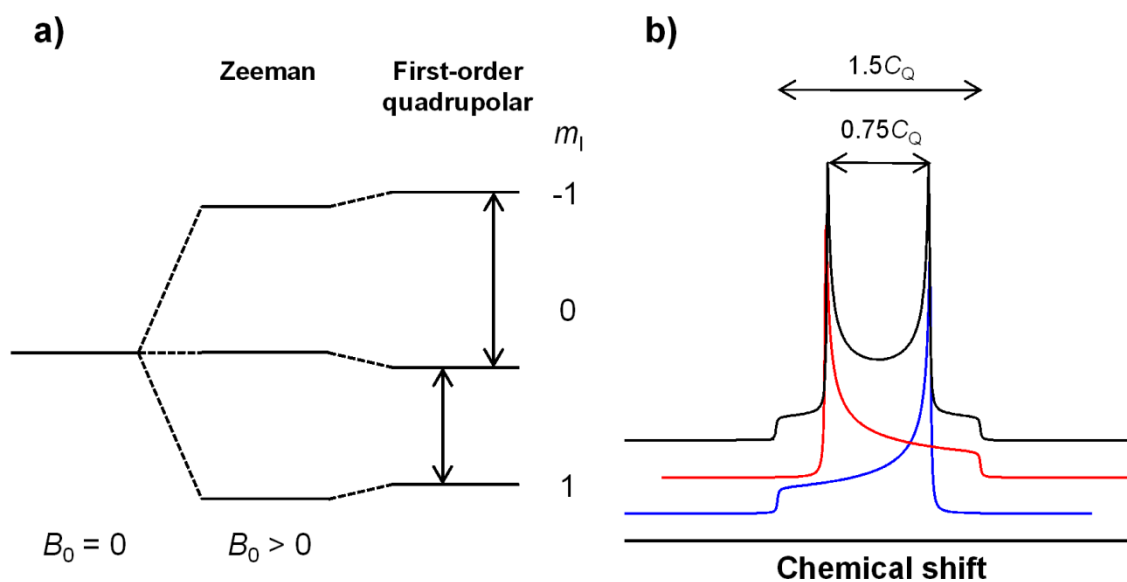
Figure 1-22: (a) Energy level diagram of ^{2}H ($I = 1$), showing how the splitting due to the Zeeman interaction is perturbed to first-order by the quadrupolar interaction. (b) Schematic illustration of the formation of a static ^{2}H powder pattern with a typical Pake doublet ($\eta_Q = 0$). The doublet is due to the two allowed transitions.

^{2}H solid-state NMR spectroscopy is one of the most extensively used tools for studying molecular motion, since its line shape is sensitive to both how the molecule moves and how fast it moves.[7,9-11,37,77] ^{2}H ($I = 1$) is a quadrupolar nucleus with rather

small quadrupole moment (Q = 2.860 mb[39]). Therefore, the quadrupolar coupling constants of ^{2}H are small in most compounds (between 140 and 220 kHz).[7] However, the static ^{2}H NMR pattern is significantly broadened by the first-order quadrupolar interaction due to the absence of the CT (Figure 1-22). Other NMR interactions including chemical shielding and dipolar coupling are typically negligible compared to the first-order quadrupolar interaction. The two allowed transitions (m = 1 $\leftrightarrow$ 0 and 0 $\leftrightarrow$ –1) give rise to a symmetric doublet powder line shape. When $\eta_Q = 0$, the resulting ^{2}H spectrum is a typical Pake doublet with the horn separation equal to 0.75C_Q.

A static C–^{2}H or O–^{2}H bond always displays a Pake doublet-like NMR pattern because ^{2}H is in an axial-symmetric environment (V_{ZZ} is along the bond while V_{XX} and V_{YY} are equal and both are perpendicular to the bond). However, the line shape can change when thermal motion arises. As Figure 1-23 shows, motions that change the orientation of the EFG tensor (*e.g.*, in-plane rotation of C_6D_6 about its C_6 axis) starts to affect the line shape at rates of about 10^4 s^{-1}. When the rate constant increases, the line shape evolves gradually until at about 10^7 s^{-1} or faster the line shape can be described by an averaged effective tensor. The regimes with rate constants $< 10^4$ or $> 10^7$ s^{-1}, in which the observed line shape is independent of the rate constant, are called slow-limit or fast-limit regimes, respectively; while the intermediate regime is in-between. The motionally averaged and intermediate line shapes are characteristic of the motions (Figure 1-23), providing valuable information to aid the development of the dynamic models and understand the guest-host interactions inside of the micropores (See *Chapter 5*). For instance, in the fast-limit regime, the flip-flop of benzene-d$_4$ about its C_2 axis not only narrows the ^{2}H NMR pattern but also changes the line shape ($\eta_Q \neq 0$). However, only the line width decreases when the motion has a C_3 or higher symmetry. The motionally averaged C_Q for in-plane rotation of C_6D_6 about its C_6 axis is half of the C_Q of the static C–^{2}H and one third for methyl C–^{2}H rotation about its C_3 axis. The ^{2}H NMR pattern is further narrowed if multiple motions occur at the same time.
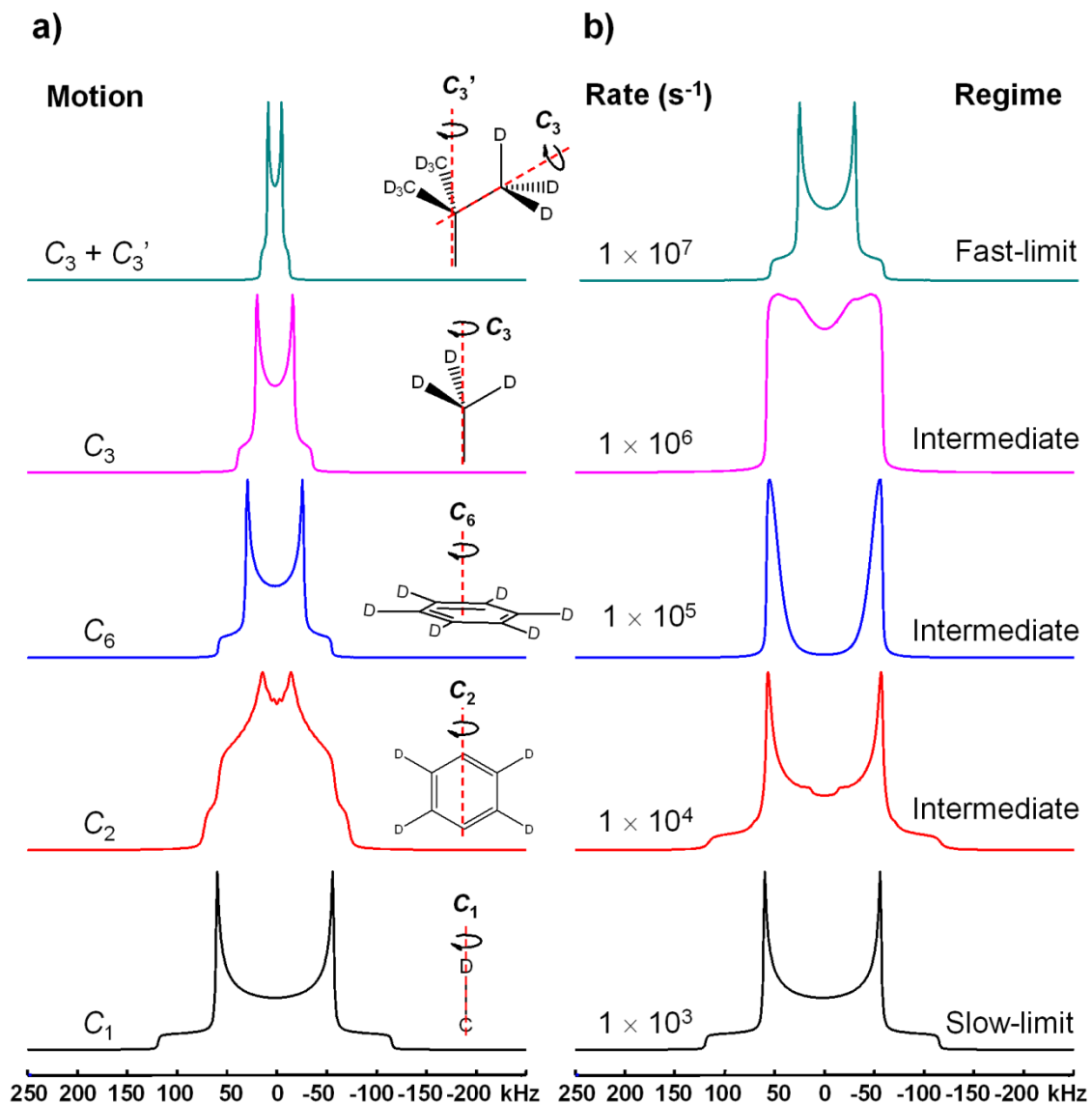
Figure 1-23: Analytical simulations (performed using EXPRESS software, $C_Q = 155$ kHz, $\eta_Q = 0.0$) of theoretical ^{2}H powder patterns for (a) different motions in the fast-limit regime, and (b) in-plane rotation of C_6D_6 about its C_6 axis (referred to as C_6) as a function of rate constant. The motions in (a) are C_1 rotation about C–^{2}H bond (referred to as C_1), flip-flop of benzene-d$_4$ about its C_2 axis (referred to as C_2), methyl C–^{2}H rotation about its C_3 axis (referred to as C_3), and the three deuterated methyl groups of t-butyl rotate about their C_3 axes while the t-butyl group as a whole also rotate about its C_3' axis (referred to as $C_3 + C_3'$).

1.2.4　Theoretical calculations

During theoretical calculations, a model of a real system is built and its behavior is explored. The model is a mathematical one and the exploration is done on a computer. The generality of a given model is established by comparing the calculated behavior to experimental one for a wide variety of systems. The postulates and theorems of quantum mechanics form the solid foundation for the predication of observable properties: "If one can solve the Schrödinger equation for something—an atom, a molecule, assemblies of atoms in solids or liquids—one can predict every physical property".[24,78,79]

1.2.4.1　The First-Principles Rationale

Since electrons are much lighter than nuclei, it is possible to freeze the positions of the latter and only treat the former. This leads to the famous Born–Oppenheimer approximation, in which the electronic and nuclear degrees of freedom can be separated. The behavior of electrons governs most properties of materials. The properties of any material from first-principles are based on fundamental physical laws and without using free parameter, by solving the Schrödinger equation for the electrons in that material. However, the exact solutions exist only for the system with a single electron ("one-electron"). An approximation is obtained for systems with interacting electrons ("many-body") by several computational approaches, for instance, the density functional theory (DFT).

1.2.4.2　Density Functional Theory

DFT is based on two simple principles: 1) The total energy of a system of electrons and nuclei is a unique functional of the electron density; and 2) the variational minimum of the energy is exactly equivalent to the true ground-state energy. The practical tools for applying DFT are the Kohn–Sham equations, which treats the electron density as the fundamental variable and exactly maps the many-body Schrödinger equation onto a set of N equations involving one-electron wavefunctions:[24]

$$-\frac{\hbar^2}{2m_e}\nabla^2\Psi(\boldsymbol{r}) + v_{\text{eff}}(\boldsymbol{r})\psi(\boldsymbol{r}) = \varepsilon\psi(\boldsymbol{r}) \qquad (\textbf{Equation 1-29})$$

where the Kohn–Sham potential, $\upsilon_{\text{eff}}(\boldsymbol{r})$ contains terms arising from the interaction with the ionic charges $V_{\text{ion}}(\boldsymbol{r})$, the Coulomb interaction energy of the charge density interacting with itself (*i.e.*, the Hartree energy), and a potential V_{xc}, which describes the effects of exchange and correlation between the electrons. The form of the potential V_{xc} is unknown and certain type of approximations is essential, such as Becke's 3-parameter hybrid density exchange functional with Lee, Yang and Parr correlation functional (B3LYP) and Perdew, Burke and Ernzerhof correlation functional (PBE).

1.2.4.3   Basis Sets

The basis set is a set of mathematical functions from which the wave function is constructed. Each molecular orbital can be expressed as a linear combination of basis functions. An infinite basis set permits an optimal description of the electron density. However, the computational cost increases exponentially with the number of basis functions used. In practice, a basis set is chosen to ensure the calculation as efficient as possible. Different methods require different types of basis sets.

1.2.4.3.1   Gaussian-Type Orbital

DFT calculations of molecules or clusters (using the Gaussian software) employ the atomic orbital-like basis functions with the form of a Gaussian function. The general functional form of a normalized Gaussian-type orbital (GTO) in atom-centered Cartesian coordinates is[78]

$$\phi(x,y,z;a,i,j,k) = \left(\frac{2\alpha}{\pi}\right)^{3/4} \left[\frac{(8\alpha)^{i+j+k} i!\, j!\, k!}{(2i)!\, (2j)!\, (2k)!}\right]^{1/2} x^i y^j z^k e^{-\alpha(x^2+y^2+z^2)}$$

(**Equation 1-30**)

where α is an exponent controlling the width of the GTO, and i, j, and k are non-negative integers that represent the nature of the orbital in a Cartesian sense. For instance, when all three indices are zero, the GTO has spherical symmetry, and is a *s*-type GTO. When exactly one of the indices is one, the function has axial symmetry about a single Cartesian axis and is a *p*-type GTO. There are three possibilities for which index is one,

corresponding to the p_x, p_y, and p_z orbitals. When the sum of three indices is equal to two, it is a *d*-type GTO. Although there are six possible Cartesian prefactors of x^2, y^2, z^2, xy, xz, and *yz*, only five *d*-type functions are required to represent the *d*-orbitals. These five functions are typically referred to as *xy*, *xz*, *yz*, $x^2 - y^2$, and z^2.

1.2.4.3.2   Plane Waves

DFT calculations of crystals (using the CASTEP code) employ the plane-wave basis sets. In this method the model system is constructed as a 3D periodic supercell which allows Bloch's theorem to be applied to the electron wavefunctions:[79]

$$\psi_{n,k}(\boldsymbol{r}) = u_{n,k}(\boldsymbol{r})\exp(i\boldsymbol{k}\cdot\boldsymbol{r}) \qquad \textbf{(Equation 1-31)}$$

where the $u_{n,k}$ are the expansion coefficients. The function $u(\boldsymbol{r})$ has the periodicity of the supercell, which is a series expansion in terms of a set of plane-wave basis functions. Therefore each single-electron wavefunction $\psi_{n,k}$ is written as

$$\psi_{n,k}(\boldsymbol{r}) = \sum_G u_{n,k}(\boldsymbol{G}) \exp(i(\boldsymbol{k} + \boldsymbol{G})\cdot\boldsymbol{r}) \qquad \textbf{(Equation 1-32)}$$

where the sum is over all reciprocal lattice vectors $\boldsymbol{G}$. To truncate the basis set, the sum is limited to a set of reciprocal lattice vectors contained within a sphere with a radius defined by the cutoff energy, E_{cut}:

$$\frac{\hbar^2|\boldsymbol{k}+\boldsymbol{G}|^2}{2m} \leq E_{cut} \qquad \textbf{(Equation 1-33)}$$

Therefore the basis set is defined by the maximum kinetic energy component it contains. Generally speaking, the higher the cutoff energy is, the more accuracy the CASTEP calculation has. A fast-Fourier transformation (FFT) can be used to change the representation of the eigenstates from a sum of Fourier components to a uniform grid of points in the real-space unit cell.

A serious problem of a plane-wave basis set is that empty space has the same quality of representation—and cost—as regions of interest. Pseudopotentials are used to overcome this problem. A pesudopotential replaces both the atomic nucleus and the core

electrons by a fixed effective potential that in a special sense reproduces the effect of the nuclear potential and the orthogonality requirement. Therefore only the valence electrons are considered.

1.3 Outline of the Thesis

This thesis is organized in the following way. *Chapters 2–6* are focused on the SSNMR investigations of metal–organic frameworks. *Chapter 2* describes how natural abundance ^{25}Mg SSNMR spectroscopy was successfully used to probe the local Mg environments and follow the rehydration/adsorption of an important Mg-containing MOF, CPO-27-Mg. The next chapter, *Chapter 3* contains a detailed SSNMR characterization of the multiple (four) non-equivalent Mg sites of another prototypical Mg-containing MOF, microporous α-Mg$_3$(HCOO)$_6$ at natural abundance. The H and C sites of this MOF were further resolved by SSNMR experiments in *Chapter 4*. In *Chapter 5*, the thermal motions of water as well as several volatile organic compounds (VOCs) adsorbed on the exposed metal centers of CPO-27-M (M = Mg, Co, Ni, Zn) were detected by variable-temperature (VT) ^{2}H solid-state NMR spectroscopy, providing insights into the guest-host interactions. ^{17}O-enriched α-Mg$_3$(HCOO)$_6$ and CPO-27-Mg were prepared and their non-equivalent framework oxygens were distinguished by ^{17}O SSNMR spectroscopy (shown in *Chapter 6*). A facile approach was also developed to estimate the degree of oxygen-enrichment for these MOFs. In *Chapter 7*, a multinuclear solid-state NMR study of a group of novel inorganic microporous materials (microporous titanosilicate, TiSiO$_4$) is presented. ^{23}Na and ^{39}K SSNMR spectroscopy were used to investigate the extra-framework ions, while ^{29}Si and $^{47/49}$Ti SSNMR spectroscopy were employed to study the frameworks. Many SSNMR spectra shown in this thesis were acquired at a high magnetic field of 21.1 T. The results from theoretical calculations were also utilized to assist in the interpretation of experimental spectra. *Chapter 8* is the final chapter, in which a brief summary of this thesis and some suggestions for future work are given.

1.4 References

(1) Everett, D. H. *Pure Appl. Chem.* **1972**, *31*, 578-638.

(2) Inui, T.; Namba, S.; Tatsumi, T.; Eds. *Chemistry of Microporous Crystals*; Elsevier: Tokyo: Kodansha; Amsterdam; New York, **1991**.

(3) Öhlmann, G.; Pfeifer, H.; Fricke, R.; Eds. *Catalysis and Adsorption by Zeolites*; Elsevier: Amsterdam ; New York, **1991**.

(4) van Bekkum, H.; Flanigen, E. M.; Jacobs, P. A.; Jansen, J. C.; Eds. *Introduction to Zeolite Science and Practice: 2nd Completely Revised and Expanded Edition.*; Elsevier: Amsterdam ; New York, **2001**.

(5) Special Issue for Metal–Organic Frameworks: Zhou, H.-C.; Long, J. R.; Yaghi, O. *Chem. Rev.* **2012**, *112*, 673-1268.

(6) MacGillivray, L. R.; Eds. *Metal-Organic Frameworks : Design and Application*; Wiley: Hoboken, N.J., **2010**.

(7) Duer, M. J. *Solid State NMR Spectroscopy: Principles and Applications*; Blackwell Science: Oxford ; Malden, MA, **2002**.

(8) MacKenzie, K. J. D.; Smith, M. E. *Multinuclear Solid-State NMR of Inorganic Materials*; 1st ed.; Pergamon: Oxford ; New York, **2002**.

(9) Bakhmutov, V. I. *Solid-state NMR in materials science: principles and applications*; CRC Press: Boca Raton, FL, **2012**.

(10) Sutrisno, A.; Huang, Y. *Solid State Nucl. Magn. Reson.* **2013**, *49-50*, 1-11.

(11) Hoffmann, H. C.; Debowski, M.; Mueller, P.; Paasch, S.; Senkovska, I.; Kaskel, S.; Brunner, E. *Materials* **2012**, *5*, 2537-2572.

(12) Meier, W. M.; Olson, D. H.; Baerlocher, C. *Atlas of zeolite structure types*; 4th rev. ed.; Elsevier: London; Boston; Singapore; Sydney; Toronto; Wellington, **1996**.

(13) Ferdov, S.; Kolitsch, U.; Lengauer, C.; Tillmanns, E.; Lin, Z.; Sa Ferreira, R. A. *Acta Crystallogr., Sect. E* **2007**, *E63*, i186.

(14) Dadachov, M. S.; Rocha, J.; Ferreira, A.; Lin, Z.; Anderson, M. W. *Chem. Commun.* **1997**, *1997*, 2371-2372.

(15) Poojary, D. M.; Cahill, R. A.; Clearfield, A. *Chem. Mater.* **1994**, *6*, 2364-2368.

(16) Anderson, M. W.; Terasaki, O.; Ohsuna, T.; Philippou, A.; MacKay, S. P.; Ferreira, A.; Rocha, J.; Lidin, S. *Nature* **1994**, *367*, 347-351.

(17) Uma, S.; Rodrigues, S.; Martyanov, I. N.; Klabunde, K. J. *Microporous Mesoporous Mater.* **2004**, *67*, 181-187.

(18) Lamberti, C. *Microporous Mesoporous Mater.* **1999**, *30*, 155-163.

(19) Li, H.; Eddaoudi, M.; O'Keeffe, M.; Yaghi, M. *Nature* **1999**, *402*, 276-279.

(20)   Gascon, J.; Aktay, U.; Hernandez-Alonso, M. D.; van Klink, G. P. M.; Kapteijn, F. *J. Catal.* **2009**, *261*, 75-87.

(21)   Morris, R. E.; Weigel, S. J. *Chem. Soc. Rev.* **1997**, *26*, 309-318.

(22)   Cooper, E. R.; Andrews, C. D.; Wheatley, P. S.; Webb, P. B.; Wormald, P.; Morris, R. E. *Nature* **2004**, *430*, 1012-1016.

(23)   Waseda, Y.; Matsubara, E.; Shinoda, K. *X-Ray Diffraction Crystallography: Introduction, Examples and Solved Problems*; Springer-Verlag Berlin Heidelberg: Berlin, Heidelberg, **2011**.

(24)   Harris, R. K.; Wasylishen, R. E.; Duer, M. J.; Eds. *NMR Crystallography*; Wiley: Chichester, U.K., **2009**.

(25)   Fyfe, C. A.; Feng, Y.; Grondey, H.; Kokotailo, G. T.; Gies, H. *Chem. Rev.* **1991**, *91*, 1525-1543.

(26)   Charpentier, T. *Solid State Nucl. Magn. Reson.* **2011**, *40*, 1-20.

(27)   Bonhomme, C.; Gervais, C.; Babonneau, F.; Coelho, C.; Pourpoint, F.; Azais, T.; Ashbrook, S. E.; Griffin, J. M.; Yates, J. R.; Mauri, F.; Pickard, C. J. *Chem. Rev.* **2012**, *112*, 5733-5779.

(28)   Emsley, J. W.; Feeney, J. *Prog. Nucl. Magn. Reson. Spectrosc.* **1995**, *28*, 1-9.

(29)   Andrew, E. R.; Szczesniak, E. *Prog. Nucl. Magn. Reson. Spectrosc.* **1995**, *28*, 11-36.

(30)   Rabi, I. I.; Zacharias, J. R.; Millman, S.; Kusch, P. *Phys. Rev.* **1938**, *53*, 318.

(31)   Herzfeld, J.; Berger, A. E. *J. Chem. Phys.* **1980**, *73*, 6021-6030.

(32)   Pake, G. E. *J. Chem. Phys.* **1948**, *16*, 327-336.

(33)   Schnell, I.; Spiess, H. W. *J. Magn. Reson.* **2001**, *151*, 153-227.

(34)   Cohen, M. H.; Reif, F. *Solid State Phys.* **1957**, *5*, 321-438.

(35)   Ashbrook, S. E. *Phys. Chem. Chem. Phys.* **2009**, *11*, 6892-6905.

(36)   Rose, M. E. *Elementary Theory of Angular Momentum*; Wiley: New York, **1957**.

(37)   Schmidt-Rohr, K.; Spiess, H. W. *Multidimensional Solid-State NMR and Polymers*; Academic Press: London ; San Diego, **1994**.

(38)   Harris, R. K.; Becker, E. D.; Cabral De Menezes, S. M.; Goodfellow, R.; Granger, P. *Pure Appl. Chem.* **2001**, *73*, 1795-1818.

(39)   Pyykkö, P. *Mol. Phys.* **2008**, *106*, 1965-1974.

(40)   Lewandowski, J. R.; Dumez, J.-N.; Akbey, U.; Lange, S.; Emsley, L.; Oschkinat, H. *J. Phys. Chem. Lett.* **2011**, *2*, 2205-2211.

(41)   Reif, B. *J. Magn. Reson.* **2012**, *216*, 1-12.

(42)   Andrew, E. R.; Bradbury, A.; Eades, R. G. *Nature* **1959**, *183*, 1802-1803.

(43)   Lowe, I. J. *Phys. Rev. Lett.* **1959**, *2*, 285-287.

(44)   Hartmann, S. R.; Hahn, E. L. *Phys. Rev.* **1962**, *128*, 2042-2053.

(45)   Gabrielse, W.; Angad Gaur, H.; Feyen, F. C.; Veeman, W. S. *Macromolecules* **1994**, *27*, 5811-5820.

(46)   Burum, D. P.; Bielecki, A. *J. Magn. Reson.* **1991**, *94*, 645-652.

(47)   Van Rossum, B. J.; Foerster, H.; de Groot, H. J. M. *J. Magn. Reson.* **1997**, *124*, 516-519.

(48)   Van Rossum, B. J.; De Groot, C. P.; Ladizhansky, V.; Vega, S.; De Groot, H. J. M. *J. Am. Chem. Soc.* **2000**, *122*, 3465-3472.

(49)   Lee, M.; Goldburg, W. I. *Phys. Rev.* **1965**, *140*, 1261-1271.

(50)   Bielecki, A.; Kolbert, A. C.; Levitt, M. H. *Chem. Phys. Lett.* **1989**, *155*, 341-346.

(51)   Bennett, A. E.; Rienstra, C. M.; Auger, M.; Lakshmi, K. V.; Griffin, R. G. *J. Chem. Phys.* **1995**, *103*, 6951-6958.

(52)   Larsen, F. H.; Jakobsen, H. J.; Ellis, P. D.; Nielsen, N. C. *J. Phys. Chem. A* **1997**, *101*, 8597-8606.

(53)   Hahn, E. L.; Maxwell, D. E. *Phys. Rev.* **1952**, *84*, 1246-1247.

(54)   Maricq, M. M.; Waugh, J. S. *J. Chem. Phys.* **1979**, *70*, 3300-3316.

(55)   Perras, F. A.; Viger-Gravel, J.; Burgess, K. M. N.; Bryce, D. L. *Solid State Nucl. Magn. Reson.* **2013**, *51-52*, 1-15.

(56)   Tang, J. A.; Masuda, J. D.; Boyle, T. J.; Schurko, R. W. *ChemPhysChem* **2006**, *7*, 117-130.

(57)   Bhattacharyya, R.; Frydman, L. *J. Chem. Phys.* **2007**, *127*, 194503/194501-194503/194508.

(58)   O'Dell, L. A.; Schurko, R. W. *Chem. Phys. Lett.* **2008**, *464*, 97-102.

(59)   Aue, W. P.; Bartholdi, E.; Ernst, R. R. *J. Chem. Phys.* **1976**, *64*, 2229-2246.

(60)   Feike, M.; Demco, D. E.; Graf, R.; Gottwald, J.; Hafner, S.; Spiess, H. W. *J. Magn. Reson., Ser. A* **1996**, *122*, 214-221.

(61)   Feike, M.; Graf, R.; Schnell, I.; Jaeger, C.; Spiess, H. W. *J. Am. Chem. Soc.* **1996**, *118*, 9631-9634.

(62)   Brown, S. P. *Prog. Nucl. Magn. Reson. Spectrosc.* **2007**, *50*, 199-251.

(63)   Cadars, S.; Brouwer, D. H.; Chmelka, B. F. *Phys. Chem. Chem. Phys.* **2009**, *11*, 1825-1837.

(64)   Frydman, L.; Harwood, J. S. *J. Am. Chem. Soc.* **1995**, *117*, 5367-5368.

(65)   Medek, A.; Harwood, J. S.; Frydman, L. *J. Am. Chem. Soc.* **1995**, *117*, 12779-12787.

(66)   Massiot, D.; Touzo, B.; Trumeau, D.; Coutures, J. P.; Virlet, J.; Florian, P.; Grandinetti, P. J. *Solid State Nucl. Magn. Reson.* **1996**, *6*, 73-83.

(67)   Soerensen, O. W.; Rance, M.; Ernst, R. R. *J. Magn. Reson.* **1984**, *56*, 527-534.

(68)   Amoureux, J.-P.; Fernandez, C.; Steuernageel, S. *J. Magn. Reson., Ser. A.* **1996**, *123*, 116-118.

(69)   Amoureux, J.-P.; Fernandez, C.; Frydman, L. *Chem. Phys. Lett.* **1996**, *259*, 347-355.

(70)   Gan, Z.; Kwak, H.-T. *J. Magn. Reson.* **2004**, *168*, 346-351.

(71)   Amoureux, J. P.; Delevoye, L.; Steuernagel, S.; Gan, Z.; Ganapathy, S.; Montagne, L. *J. Magn. Reson.* **2005**, *172*, 268-278.

(72)   Davis, A. L.; Keeler, J.; Laue, E. D.; Moskau, D. *J. Magn. Reson.* **1992**, *98*, 207-216.

(73)   Hu, J. Z.; Wang, W.; Liu, F.; Solum, M. S.; Alderman, D. W.; Pugmire, R. J.; Grant, D. M. *J. Magn. Reson., Ser. A* **1995**, *113*, 210-222.

(74)   Struppe, J. *Introduction to Solid State NMR Experiments on Avance Spectrometers*; BrukerBiospin: Billerica, Massachusetts, **2001**.

(75)   Bax, A.; Szeverenyi, N. M.; Maciel, G. E. *J. Magn. Reson.* **1983**, *52*, 147-152.

(76)   Gan, Z. *J. Am. Chem. Soc.* **1992**, *114*, 8307-8309.

(77)   Shantz, D. F.; Lobo, R. F. *Top. Catal.* **1999**, *9*, 1-11.

(78)   Cramer, J. C. *Essentials of Computational Chemistry: Theories and Models*; 2nd ed.; Wiley: Chichester, West Sussex, England; Hoboken, NJ, **2004**.

(79)   Segall, M. D.; Lindan, P. J. D.; Probert, M. J.; Pickard, C. J.; Hasnip, P. J.; Clark, S. J.; Payne, M. C. *J. Phys.: Condens. Matter* **2002**, *14*, 2717-2744.

Chapter 2

2 ^{25}Mg Solid-State NMR: A sensitive Probe of Adsorbing Guest Molecules on a Metal Center in Metal–Organic Framework CPO-27-Mg[*]

2.1 Introduction
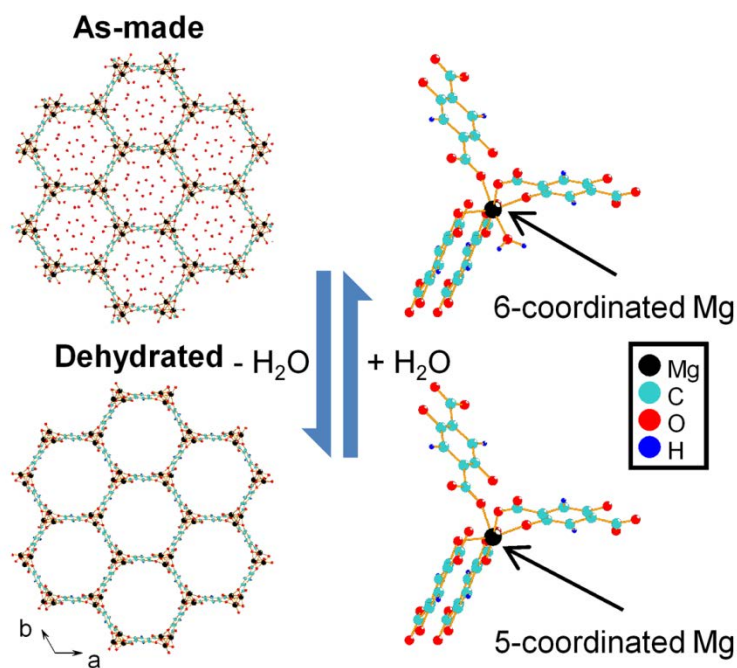
Figure 2-1: The reversible transformation of a local Mg environment in CPO-27-Mg. For clarity, the hydrogens of water in the channels are omitted.

Metal–organic frameworks (MOFs), an important class of porous materials, have attracted much attention in recent years due to their promising properties such as rich structural diversity, large surface area, tunable porosity, high thermal stability, and selective adsorption, which make them suitable for many applications including gas separation and storage.[1] However, the guest selectivity, maximum uptake and dynamic

---

storage capacity of classical MOFs (that only consist of fully coordinated metal sites) are limited by the lack of chemical bonding between the adsorbate and metal center. Recently, a new MOF with a coordinately unsaturated metal site, namely CPO-27-Mg[2] (also referred to as Mg-MOF-74[3] or Mg/DOBDC,[4,5] DOBDC = 2,5-dioxido-1,4-benzene-dicarboxylate), has shown to be a good candidate for gas separation and storage.[5-7] As illustrated in Figure 2-1, the framework of as-made CPO-27-Mg is based on the interconnecting helical chains of edge-shared MgO_6 units, forming one-dimensional honeycomb channels along the c axis. In each MgO_6, five of the six oxygens belong to four organic linkers and the remaining oxygen is from a water molecule directly bound to the Mg. This water molecule can be removed upon dehydration. The metal center can then interact strongly with the guest species adsorbed on this coordination site vacated by dehydration. Such interaction is considered to be responsible for good guest selectivity and large maximum uptake.[7]

Due to the lack of suitable single crystals for X-ray diffraction, the structures of as-made[2] and dehydrated[7] CPO-27-Mg were determined from the more limited powder X-ray and neutron diffraction data. Because diffraction-based techniques are only sensitive to the long-range ordering, structural information from complementary techniques is desirable. Solid-state NMR (SSNMR) spectroscopy is a method complementary to XRD because it is sensitive to local ordering and geometries. ^{25}Mg SSNMR spectroscopy has been shown to be a sensitive probe for local Mg environments in various materials.[8-21] However, it has not been utilized to directly characterize the local Mg environment in MOF-based materials because ^{25}Mg (I = 5/2) has a quadrupole moment, a small gyromagnetic ratio (γ = -1.639 × 10^7 rad·s^{-1}·T^{-1}) and a low natural abundance (10.0%). These unfavorable NMR properties result in low sensitivity and broad resonances. The sensitivity in MOF systems is further decreased due to a very low ^{25}Mg concentration resulting from the low densities. In CPO-27-Mg, the number of ^{25}Mg per nm^3 is 0.45 compared to the number for the dense MgO phase at 5.3. As shown by a recent study, these problems associated with low-γ unreceptive quadrupolar nuclei in MOFs can be alleviated by performing NMR experiments at very high magnetic fields.[22]

In this work, natural abundance ^{25}Mg SSNMR spectroscopy is employed to directly study the effect of dehydration and rehydration as well as adsorption of two volatile organic compounds (VOCs) on the local Mg structure in CPO-27-Mg at an ultrahigh magnetic field of 21.1 T.

2.2   Experimental Section

2.2.1   Sample Preparation

As-made CPO-27-Mg was synthesized following the procedure described by Dietzel and co-workers.[2] 0.75 mmol 2,5-dioxido-1,4-benzenedicarboxylic acid (H$_4$DOBDC, Sigma-Aldrich, 98%) was dissolved in 10 mL tetrahydrofuran (THF, reagent grade, Caledon) in a Teflon-lined inlet of an autoclave (23 mL). An aqueous sodium hydroxide solution (3 mL, 1 M) was added to this solution. 1.5 mmol magnesium nitrate hexahydrate (Mg(NO$_3$)$_2$·6H$_2$O, Sigma-Aldrich, 99%) was first dissolved in 5 mL deionized water and then added to the Teflon inlet while stirring, upon which a yellow precipitate formed. The autoclave was sealed and the mixture was reacting at 110 °C for 3 d. The resulting light yellow powder was filtered, repeatedly washed with THF, and dried at room temperature (yield: 75% based on Mg). In order to obtain dehydrated CPO-27-Mg, as-made sample was pre-exchanged with fresh methanol several times and activated under dynamic vacuum at 523 K for 16 h. Rehydrated CPO-27-Mg samples were prepared by storing the dehydrated sample over a saturated NH$_4$Cl(aq) atmosphere at room temperature as a function of rehydration time. The saturated adsorption of acetone and acetonitrile in CPO-27-Mg was performed by first suspending ~0.35 g dehydrated CPO-27-Mg powder in ~5 mL dry solvents, then stirring overnight, and finally allowing the excess solvent to evaporate. All operations were done under a N$_2$ atmosphere. All CPO-27-Mg samples were stored in sealed vials.

2.2.2   NMR Characterizations and Theoretical Calculations

Natural abundance ^{25}Mg solid-state NMR measurements were performed at 21.1 T on a 900 MHz Bruker Avance II spectrometer at the National Ultrahigh-field NMR Facility for Solids in Ottawa, Canada, with a ^{25}Mg Larmor frequency of 55.1 MHz. Static ^{25}Mg NMR spectra were acquired with the quadrupolar echo sequence[23] on a home-built

7 mm H/X low-γ probe for stationary samples with a dual resonator design. The solution 90° pulse for 1M $MgCl_2$ aqueous solution was 9 μs, corresponding to a selective 90° pulse of 3 μs for solids. To ensure that the results presented in Figures 2-2 and 2-4 are semiquantitative, the pulse delay was varied. Because the spectra acquired using 1, 3, and 5 s looked the same, the pulse delay of 1 s was used. The chemical shift of ^{25}Mg was referenced to the 1 M $MgCl_2$ aqueous solution at 0 ppm. The spectral width was 200 kHz. To semiquantitatively analyze the amount of observable ^{25}Mg NMR signals, all of the spectra presented in Figures 2-2 and 2-4 were acquired under identical spectrometer conditions, including the same number (16384) of scans, by using approximately the same amount of CPO-27-Mg samples (205 ± 20 mg). For selected samples (dehydrated and 0.6H_2O/Mg CPO-27-Mg), the spectra were also acquired with significantly more scans (65536 and 49152 scans for dehydrated and 0.6H_2O/Mg CPO-27-Mg, respectively, shown in Figure 2-A3) to confirm the line shape in Figures 2-2 and 2-4. All ^{25}Mg NMR parameters, including C_Q, η_Q, and δ_{iso}, were determined by analytical simulations of NMR spectra using the WSOLIDS simulation package.[24]

Ab initio calculations were performed using the Gaussian 09 program[25] running on SHARCNET (www.sharcnet.ca). ^{25}Mg EFG tensors were calculated by employing the B3LYP method with the 6-31G** basis set and using the GIAO method. The model clusters used in the calculations were truncated from the periodic structure of as-made CPO-27-Mg and terminated with H atoms, which contains one Mg center and four 2,5-dioxido-1,4-benzene-dicarboxylate ligands (Figure 2-1). The ^{25}Mg EFG tensor parameters were extracted from the Gaussian output files by the EFGShield program.[26] Calculated ^{25}Mg isotropic chemical shielding (σ_{iso}) values for all CPO-27-Mg clusters were converted to the corresponding chemical shift (δ_{iso}) values by referencing them to $Mg(H_2O)_6^{2+}$: $\delta_{iso} = \sigma_{ref} - \sigma_{iso}$ (all in ppm), where σ_{ref} corresponds to the calculated chemical shielding of $Mg(H_2O)_6^{2+}$ whose geometry was pre-optimized by MP2 method.

2.3 Results and Discussion
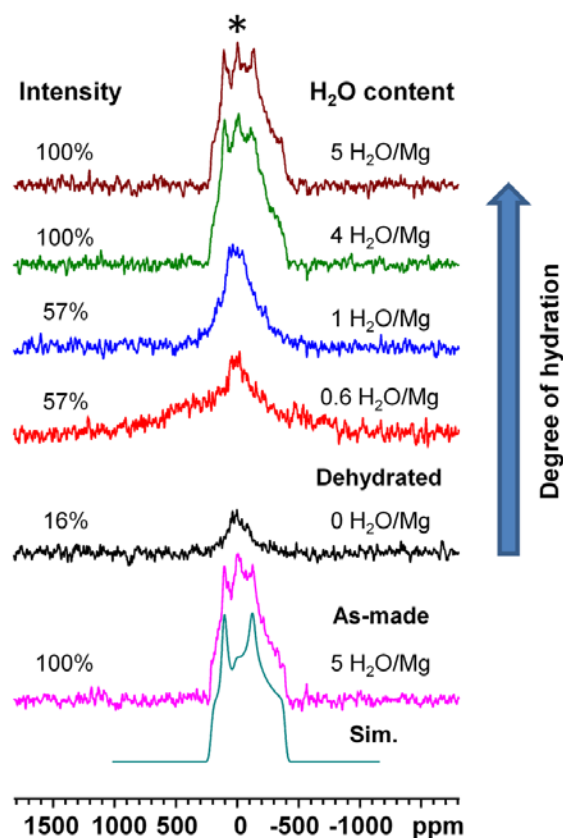
Figure 2-2: [25]Mg static SSNMR spectra of CPO-27-Mg as a function of rehydration degree. All spectra were acquired under the same spectrometer conditions, 16384 scans and a pulse delay of 1 s. The * indicates a small amount of impurity.

As mentioned earlier, a previous powder XRD study suggests that the space group (*R*-3) of CPO-27-Mg remains unchanged upon dehydration.[2] The PXRD patterns of as-made and fully dehydrated CPO-27-Mg obtained in this work (Figure 2-A1, appendix) are in good agreement with those previously reported,[2,7] which clearly indicate that the long-range ordering is preserved upon dehydration. ^{13}C MAS NMR spectra of CPO-27-Mg before and after dehydration (Figure 2-A2) also look very similar, confirming that the framework remains intact. However, the corresponding [25]Mg static SSNMR spectra acquired at 21.1 T (Figure 2-2) are remarkably different. For as-made CPO-27-Mg, its [25]Mg static SSNMR spectrum has a well-defined second-order quadrupolar powder pattern typical of crystalline systems, which can be well simulated with one set of [25]Mg

electric field gradient (EFG) parameters: $C_Q = 6.4(4)$ MHz, $\eta_Q = 0.5(1)$ and $\delta_{iso} = 12(5)$ ppm. The fact that the spectrum can be well simulated with a single Mg site is in agreement with crystal structure. The nonzero η_Q value is consistent with the low Mg site symmetry (C_1). No chemical shift anisotropy was included in the simulation, indicating that the observed spectrum is mainly dominated by the quadrupolar interaction. The δ_{iso} falls in the normal range of Mg oxyanion compounds, but the C_Q value is rather large for a typical six-coordinated Mg.[8] However, the distortion of the MgO_6 octahedron is only moderately large (the variations in the Mg–O distances and the O–Mg–O bond angles are in the range of 1.97–2.17 Å and 80.2–99.2°, respectively). Because the quadrupolar coupling is affected by longer-range interactions, the relatively large $C_Q(^{25}Mg)$ must reflect the contributions from four organic linkers bound to the Mg and their relative orientations as well as the water molecule.

The ^{25}Mg static spectrum of fully dehydrated CPO-27-Mg looks distinctly different from that of the as-made phase (Figure 2-2), where only a very weak, featureless peak was observed. The most striking observation is that for a fully dehydrated phase more than 80% of the Mg became NMR "invisible" upon dehydration. The large amount of 'invisible' Mg is likely due to the fact that these Mg sites have large C_Q's. The Mg ions in the dehydrated phase are indeed expected to have much larger C_Q's compared to that in the as-made sample due to the alteration of the coordination geometry to a distorted square-pyramid. For Mg-containing organic compounds, the C_Q's for the Mg in the square-pyramid geometry are known to be rather large (about 13 MHz) and were only observed using ^{25}Mg-enriched samples.[19] The Mg in dehydrated CPO-27-Mg may well have a comparable, if not larger, C_Q, yielding a spectrum too broad to be measured at natural abundance even at 21.1 T. Indeed, our density functional theory (DFT) calculation confirms a large $C_Q(^{25}Mg)$ of 14.1 MHz for the dehydrated phase. A recent work showed that the "hidden" Mg with a large C_Q in a crystalline mineral can be observed at natural abundance by using sensitivity enhancement techniques such as QCPMG.[20] Unfortunately, our attempts to acquire QCPMG spectra of various dehydrated samples failed due to the very short T_2 (< 1 ms), although we were able to acquire a QCPMG spectrum of the as-made sample (spectrum not shown). The observed signal of

the dehydrated sample does not have a typical line shape arising from the quadrupolar interaction in a crystalline phase. The peak is asymmetrically broadened with a tail at the low-frequency side, which is likely the "tip" of a very broad distribution of C_Q due to a range of slightly different Mg environments. The NMR results suggest that although the PXRD pattern shows that the long-range ordering is preserved upon dehydration, the local Mg environment is disordered. The disorder is likely due to the fact that dehydration causes the DOBDC linkers bound to a Mg to slightly change their orientations relative to one other as well as the Mg–O bond length and O–Mg–O bond angles. Such changes appear to vary from site to site, leading to a distribution of C_Q. Furthermore, the distortion to the square-pyramid geometry brought about by the changes mentioned above results in a remarkable increase in the $C_Q(^{25}Mg)$, leading to the loss of a large amount of ^{25}Mg signal. The situation is somewhat reminiscent of zeolite dehydration. The tetrahedral Al atoms in hydrated zeolites have a rather small $C_Q(^{27}Al)$. Dehydration leads to a dramatic increase in $C_Q(^{27}Al)$, resulting in a large portion of the ^{27}Al spins becoming NMR-invisible.[27] The PXRD patterns of dehydrated zeolites also indicate high sample crystallinity, whereas ^{27}Al NMR spectra show a distribution of $C_Q(^{27}Al)$. A recent ^{67}Zn SSNMR study also showed that the desolvation led to the distortion of Zn environment in IRMOF-1.[22]

To better understand the effect of coordinated water on the Mg environment, we systematically examined the rehydration. Figure 2-2 shows the ^{25}Mg static SSNMR spectra of CPO-27-Mg as a function of a degree of rehydration. At the beginning of rehydration ($0.6H_2O/Mg$), although the PXRD pattern (Figure 2-A1) looks identical to that of fully dehydrated phase, the corresponding ^{25}Mg NMR spectrum exhibits observable changes. Specifically, it now shows a featureless peak (similar to that observed in the fully dehydrated phase) superimposed on top of a very broad resonance with a breadth of about 110 kHz. This very broad new signal is assigned to the Mg atoms whose open sites are now occupied by the added H_2O. Because local geometries of these Mg ions are octahedral, they have smaller $C_Q(^{25}Mg)$ and start becoming detectable. It is worth mentioning that the breadth of this signal from newly formed MgO_6 is larger than that of the as-made phase, suggesting that the spatial arrangement of the ligands around

the metal has not fully relaxed back to the state of fully hydrated phase. The water exchange between Mg sites may also exist.
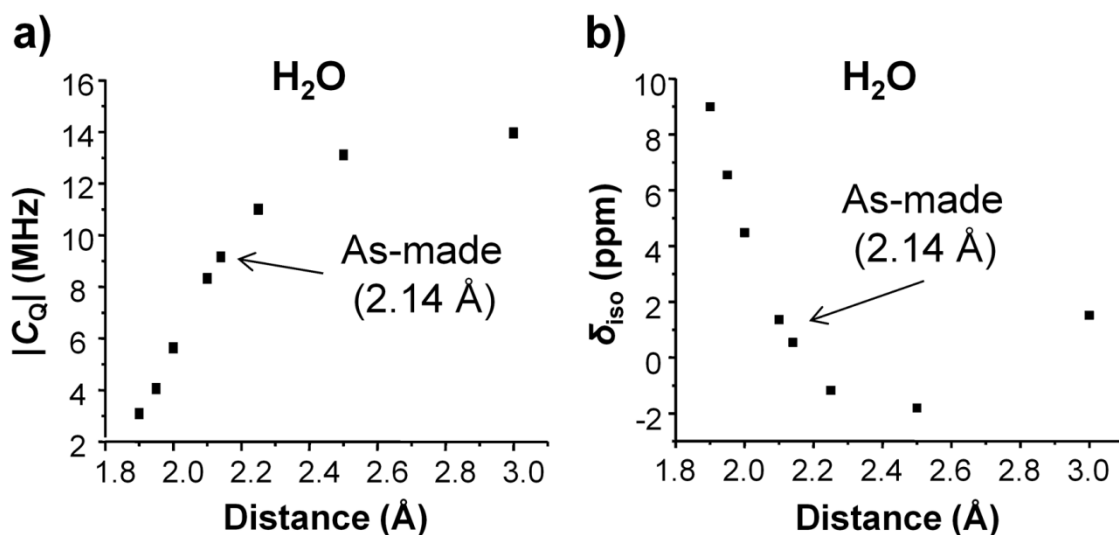
Figure 2-3: The plot of calculated (a) $C_Q(^{25}Mg)$ and (b) $\delta_{iso}(^{25}Mg)$ as a function of the Mg–OH$_2$ distance.

When the rehydration degree increases to approximately one water molecule per metal center (1H$_2$O/Mg), the broad new peak observed in the previous (0.6H$_2$O/Mg) sample now has a breadth similar to that of the as-made sample, implying that for these Mg ions, the local Mg environments gradually revert back to that in the hydrated phase. It is noticed that although in this sample every Mg, in principle, can adsorb one water molecule, the observed ^{25}Mg intensity only counts for 57% of that seen in the as-made sample. There are several possible reasons for this observation. First, under the experimental conditions employed, the water molecules may not be homogenously distributed within the channels. It is possible that the water initially coordinated to the metal interacts with the water molecules subsequently entering the channel via hydrogen bonding, leaving a significant number of five-coordinated Mg unaffected. Second, even if, on average each Mg adsorbs one water molecule, there will be a distribution of the EFG parameters and chemical shift if the Mg–OH$_2$ bond length varies from site to site. To verify this argument, we carried out the DFT calculations on the Mg(OH$_2$)(DOBDC)$_4^{3-}$ cluster (Figure 2-3). Specifically, we calculated the NMR parameters as a function of the

Mg–OH$_2$ bond length and the results show that (1) while the δ_{iso} changes little, the C_Q varies in a very wide range, consistent with the disordering, and (2) the large Mg–OH$_2$ distances can lead to very large C_Q(^{25}Mg)'s, resulting in the "hidden" Mg. When the degree of hydration is increased to 4 and 5H$_2$O/Mg, the number of ^{25}Mg spins observed and their line shape change back to those of the as-made sample. The results indicate that when a large amount of water is available, the local Mg environment can be completely restored.
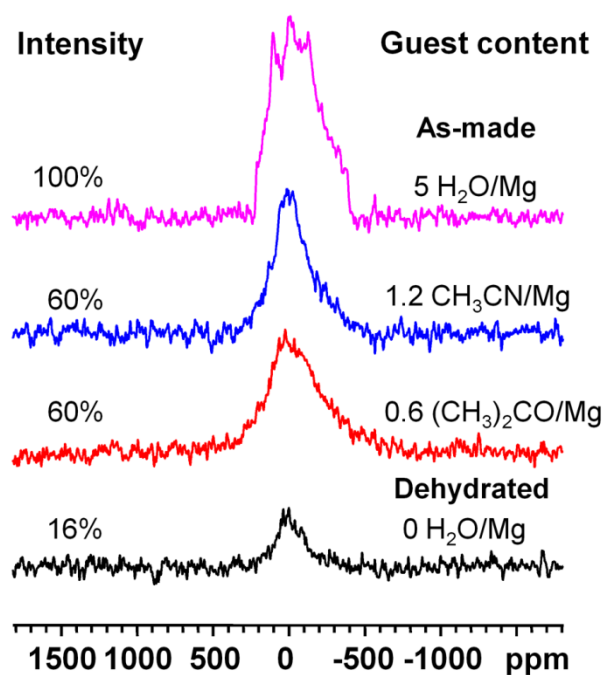
Figure 2-4: ^{25}Mg static SSNMR spectra of CPO-27-Mg loaded with different guest species. All spectra were acquired under the same spectrometer conditions, 16384 scans and a pulse delay of 1 s.

Recently, MOFs have been used as sensors to detect VOCs.[1] CPO-27-Mg certainly has a potential for such application due to the strong interactions between analyte and the open Mg site. Therefore, understanding the effect of adsorption of VOCs on the local Mg geometry is important. We acquired ^{25}Mg static SSNMR spectra of CPO-27-Mg loaded with acetone and acetonitrile (Figure 2-4). In order to maximize the adsorbate effect, saturated adsorption conditions were used. While the PXRD patterns of CPO-27-Mg loaded with two organics (Figure 2-A1) look identical to that of the as-made

phase, the corresponding ^{25}Mg SSNMR spectra are markedly different. The spectrum of the sample loaded with CH_3CN looks similar to that of CPO-27-Mg with $1H_2O$/Mg, indicating that adsorption of CH_3CN also leads to partial line narrowing due to the formation of some octahedral Mg sites. The line shape suggests a distribution of Mg coordination environments. Similarly, adsorption of acetone also increases the intensity of the Mg, while the Mg environment remains disordered. The computational modeling indicates that the EFG parameters are sensitive to both the orientation of the acetone (Figure 2-A5) and its distance to the Mg (Figure 2-5), the observed disorder originates mainly from the variation in the $Mg–OC(CH_3)_2$ distance from site to site. A ^{2}H SSNMR study of CPO-27-Mg is currently performed in our group to understand the dynamics of water and the organics adsorbed at Mg.
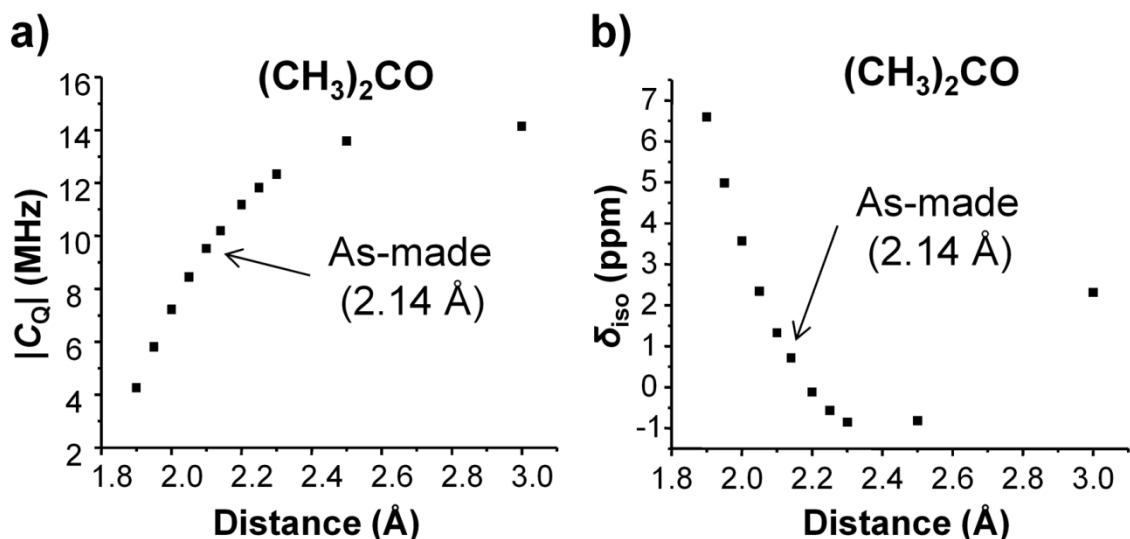
Figure 2-5: The plot of calculated (a) $C_Q(^{25}Mg)$ and (b) $\delta_{iso}(^{25}Mg)$ as a function of the $Mg–OC(CH_3)_2$ distance.

2.4 Conclusions

In summary, ^{25}Mg SSNMR spectra clearly show that upon removal of the water molecule bound to the Mg, the local Mg structure changes from a perfectly ordered to disordered environment, although long-range ordering of the framework remains. A large amount of ^{25}Mg spins become NMR invisible even at 21.1 T due to the large C_Q resulting from the distorted square-pyramid geometry. The Mg disordering persists if the sample is

only partially rehydrated. The local ordering can only be restorted completely if enough water is available. For the CPO-27-Mg loaded with organics, the [25]Mg environments are also disordered although their PXRD patterns indicate the samples remain highly crystalline. The origins of the disordering are discussed based on the NMR data and computational modeling. This work demonstrates the power of [25]Mg SSNMR spectroscopy to characterize Mg-containing MOFs as it provides key information on the local Mg environment complementary to XRD.

2.5 References

(1)   Special issue for Metal–Organic Frameworks: Zhou, H.-C.; Long, J. R.; Yaghi, O. M. *Chem. Rev.* **2012**, *112*, 673-1268.

(2)   Dietzel, P. D. C.; Blom, R.; Fjellvaag, H. *Eur. J. Inorg. Chem.* **2008**, *2008*, 3624-3632.

(3)   Rosi, N. L.; Kim, J.; Eddaoudi, M.; Chen, B.; O'Keeffe, M.; Yaghi, O. M. *J. Am. Chem. Soc.* **2005**, *127*, 1504-1518.

(4)   McDonald, T. M.; lee, W. R.; Mason, J. A.; Wiers, B. M.; Hong, C. S.; Long, J. R. *J. Am. Chem. Soc.* **2012**, *134*, 7056-7065.

(5)   Caskey, S. R.; Wong-Foy, A. G.; Matzger, A. J. *J. Am. Chem. Soc.* **2008**, *130*, 10870-10871.

(6)   Yazaydin, A. O.; Snurr, R. Q.; Park, T.-H.; Koh, K.; Liu, J.; LeVan, M. D.; Benin, A. I.; Jakubczak, P.; Lanuza, M.; Galloway, D. B.; Low, J. J.; Willis, R. R. *J. Am. Chem. Soc.* **2009**, *131*, 18198-18199.

(7)   Wu, H.; Zhou, W.; Yildirim, T. *J. Am. Chem. Soc.* **2009**, *131*, 4995-5000.

(8)   Freitas, J. C. C.; Smith, M. E. *Annu. Rep. NMR Spectrosc.* **2012**, *75*, 25-114 and the references therein.

(9)   Hung, I.; Schurko, R. W. *Solid State Nucl. Magn. Reson.* **2003**, *24*, 78-93.

(10)   Bastow, T. J. *Chem. Phys. Lett.* **2002**, *354*, 156-159.

(11)   Widdifield, C. M.; Bryce, D. L. *Phys. Chem. Chem. Phys.* **2009**, *11*, 7120-7122.

(12)   Davis, M. C.; Brouwer, W. J.; Wesolowski, D. J.; Anovitz, L. M.; Lipton, A. S.; Mueller, K. T. *Phys. Chem. Chem. Phys.* **2009**, *11*, 7013-7021.

(13)   Lipton, A. S.; Heck, R. W.; Primak, S.; McNeill, D. R.; Wilson, D. M.; Ellis, P. D. *J. Am. Chem. Soc.* **2008**, *130*, 9332-9341.

(14)   Kroeker, S.; Stebbins, J. F. *Am. Mineral.* **2000**, *85*, 1459-1464.

(15)   Sideris, P. J.; Nielsen, U. G.; Gan, Z.; Grey, C. P. *Science* **2008**, *321*, 113-117.

(16) Zhu, J.; Huang, Y. *Can. J. Chem.* **2011**, *89*, 803-813.

(17) Pallister, P. J.; Moudrakovski, I. L.; Ripmeester, J. A. *Phys. Chem. Chem. Phys.* **2009**, *11*, 11487-11500.

(18) Cahill, L. S.; Hanna, J. V.; Wong, A.; Freitas, J. C. C.; Yates, J. R.; Harris, R. K.; Smith, M. E. *Chem. Eur. J.* **2009**, *15*, 9785-9798.

(19) Wong, A.; Ida, R.; Mo, X.; Gan, Z.; Poh, J.; Wu, G. *J. Phys. Chem. A* **2006**, *110*, 10084-10090.

(20) Griffin, J. M.; Berry, A. J.; Ashbrook, S. E. *Solid State Nucl. Magn. Reson.* **2011**, *40*, 91-99.

(21) Laurencin, D.; Gervais, C.; Stork, H.; Kramer, S.; Massiot, D.; Fayon, F. *J. Phys. Chem. C* **2012**, *116*, 19984-19995.

(22) Sutrisno, A.; Terskikh, V. V.; Shi, Q.; Song, Z.; Dong, J.; Ding, S. Y.; Wang, W.; Provost, B. R.; Daff, T. D.; Woo, T. K.; Huang, Y. *Chem. Eur. J.* **2012**, *18*, 12251-12259.

(23) Kunwar, A. C.; Turner, G. L.; Oldfield, E. *J. Magn. Reson.* **1986**, *69*, 124-127.

(24) *WSolids1: Solid-State NMR Spectrum Simulation*, v. 1. 17. 30. ed.; 2001.

(25) Frisch, M. J. *Gaussian 09*, revision A.1; Gaussian, Inc.: Wallingford, CT, 2009.

(26) Adiga, S.; Aebi, D.; Bryce, D. L. *Can. J. Chem.* **2007**, *85*, 496-505.

(27) Ernst, H.; Freude, D.; Wolf, I. *Chem. Phys. Lett.* **1993**, *212*, 588-596.

2.6 Appendix

Section A1: Powder XRD Characterization of CPO-27-Mg Samples

The identity and purity of CPO-27-Mg samples were confirmed by powder XRD. PXRD patterns (Figure 2-A1) were recorded on a Rigaku diffractometer equipped with a graphite monochromator using Co Kα radiation ($\lambda = 1.7902$ Å). Diffraction data were collected from 5° to 65° in 2θ at a step size of 0.02°.
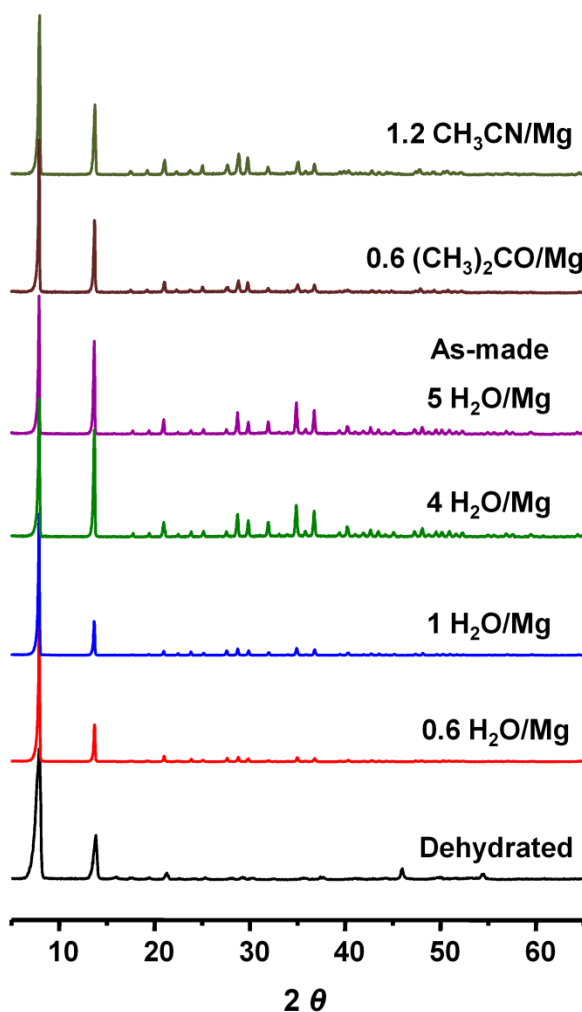
Figure 2-A1: Powder XRD patterns of CPO-27-Mg samples.

The guest contents of CPO-27-Mg samples were measured by thermogravimetric analysis (TGA). The samples were heated under N_2 atmosphere on a Mettler Toledo

TGA/DTA851e instrument from 25 to 500 °C at a constant heating rate of 10 °C/min. The samples were also characterized by ^{13}C SSNMR experiments to confirm the inclusion of guest species (Figure 2-A2).

Section A2: ^{13}C Solid-State NMR Characterization of CPO-27-Mg Samples
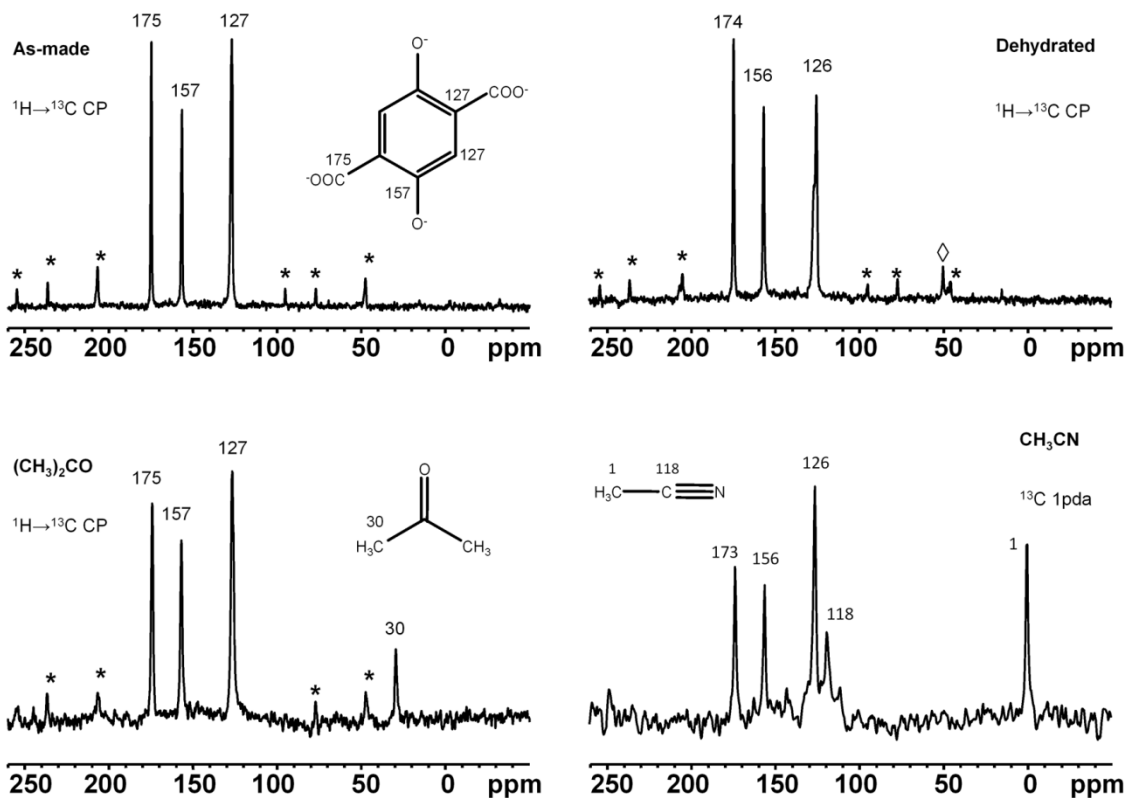
Figure 2-A2: [13]C MAS spectra of CPO-27-Mg samples. [1]H→[13]C CP: contact time = 10 ms. * indicates spinning sidebands. ◊: residual CH_3OH.

Magic-angle spinning (MAS) ^{13}C SSNMR spectra were collected on a Varian Infinity Plus 400 WB spectrometer operating at 100.5 MHz at a magnetic field of 9.4 T using a 4 mm triple-tuned T3 MAS probe with a spinning speed of 8 kHz. For ^{13}C one-pulse experiments with ^{1}H decoupling (1pda), a 30° pulse (1.5 μs) was used. The radio-frequency field for ^{1}H decoupling was approximately 40 kHz, and the pulse delay of ^{13}C was 30 s. In the case of [1]H→[13]C cross-polarization (CP) experiments, the Hartmann-Hahn matching conditions were calibrated on solid admantane, which is also a secondary

reference for ^{13}C chemical shift (δ_{iso} = 37.8 ppm for the methylene signal). Proton 90° pulse width was 5.3 μs, and a proton pulse delay of 10 s was used.

Three peaks were observed in the ^{13}C MAS spectra of the CPO-27-Mg samples. Two of the three chemically inequivalent carbon atoms of benzene rings have very similar chemical shifts, giving rise to an overlapping peak at 127 ppm, which could not be resolved under the experimental conditions we used. The adsorbed acetone and acetonitrile were also confirmed.

Section A3: Additional ^{25}Mg Static Spectra of CPO-27-Mg Samples

Due to the spectrometer-time limit, ^{25}Mg spectra in Figure 2-2 and 2-4 were all recoded with 16384 scans. To ensure all the spectral features were captured, we selected two (dehydrated and 0.6H$_2$O/Mg CPO-27-Mg) samples and obtained their spectra with a better S/N ratio by acquiring them with significantly more scans (65536 and 49152 scans for dehydrated and 0.6H$_2$O/Mg CPO-27-Mg, respectively). The resulting spectra are compared to those obtained with 16384 scans in Figure 2-A3. As one can see clearly, no additional feature is identified.
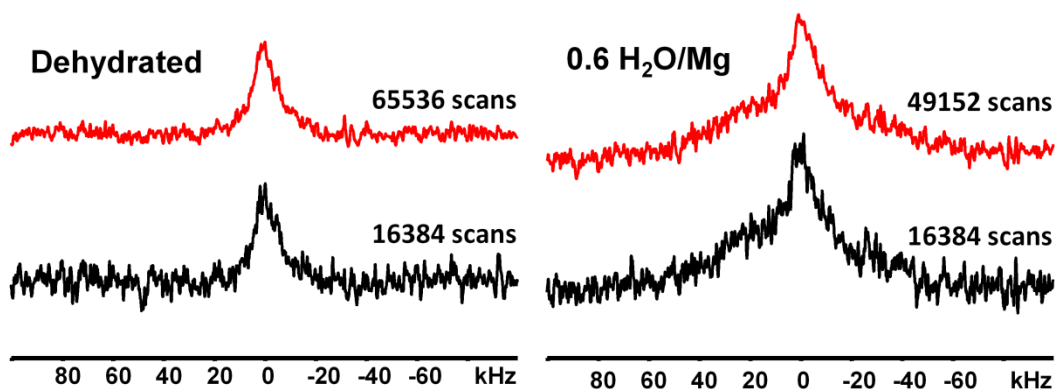
Figure 2-A3: ^{25}Mg static spectra of selected CPO-27-Mg samples at 21.1 T.

Section A4: Theoretical Calculations of ^{25}Mg EFG Parameters

The calculated ^{25}Mg EFG parameters of as-made and dehydrated CPO-27-Mg were listed in Table 2-A1. Although the DFT calculation overestimated the C_Q of as-

made CPO-27-Mg, the results do confirm the predication that the $C_Q(^{25}Mg)$ in dehydrated sample is significantly larger than that of the as-made sample.

Table 2-A1: Calculated ^{25}Mg EFG tensors of as-made and dehydrated CPO-27-Mg.

Sample	$|C_Q|$ (MHz)	η_Q	δ_{iso} (ppm)
As-made	9.11	0.46	0.54
Dehydrated	14.10	0.32	6.50
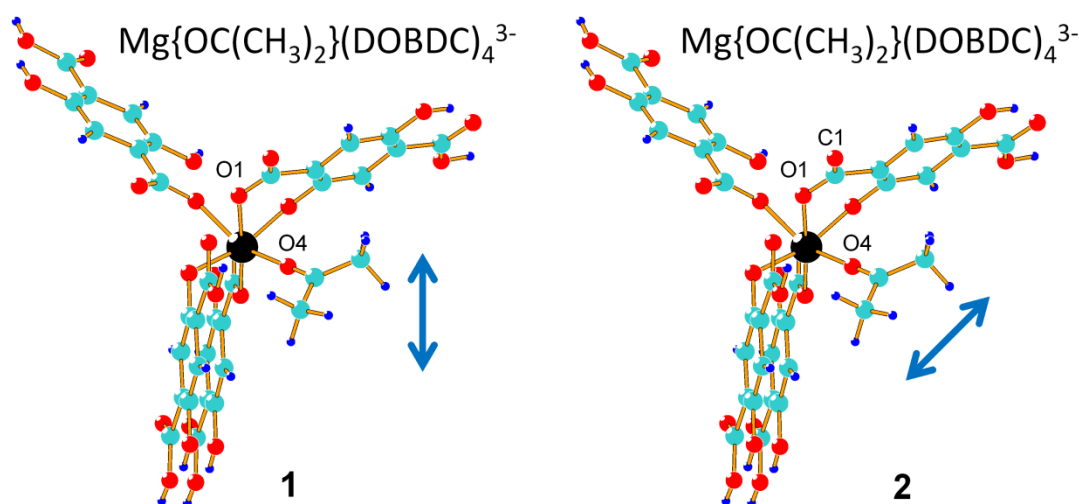
Figure 2-A4: Two types of distortion used in the DFT calculations to describe the effect of bond angle. Arrows indicate the change of guest locations.

The acetone was chosen to represent the organics loaded inside the CPO-27-Mg samples. The effect of acetone orientations was probed by systematically: (1) varying the O1–Mg–O4 angle from 92.8° while keeping the Mg–O distance at 2.14 Å (the values taken from the structure of as-made CPO-27-Mg). See the distortion **1** in Figure 2-A4; (2) altering the C1–O1–Mg–O4 dihedral angle from 49.6° in the as-made sample. See the distortion **2** in Figure 2-A4. The results are shown in Figures 5-A5. In general, the effect of the Mg–O bond length on NMR parameters is much larger than that of the bond angle. Therefore, the observed distribution of the $C_Q(^{25}Mg)$ is likely due to the distribution of the Mg–O distances.
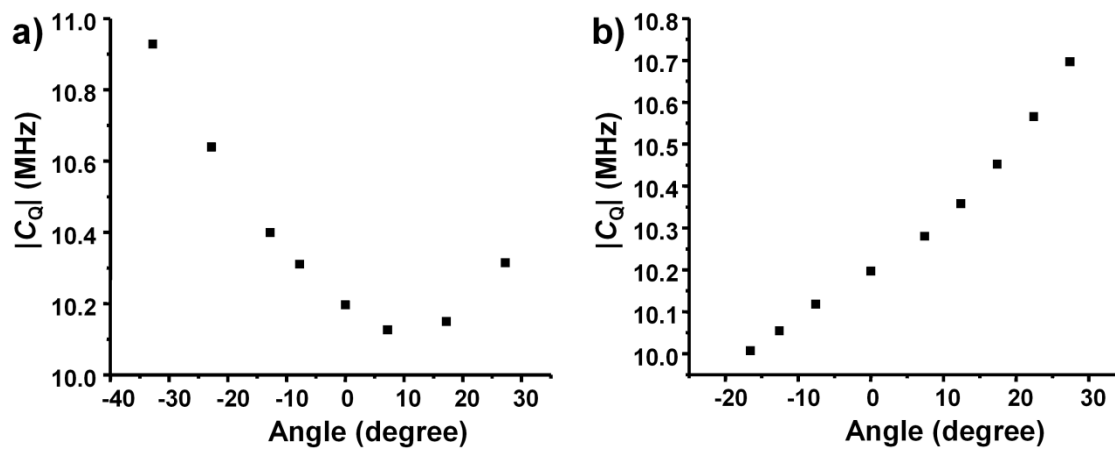
Figure 2-A5: The plot of calculated $C_Q(^{25}\text{Mg})$ as a function of: (a) O1–Mg–O4 angle from 92.8° and (b) C1–O1–Mg–O4 angle from 49.6°.

Chapter 3

3 Resolving Multiple Non-Equivalent Metal Sites in Magnesium-Containing Metal–Organic Frameworks by Natural Abundance ^{25}Mg Solid-State NMR Spectroscopy[†]

3.1 Introduction

Metal–organic frameworks (MOFs) are a group of novel inorganic–organic hybrid porous materials. Because of their many unique properties including rich structural diversity, large surface area, tunable porosity, high thermal stability and selective adsorption, MOFs are suitable for a broad range of applications, in particular for gas separation and storage.[1] In recent years, incorporating Mg^{2+} into MOFs has drawn much attention since it is inexpensive, nontoxic, and especially, has low atomic weight.[2] Structural characterization is very important for these MOFs. Unfortunately, due to the difficulty in obtaining suitable single crystals for X-ray diffraction, many MOFs' structures were determined from more limited powder XRD data. In such cases an unambiguous structure solution requires additional information from complementary techniques such as solid-state NMR (SSNMR) spectroscopy. The number of non-equivalent metal centers is usually determined by crystal symmetry. Therefore, it is desirable to directly determine the number of non-equivalent Mg sites by ^{25}Mg SSNMR spectroscopy. However, although recent work[3-17] has demonstrated that ^{25}Mg SSNMR spectroscopy can be employed as a powerful tool to characterize Mg-containing minerals, organometallics, and biomolecules, directly probing the local Mg structure in MOF-based materials by natural abundance ^{25}Mg SSNMR spectroscopy is still rare.[18] This is due to several reasons: 1) the low intrinsic sensitivity arising from the unfavorable ^{25}Mg ($I = 5/2$) nuclear properties, such as a small gyromagnetic ratio (γ) of -1.639 × 10^7 rad·s^{-1}·T^{-1} and a relatively low natural abundance of 10.0%,[19] 2) a relatively large quadrupole moment of

---

[†] A version of this chapter (except the data of the acetone sample) has been published elsewhere: Xu, J.; Terskikh, V. V.; Huang, Y. *Chem. Eur. J.* **2013**, *19*, 4432-4436. Reproduced by the permission of John Wiley and Sons.

199.4 mb,[20] 3) a very low ^{25}Mg concentration due to low densities of MOFs. For example, the number of ^{25}Mg atoms per nm^3 in microporous α-Mg$_3$(HCOO)$_6$ (a MOF examined in this work) is only 0.73 compared to the number for the dense MgO at 5.3. Furthermore, ^{25}Mg has a narrow chemical shift range, which makes it challenging to differentiate multiple Mg sites with very similar local environments. Nevertheless, several recent studies have demonstrated that the low-sensitivity associated with low-γ unreceptive quadrupolar nuclei in MOFs can be alleviated by performing NMR experiments at high magnetic fields.[3-6,18,21]

Herein, using microporous α-Mg$_3$(HCOO)$_6$, a representative Mg-containing MOF as an example, we demonstrate that multiple (four) non-equivalent Mg sites with very similar local structures can be directly differentiated by ^{25}Mg natural abundance two-dimensional triple-quantum magic-angle spinning (3QMAS)[22] at a magnetic field of 21.1 T in combination with theoretical calculations using the density functional theory (DFT) gauge including projector augmented wave (GIPAW) method.[23,24, 3a-d]

Microporous α-Mg$_3$(HCOO)$_6$ is an important commercialized MOF (trade name Basosive M050).[25-27] It can be facilely prepared on a large scale under solvent-free conditions using low-cost and nontoxic starting materials such as MgO and formic acid. It displays permanent porosity up to 400 °C after desolvation (activation) as well as exceptional stability in many solvents. Microporous α-Mg$_3$(HCOO)$_6$ has been demonstrated to have great potential in gas separation such as separating C$_2$H$_2$ from CO$_2$ and CO from H$_2$.[28-30] Another reason for choosing this MOF is because good single crystal structures[25] are available, against which the viability of NMR approach can be checked.

In this work, we examined natural abundance ^{25}Mg SSNMR spectra of four samples of microporous α-Mg$_3$(HCOO)$_6$: as-made (*i.e.*, containing solvent DMF molecules), activated (empty framework), acetone- and benzene-loaded phases (hereafter referred to as DMF, activated, acetone and benzene samples, respectively).

3.2   Experimental Section

3.2.1   Sample Preparation

As-made microporous α-Mg$_3$(HCOO)$_6$ (DMF sample) was prepared following the method described by Rood and co-workers.[25] A typical synthesis of as-made microporous α-Mg$_3$(HCOO)$_6$ involves mixing 3 mmol Mg(NO$_3$)$_2$·6H$_2$O (Sigma-Aldrich, 99%), 6 mmol formic acid (Alfa Aesar, 97%), and 10 mL N,N'-dimethylformamide (DMF, Reagent grade, Caledon) in a 23 mL Teflon-lined autoclave and then heated at 383 K for 2 days. The product was washed with DMF and recovered by vacuum filtration as a white powder. The activated phase was obtained by heating the DMF phase under dynamic vacuum at 150 °C for 1 d. To prepare the acetone and benzene samples, the crystalline activated phase was soaked in 2 mL of dry acetone or benzene and kept for 2 d. The excess solvents were allowed to evaporate in the air. All samples were stored in sealed vials. The purity and crystallinity of microporous α-Mg$_3$(HCOO)$_6$ samples were confirmed by powder X-ray diffractions (Figure 3-A1, appendix). The PXRD patterns were recorded on a Rigaku diffractometer equipped with a graphite monochromator using Co Kα radiation (λ = 1.7902 Å). Diffraction data were collected from 5° to 45° in 2θ at a step size of 0.02°. The guest content was measured by thermogravimetric analysis (TGA) (Figure 3-A2). The samples were heated under a N$_2$ atmosphere on a Mettler Toledo TGA/DTA851e instrument from 25 to 500 °C at a heating rate of 10 °C/min. The occlusion of guest species was also confirmed by ^{13}C SSNMR experiments (Figure 3-A3).

3.2.2   NMR Characterizations and Theoretical Calculations

^{25}Mg solid-state NMR measurements were performed at 21.1 T (where the Larmor frequency of ^{25}Mg is 55.09 MHz) on a Bruker Avance II spectrometer at the National Ultrahigh-field NMR Facility for Solids in Ottawa, Canada. Static ^{25}Mg NMR were acquired with the 90°-τ-90° echo sequence[31] with continuous-wave proton decoupling on a home-built 7 mm H/X low-γ probe for stationary samples with a dual resonator design. The one-pulse ^{25}Mg MAS experiments employed a Bruker 7 mm double resonance MAS probe with a spinning rate of 5 kHz and continuous-wave proton decoupling. The solution 90° pulse for 1M MgCl$_2$ aqueous solution was 9 μs,

corresponding to a selective 90° pulse of 3 μs for solids. The interpulse delay τ in static experiments was 200 μs. The ^{1}H decoupling radio frequency power was about 30 kHz. The rotor-synchronized ^{25}Mg 3QMAS spectra with a spinning rate of 5 kHz were acquired using both the standard 3-pulse Z-filter sequence[32] and the soft-pulse-added-mixing (SPAM) MQMAS sequence[33,34] for comparison purposes. The durations of excitation, conversion and Z-filter selective pulses were 10.0, 4.2 and 10.0 μs, respectively. SPAM 3QMAS data were collected under the echo/anti-echo mode. In a typical SPAM 3QMAS experiment, 2400 scans were acquired for each t_1 increment, with 64 increments in F1 dimension accumulated. The total experiment time was about 48 hours per 3QMAS experiment (Table 3-A1). FID signals were Fourier-transformed and sheared to obtain the separate F1 and F2 dimensions using the Bruker Topspin software. The chemical shift of ^{25}Mg was referenced to 1 M MgCl$_2$ aqueous solution at 0 ppm. The pulse delay of ^{25}Mg was checked from 0.5 s to 20 s, and 1 s was used for all ^{25}Mg SSNMR experiments. The numbers of scans for all ^{25}Mg SSNMR experiments were listed in Table 3-A1. All ^{25}Mg SSNMR spectra were simulated using the QuadFit software.[35]

Gauge including projector augmented wave (GIPAW) quantum chemical calculations were conducted using the CASTEP code (version 4.4, Accelrys Materials Studio) running on a HP xw4400 workstation with a single Intel dual-core 2.67 GHz processor and 8 GB DDR RAM. The NMR module was used to calculate the ^{25}Mg electric field gradient (EFG) tensors. Unit cell parameters and atomic coordinates were taken from their crystal structures.[25] The calculations were performed using ultra-soft pseudopotentials generated from the "on-the-fly" method implemented within the CASTEP. The Generalized Gradient Approximation (GGA) with Perdew, Burke and Ernzerhof (PBE) correlation functional was used. Because the unit cells are large (> 1000 Å^3), plane-wave cut-off energy of 450 eV was applied to all calculations. The H positions of four samples were optimized prior to the NMR calculations. The $C_Q(^{25}$Mg) values were produced automatically from the EFG tensor by the CASTEP program and they were corrected using the equation $C_Q(^{25}$Mg, corrected) = [$C_Q(^{25}$Mg, CASTEP) + 0.13] / 1.225 (in MHz) to account for overestimation.[5] The isotropic chemical shift for ^{25}Mg was

computed using the correlation $\sigma_{iso}(^{25}Mg, corrected) = [565.23 - \sigma_{iso}(^{25}Mg, CASTEP)] /$ 1.049 (in ppm) in the above-mentioned literature.

3.3 Results and Discussion

The crystal structures of four microporous α-$Mg_3(HCOO)_6$ samples determined from single crystal XRD data indicate that they have the same space group ($P2_1/n$), containing four crystallographically distinct Mg sites [4(Mg1, Mg3) 2(Mg2, Mg4)].[25] The frameworks of four samples are identical in terms of their topology. As illustrated in Figure 3-1 (using the DMF phase as an example), the framework is constructed by interconnecting one-dimensional chains of edge-shared octahedra of Mg1 and Mg3 with vertex-shared MgO_6 octahedra of Mg2 and Mg4 via Mg1, forming narrow one-dimensional zig-zag channels along the b direction with a dimension of 4.5 Å × 5.5 Å. The coordination environments of individual Mg sites are also shown. All formate anions adopt similar bonding modes that one oxygen bridges to two Mg centers (μ^2-oxygen) and the other one only connects to one Mg (μ^1-oxygen). Although each Mg is octahedrally bound to six different formate anions, there are three types of coordination environments for four Mg sites: Mg1 bonds to six μ^2-oxygens; both Mg2 and Mg4 bond to four μ^1-oxygens and two μ^2-oxygens, whereas Mg3 is bound to two μ^1-oxygens and four μ^2-oxygens.
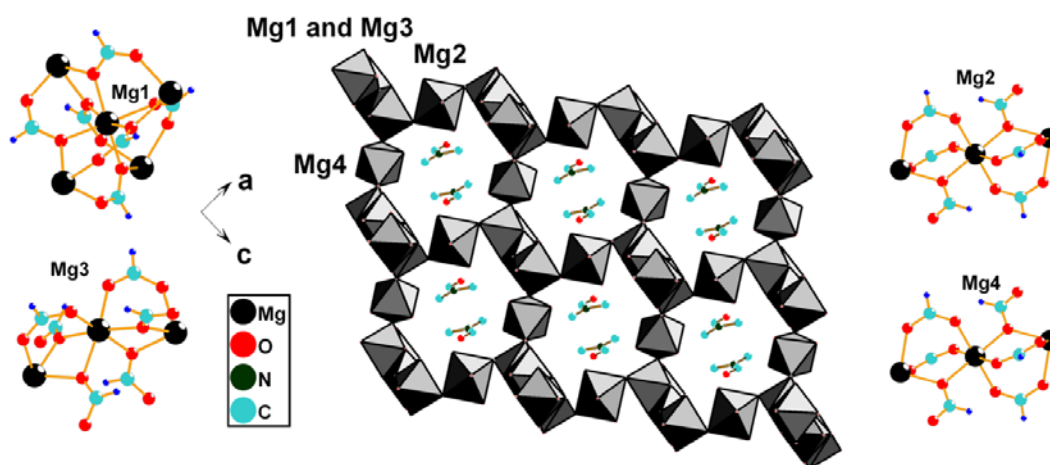
Figure 3-1: The framework and Mg coordination environments of the DMF sample. Hydrogen atoms of the encapsulated DMF are omitted for clarity.

The static ^{25}Mg spectra of four phases were first acquired at 21.1 T (Figure 3-2a). None of the spectra exhibits the typical second-order quadrupolar line shape of the central transition expected from a single Mg site, indicating that the observed spectra contain overlapping signals, consistent with the fact that all samples have multiple Mg sites. It is noteworthy that the ^{25}Mg spectra of four samples look distinctly different, suggesting that the ^{25}Mg static NMR spectra are very sensitive to the guest species present inside of the framework, even though their powder XRD patterns are very similar (Figures 3-A1). Fitting the static spectra with four sites is very difficult, if not impossible, because of the large number of variables. The small spectral widths (about 5 kHz) allow us to apply magic-angle spinning (MAS) technique to reduce the line broadening due to the second-order quadrupolar and chemical shielding interactions. Despite the fact that the line widths under MAS conditions are reduced significantly (Figure 3-2b), the multiple signals in ^{25}Mg MAS spectra still remain unresolved due to the combination of very similar chemical shifts and residual second-order quadrupolar interactions.
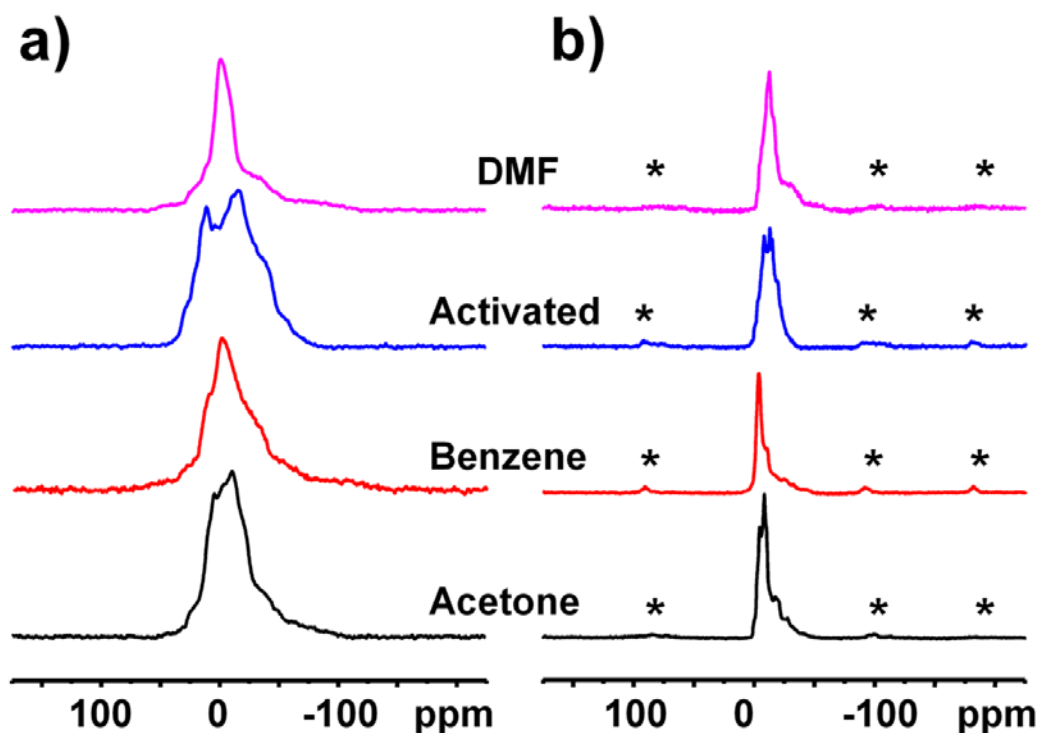
Figure 3-2: (a) Natural abundance ^{25}Mg static, and (b) 5 kHz MAS spectra of four microporous α-Mg$_3$(HCOO)$_6$ phases at 21.1 T. *: spinning sidebands.

To achieve higher resolution, we applied a two-dimensional (2D) triple-quantum magic-angle spinning (3QMAS) method.[22] This 2D technique can achieve high-resolution by eliminating the second-order quadrupolar interaction experienced by half-integer quadrupolar nuclei including ^{25}Mg, and can also be employed to separate multiple sites whose signals overlap in 1D spectra.

The 3QMAS experiment was first performed on the activated phase using the standard Z-filter sequence.[32] However, after acquiring data for nearly two days, the signal-to-noise (S/N) ratio of the spectrum (Figure 3-A4, A5) was still too poor to resolve individual sites. A soft-pulse-added-mixing (SPAM) modification of 3QMAS[33,34] was then used for improved sensitivity. This approach has been shown to be effective for ^{25}Mg in layered double hydroxides.[36-38]
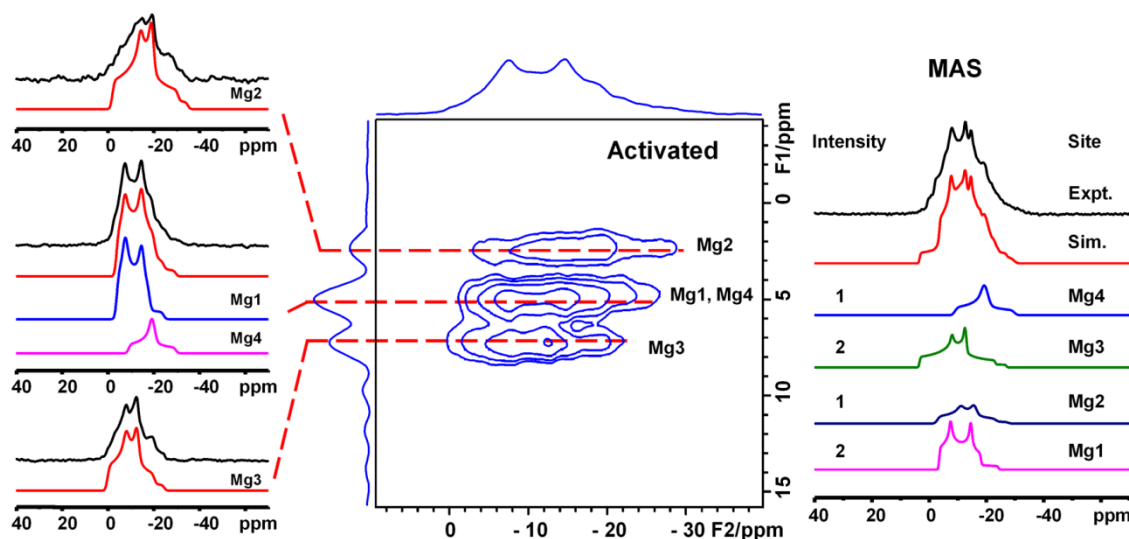
Figure 3-3: Natural abundance ^{25}Mg SPAM-3QMAS spectrum of the activated sample. The dashed lines correspond to the slices taken for simulation. The MAS spectrum simulated with the parameters obtained from 3QMAS is also shown.

The ^{25}Mg SPAM-3QMAS spectrum of the activated sample clearly exhibits several resolved peaks on the high-resolution (F1) dimension centered at 2, 5 and 7.5 ppm (Figure 3-3). The cross-sections at the chemical shift positions of the two peaks at 2 and 7.5 ppm can each be fitted with a single resonance; whereas the slice taken through the peak at 5 ppm on F1 had to be fitted by two Mg sites. The NMR parameters,

including quadrupolar coupling constant (C_Q), asymmetry parameter (η_Q) and isotropic chemical shift (δ_{iso}) determined in the 3QMAS experiment, are further refined by simulating the ^{25}Mg 1D MAS spectrum (Figure 3-3 and Table 3-1). Since 3QMAS is not a quantitative technique, simulation of the 1D MAS spectrum also allows one to obtain correct relative intensities of four Mg sites. Similarly, SPAM-3QMAS spectra of the other three phases were also obtained (Figure 3-4–6) and revealed that DMF, acetone and benzene samples also have four Mg sites. It is worth mentioning that all four Mg sites of the acetone sample can be directly resolved in the 2D SPAM-3QMAS spectrum. The NMR parameters of these phases are given in Table 3-1. The fact that four Mg sites were observed in DMF, activated, acetone and benzene samples is consistent with the proposed crystal structures based on the single crystal XRD data. It should be pointed out that for this particular MOF, the ^{25}Mg SSNMR spectra provide a resolution similar to that of the ^{13}C MAS NMR spectra. The crystal structures suggest that for all four phases, there are six crystallographically non-equivalent framework carbons. All six carbons are identified for DMF, activated, acetone and benzene phases. The high magnetic field allows significant sensitivity enhancement, a substantial decrease in the residual line broadening due to the second-order quadrupolar interaction, and an increase in the dispersion of the chemical shift. The measured C_Q values for all four sites in all four samples fall in the range between 0.9–3.0 MHz, implying that the electric field gradients (EFGs) at Mg sites are fairly small. Previous studies on the dense Mg(HCOO)$_2$·2H$_2$O showed that the Mg site bound to six different formate ligands has a C_Q of 2.4 MHz.[5] All η_Q values are non-zero, indicating that the EFG tensors are not axial symmetric, which is consistent with the low site symmetries (C_1 for Mg1 and Mg3 and C_i for Mg2 and Mg4, respectively). The δ_{iso} values (-14 to 4 ppm) are also in the normal range of Mg oxyanion compounds. Using the EFG parameters derived from the MAS spectra, the ^{25}Mg static spectra can also be simulated reasonably well without chemical shift anisotropy (Figure 3-A6), suggesting that the static spectra are mainly dominated by the quadrupolar interactions.
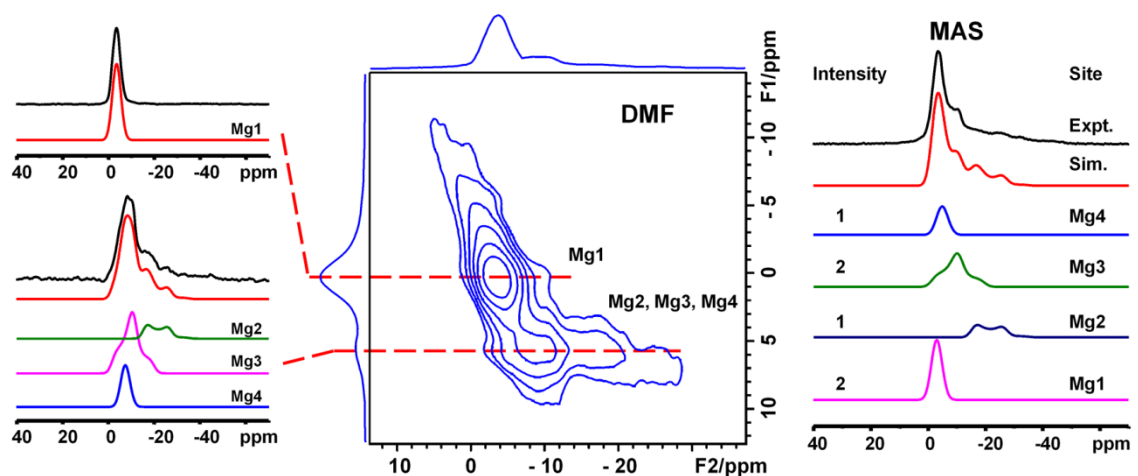
Figure 3-4: Natural abundance ^{25}Mg SPAM-3QMAS spectrum of the DMF sample. The dashed lines correspond to the slices taken for simulation. The MAS spectrum simulated with the parameters obtained from 3QMAS is also shown.
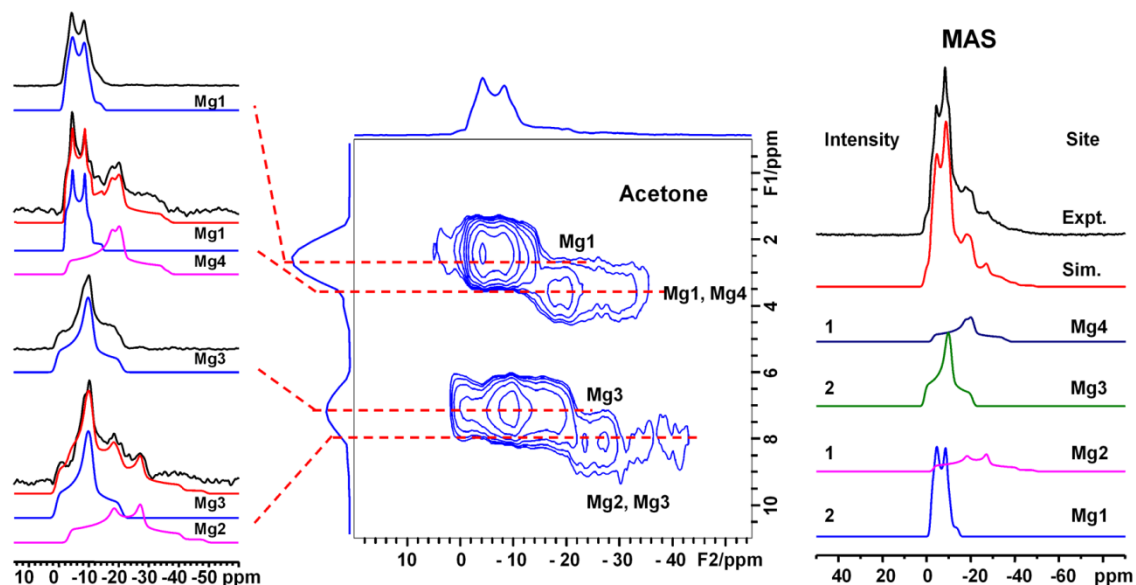
Figure 3-5: Natural abundance ^{25}Mg SPAM-3QMAS spectrum of the acetone sample. The dashed lines correspond to the slices taken for simulation. The MAS spectrum simulated with the parameters obtained from 3QMAS is also shown.
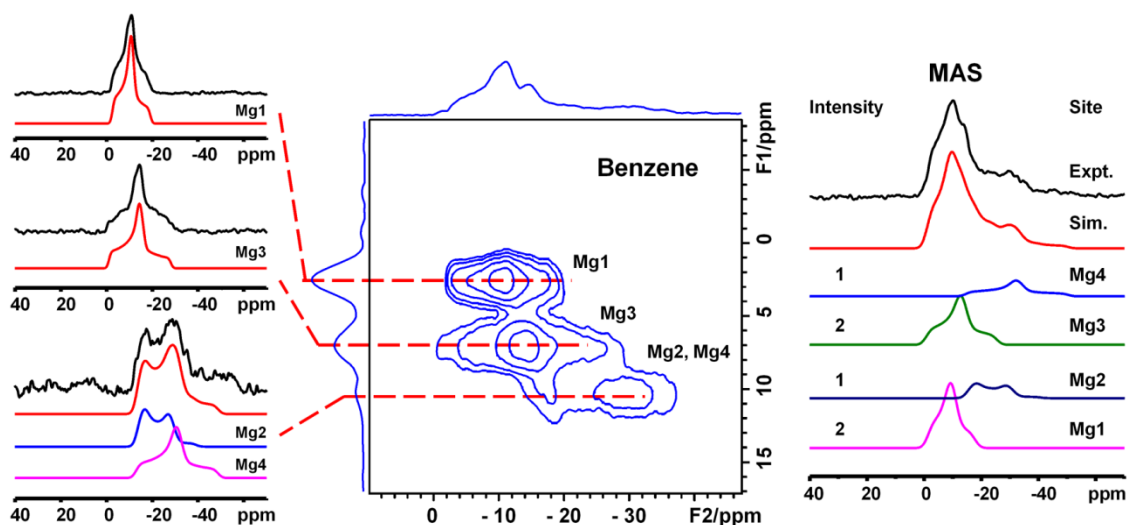
Figure 3-6: Natural abundance ^{25}Mg SPAM-3QMAS spectrum of the benzene sample. The dashed lines correspond to the slices taken for simulation. The MAS spectrum simulated with the parameters obtained from 3QMAS is also shown.

Table 3-1: Experimental and calculated ^{25}Mg NMR parameters.

Sample	Site	$|C_Q|$ [MHz]		η_Q		δ_{iso} [ppm]		Area [%]
		Exptl	Calcd	Exptl	Calcd	Exptl	Calcd	
DMF	Mg1	0.9(1)	1.45	1.0(1)	0.75	-1(3)	3.78	36(2)
	Mg2	2.2(1)	3.49	0.1(1)	0.37	-13(3)	-0.41	16(2)
	Mg3	1.8(1)	1.96	1.0(1)	0.76	-1(3)	4.17	32(2)
	Mg4	1.0(1)	2.82	1.0(1)	0.93	-2(3)	-0.53	16(2)
activated	Mg1	2.1(1)	2.23	0.3(1)	0.15	-2(3)	2.41	33(2)
	Mg2	2.2(1)	2.48	0.6(1)	0.97	-2(3)	-1.72	18(2)
	Mg3	2.4(1)	2.25	0.7(1)	0.89	4(3)	2.71	32(2)
	Mg4	1.9(1)	2.10	1.0(1)	0.72	-9(3)	-2.50	17(2)
acetone	Mg1	1.7(1)	1.58	0.4(1)	0.43	-1(3)	3.95	33(2)
	Mg2	3.0(1)	2.51	0.6(1)	0.81	-2(3)	0.56	17(2)
	Mg3	2.0(1)	1.88	0.9(1)	0.96	1(3)	4.87	33(2)
	Mg4	2.5(1)	2.47	0.9(1)	0.88	-3(3)	-0.44	17(2)
benzene	Mg1	1.7(1)	1.78	1.0(1)	0.54	-1(3)	3.08	36(2)
	Mg2	2.4(1)	3.05	0.2(1)	0.86	-12(3)	-0.80	14(2)
	Mg3	2.1(1)	2.23	1.0(1)	0.79	-1(3)	3.45	36(2)
	Mg4	2.5(1)	3.18	1.0(1)	0.89	-14(3)	-0.29	14(2)

Although four Mg sites for each sample have been identified, their assignments are not straightforward. As mentioned earlier, the proposed crystal structures indicate the occupancies of Mg1 : Mg2 : Mg3 : Mg4 are 2 : 1 : 2 : 1. Thus, the two resonances with stronger relative intensities can be unambiguously assigned to Mg1 and Mg3, and the two peaks with weaker intensities to Mg2 and Mg4. Although Mg1 and Mg3 can be distinguished from Mg2 and Mg4, further assignment is, however, difficult. In the literature, spectral assignment sometimes was accomplished by using the empirical correlations between the NMR parameters (C_Q and/or δ_{iso}) and local Mg geometry. However, recent studies have shown that such empirical relationships do not always give correct assignments for the multiple ^{25}Mg sites. Instead, first-principles calculation of ^{25}Mg NMR parameters by using GIPAW approach implemented in the CASTEP code has proven to be a reliable method for spectral interpretation and assignment.[3-6] For this reason, we carried out the GIPAW plane-wave pseudopotential DFT calculations of ^{25}Mg EFG and nuclear magnetic shielding tensors for all four microporous α-Mg$_3$(HCOO)$_6$ samples. The results are presented in Table 3-1.

For all four phases the calculated C_Q^{calcd}(Mg3) is greater than C_Q^{calcd}(Mg1). Therefore, we assigned the observed signal with a larger C_Q to Mg3. This assignment is further supported by the trend that the calculated chemical shifts of Mg3 are always more deshielded than Mg1 in all four samples, which is consistent with the experimental results (Table 3-1). Similarly, Mg2 and Mg4 can also be differentiated based on the theoretical calculation results. For the DMF, activated, and acetone samples, the Mg resonance with a larger C_Q is assigned to Mg2, whereas for benzene sample, the assignment of Mg2 and Mg4 is the opposite.

One special feature of MOFs is that their frameworks can be flexible.[39-43] For example, microporous α-Mn$_3$(HCOO)$_6$, an analogue of microporous α-Mg$_3$(HCOO)$_6$, shows temperature-triggered gate opening for N$_2$ and Ar due to dynamic opening of the pore aperture.[44] Since the GIPAW calculation is based on the crystal structure obtained at 100 K and the ^{25}Mg SSNMR spectra were obtained at ambient temperature, it is necessary to check if microporous α-Mg$_3$(HCOO)$_6$ framework exhibits a significant flexibility at room temperature. To this end, ^{2}H NMR has been shown to be effective for

the study of framework flexibility.[40-43] We prepared microporous α-Mg$_3$(DCOO)$_6$ using deuterated formic acid. The ^{2}H static SSNMR spectrum of activated α-Mg$_3$(DCOO)$_6$ acquired at room temperature exhibits a typical Pake powder pattern (Figure 3-A7). Both the shape of the pattern and the C_Q value (155 kHz) are typical of the static C–^{2}H bonds, which suggests that the framework is likely rigid.

3.4 Conclusions

In conclusion, using a representative MOF, microporous α-Mg$_3$(HCOO)$_6$, as an example, we have demonstrated that multiple non-equivalent Mg (four) sites can be directly differentiated by performing ^{25}Mg 3QMAS SSNMR experiments at a magnetic field of 21.1 T at natural abundance. The ability to acquire high-quality two-dimensional ^{25}Mg spectra at natural abundance is important since the cost of isotopic enrichment can be prohibitively high. The capability of differentiating multiple Mg sites with very similar local Mg environments is critical because it allows one to directly compare the NMR spectra with the X-ray determined structure. We feel that the approach described and the results presented in this work can be used as a benchmark for determining the structures of Mg-containing MOFs with unknown or poorly described structures. It is also worth mentioning that although overlapping, the ^{25}Mg 1D MAS spectra are sensitive to the subtle change in the local Mg environments and the spectra at 21.1 T can be obtained in about 30 minutes at natural abundance. Therefore, ^{25}Mg MAS NMR has the potential to be used for *in situ* monitoring of changes in the MOF framework during catalysis, adsorption and phase transition induced by temperature and pressure.

3.5 References

(1)   Special issue for Metal–Organic Frameworks: Zhou, H.-C.; Long, J. R.; Yaghi, O. M. *Chem. Rev.* **2012**, *112*, 673-1268.

(2)   Banerjee, D.; Parise, J. B. *Cryst. Growth Des.* **2011**, *11*, 4704-4720.

(3)   Freitas, J. C. C.; Smith, M. E. *Annu. Rep. NMR Spectrosc.* **2012**, *75*, 25-114 and the references therein.

(4)   Pallister, P. J.; Moudrakovski, I. L.; Ripmeester, J. A. *Phys. Chem. Chem. Phys.* **2009**, *11*, 11487-11500.

(5) Cahill, L. S.; Hanna, J. V.; Wong, A.; Freitas, J. C. C.; Yates, J. R.; Harris, R. K.; Smith, M. E. *Chem. Eur. J.* **2009**, *15*, 9785-9798.

(6) Laurencin, D.; Gervais, C.; Stork, H.; Kramer, S.; Massiot, D.; Fayon, F. *J. Phys. Chem. C* **2012**, *116*, 19984-19995.

(7) Hung, I.; Schurko, R. W. *Solid State Nucl. Magn. Reson.* **2003**, *24*, 78-93.

(8) Bastow, T. J. *Chem. Phys. Lett.* **2002**, *354*, 156-159.

(9) Wong, A.; Ida, R.; Mo, X.; Gan, Z.; Poh, J.; Wu, G. *J. Phys. Chem. A* **2006**, *110*, 10084-10090.

(10) Widdifield, C. M.; Bryce, D. L. *Phys. Chem. Chem. Phys.* **2009**, *11*, 7120-7122.

(11) Davis, M. C.; Brouwer, W. J.; Wesolowski, D. J.; Anovitz, L. M.; Lipton, A. S.; Mueller, K. T. *Phys. Chem. Chem. Phys.* **2009**, *11*, 7013-7021.

(12) Lipton, A. S.; Heck, R. W.; Primak, S.; McNeill, D. R.; Wilson, D. M.; Ellis, P. D. *J. Am. Chem. Soc.* **2008**, *130*, 9332-9341.

(13) Kroeker, S.; Stebbins, J. F. *Am. Mineral.* **2000**, *85*, 1459-1464.

(14) Zhu, J.; Huang, Y. *Can. J. Chem.* **2011**, *89*, 803-813.

(15) Griffin, J. M.; Berry, A. J.; Ashbrook, S. E. *Solid State Nucl. Magn. Reson.* **2011**, *40*, 91-99.

(16) Sham, S.; Wu, G. *Inorg. Chem.* **2000**, *39*, 4-5.

(17) Shimoda, K.; Tobu, Y.; Hatakeyama, M.; Nemoto, T.; Saito, K. *Am. Mineral.* **2007**, *92*, 695-698.

(18) Xu, J.; Terskikh, V. V.; Huang, Y. *J. Phys. Chem. Lett.* **2013**, *4*, 7-11.

(19) Harris, R. K.; Becker, E. D.; Cabral De Menezes, S. M.; Goodfellow, R.; Granger, P. *Pure Appl. Chem.* **2001**, *73*, 1795-1818.

(20) Pyykkö, P. *Mol. Phys.* **2008**, *106*, 1965-1974.

(21) Sutrisno, A.; Terskikh, V. V.; Shi, Q.; Song, Z.; Dong, J.; Ding, S. Y.; Wang, W.; Provost, B. R.; Daff, T. D.; Woo, T. K.; Huang, Y. *Chem. Eur. J.* **2012**, *18*, 12251-12259.

(22) Frydman, L.; Harwood, J. S. *J. Am. Chem. Soc.* **1995**, *117*, 5367-5368.

(23) Charpentier, T. *Solid State Nucl. Magn. Reson.* **2011**, *40*, 1-20.

(24) Bonhomme, C.; Gervais, C.; Babonneau, F.; Coelho, C.; Pourpoint, F.; Azais, T.; Ashbrook, S. E; Griffin, J. M.; Yates, J. R.; Mauri, F.; Pickard, C. J. *Chem. Rev.* **2012**, *112*, 5733-5779.

(25) Rood, J. A.; Noll, B. C.; Henderson, K. W. *Inorg. Chem.* **2006**, *45*, 5521-5528.

(26) Leung, E.; Mueller, U.; Cox, G.; Hoeffken, H. W. *WO 2009115513 A1*, BASF SE, Germany, WO, **2009**, p. 21.

(27) Leung, E.; Mueller, U.; Cox, G. *WO 2010106121 A1*, BASF SE, Germany, WO, **2010**, p. 12.

(28)   Fischer, M.; Hoffmann, F.; Froeba, M. *ChemPhysChem* **2010**, *11*, 2220-2229.

(29)   Fischer, M.; Hoffmann, F.; Froeba, M. *RSC Advances* **2012**, *2*, 4382-4396.

(30)   Samsonenko, D. G.; Kim, H.; Sun, Y.; Kim, G.-H.; Lee, H.-S.; Kim, K. *Chem. Asian J.* **2007**, *2*, 484-488.

(31)   Kunwar, A. C.; Turner, G. L.; Oldfield, E. *J. Magn. Reson.* **1986**, *69*, 124-127.

(32)   Amoureux, J. P.; Fernandez, C.; Steuernageel, S. *J. Magn. Reson., Ser. A* **1996**, *123*, 116-118.

(33)   Gan, Z.; Kwak, H.-T. *J. Magn. Reson.* **2004**, *168*, 346-351.

(34)   Amoureux, J. P.; Delevoye, L.; Steuernagel, S.; Gan, Z.; Ganapathy, S.; Montagne, L. *J. Magn. Reson.* **2005**, *172*, 268-278.

(35)   Kemp, T. F.; Smith, M. E. *Solid State Nucl. Magn. Reson.* **2009**, *35*, 243-252.

(36)   Sideris, P. J.; Nielsen, U. G.; Gan, Z.; Grey, C. P. *Science.* **2008**, *321*, 113-117.

(37)   Gan, Z.; Gorkov, P. L.; Brey, W. W.; Sideris, P. J.; Grey, C. P. *J. Magn. Reson.* **2009**, *200*, 2-5.

(38)   Sideris, P. J.; Blanc, F.; Gan, Z.; Grey, C. P. *Chem. Mater.* **2012**, *24*, 2449-246.

(39)   Kubota, Y.; Takata, M.; Kobayashi, T. C.; Kitagawa, S. *Coord. Chem. Rev.* **2007**, *251*, 2510-2521.

(40)   Férey, G.; Serre, C. *Chem. Soc. Rev.* **2009**, *38*, 1380-1399.

(41)   Kolokolov, D. I.; Jobic, H.; Stepanov, A. G.; Guillerm, V.; Devic, T.; Serre, C.; Férey, G. *Angew. Chem., Int. Ed.* **2010**, *49*, 4791-4794.

(42)   Kolokolov, D. I.; Stepanov, A. G.; Guillerm, V.; Serre, C.; Frick, B.; Jobic, H. *J. Phys. Chem. C* **2012**, *116*, 12131-12136.

(43)   Shustova, N. B.; Ong, T.-C.; Cozzolino, A. F.; Michaelis, V. K.; Griffin, R. G.; Dinca, M. *J. Am. Chem. Soc.* **2012**, *134*, 15061-15070.

(44)   Kim, H.; Samsonenko, D. G.; Yoon, M.; Yoon, J. W.; Hwang, Y. K.; Chang, J. S.; Kim, K. *Chem. Commun.* **2008**, 4697-4699.

3.6   Appendix

Section A1: Powder XRD and TGA Results
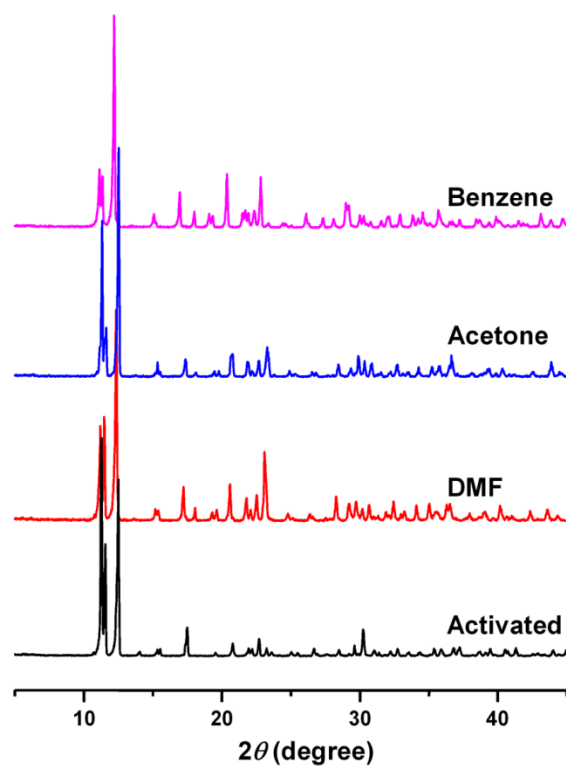
Figure 3-A1: Powder XRD patterns of four microporous α-Mg$_3$(HCOO)$_6$ samples.
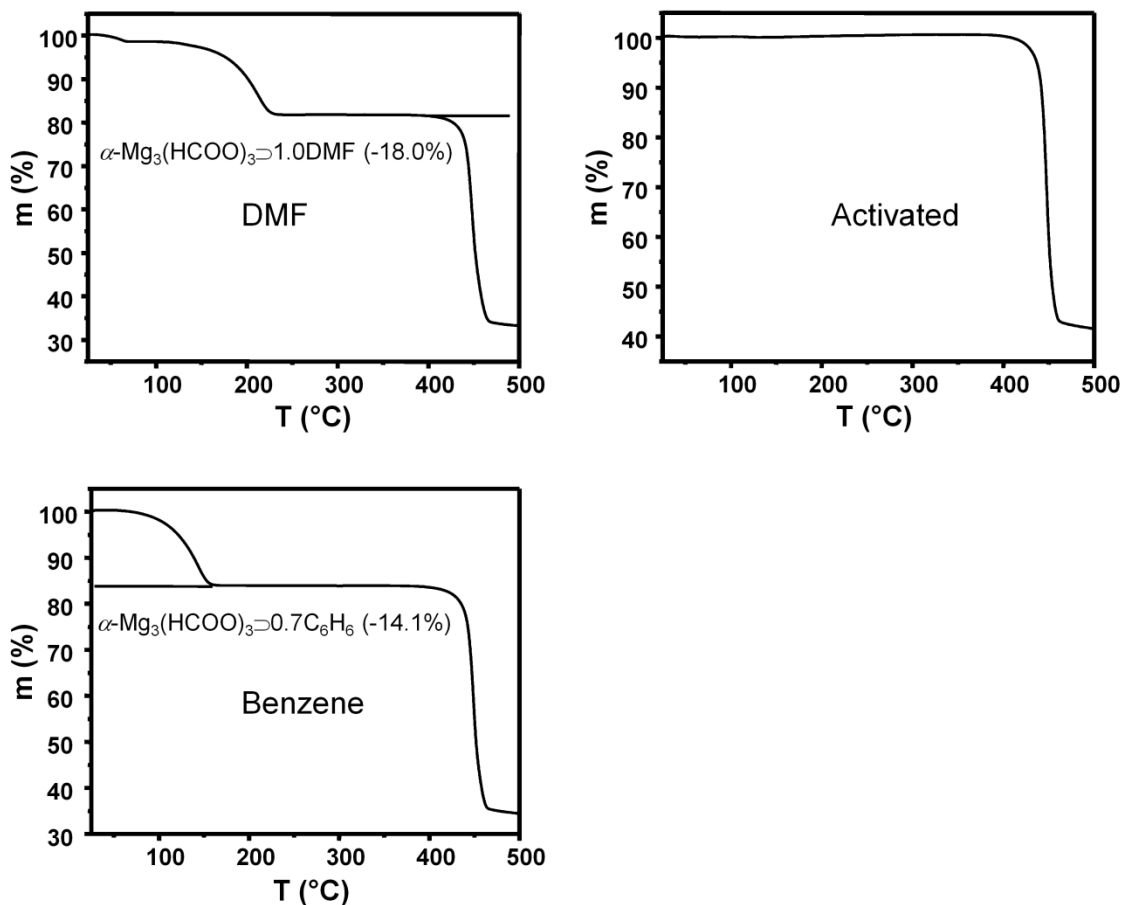
Figure 3-A2: TGA traces of microporous α-Mg$_3$(HCOO)$_6$ samples.

Section A2: SSNMR Characterizations

^{1}H→^{13}C cross-polarization (CP) MAS SSNMR spectra were also collected on a Varian Infinity Plus 400 WB spectrometer at 100.5 MHz at a magnetic field of 9.4 T using a 4 mm triple-tuned T3 MAS probe with a spinning speed of 10 kHz. The Hartmann-Hahn matching conditions were calibrated on solid admantane, which is also a secondary reference for ^{13}C chemical shift (δ_{iso} = 37.8 ppm for the methylene signal). ^{1}H 90° pulse width was 4.3 μs, and the pulse delay of ^{1}H was 10 s. The contact time was 5 ms. High power two-pulse phase-modulated (TPPM) decoupling was used to achieve the high resolution of ^{13}C spectra. Five ^{13}C peaks were observed in the region between 167 ppm and 174 ppm (which are assigned to six framework carbons) for all four samples. The solvent signals were labeled.
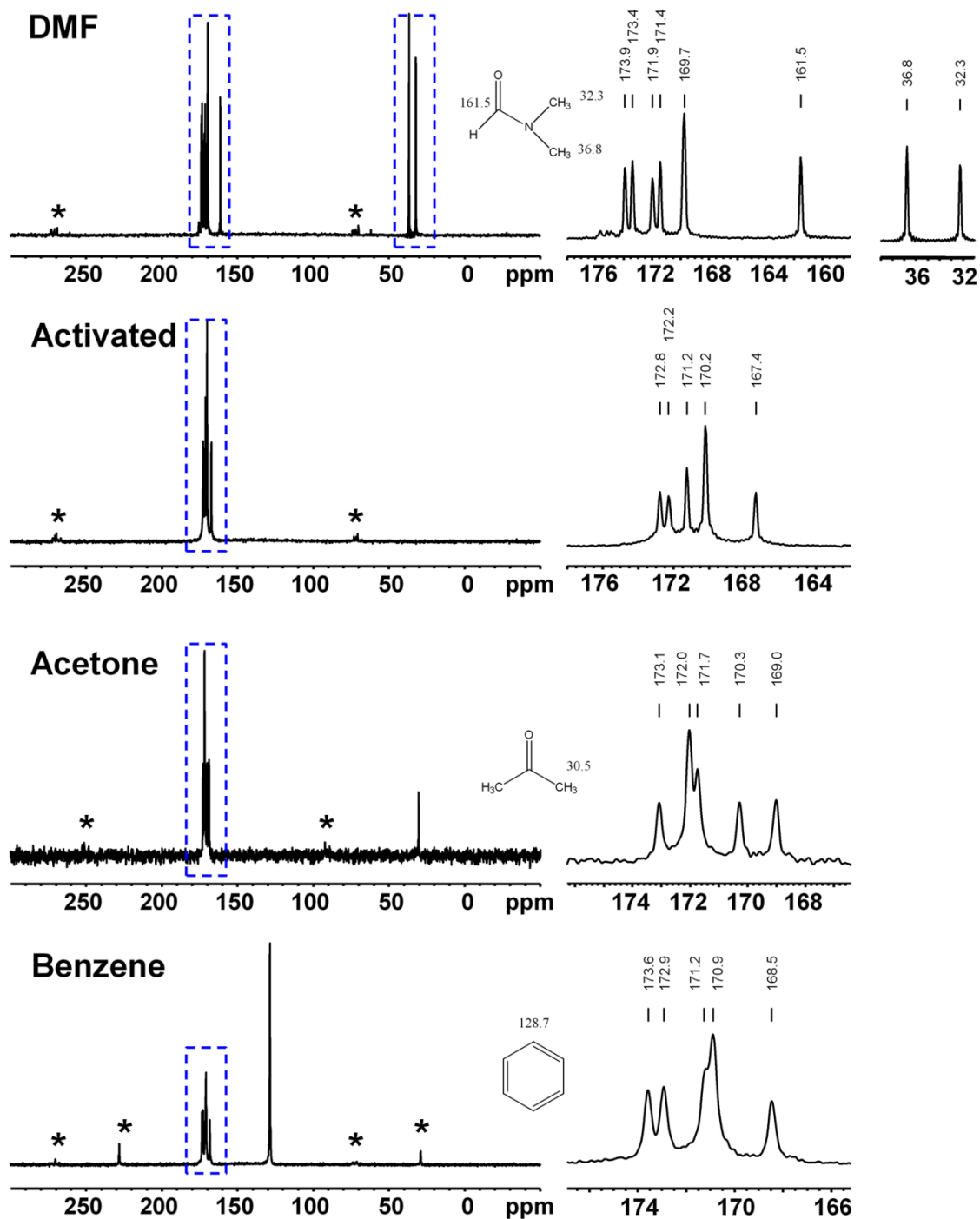
Figure 3-A3: $^1H \rightarrow ^{13}C$ CPMAS spectra of four microporous α-Mg$_3$(HCOO)$_6$ samples. *: spinning sidebands.

The principle of SPAM-3QMAS is briefly described in Figure 3-A4. In standard Z-filter 3QMAS experiment, only one coherence transfer pathway is used; whereas in

SPAM-3QMAS experiment, the other two pathways are also implemented, giving rise to twice as much signal or even better compared to that of Z-filter 3QMAS. In this paper, a significant improvement of the resolution of 3QMAS spectrum has been observed using the activated sample as an example (Figure 3-A5).
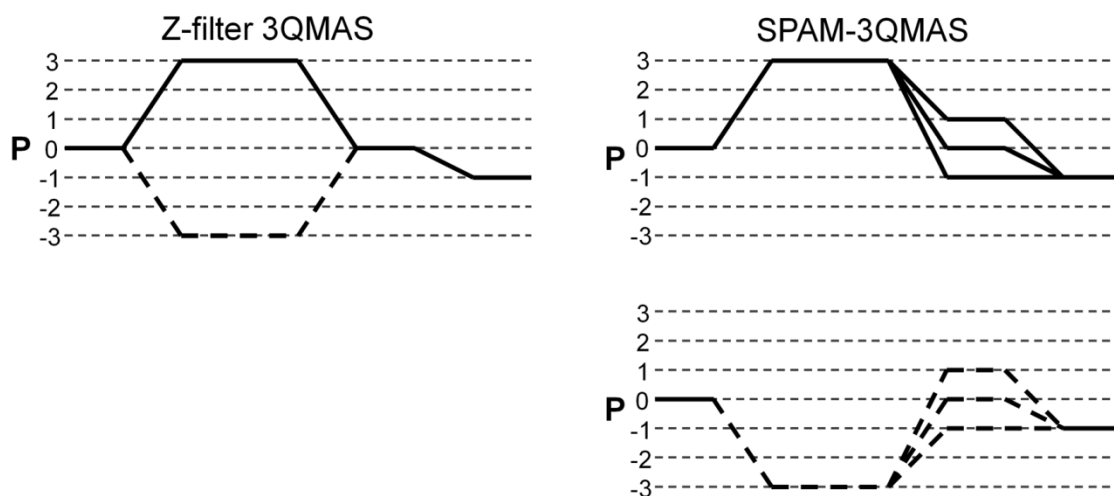
Figure 3-A4: Coherence transfer pathways of the Z-filter (left) and SPAM 3QMAS (right) experiments. Solid line: the echo pathway. Dashed line: the anti-echo pathway.
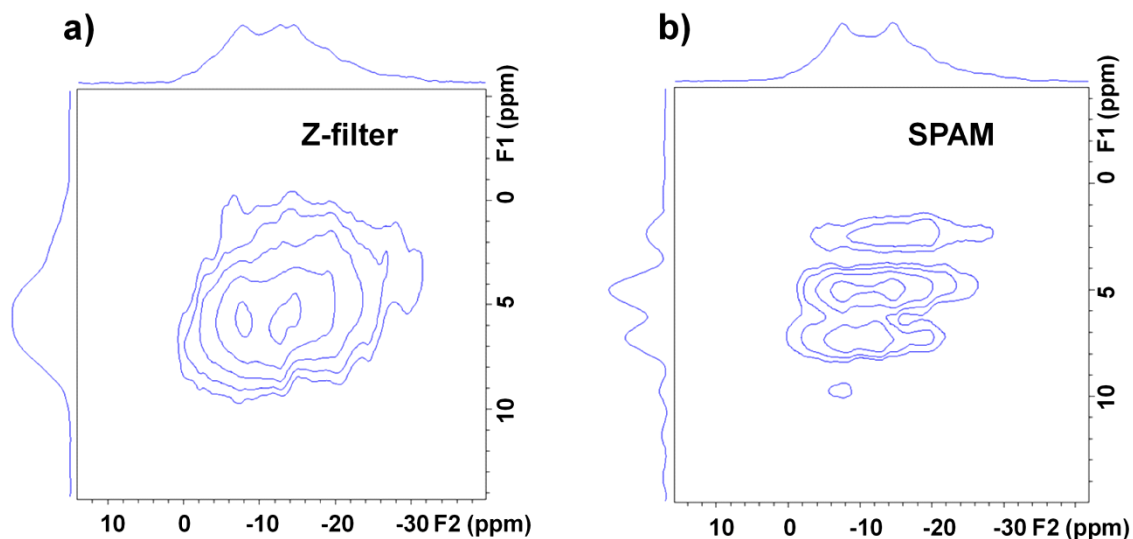
Figure 3-A5: Z-filter (left) and SPAM (right) 3QMAS spectra of the activated sample.

Table 3-A1: The number of scans for ^{25}Mg SSNMR experiments (pulse delay: 1 s).

Sample	Number of scans		
	Static	MAS	SPAM-3QMAS
DMF	16384	2048	4320×48
activated	16384	2048	2400×64
acetone	16384	2048	2400×64
benzene	16384	2048	3600×48
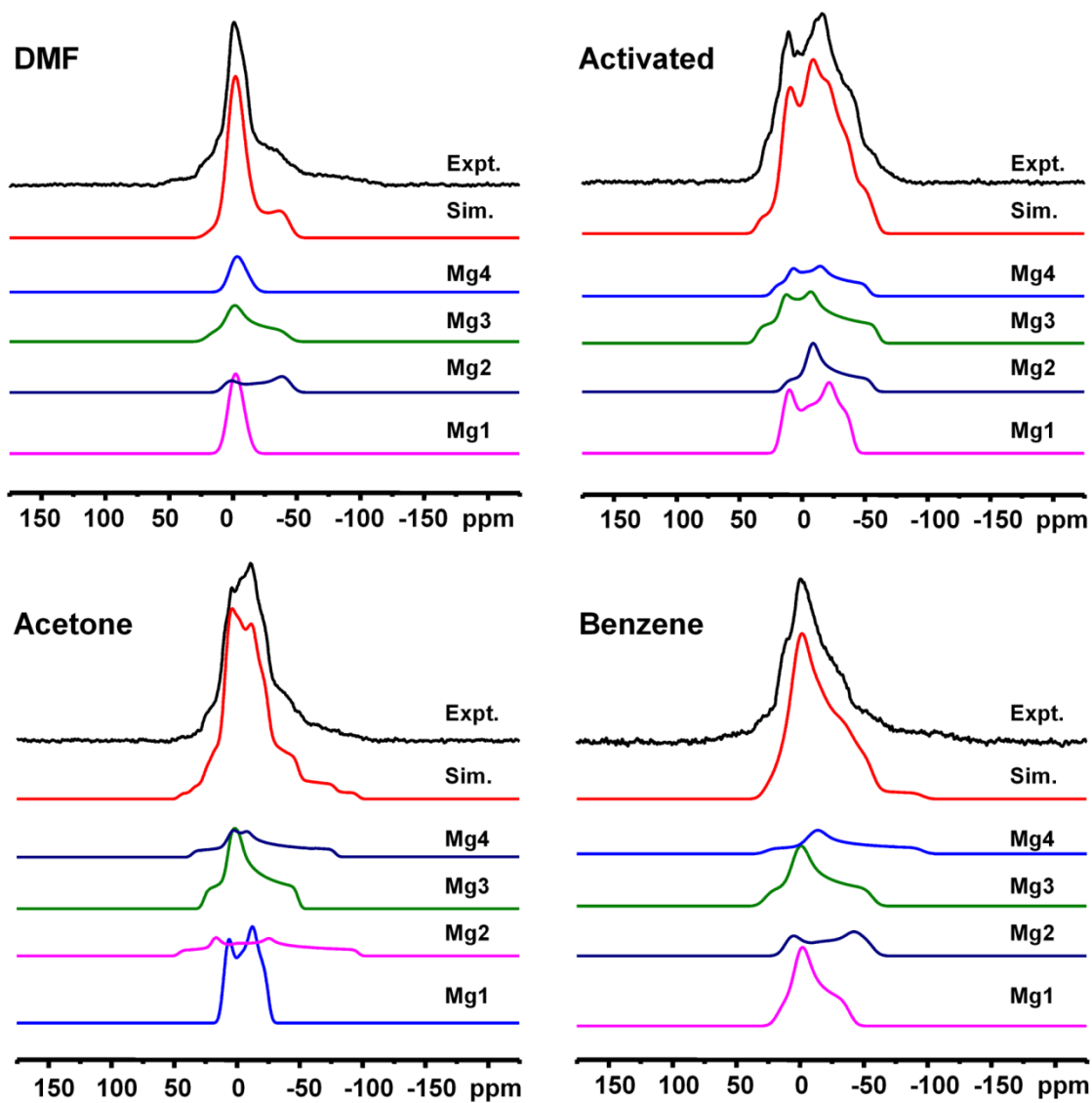
Figure 3-A6: Simulated ^{25}Mg static NMR spectra of four microporous α-Mg$_3$(HCOO)$_6$ samples.

To understand the flexibility of the framework, the static ^{2}H NMR spectrum of the framework-deuterated microporous α-Mg$_3$(DCOO)$_6$ was measured on a Varian Infinity Plus 400 WB spectrometer at 61.3 MHz at a magnetic field of 9.4 T using a horizontal 5 mm static probe and quadrupole echo sequence. The 90° pulse of ^{2}H was 3.6 μs and the interpulse delay τ was set to be 30 μs. The pulse delay was 2 s. The number of scans was 8160. As Figure 3-A7 illustrates, a typical Pake doublet was observed. The horn separation of 116 kHz corresponds to a C_Q(^{2}H) of 155 kHz, indicating a C–^{2}H bond with the negligible motion at room temperature.
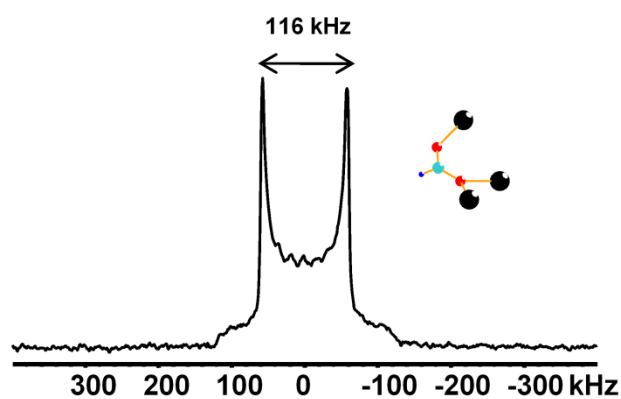
Figure 3-A7: ^{2}H static SSNMR spectrum of the activated microporous α-Mg$_3$(DCOO)$_6$.

Chapter 4

4 Determining the Numbers of Non-Equivalent H and C Sites in Metal–Organic Framework α-Mg$_3$(HCOO)$_6$ by Ultrahigh-Resolution Multinuclear Solid-State NMR at 21.1 T

4.1 Introduction

Metal–organic frameworks (MOFs) are a large group of inorganic-organic hybrid porous materials with three-dimensional frameworks, obtained by the interconnection of metal ions by various organic linkers. Because of their promising properties including rich structural diversity, high thermal stability, and selective adsorption, MOFs have attracted tremendous attention in a broad range of applications, in particular as gas separation and storage materials.[1] Understanding the relationships between the properties of MOFs and their structures is of fundamental importance for the applications. For instance, the selectivity of MOFs has its origin from both the long- and short- range ordering of the structure. On one hand, the micropores of MOFs, whose size, shape and connectivity are determined by the long-range ordering, block the large molecules and allow the small molecules to pass (the so-called "molecular sieving effect"). On the other hand, possible guest-framework interactions such as hydrogen bonding and Van der Waals forces, which are at the molecular-level, can significantly enhance the selectivity. However, the structures of many MOFs are determined from the more limited powder XRD data due to the lack of suitable single crystals for X-ray diffraction. Moreover, even if high-quality crystals are available, the single-crystal XRD data are typically collected at a temperature much lower than what is used for the applications. In such cases, an unambiguous structure solution of MOFs requires additional information from other techniques such as solid-state NMR (SSNMR) spectroscopy.[2,3]

SSNMR spectroscopy is complementary to XRD because it can provide the molecular-level information around the NMR-active nucleus of interest. One good example is the weak C–H···O hydrogen bond.[4] Due to the difficulty of locating protons by XRD, it is not straightforward to distinguish whether an apparent close C–H···O

proximity is virtually a bonding interaction. This question can be solved by SSNMR experiments because ^{1}H chemical shift is very sensitive to hydrogen bonding.[5] The typically strong ^{1}H–^{1}H homonuclear dipolar coupling, as the consequence of the large gyromagnetic ratio (γ) of ^{1}H, provides great opportunities for the measurement of ^{1}H–^{1}H internuclear distances since the discovery of NMR phenomenon.[6,7] Valuable long-range structural information such as the crystal symmetry[8,9] is also available from the SSNMR data, since the number of NMR peaks of each nucleus should equal to the number of crystallographically non-equivalent sites. In recent years, the advance of ultrahigh-resolution SSNMR techniques has allowed the direct comparison of the NMR spectra with the X-ray determined structure for MOFs.[10,11]

SSNMR spectroscopy has been extensively used for the characterization of MOFs.[2,3] ^{1}H and ^{13}C SSNMR experiments have become a routine technique to study organic linkers.[12-19] ^{2}H NMR experiment is employed to examine the flexibility of the framework and the dynamics of the guest species inside of micropores.[20-23] The local environments around several metal centers are also probed by SSNMR experiments, such as ^{27}Al,[24-26] ^{45}Sc,[27] ^{71}Ga,[28] ^{25}Mg[11,29] and ^{67}Zn[10]. Despite its importance, direct determination of the number of non-equivalent sites by SSNMR experiments, in particular H, is rare due to the poor ^{1}H spectral resolution in solids, which is severely limited by the narrow ^{1}H chemical shift range and the strong ^{1}H–^{1}H homonuclear dipolar coupling.[30] Several approaches were used in the literature to mitigate this problem including ultrafast magic-angle spinning (MAS)[30,31] and "isotopic (^{2}H) dilution".[32-35] Moreover, performing ^{1}H SSNMR experiments at high magnetic fields provides an additional benefit in spectral resolution since chemical shifts (in Hz) scale linearly with the magnetic field strength, while ^{1}H–^{1}H dipolar coupling remains constant. However, the systematic examination of the feasibility of these strategies in MOFs, which usually consist of three-dimensional networks of dipolar coupling, is absent to date.

Herein, ultrahigh-resolution ^{1}H SSNMR spectra of an important commercialized MOF, microporous α-Mg$_3$(HCOO)$_6$ (trade name: Basosive M050),[36-38] were acquired using the above-mentioned resolution enhancement strategies. One reason for choosing this MOF is that good single crystal structures at 110 K are available,[36] including

activated and several guest-loaded phases, against which the validity of the NMR approach can be checked. In addition, microporous α-$Mg_3(HCOO)_6$ is one of the most challenging MOFs for ^{1}H SSNMR experiments since it has six non-equivalent H sites with identical chemical environment. Finally, six H sites are bound to six different C sites, opening up the possibilities of using the known assignment of [1]H (or ^{13}C) peaks to identify unknown [13]C (or ^{1}H) peaks.

In this work, five microporous α-$Mg_3(HCOO)_6$ samples were studied: activated (desolvated) phase and four guest-loaded phases (DMF, benzene, acetone and pyridine, hereafter referred to as activated, DMF, benzene, acetone and pyridine samples, respectively). The frameworks of these samples were partially deuterated to weaken the dipolar coupling network; while guest molecules were fully deuterated, eliminating the guest signals. The single-crystal XRD data of these samples are reported in the literature except the pyridine sample. The results indicate that multiple (six) H sites could be differentiated by one-dimensional ^{1}H ultrafast MAS (62.5 kHz) experiments for all samples. Multiple (six) C sites were also resolved in 1D [1]H$\rightarrow$[13]C cross-polarization (CP) MAS experiments. Their assignments were made according to [1]H–[1]H double-quantum (DQ) experiments using the back-to-back (BABA) sequence,[39] and frequency switched Lee-Goldberg (FSLG) [1]H–[13]C hetero-nuclear correlation (HETCOR) experiments,[40] combined with first-principle theoretical calculations (CASTEP) using the density-functional theory (DFT) gauge including projector augmented wave (GIPAW) method.[41,42] In addition, the ^{13}C chemical shift anisotropy (CSA) of activated, DMF and benzene samples were obtained by [1]H–[13]C phase-corrected magic-angle turning (PHORMAT) experiments.[43] ^{2}H and [25]Mg SSNMR experiments also provided valuable structural information on selected samples.

4.2 Experimental Section

4.2.1 Sample Preparation

As-made fully protonated sample (α-$Mg_3(HCOO)_6$) was prepared following the method described by Rood and co-workers.[36] As-made deuterium-diluted sample (α-$Mg_3(H/DCOO)_6$, H atom% ~ 20%, measured by the mass spectrometry analysis) was

synthesized using the mixture of HCOOH/DCOOH (CDN Isotopes, 99% D atom%, 95% w/w in H_2O) with a molar ratio of 1 : 5 as the starting material. The activated phase was obtained by activating the as-made phase under dynamic vacuum at 150 °C for 1 d. To prepare the four guest-loaded phases (DMF, benzene, acetone and pyridine), ~ 0.5 g of the crystalline activated phase was soaked in 1 mL of dry deuterated solvents (Cambridge Isotopes, 99.5% D atom%) and kept for 1 d. The excess solvent was allowed to evaporate under a N_2 atmosphere. All samples were stored in sealed vials. The identity of the samples was examined by powder X-ray diffraction. The PXRD patterns (Figure 4-A1, Appendix) were recorded on a Rigaku diffractometer equipped with a graphite mono-chromator using Co Kα radiation (λ = 1.7902 Å). Diffraction data were collected from 5° to 45° in 2θ at a step size of 0.02°. The unit cell parameters (Table 4-A1) were refined from powder XRD patterns using the CRYSFIRE powder indexing system. The guest content was measured by thermogravimetric analysis (TGA) (Figure 4-A2). The samples were heated under a N_2 atmosphere on a Mettler Toledo TGA/DTA851e instrument from 25 to 500 °C at a heating rate of 10 °C/min.

4.2.2   NMR Characterizations and Theoretical Calculations

^{1}H, ^{13}C and ^{25}Mg SSNMR experiments were performed at 21.1 T (where the Larmor frequency of ^{1}H is 899.9 MHz) on a Bruker Avance II spectrometer at the National Ultrahigh-field NMR Facility for Solids in Ottawa, Canada.

4.2.2.1 ^{1}H Measurements

One-pulse ^{1}H MAS spectra were acquired using a 1.3 mm H/X MAS Bruker probe with a spinning speed of 62.5 kHz, and a 4 mm HCN MAS Bruker probe with a spinning speed of 18 kHz, respectively. A ^{1}H pulse length of 1.0 μs, corresponding to the 45° pulse, was used for the MAS experiments performed on the 1.3 mm probe. A 90° pulse (2.5 μs) of ^{1}H was used for the MAS experiments done on the 4 mm probe. The static ^{1}H NMR spectra were also collected using the 90°-τ-90° echo[44] for comparison purposes. The interpulse delay τ was 60 μs. Rotor-synchronized 2D ^{1}H–^{1}H back-to-back (BABA) double-quantum (DQ) experiments[45] were performed using the 4 mm probe at 18 kHz MAS. 128 points were collected in the indirect DQ dimension with 16 scans.

During excitation and reconversion, the BABA scheme was used to recouple the ^{1}H–^{1}H dipolar coupling. Excitation over one rotor cycle (55.6 μs), two rotor cycles (111.1 μs) and four rotor cycles (166.7 μs) were used. All ^{1}H pulse lengths were measured on adamantane and the chemical shift of ^{1}H was also referenced to adamantane at 1.74 ppm.

4.2.2.2 ^{13}C Measurements

^{1}H→^{13}C cross-polarization (CP) MAS experiments were acquired using a 4 mm HCN Bruker probe, with a spinning speed of 18 kHz and a contact time of 2 ms. In this case, the ^{13}C signals of deuterated guest molecules were eliminated because of the absence of nearby protons. All ^{1}H→^{13}C CPMAS measurements were done with high-power ^{1}H decoupling using the two-pulse-phase-modulation (TPPM) scheme.[46] The phase increment of TPPM decoupling was 15° and the TPPM pulse length was 4.58 μs. 2D ^{1}H–^{13}C frequency switched Lee-Goldberg heteronuclear correlation (FSLG-HETCOR) experiments[40] were performed at 18 kHz MAS with a very short contact time of 35 μs to avoid unwanted long-range correlations. 64 points with 6 Lee-Goldberg cycles as the increment of indirect (^{1}H) dimension and 256 scans for each point were collected. 2D ^{1}H–^{13}C phase-corrected magic-angle turning (PHORMAT) experiments[43] were carried out on 100% H activated, DMF and benzenes samples at 2 kHz MAS with a contact time of 2 ms. The echo delay time was 20 μs. The 2D data were collected with 96 values with the evolution variable incremented by 33.3 μs under the echo/anti-echo mode. Fourteen rotor cycles were used to prevent negative delays. All ^{13}C pulse lengths were measured on glycine and the chemical shift of ^{13}C was also referenced to the –COOH group of glycine at 176.5 ppm. Deconvolution of ^{1}H and ^{13}C spectra were done under the line fitting mode of the NUTS 2005 software with Gaussian line shapes. The full-width at half-heights (hereafter referred to as line width) of ^{1}H and ^{13}C peaks were determined by deconvolution. The Herzfeld-Berger spinning sidebands analyses[47] of the extracted slices of 2D ^{1}H–^{13}C PHORMAT spectra were performed using the Bruker Topspin software.

4.2.2.3 ^{25}Mg Measurements

Static ^{25}Mg NMR experiments were acquired with the 90°-τ-90° echo sequence[44] with continuous-wave proton decoupling on a home-built 7 mm H/X low-γ probe for

stationary samples with a dual resonator design. One-pulse ^{25}Mg MAS experiments employed a Bruker 7 mm H/X MAS probe with a spinning speed of 5 kHz. The selective 90° pulse of ^{25}Mg for solids was 3 μs, corresponding to a solution 90° pulse of 9 μs (on 1 M MgCl$_2$ aqueous solution). The interpulse delay τ in static experiments was 200 μs. The ^{1}H decoupling RF power was about 30 kHz. Rotor-synchronized 2D soft-pulse-added-mixing (SPAM) triple-quantum MAS (3QMAS) experiments[48-50] were performed with a spinning speed of 5 kHz. The durations of excitation, conversion and soft pulses were 10.0, 4.2 and 10.0 μs. SPAM-3QMAS data were collected under the echo/anti-echo mode. 3200 scans were acquired for each point of indirect dimension, with 24 increments accumulated. FID signals were Fourier-transformed and sheared to obtain the separate F1 and F2 dimensions using the Bruker Topspin software. All ^{25}Mg SSNMR spectra were simulated using the QuadFit software.[51] The chemical shift of ^{25}Mg was referenced to 1 M MgCl$_2$ aqueous solution at 0 ppm.

4.2.2.4 ^{2}H Measurements

To understand the dynamics of benzene and pyridine, static ^{2}H NMR spectra of α-Mg$_3$(HCOO)$_6$⊃C$_6$D$_6$ and α-Mg$_3$(HCOO)$_6$⊃pyridine-d$_5$ were measured on a Varian Infinity Plus 400 WB spectrometer at 61.3 MHz at a magnetic field of 9.4 T using a horizontal 5 mm static probe and quadrupole echo sequence.[52] The 90° pulse of ^{2}H was 3.6 μs and the interpulse delay τ was set to be 30 μs.

The other details of SSNMR experiments, including the numbers of scans and pulse delays, were shown in Table 4-A2 (Appendix).

4.2.2.5   First-Principle Calculations

Gauge-including projector augmented wave (GIPAW) quantum chemical calculations were conducted using the CASTEP code (version 4.4, Accelrys Materials Studio) running on a HP xw4400 workstation with a single Intel dual-core 2.67 GHz processor and 8 GB DDR RAM. The NMR module was used to calculate the NMR parameters. Unit cell parameters and atomic coordinates of activated, DMF, benzene and acetone samples were taken from their crystal structures,[36] whereas the model structure of

pyridine phase for CASTEP calculation has to be proposed. All theoretical calculations were performed using ultra-soft pseudopotentials generated from the "on-the-fly" method implemented within the CASTEP. The generalized gradient approximation (GGA) with Perdew, Burke and Ernzerhof (PBE) functional was used. Because the unit cells are large (> 1000 Å^3), plane-wave cut-off energy of 500 eV (medium accuracy) was applied. The proton positions were first normalized by the Mercury software and then optimized by CASTEP prior to the calculation of NMR parameters. The isotropic chemical shielding of ^{1}H, ^{13}C and ^{25}Mg as well as the EFG parameters of ^{25}Mg were produced automatically by the CASTEP program. The isotropic chemical shifts for ^{1}H and ^{13}C were computed using the relationships in the literature: $\delta_{iso}(^1H) = 31.18 - \sigma_{iso}(^1H, CASTEP)$ (in ppm) and $\delta_{iso}(^{13}C) = 170.1 - \sigma_{iso}(^{13}C, CASTEP)$ (in ppm).[53] The $C_Q(^{25}Mg)$ values were corrected using the equation $C_Q(^{25}Mg, corrected) = [C_Q(^{25}Mg, CASTEP) + 0.13] / 1.225$ (in MHz) to account for overestimation.[54] The isotropic chemical shift for ^{25}Mg was obtained using the correlation $\delta_{iso}(^{25}Mg, corrected) = [565.23 - \sigma_{iso}(^{25}Mg, CASTEP)] / 1.049$ (in ppm).[54]

4.3   Results and Discussion
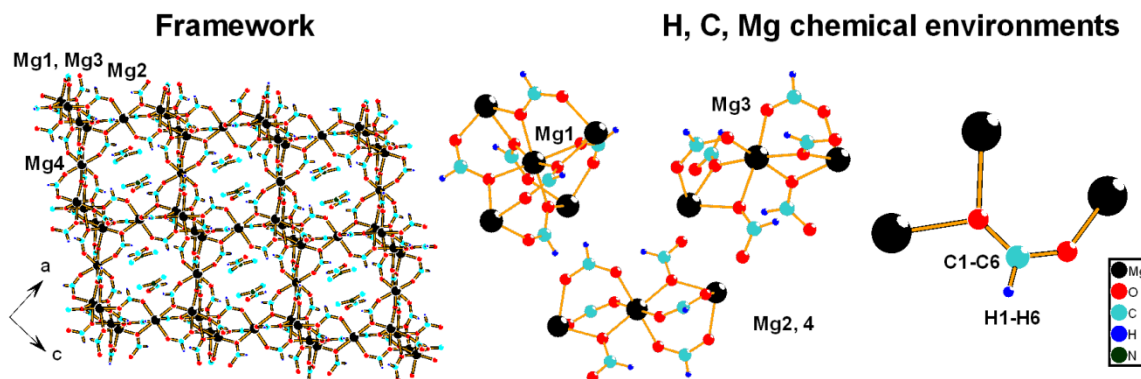
Figure 4-1: Left: The framework of the DMF phase. Right: Chemical environments of H, C and Mg. Hydrogen atoms of the encapsulated DMF are omitted for clarity.

Single-crystal XRD data of activated, DMF, benzene and acetone phases indicate that four samples belong to the same space group ($P2_1/n$).[36] The frameworks of four samples are identical in terms of their topology, containing four crystallographically non-equivalent Mg sites, six non-equivalent H sites, six non-equivalent C sites and twelve non-equivalent O sites. The multiplicity of six H (or C) sites is equal. As shown in Figure

4-1, the framework is constructed by linking one-dimensional chains of edge-shared MgO_6 octahedra of Mg1 and Mg3 with corner-shared octahedra of Mg2 and Mg4 via Mg1, forming narrow 1D zig-zag channels along the *b* direction. The chemical environments of six H (or C) sites are identical: all formate anions adopt the same bonding mode that one oxygen bridges to two Mg centers (μ^2-oxygen) and the other one connects to one Mg (μ^1-oxygen). Each Mg is bound to six different formate anions. Therefore, there are three types of coordination environments for four Mg sites: Mg1 bonds to six μ^2-oxygens; both Mg2 and Mg4 bond to four μ^1-oxygens and two μ^2-oxygens, whereas Mg3 is bound to two μ^1-oxygens and four μ^2-oxygens.

4.3.1   Activated Phase
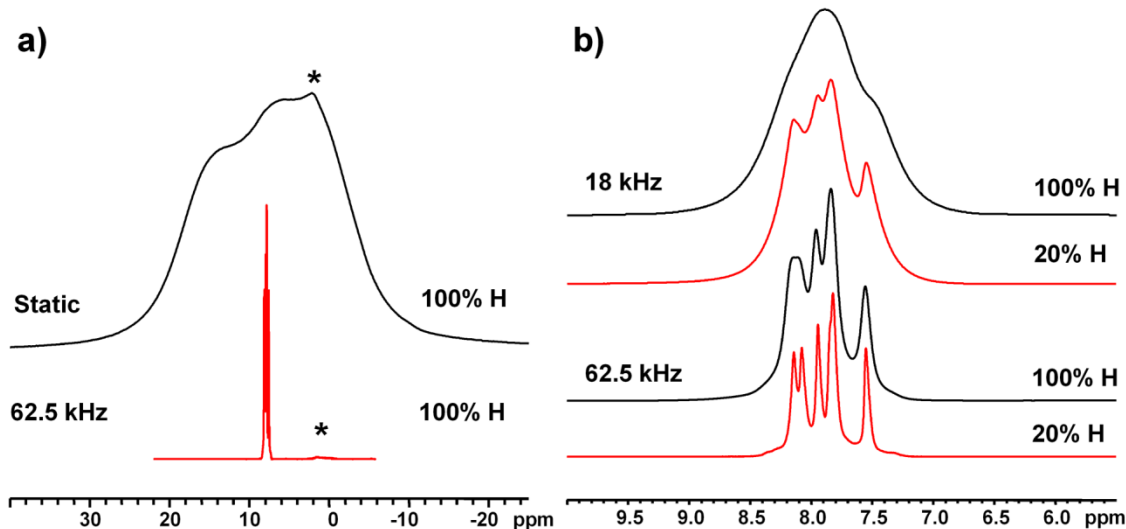
Figure 4-2: Illustration of the enhancement of ^{1}H spectral resolution for the activated sample by: (a) MAS and (b) MAS combined with the isotopic dilution. *: residual DMF signal.

As discussed earlier, the spectral resolution of ^{1}H SSNMR experiments is severely limited by the line broadening induced by the strong ^{1}H–^{1}H dipolar coupling. For ^{1}H, the static spectrum of the fully protonated (100% H) activated phase at 21.1 T was first acquired (Figure 4-2a), which consists of a broad and featureless profile with the line width of ~ 20 kHz. The shortest distances between two framework protons, measured from the reported crystal structure,[36] are typically around 3 Å in the activated sample,

implying efficient dipolar coupling between neighboring protons. Moreover, every proton has several nearby protons, forming a dense, three-dimensional network of dipolar coupling. The first resolution enhancement strategy is ultrafast MAS, since the line broadening due to ^{1}H–^{1}H dipolar coupling can be markedly averaged by MAS and the residual ^{1}H line width is approximately inversely proportional to the spinning speed.[31,55] Two spinning speeds were selected in this work to examine the effect of MAS speed (Figure 4-2b): 18 and 62.5 kHz, which are among the highest spinning speeds of the 4 mm and 1.3 mm probe, respectively. Spinning the sample at 18 kHz yielded a spectrum that still consists of a single profile, but has a much smaller line width (~ 700 Hz) than the static spectrum. However, much improved spectral resolution was observed in the 62.5 kHz MAS ^{1}H spectrum, which clearly exhibits four resolved peaks, implying the important role of ultrafast MAS in ultrahigh-resolution ^{1}H SSNMR experiments. The second strategy, isotopic dilution, was then combined with ultrafast MAS to further enhance the ^{1}H spectral resolution. The dipolar coupling network of ^{1}H is weakened by the substitution of ^{1}H by ^{2}H, owing to the much smaller (~ 15%) gyromagnetic ratio of ^{2}H. After substituting ~80% of framework ^{1}H by ^{2}H (such sample is hereafter referred to as the 20% H sample), five sharp ^{1}H peaks were resolved at 62.5 kHz in a narrow chemical shift range of ~ 0.5 ppm. Four peaks have similar intensities while the most intense peak (at ~ 7.8 ppm) has a shoulder and can be viewed as a superimposition of two resonances. Therefore, it seems like all six H sites have been directly differentiated.

The accurate values of ^{1}H chemical shifts were obtained by the deconvolution of the 62.5 kHz MAS ^{1}H spectrum of the 20% H activated sample. As expected, six ^{1}H peaks were yielded with approximately equal intensities after deconvolution (Figure 4-3a), consistent with the crystal structure proposed by the single-crystal XRD data. The results imply that ultrahigh-resolution ^{1}H SSNMR spectrum could be collected using the combination of ultrafast MAS, isotopic dilution and high magnetic field. Furthermore, the ultrahigh-resolution spectrum acquired could be utilized to directly differentiate the six crystallographically non-equivalent but chemically equivalent H sites. It should also be highlighted that the ^{1}H line widths of six H sites are 35–53 Hz (0.04–0.06 ppm) for the 20% H sample and 79–116 Hz (0.09–0.13 ppm) for the 100% H sample, both of which are rather small for ^{1}H NMR in solids.
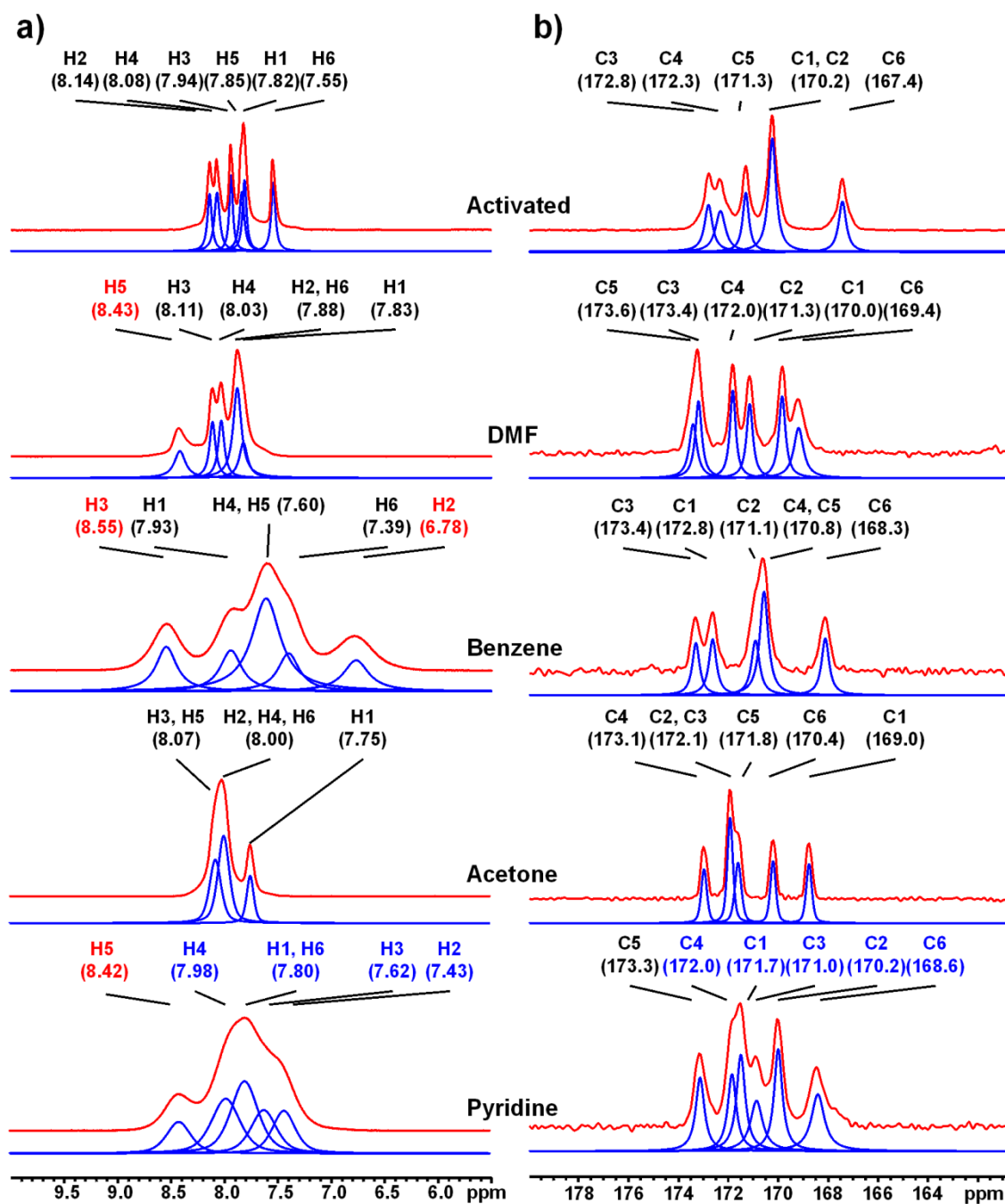
Figure 4-3: Experimental and deconvoluted 62.5 kHz MAS (a) ^{1}H and (b) 18 kHz ^{1}H→^{13}C CPMAS (with a contact time of 2 ms) spectra of the 20% H α-Mg$_3$(HCOO)$_6$ samples. The protons labeled with red color exhibit significant guest-induced shifts while the protons and carbons labeled with blue color were only tentatively assigned.

The next question to be addressed is how to assign the six ^{1}H NMR peaks to the six crystallograhpic H sites. It is well-known that protons in different functional groups have distinct chemical shift ranges characteristic of the structure.[56] However, the six non-equivalent H sites have identical chemical environment. In such case, ^{1}H spectral assignment was sometimes accomplished by using the reported empirical correlations between the ^{1}H chemical shift and local H geometry such as H–C distances.[57] Unfortunately, the hydrogen atoms of the activated sample (as well as the DMF, benzene and acetone samples) were not located by single-crystal XRD data but arbitrarily placed on the reported positions with an equal H–C distance of 0.930 Å for all samples. Therefore, it is not possible to assign the ^{1}H signals based on the H–C distances from the single-crystal XRD data. Furthermore, the H–C distance of 0.930 Å is significantly shorter than the normal H–C distances (~1.10 Å) of formate-containing compounds.[58] In recent years, first-principle calculations of ^{1}H chemical shifts using GIPAW method implemented in the CASTEP code, has been proven to be a reliable method for spectral interpretation and assignment.[41,42] CASTEP calculations were performed on the activated sample. The proton locations were optimized by the CASTEP prior to the calculation of NMR parameters, yielding H–C distances of formate anions between 1.104 and 1.114 Å (Table 4-A3). The calculated ^{1}H isotropic chemical shifts of the activated sample are presented in Table 4-1. Since they are extremely similar, a small error of the H–C distance can result in an evident change of the ^{1}H assignment. As a result, additional structural information is essential to confirm and refine the ^{1}H assignment suggested by the CASTEP results.

A coin has two sides, a head and a tail. Although the strong [1]H–[1]H homonuclear dipolar coupling is the major obstacle of ultrahigh-resolution ^{1}H SSNMR experiments, it does open up great opportunities for the measurement of [1]H–[1]H internuclear distance by several NMR techniques.[7] One of such techniques is 2D [1]H–[1]H double-quantum (DQ) experiment using the back-to-back (BABA) sequence,[39] which can provide valuable structural information in terms of the spatial proximity between two protons. As shown in the literature, it can probe the proton pairs with the dipolar coupling constant as weak as ~ 250 Hz (distance: ~ 8 Å). In 2D [1]H–[1]H BABA DQ experiments, the observed DQ signal is the consequence of homonuclear dipolar coupling between protons: Peaks along

the diagonal (self-correlation peaks) correspond to correlations from two equivalent protons; whereas cross peaks (along the indirect DQ dimension) are correlations from two non-equivalent protons.
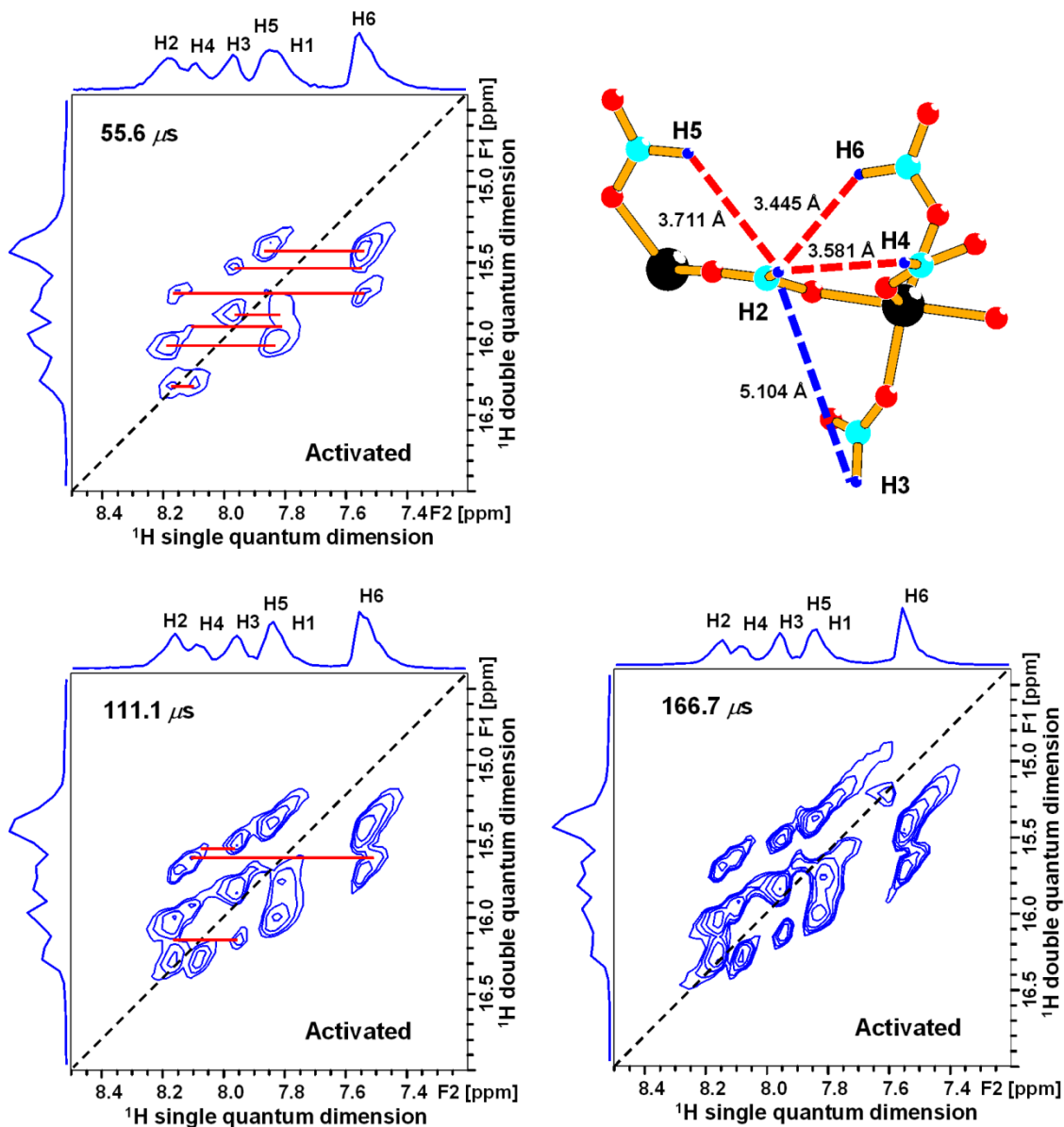
Figure 4-4: 2D ^{1}H–^{1}H BABA DQ spectra of the 20% H activated sample as a function of excitation time (spinning speed: 18 kHz). Diagonals (dash lines) are drawn to illustrate the self-correlation peaks while horizontal lines (labeled in red) indicate the cross peaks. Only new correlations are shown at longer excitation time for clarity. Three spectra have the same contour levels. The neighboring protons around H2 are shown at top right.

The 2D ^{1}H–^{1}H BABA DQ spectra of the 20% H activated sample as a function of excitation time (one, two, and four rotor cycles, corresponding to 55.6, 111.1, and 166.7 μs, respectively) are illustrated in Figure 4-4. Three DQ spectra were set to have the same contour levels to conveniently compare the DQ intensity at different excitation time. Moreover, the excitation time τ_{exc} were also set to be short enough to ensure it is in the interval over which the DQ intensity is monotonically increasing: $\tau_{exc} < 0.75 / D^{IS}$, where D^{IS} is the dipolar coupling constant of the proton pair.[30] For the activated sample, the shortest distance between two neighboring protons is ~ 3 Å,[36] resulting in a dipolar coupling constant of ~ 4.5 kHz. The corresponding τ_{exc} range for monotonically increasing is < 167 μs, implying that the intensity of DQ peaks is always growing in this work. The growth rate of DQ intensity is governed by the strength of dipolar coupling: The stronger the dipolar coupling is, the faster the DQ intensity grows.[30] Therefore, the DQ correlation of two dipolar-coupled protons with a longer ^{1}H–^{1}H internuclear distance is expected to be observed in the 2D DQ spectrum (*i.e.*, the DQ intensity is higher than the cut-off intensity of contours) at a longer excitation time. Herein, self-correlation peaks are first examined because there are only six possible correlations between two equivalent protons while there are fifteen between two non-equivalent protons. At the shortest excitation time (55.6 μs), only the peak at ~ 8.16 ppm along the single quantum (SQ) dimension is on the diagonal, which can be unambiguously assigned to H2 because the H2–H2 distance (2.742 Å, see Table 4-A4, in which ^{1}H–^{1}H distances are calculated from the H-optimized structure) is the shortest. At longer excitation time, the two peaks at ~ 7.95 and ~ 7.84 ppm along the SQ dimension, respectively, overlap with the diagonal. The two self-correlation peaks must be H3 (H3–H3 distance: 4.035 Å) and H5 (H5–H5 distance: 5.869 Å). In order to distinguish H3 from H5, the cross peaks between them and H2 are studied: As Figure 4-4 shows, there are four neighboring non-equivalent protons around H2: H3, H4, H5, and H6. The distance between H2 and H3 (5.104 Å) is markedly longer than those between H2 and the other protons (< 4 Å). Therefore, the peak at ~ 7.95 ppm is H3 because the cross peaks of H2–H3 can only be observed at 111.1 μs or longer. The assignment of H1, H4, and H6 is further performed by matching the ^{1}H–^{1}H distances between the known H sites (H2, H3, and H5) and them with the experimentally observed cross peaks (Table 4-A5). For instance, the peak at ~ 8.07 ppm is assigned to H4 because

the H3–H4 correlation (with a H3–H4 distance of 4.621 Å) can only be observed at longer excitation time. Other details of such analysis are not shown. The final assignment of six H sites is exhibited in Figure 4-3a and Table 4-1. The ^{1}H isotropic chemical shifts are all in the normal range of formate-containing materials (~ 8 ppm).[56]

Table 4-1: Experimental and calculated ^{1}H and ^{13}C isotropic chemical shifts.

Sample	H Site	δ_{iso}(^{1}H) [ppm] Exptl	δ_{iso}(^{1}H) [ppm] Calcd	Area [%]	C Site	δ_{iso}(^{13}C) [ppm] Exptl	δ_{iso}(^{13}C) [ppm] Calcd	Area [%]
activated	H1	7.81	8.37	16.9	C1	170.2	168.9	17.8
	H2	8.14	8.66	14.9	C2	170.2	169.1	17.8
	H3	7.94	8.31	15.6	C3	172.8	171.0	15.6
	H4	8.07	8.77	18.5	C4	172.3	171.9	17.3
	H5	7.84	8.30	17.5	C5	171.3	169.4	15.3
	H6	7.55	8.22	16.7	C6	167.4	164.7	16.3
DMF	H1	7.83	8.41	14.1	C1	170.1	168.6	18.5
	H2	7.88	7.95	18.4	C2	171.3	169.3	16.1
	H3	8.11	8.61	16.4	C3	173.4	172.3	17.1
	H4	8.03	8.65	17.8	C4	172.0	172.1	17.2
	H5	8.43	9.01	14.9	C5	173.6	173.0	14.5
	H6	7.88	8.38	18.4	C6	169.4	168.4	16.7
benzene	H1	7.94	8.04	14.6	C1	172.8	169.8	16.7
	H2	6.78	6.58	13.1	C2	171.1	169.3	17.5
	H3	8.55	9.15	15.1	C3	173.5	173.0	14.9
	H4	7.60	8.18	21.9	C4	170.8	170.2	17.0
	H5	7.60	8.02	21.9	C5	170.8	172.0	17.0
	H6	7.40	7.77	13.4	C6	168.4	167.3	16.9
acetone	H1	7.75	8.17	16.1	C1	169.0	168.8	17.0
	H2	8.00	7.87	16.1	C2	172.1	170.6	14.9
	H3	8.07	8.28	17.8	C3	172.1	172.7	14.9
	H4	8.00	8.44	16.1	C4	173.1	171.4	15.6
	H5	8.07	8.40	17.8	C5	171.8	171.8	20.2
	H6	8.00	8.34	16.1	C6	170.4	169.2	17.4
pyridine[a]	H1	7.80	7.43	15.5	C1	171.7	169.9	19.4
	H2	7.43	6.86	15.4	C2	170.2	170.6	19.3
	H3	7.62	8.72	17.4	C3	171.0	173.5	14.3
	H4	7.98	8.15	24.4	C4	172.0	171.3	15.2
	H5	8.42	7.55	11.9	C5	173.3	171.5	14.7
	H6	7.80	7.46	15.5	C6	168.6	167.3	17.1

a: Only the assignment of H5 is unambiguous. H2 and H3 are distinguished from H1, H4 and H6 by [1]H–[1]H BABA DQ experiments; whereas the protons in each group can only be tentatively assigned based on the assignment of these protons in the DMF sample.
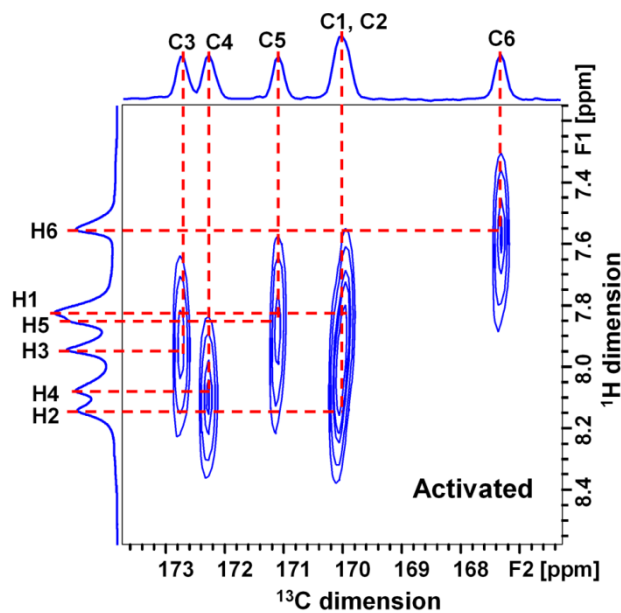
Figure 4-5: 2D ^{1}H–^{13}C FSLG-HETCOR spectrum (contact time: 35 μs) of the 20% H activated sample (spinning speed: 18 kHz). The dashed lines indicate the direct bonding between ^{1}H and ^{13}C. The 62.5 kHz MAS ^{1}H spectrum was used as the projection along the indirect (^{1}H) dimension.

Ultrahigh-resolution ^{1}H→^{13}C CPMAS spectrum of the 20% H activated sample was also acquired. As Figure 4-3b illustrates, five well-resolved ^{13}C peaks (line width ~ 40 Hz, or 0.18 ppm) are observed, four of which have approximately the same intensity while the other one has about twice intensity. Due to very similar H–C distances, ^{1}H→^{13}C CPMAS is quantitative in this case. Direct observation of six C sites with equal population agrees well with the proposed structure based on the single-crystal XRD data. The ^{13}C chemical shifts are typical of formate-containing materials (~170 ppm).[59] The assignment of ^{13}C peaks is then related to that of ^{1}H peaks via 2D ^{1}H–^{13}C frequency switched Lee-Goldberg heteronuclear correlation (FSLG-HETCOR) experiment with a very short contact time of 35 μs, by which only the directly bonded H–C moiety is probed.[40] FSLG, as a ^{1}H–^{1}H homonuclear decoupling sequence,[60] was applied during the ^{1}H evolution period to reduce the residual line broadening. Moreover, the 62.5 kHz MAS ^{1}H spectrum is used as the projection along the indirect (^{1}H) dimension. From the 2D ^{1}H–^{13}C FSLG-HETCOR spectrum (Figure 4-5), the ^{1}H peak of H3 correlates to only one ^{13}C peak at ~ 172.8 ppm. Therefore, this ^{13}C peak is unambiguously assigned to C3. The

same situation occurs for H4, H5, and H6 as well. However, the ^{1}H peaks of H1 and H2 are both related to the same ^{13}C peak at ~ 170.2 ppm, validating that this ^{13}C peak does correspond to two C sites. The final assignment of six ^{13}C peaks is exhibited in Figure 4-3b and Table 4-1.
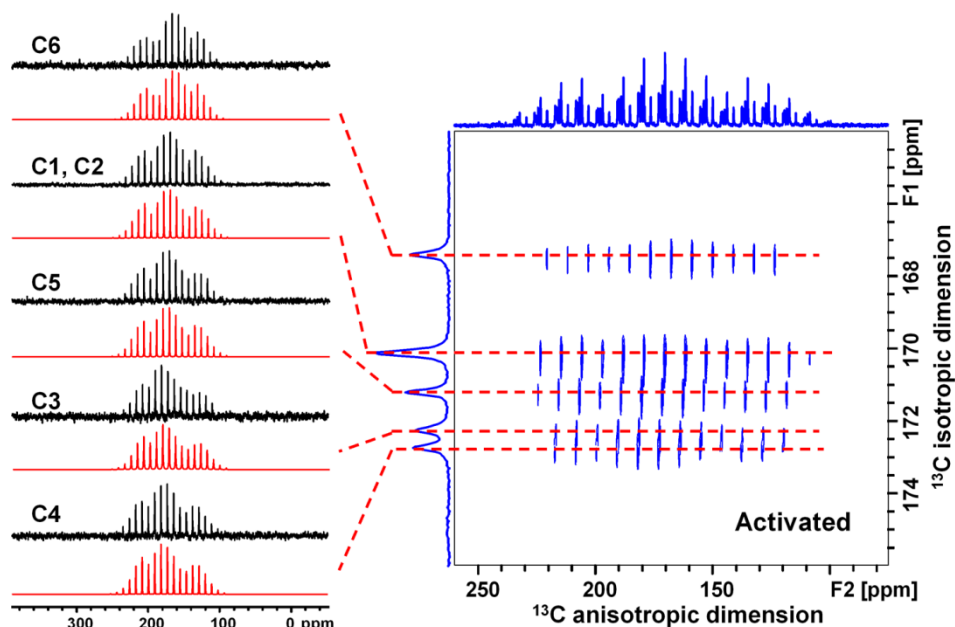
Figure 4-6: 2D [1]H-^{13}C PHORMAT spectrum of the 100% H activated sample (spinning speed: 2 kHz). The dashed lines correspond to the slices taken for simulation.

It has been demonstrated that the CSA tensor is generally more sensitive to the local environment than the isotropic shift.[61,62] Herein, ^{13}C CSA tensors of the activated sample were extracted by 2D [1]H–[13]C phase-corrected magic-angle turning (PHORMAT) experiments,[43] which correlate the ^{13}C CSA tensors in the direct (anisotropic) dimension with their isotropic chemical shifts in the indirect (isotropic) dimension. In our case, six C sites have identical chemical environment and thus similar NMR parameters, making their spinning sideband patterns overlapped and the 1D MAS spectrum too complicated to be simulated. As Figure 4-6 illustrates, PHORMAT experiment separates the entire 1D MAS spinning sideband manifold into the spinning sideband pattern of individual C sites according to their isotropic chemical shifts. The ^{13}C CSA tensors (Table 4-2) were then obtained by simulating the spinning sideband patterns by the Herzfeld-Berger analysis. The experimental ^{13}C CSA tensors of six C sites are very similar: the spans are between

120.0 and 128.0 ppm and skews are between -0.10 and 0.18, both of which are in the normal range of formate-containing materials.[59]

Table 4-2: Experimental and calculated ^{13}C CSA tensors.

Sample	C Site	$\Omega(^{13}$C) [ppm]		$\kappa(^{13}$C) [ppm]	
		Exptl	Calcd	Exptl	Calcd
activated	C1	126.9	141.7	0.08	0.05
	C2	126.9	139.3	0.08	0.07
	C3	125.7	140.6	0.17	-0.03
	C4	127.7	141.2	0.18	-0.08
	C5	128.0	140.6	0.08	0.02
	C6	120.0	139.7	-0.10	0.23
DMF	C1	128.3	141.7	0.07	0.04
	C2	134.1	143.5	0.05	-0.02
	C3	133.1	144.8	0.16	-0.07
	C4	138.8	144.0	0.07	-0.12
	C5	134.9	142.5	0.27	-0.26
	C6	128.3	142.7	0.07	-0.01
benzene	C1	130.6	140.6	0.08	0.08
	C2	127.9	143.9	0.14	-0.07
	C3	128.8	145.3	0.13	-0.07
	C4	127.9	143.9	0.14	-0.04
	C5	127.9	142.8	0.14	-0.12
	C6	123.3	142.8	0.01	0.09

In summary, several approaches can be used to assign the ^{1}H and ^{13}C peaks of the activated sample: 1) the ^{1}H peaks are assigned by ^{1}H–^{1}H BABA DQ experiments while the ^{13}C peaks are assigned by ^{1}H–^{13}C FSLG-HETCOR experiments; 2) the ^{1}H peaks are assigned by the calculated ^{1}H isotropic chemical shifts while the ^{13}C peaks are assigned by ^{1}H–^{13}C FSLG-HETCOR experiments; 3) the ^{13}C peaks are assigned by the calculated ^{13}C isotropic chemical shifts while the ^{1}H peaks are assigned by ^{1}H–^{13}C FSLG-HETCOR experiments; 4) the ^{13}C peaks are assigned by the calculated ^{13}C CSA tensors while the ^{1}H peaks are assigned by ^{1}H–^{13}C FSLG-HETCOR experiments. However, the ^{1}H and ^{13}C assignments made by different approaches are not consistent with each other. It is believed that the first approach, which is also the one used to assign the ^{1}H and ^{13}C peaks of the other samples, is most reliable. The reason is described as follow: As shown in Table 4-1, the calculated isotropic chemical shifts of ^{1}H (or ^{13}C) are in a very narrow

range (~ 0.5 ppm for ^{1}H or ~ 3 ppm for ^{13}C except C6) due to the identical chemical environment of six H (or C) sites, implying that a small error of the CASTEP calculations (or the crystal structure) can lead to a significant change of the [1]H (or ^{13}C) assignment. Moreover, the calculated ^{13}C CSA tensors (Table 4-2) are also fairly similar. In sharp contrast to such calculation-based assignments, the assignment according to the [1]H–[1]H internuclear distances is not sensitive to the misplacement of the protons. For instance, as Table 4-A5 illustrates, the longest distance of two non-equivalent protons whose cross peaks can be observed at 55.6 μs is 3.830 Å (*i.e.*, H3–H5) while the shortest distance of two non-equivalent protons whose cross peaks can be observed at 111.1 μs is 4.278 Å (*i.e.*, H4–H6). Therefore, even a very large error (± 0.2 Å) of H–C distances, which is unlikely to happen, has no effect on the identity of the two correlations. It is also worth mentioning that although the quality of the structure such as the H–C distances has been significantly improved by the CASTEP calculation, it can be further refined: The ^{13}C spans are overestimated by ~ 15–20 ppm from the calculation results for all six C sites. However, due to the limited computational capacity, further refinements of the crystal structure were not performed in this work.

4.3.2   DMF, Benzene and Acetone Phases

As Figure 4-3a shows, ultrahigh-resolution ^{1}H SSNMR spectra were also obtained for the DMF, benzene and acetone samples, using the approach described in the former section. It is noteworthy that their ^{1}H spectra look distinct from each other, implying the extremely high sensitivity of ^{1}H NMR parameters to the local H environments. Three (for the acetone sample) to five (for the DMF and benzene samples) ^{1}H peaks were clearly resolved from the 62.5 kHz MAS ^{1}H spectra of the 20% H samples. The number of non-equivalent H sites (six) and their populations (equal population) can be directly confirmed by the deconvolution of the ^{1}H spectra except the populations for the benzene sample, where the residual signal of benzene-d_6 (C_6D_6)[56] overlaps with the framework ^{1}H signals. It should be noticed that the ^{1}H peak at 8.43 ppm is well separated from the other five ^{1}H peaks for the DMF sample while the ^{1}H peaks at 8.55 and 6.78 ppm are well separated from the other four ^{1}H peaks for the benzene sample, the origin of which will be discussed in the next section.
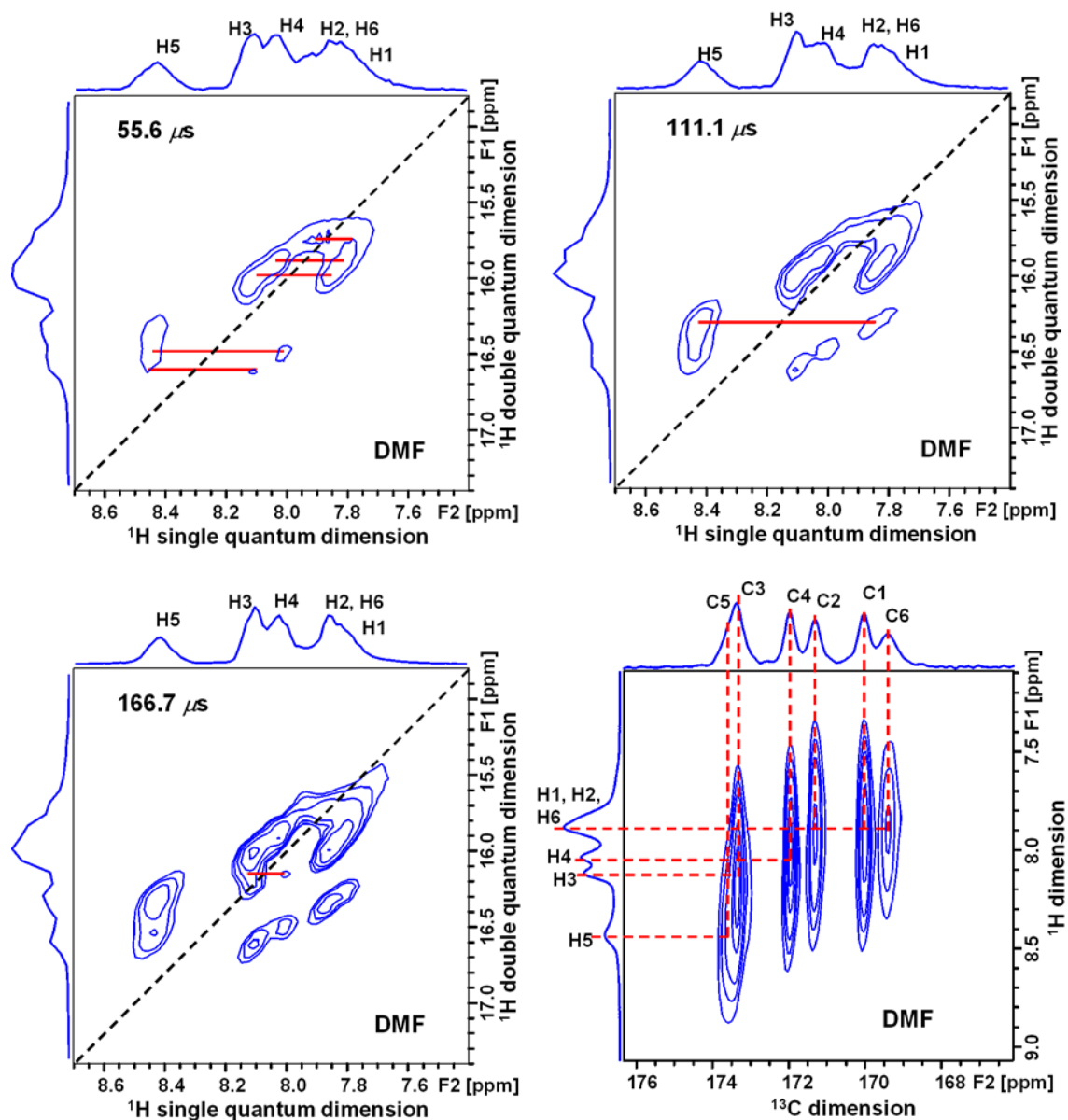
Figure 4-7: 2D ^{1}H–^{1}H BABA DQ spectra of the 20% H DMF sample as a function of excitation time (spinning speed: 18 kHz). Three DQ spectra were set to have the same contour levels. Bottom right: 2D ^{1}H–^{13}C FSLG-HETCOR spectrum (contact time 35 μs) of the 20% H DMF sample (spinning speed: 18 kHz). The 62.5 kHz MAS ^{1}H spectrum was used as the projection along the indirect (^{1}H) dimension.
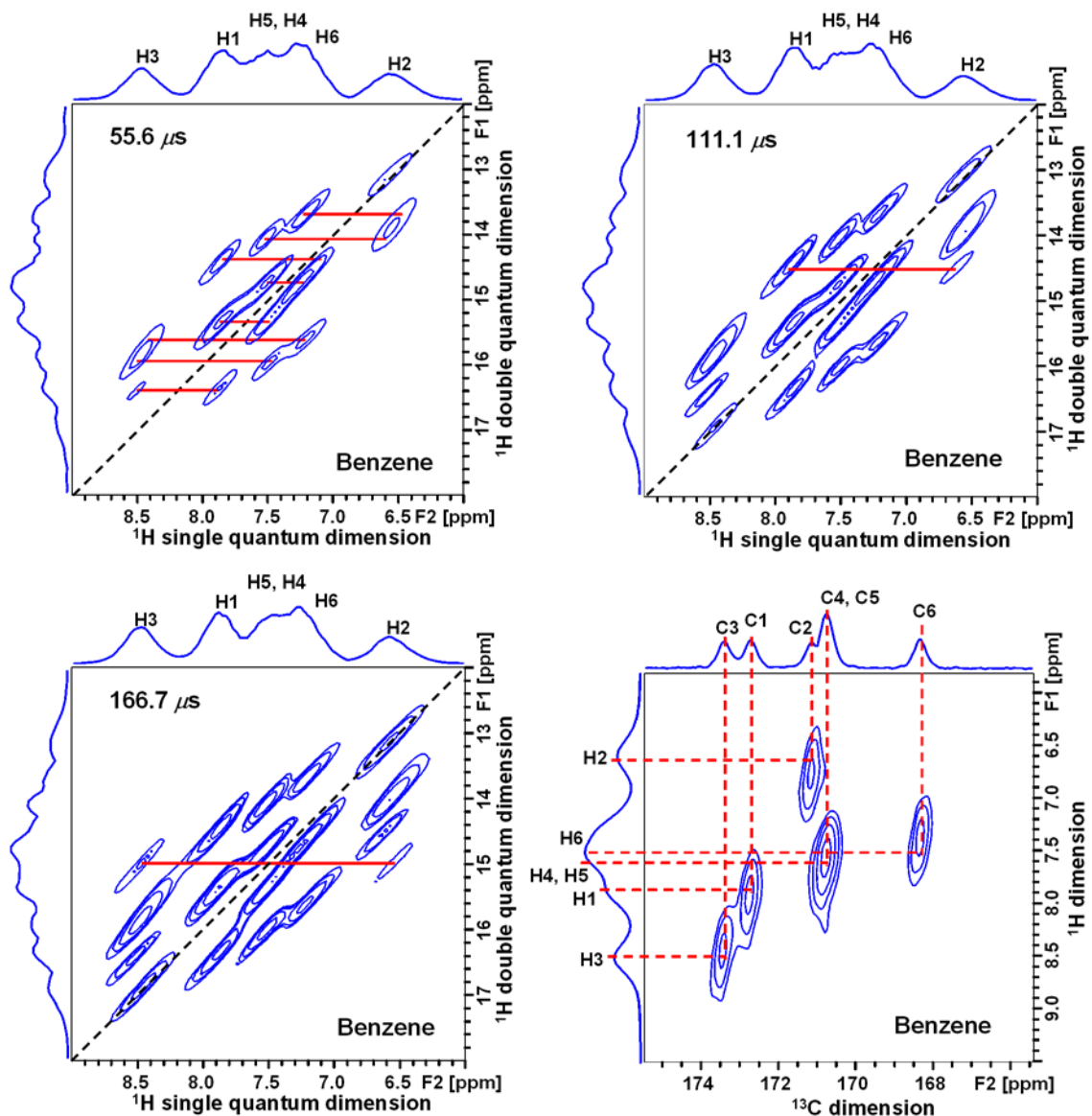
Figure 4-8: 2D ^{1}H–^{1}H BABA DQ spectra of the 20% H benzene sample as a function of excitation time (spinning speed: 18 kHz). Three DQ spectra were set to have the same contour levels. Bottom right: 2D ^{1}H–^{13}C FSLG-HETCOR spectrum (contact time 35 μs) of the 20% H benzene sample (spinning speed: 18 kHz). The 62.5 kHz MAS ^{1}H spectrum was used as the projection along the indirect (^{1}H) dimension.

The assignments of ^{1}H peaks for the DMF, benzene and acetone samples (Figure 4-3a and Table 4-1) were done based on the first approach used in the activated sample: The self-correlation peaks were first identified in ^{1}H–^{1}H BABA DQ spectra (Figure 4-7–9), and then the assignment of the other H sites was determined by relating the ^{1}H–^{1}H

distances (Table 4-A4) between the H sites already assigned and these unknown H sites with the experimentally observed cross peaks (Table 4-A5).
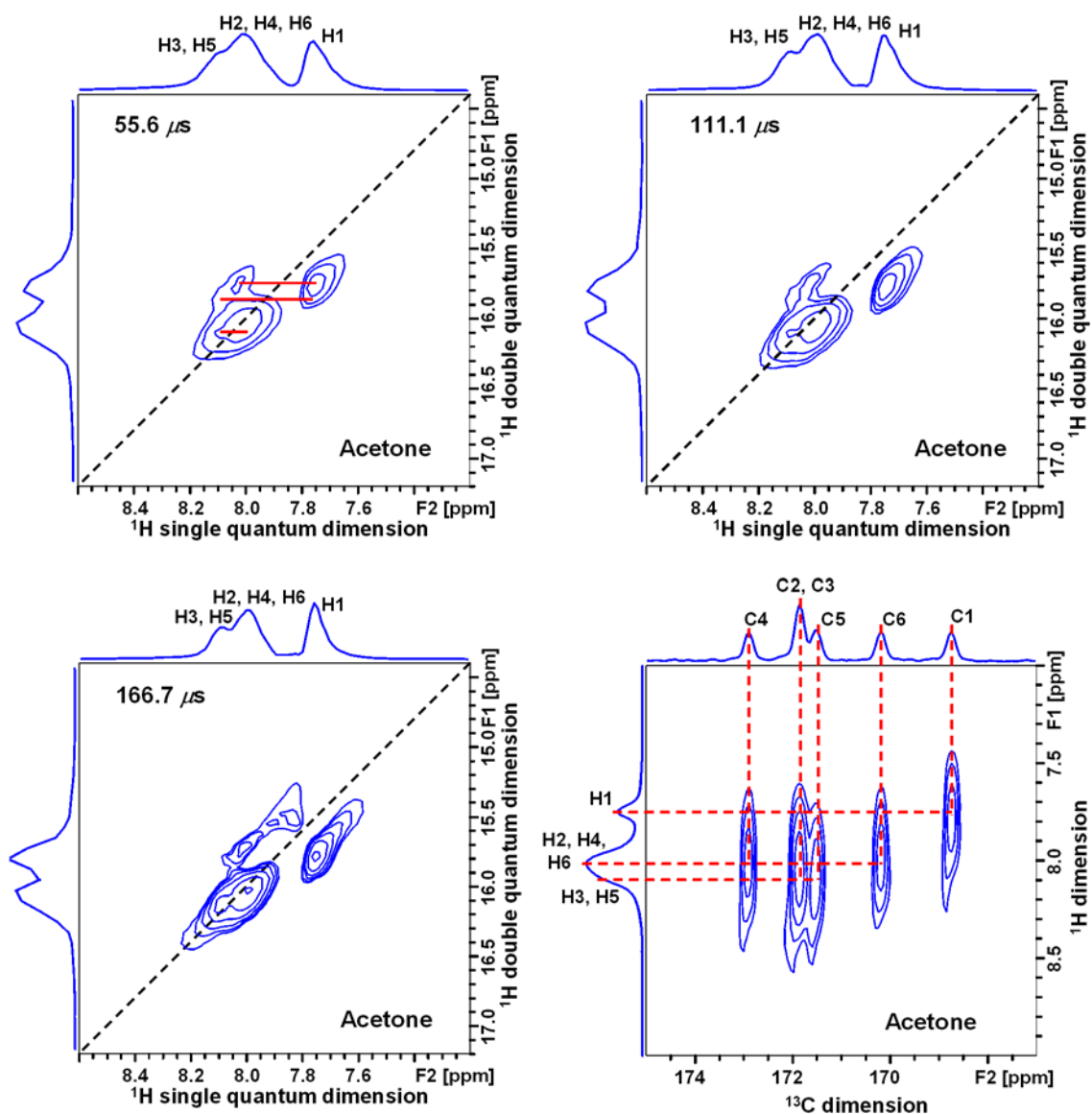
Figure 4-9: 2D ^{1}H–^{1}H BABA DQ spectra of the 20% H acetone sample as a function of excitation time (spinning speed: 18 kHz). Three DQ spectra were set to have the same contour levels. Bottom right: 2D ^{1}H–^{13}C FSLG-HETCOR spectrum (contact time 35 μs) of the 20% H acetone sample (spinning speed: 18 kHz). The 62.5 kHz MAS ^{1}H spectrum was used as the projection along the indirect (^{1}H) dimension.
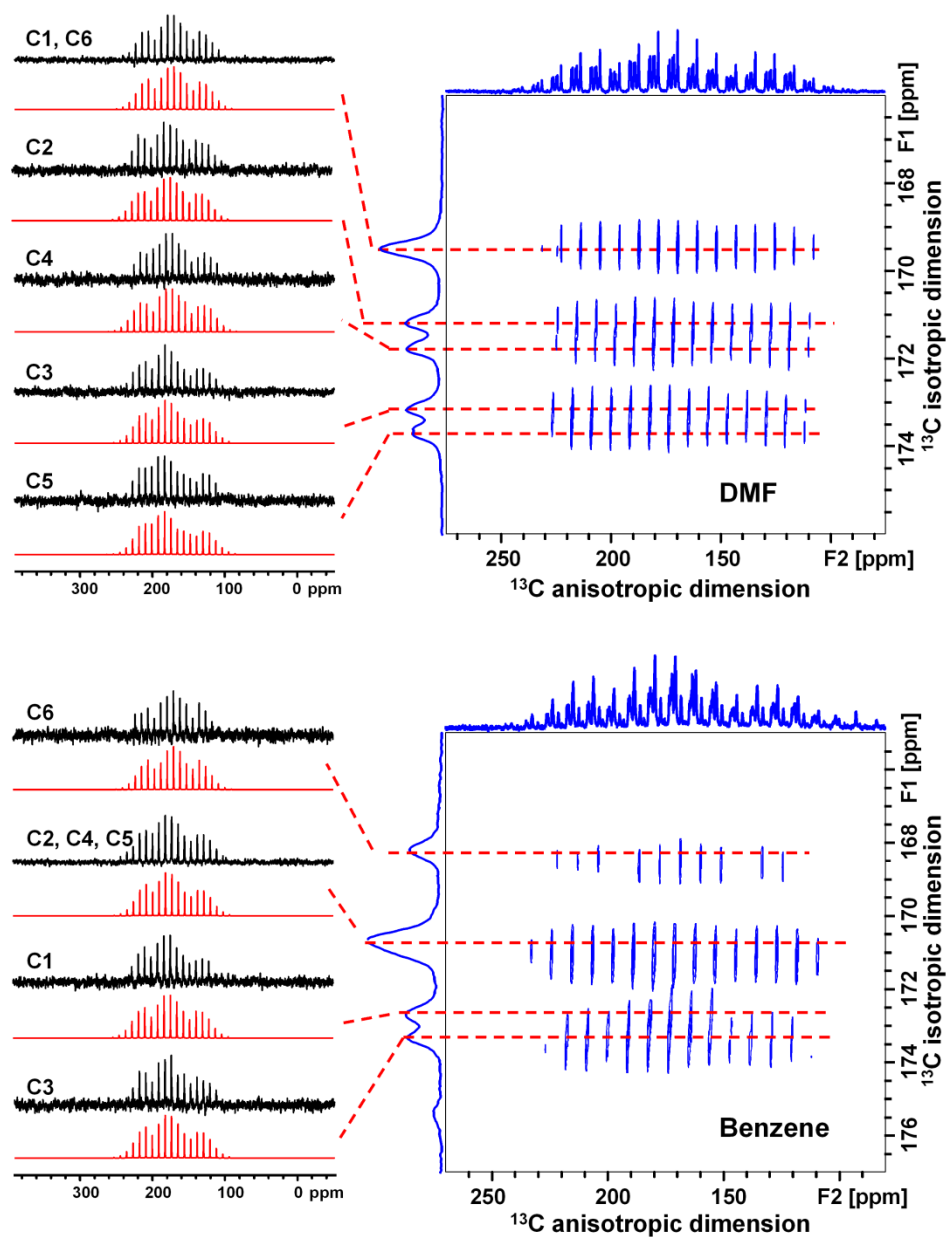
Figure 4-10: 2D ^{1}H–^{13}C PHORMAT spectra of the 100% H DMF and benzene samples (spinning speed: 2 kHz).

^{1}H→^{13}C CPMAS spectra of the DMF, benzene and acetone samples (Figure 4-3b) also exhibit very high resolution: Typically five ^{13}C peaks are well resolved. Like ^{1}H spectra, ^{13}C spectra are fingerprints of these close-related, but slightly different structures. For all three samples, the number of observed ^{13}C NMR peaks from deconvolution equals to the number of non-equivalent C sites, agreeing well with the proposed structure based

on the single-crystal XRD data.[36] The assignments of ^{13}C peaks were determined from the assignments of ^{1}H peaks by [1]H–[13]C FSLG-HETCOR experiments (Figure 4-7–9). [13]C CSA tensors of DMF and benzene samples were extracted by [1]H–[13]C PHORMAT experiments (Figure 4-10) as well. Although the ^{13}C spans of the benzene sample are very similar to those of the activated sample, they are smaller than those of the DMF sample by ~ 10 ppm, indicating that the local C environments of formate anions undergo relatively large changes after the adsorption of DMF compared to benzene. However, lacking more evidence, it is not possible to understand such changes yet.

4.3.3   Guest-Induced Shifts

As mentioned earlier, SSNMR spectroscopy is very sensitive to the short-range structural information. For example, ^{1}H SSNMR spectroscopy has been considered to be one of the most convenient ways to confirm the presence of weak hydrogen bonds.[5] In this section, the isotropic chemical shift of each framework H site, before and after guest inclusion, is examined to reveal if any significant solvent-induced shift exhibits for the DMF, benzene, and acetone samples. Such solvent-induced shifts are often a hint of possible interaction between a guest molecule and framework protons. As Figure 4-3a illustrates, a remarkable downfield shift of the H5 peak is observed, from 7.84 ppm in the activated sample to 8.43 ppm in the DMF sample, which is likely due to the formation of C–H···O hydrogen bond between framework C–H and occluded DMF molecules. A close inspection of the local environment around DMF (Figure 4-11a) implies that there are three framework protons (H2, H5, and H6) in close proximity (< 3 Å) of the carbonyl oxygen (OS) of DMF. To form a C–H···O hydrogen bond, the internuclear distance between H and O must be significantly shorter than the summation of Van der Waals radii (2.72 Å) and the C–H···O bond angle must be greater than 130°.[4,5] Therefore, among the three nearby protons, only the C5–H5···OS meets the criteria of both the short H5–OS distance (2.34 Å) and the large C5–H5···OS bond angle (158.1°), while the C2–H5···OS and C6–H6···OS hydrogen bonds are unlikely to form because of their unfavorable geometries: the C2–H2···OS angle is 87.9° and the C6–H6···OS angle is 112.4°, agreeing well with the fact that the changes of H2 and H6 chemical shifts (both are ~ 0.3 ppm) are much smaller than that of H5 (~ 0.6 ppm).
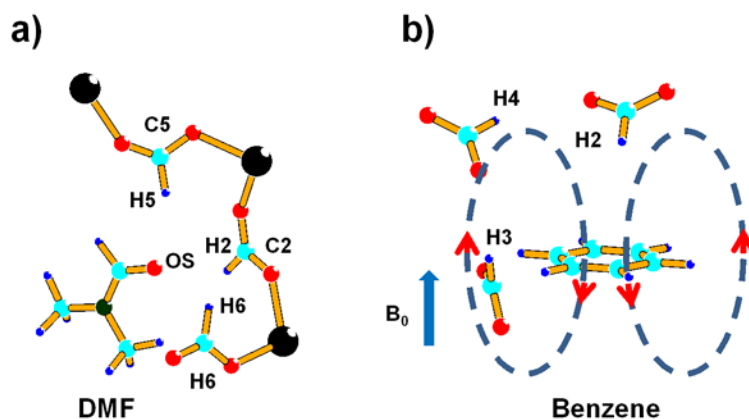
Figure 4-11: Local environments around (a) DMF and (b) benzene. For benzene, the induced magnetic field is shown to visualize the ring current effect.

For the benzene sample (Figure 4-3a), H3 has a large downfield shift from 7.94 ppm in the activated sample to 8.55 ppm in the benzene sample; whereas the H2 peak moves in an opposite manner: from 8.14 ppm to 6.78 ppm. It should be pointed out that such shifts are not the result of the change of the framework (the unit cell volume of the benzene sample is ~ 6% larger than that of the activated sample[36]) because the shifts for the other four protons are only ~ 0.2 ppm. As demonstrated in literature,[63] the magnetic shielding around the aromatic plane is highly anisotropic due to the ring current (namely the ring current effect). Figure 4-11b shows the orientations of H2 and H3 with respect to the benzene plane. H2 is above the benzene plane and thus feels an additional magnetic shielding; whereas H3 is deshielded since it is almost co-planar with benzene (the vector connecting H3 and the center of the aromatic ring is only 9° inclined with respect to the benzene plane). The other protons, such as H4, are not in favorable orientations with respect to the benzene plane. Therefore, no obvious shifts were observed for these protons. However, it is desirable to check if the benzene plane stays static at ambient temperature, since the above-mentioned interpretation is based on the structure determined by single-crystal XRD experiment at 110 K. As Figure 4-12 illustrates, two NMR experiments were carried out to probe the dynamics of benzene at ambient temperature. In the first case, ^{13}C CSA of benzene was obtained by performing ^{1}H$\rightarrow$^{13}C CPMAS experiments at different spinning speeds and then simulating the spinning sideband patterns by the Herzfeld-Berger analysis (Figure 4-12a). The measured ^{13}C CSA

tensor of benzene is: $\delta_{iso}(^{13}C) = 128.0$ ppm, $\Omega(^{13}C) = 157.6$ ppm, and $\kappa(^{13}C) = 1.00$. ^{13}C CSA tensor of static benzene is known in the literature: $\delta_{iso}(^{13}C) = 130$ ppm, $\Omega(^{13}C) = 225$ ppm, and $\kappa(^{13}C) = 0.20$.[64] Assuming an in-plane rotation of benzene about its C_6 axis, the motionally averaged ^{13}C CSA[65] is $\Omega(^{13}C) = 156.5$ ppm and $\kappa(^{13}C) = 1$, consistent with the experimental data. This motion was also confirmed by the static ^2H SSNMR experiment of α-Mg$_3$(HCOO)$_6\supset$C$_6$D$_6$ at 9.4 T (Figure 4-12b), in which a typical Pake doublet with the horn separation of $\sim$ 62 kHz was observed. The absence of out-plane motions such as π flip-flop confirms that the benzene plane does remain static.
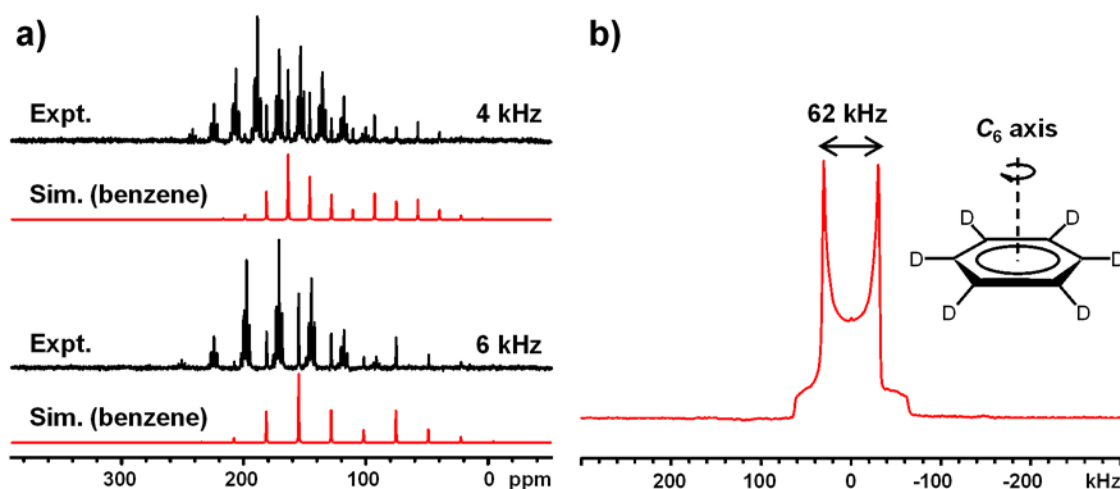
Figure 4-12: (a): $^1H\rightarrow^{13}C$ CPMAS spectra (contact time: 2 ms) of the 20% H benzene sample as a function of spinning speed. Simulated spinning sideband patterns of benzene are shown. (b): Room temperature ^2H static spectrum of α-Mg$_3$(HCOO)$_6\supset$C$_6$D$_6$ at 9.4 T.

A unique feature of the ^1H spectrum of the benzene sample is its significantly large line widths ($\sim$ 240 Hz, compared to $\sim$ 45 Hz for the activated sample and $\sim$ 75 Hz for the DMF sample). The thermal motion of benzene provides a possible explanation for the large residual ^1H line width. At ambient temperature, the in-plane rotation of benzene molecules generates time-dependent, rapid fluctuating local dipolar fields at framework protons. Under such circumstance, the residual line width due to thermal motions can only be efficiently reduced when the MAS speed (62.5 kHz in this work) is higher than the time constant of thermal motions (at the fast limit of ^2H SSNMR spectroscopy,[66,67] *i.e.*, $>10^8$ s^{-1}), as the previous literature illustrates.[68]

Due to the relatively poor spectral resolution, it is unclear if there is any evident guest-induced shift of ^{1}H for the acetone sample. Moreover, the changes of ^{13}C peaks of the three guest-loaded samples compared to the activated sample (Figure 4-3b) are also characteristic of the structure. However, the origin of such changes is not discussed here to avoid the overinterpretation of ^{13}C NMR data.

4.3.4 Pyridine Phase

In the former sections it has been demonstrated that the ultrahigh-resolution ^{1}H and ^{13}C SSNMR results directly confirmed the known structures proposed by single-crystal XRD experiments. Herein, a pyridine-loaded sample was studied to explore how much structural information can be extracted in the absence of single-crystal XRD data. The guest molecule, pyridine, was chosen because it is an aromatic compound with a size comparable to benzene. Moreover, pyridine is a good hydrogen bond acceptor whose N atom could potentially interact with framework protons, like what DMF does. Therefore, the ^{1}H spectrum of this sample can exhibit spectral features similar to those observed in the benzene and DMF samples, which could assist in the spectral interpretation.
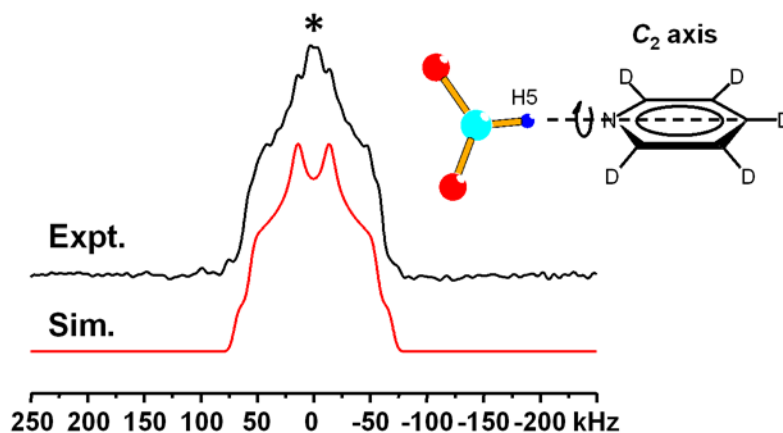
Figure 4-13: Room temperature ^{2}H static spectrum of α-Mg$_3$(HCOO)$_6 \supset$pyridine-d$_5$ at 9.4 T. *: additional motions.

The powder XRD pattern of the pyridine sample (Figure 4-A1) implies that it belongs to the $P2_1/n$ space group with unit cell parameters between those of the DMF and benzene samples (Table 4-A1). The pyridine sample therefore also has six non-equivalent

H sites with equal population, confirmed by deconvolution of the 62.5 kHz MAS ^{1}H spectrum (Figure 4-3a): five peaks were yielded, among which the most intense peak at 7.80 ppm corresponds to two H sites. The ^{1}H spectrum of the pyridine sample is similar to that of the benzene sample that both have broad ^{1}H peaks, and is similar to that of the DMF sample as well that both have one downfield peak (the peaks at 8.42 ppm for the pyridine sample and at 8.43 ppm for the DMF sample, respectively) well separated from the others. The broadening of the ^{1}H peaks for the pyridine sample is due to the thermal motions of pyridine. As Figure 4-13 illustrates, the static ^{2}H SSNMR spectrum of the pyridine sample at ambient temperature is typical for pyridine which undergoes a rapid π flip-flop motion about its C_2 axis ($C_Q(^2H) = 92$ kHz, $\eta_Q(^2H) = 0.60$).[67] Since such motion (out-plane rotation) averages the induced magnetic shielding of the aromatic ring, no ring current effect was identified. The observed π flip-flop motion suggests that there must be a strong interaction between pyridine and framework protons, such as a C–H···N hydrogen bond.[4] The observation of a downfield peak at 8.42 ppm provides another evidence of the C–H···N hydrogen bond. The assignment of this peak is thus essential because it allows one to study the details of the C–H···N hydrogen bond. According to the ^{1}H–^{1}H BABA DQ spectra (Figure 4-14), this peak can be unambiguously identified as H5: For the activated, DMF, benzene, and acetone samples, the self-correlation peak of H5 is always observed at longer excitation time than those of H2 and H3 (Table 4-A5). In the case of the pyridine sample, the self-correlation peak at 8.42 ppm along the SQ dimension was observed at 166.7 μs after those at 7.62 and 7.43 ppm (observed at 55.6 μs). Therefore the former one is H5 and the latter two are H2 and H3. The peaks at 7.80 and 7.98 ppm are assigned to H1, H4 and H6. However, it is extremely challenging to distinguish H2 from H3 (or H1 from H4 and H6, *etc.*), if not impossible. Herein, only the tentative assignment of these protons (Figure 4-3a and Table 4-1) is given according to the corresponding assignment in the DMF sample, *e.g.*, for H2 and H3, the more shielded peak at 7.43 ppm is H2 (7.88 ppm in the DMF sample) while the other one at 7.62 ppm is H3 (8.11 ppm in the DMF sample).
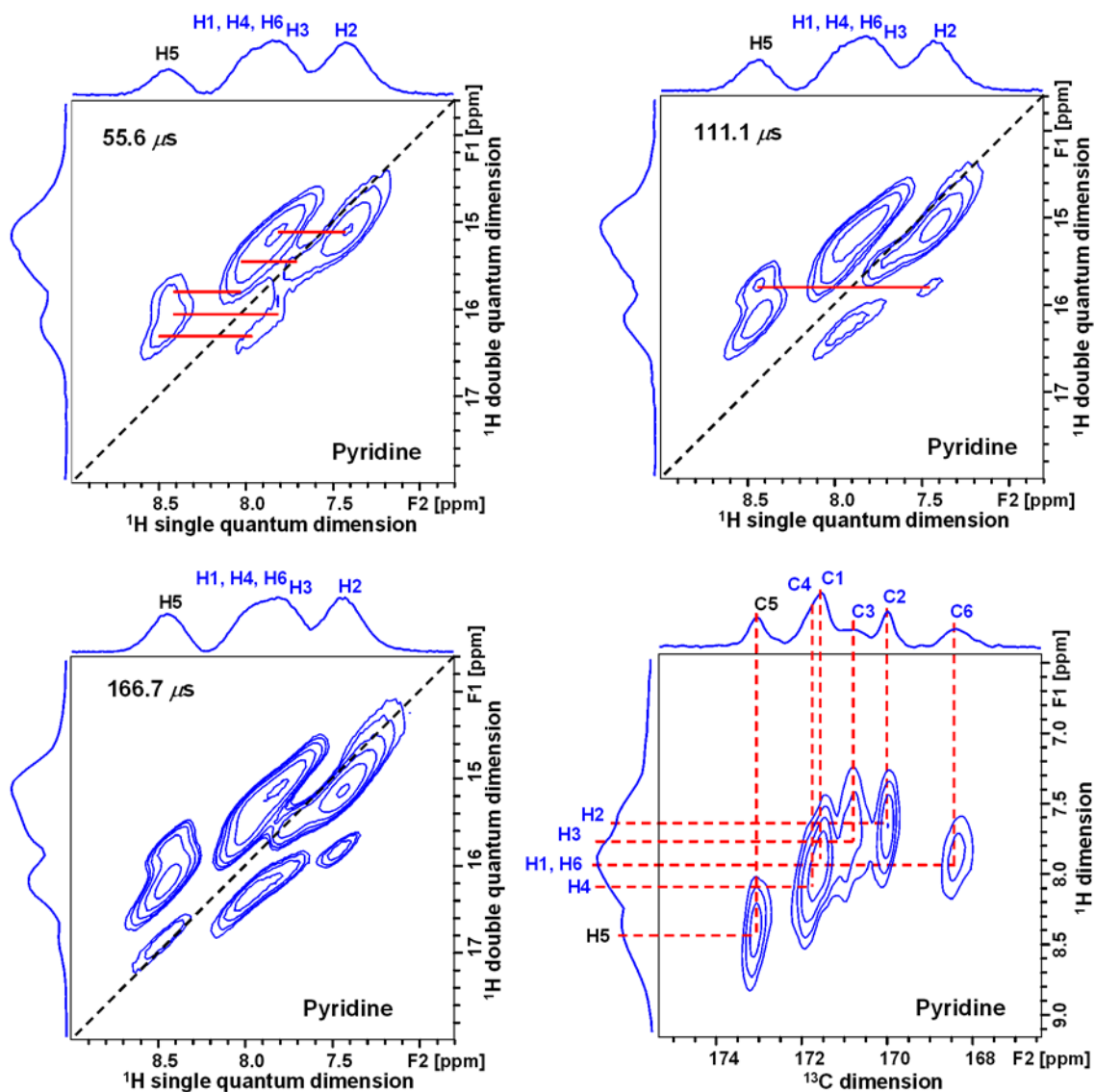
Figure 4-14: 2D ^{1}H–^{1}H BABA DQ spectra of the 20% H pyridine sample as a function of excitation time (spinning speed: 18 kHz). Three DQ spectra were set to have the same contour levels. Bottom right: 2D ^{1}H–^{13}C FSLG-HETCOR spectrum (contact time 35 μs) of the 20% H pyridine sample (spinning speed: 18 kHz). The 62.5 kHz MAS ^{1}H spectrum was used as the projection along the indirect (^{1}H) dimension. The protons and carbons labeled with blue color were only tentatively assigned.

Figure 4-3b shows that six ^{13}C peaks can be directly resolved in the ^{1}H→^{13}C CPMAS spectrum of the 20% H pyridine sample, consistent with the crystal symmetry proposed by the powder XRD pattern. It is worth mentioning that the results of ^{1}H–^{13}C

FSLG HETCOR experiment (Figure 4-14) can be used to examine the assignment of ^{1}H peaks: The integrated intensity of the peak at 7.80 ppm (31.0%, Table 4-1, assigned to two H sites) is only slightly higher than that of the peak at 7.98 ppm (24.4%, assigned to one H site). The validity of such assignment is confirmed by the fact that for the ^{1}H peaks at 7.43, 7.62 and 7.98 ppm, each peak only correlates to one ^{13}C peak whereas for the ^{1}H peak at 7.80 ppm, it correlates to two ^{13}C peaks. The assignment of ^{13}C peaks was provided based on the [1]H–[13]C connectivity. The CASTEP calculations of ^{1}H and ^{13}C NMR parameters (Table 4-1) were performed as well on the pyridine sample for comparison purposes, using a simple model structure: the framework coordinates were taken from those of the DMF sample while the guest coordinates were from those of the benzene sample. The C–H fragment of benzene in close proximity to H5 was substituted by a nitrogen atom.

A previous report (*Chapter 3*) described that the four non-equivalent Mg sites of microporous α-Mg$_3$(HCOO)$_6$ samples can be differentiated by natural abundance [25]Mg SSNMR experiments at 21.1 T.[11] In this work, the crystal symmetry of the pyridine sample is also studied by [25]Mg SSNMR spectroscopy. As a quadrupolar nucleus ($I = 5/2$), the NMR spectrum of [25]Mg is typically broadened by quadrupolar interactions that cannot be completely averaged by simple MAS experiments, resulting in a lower spectral resolution than spin-1/2 nuclei (*e.g.*, ^{13}C). Moreover, the narrow chemical shift range of [25]Mg makes the spectral resolution even worse for samples with multiple Mg sites such as microporous α-Mg$_3$(HCOO)$_6$. The acquisition of [25]Mg SSNMR spectra at natural abundance is also hindered by several factors: 1) the low intrinsic sensitivity due to the unfavorable nuclear properties of [25]Mg, such as a small gyromagnetic ratio (γ) of -1.639 $\times$ 10^7 rad·s^{-1}·T^{-1} and a relatively low natural abundance of 10.0%;[69] 2) a relatively large quadrupole moment;[70] (3) a very low [25]Mg concentration due to low densities of MOFs. The number of [25]Mg per nm^3 in microporous α-Mg$_3$(HCOO)$_6$ (0.73) is only 14% compared to the number for the dense MgO (5.3). Nevertheless, several recent studies have illustrated that the low sensitivity associated with low-γ unreceptive quadrupolar nuclei in MOFs can be alleviated by performing SSNMR experiments at high magnetic

fields.[10,11,29] The poor spectral resolution of ^{25}Mg can be significantly enhanced by two-dimensional triple-quantum MAS (3QMAS) experiments.[48-50]
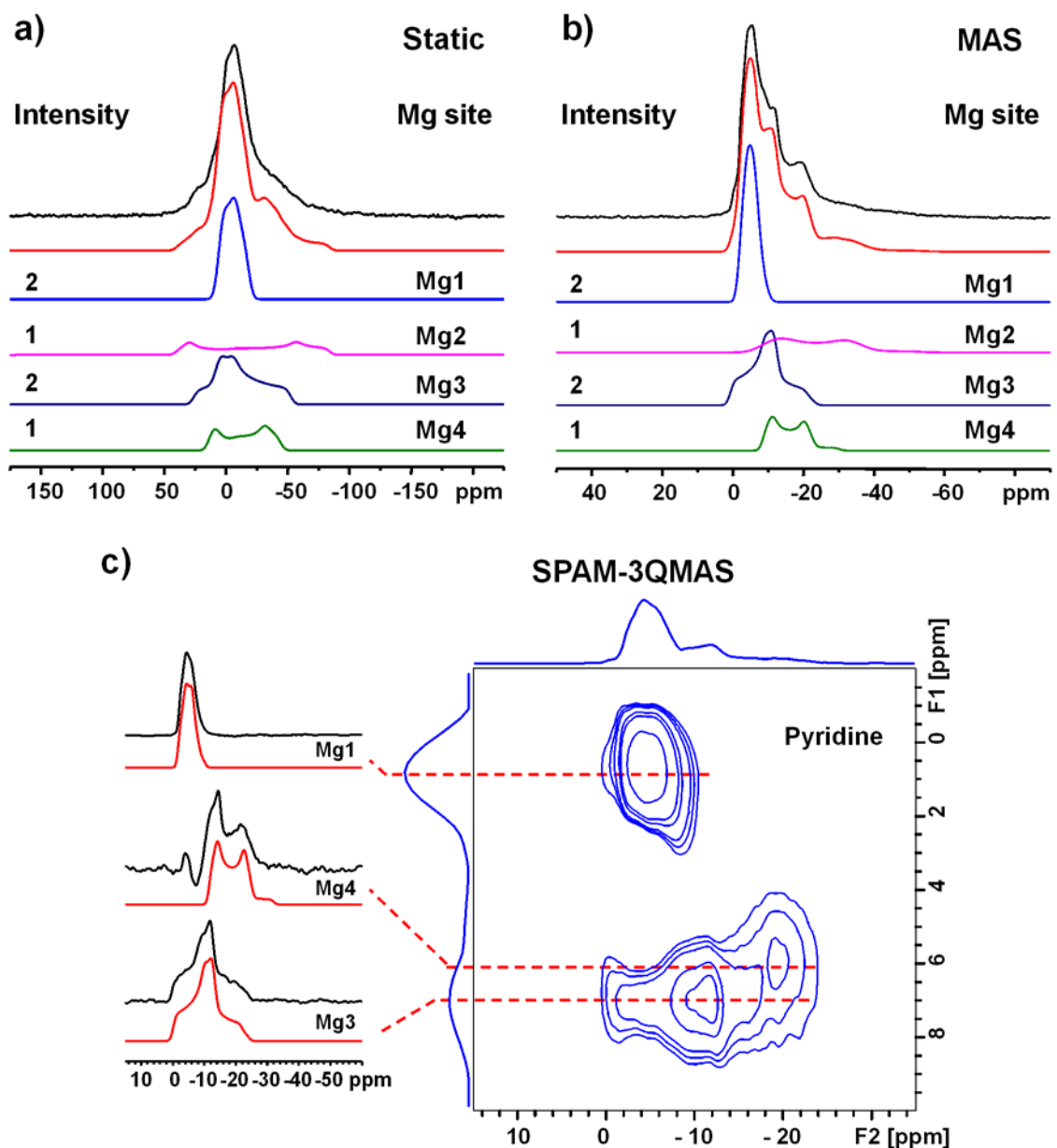
Figure 4-15: Natural abundance (a) static, (b) 5 kHz MAS, and (c) 2D SPAM-3QMAS ^{25}Mg spectra of the 20% H pyridine sample. The static and MAS spectra simulated with the parameters obtained from 3QMAS are also shown. All ^{25}Mg NMR experiments were performed at 21.1 T.

Figure 4-15 illustrates natural abundance static, 5 kHz MAS, and SPAM-3QMAS ^{25}Mg spectra of the pyridine sample at 21.1 T. It should be mentioned that both static and 1D MAS spectra of the pyridine sample are similar to those of the DMF sample,[11] consistent with what were observed in the ^{1}H SSNMR experiments. The SPAM-3QMAS ^{25}Mg spectrum of the pyridine sample clearly exhibits several resolved domains along the high-resolution (F1) dimension. Three cross-sections were extracted for simulation. The cross-section at 1 ppm along the F1 dimension can be fitted with a single resonance, and the same situation occurs for the one at 7 ppm. Although the line shape of the slice at 6 ppm is distorted, it can still be fitted reasonably well using a single resonance. It seems that the slice at 5 ppm corresponds to another Mg site but the line shape is too distorted to be simulated (not shown). Based on the NMR parameters of the three Mg sites determined in the 3QMAS experiment, the existence of the fourth Mg site was confirmed by simulating the ^{25}Mg static spectrum. The NMR parameters of the fourth Mg site were then refined by simulating the 5 kHz MAS ^{25}Mg spectrum, which allows one to obtain the correct relative intensities of four Mg sites (Table 4-3). Direct observation of four Mg sites is consistent with the assumption that the crystal symmetry of the pyridine sample is the same as the other samples. The assignment of four Mg sites is made according to the approaches demonstrated in the literature.[11] The experimental C_Q values for Mg2 (3.2 MHz) and Mg4 (2.2 MHz) are significantly larger than those of the DMF sample (2.2 MHz for Mg2 and 1.0 MHz for Mg4, respectively) while the C_Q values for Mg1 and Mg3 are not,[11] implying that the local environments of Mg2 and Mg4 must undergo larger degrees of distortion than those of Mg1 and Mg3 after the adsorption of more bulky pyridine molecules compared to DMF molecules. Such observation agrees well with the fact that the corner-shared MgO_6 units of Mg2 and Mg4 should have more flexibility than the edge-shared MgO_6 units of Mg1 and Mg3.

Table 4-3: Experimental and calculated ^{25}Mg NMR parameters of the pyridine sample.

Mg Site	C_Q(^{25}Mg) [MHz]		η_Q(^{25}Mg)		δ_{iso}(^{25}Mg) [ppm]		Area [%]
	Exptl	Calcd	Exptl	Calcd	Exptl	Calcd	
Mg1	1.3	1.79	0.5	0.55	-1.5	3.96	34
Mg2	3.2	3.38	0.2	0.17	-3.0	-0.19	16
Mg3	2.1	2.02	0.8	0.78	0.9	4.43	34
Mg4	2.2	2.66	0.2	0.87	-6.3	-0.25	16

Therefore, according to the powder XRD pattern and ^{1}H, ^{13}C, [25]Mg SSNMR data, the crystal symmetry of the unknown sample, pyridine-loaded α-$Mg_3(HCOO)_6$, is found to be identical with other α-$Mg_3(HCOO)_6$ samples. The pyridine molecule is undergoing a rapid π flip-flop motion at ambient temperature due to the C5–H5···N hydrogen bond.

4.4 Conclusions

In this work, it has been demonstrated that ultrahigh-resolution ^{1}H and ^{13}C SSNMR spectra are available for MOFs. Multiple (six) crystallographically non-equivalent, but chemically equivalent H (or C) sites of an important MOF, microporous α-$Mg_3(HCOO)_6$, can be differentiated by ^{1}H (or ^{13}C) SSNMR spectroscopy. Like fingerprints, ^{1}H and ^{13}C spectra are very sensitive to the guest molecules included inside of the channels. The four non-equivalent Mg sites of the pyridine sample were also resolved by natural abundance [25]Mg 3QMAS experiments at 21.1 T. The acquisition of ultrahigh-resolution NMR spectra is critical since it allows one to directly compare the NMR spectra with the structure determined by single-crystal XRD data. Among the interesting results, the ability of achieving ultrahigh-resolution for ^{1}H NMR in solids by the combination of ultrafast MAS (62.5 kHz), isotopic (^{2}H) dilution, and high magnetic field (21.1 T) is of particular importance because the structural information from ^{1}H SSNMR experiments complements that from single-crystal XRD which is incapable of accurately locating hydrogens. This work is also highlighted by the identification of weak C–H···O and C–H···N hydrogen bonds by ^{1}H SSNMR experiments. The aromatic current effect was observed in the benzene sample as well. We feel that the approach described and the results presented here, especially ^{1}H SSNMR experiments, can be used as a benchmark for determining the structures of MOFs and related materials with unknown or poorly described structures.

4.5 References

(1)   Special issue for Metal–Organic Frameworks: Zhou, H.-C.; Long, J. R.; Yaghi, O. M. *Chem. Rev.* **2012**, *112*, 673-1268.

(2)   Sutrisno, A.; Huang, Y. *Solid State Nucl. Magn. Reson.* **2013**, *49-50*, 1-11.

(3)   Hoffmann, H. C.; Debowski, M.; Mueller, P.; Paasch, S.; Senkovska, I.; Kaskel, S.; Brunner, E. *Materials* **2012**, *5*, 2537-2572.

(4)   Desiraju, G. R.; Steiner, T. *The Weak Hydrogen Bond in Structural Chemistry and Biology*; Oxford University Press: Oxford; New York, **1999**.

(5)   Yates, J. R.; Pham, T. N.; Pickard, C. J.; Mauri, F.; Amado, A. M.; Gil, A. M.; Brown, S. P. *J. Am. Chem. Soc.* **2005**, *127*, 10216-10220.

(6)   Pake, G. E. *J. Chem. Phys.* **1948**, *16*, 327-336.

(7)   Brown, S. P. *Prog. Nucl. Magn. Reson. Spectrosc.* **2007**, *50*, 199-251.

(8)   Fyfe, C. A.; Feng, Y.; Grondey, H.; Kokotailo, G. T.; Gies, H. *Chem. Rev.* **1991**, *91*, 1525-1543.

(9)   Harris, R. K.; Wasylishen, R. E.; Duer, M. J.; Eds. *NMR Crystallography*; Wiley: Chichester, U.K., **2009**.

(10)   Sutrisno, A.; Terskikh, V. V.; Shi, Q.; Song, Z.; Dong, J.; Ding, S. Y.; Wang, W.; Provost, B. R.; Daff, T. D.; Woo, T. K.; Huang, Y. *Chem. Eur. J.* **2012**, *18*, 12251-12259.

(11)   Xu, J.; Terskikh, V. V.; Huang, Y. *Chem. Eur. J.* **2013**, *19*, 4432-4436.

(12)   Dudenko, D. V.; Williams, P. A.; Hughes, C. E.; Antzutkin, O. N.; Velaga, S. P.; Brown, S. P.; Harris, K. D. M. *J. Phys. Chem. C* **2013**, *117*, 12258-12265.

(13)   Devautour-Vinot, S.; Maurin, G.; Serre, C.; Horcajada, P.; Paula da Cunha, D.; Guillerm, V.; de Souza Costa, E.; Taulelle, F.; Martineau, C. *Chem. Mater.* **2012**, *24*, 2168-2177.

(14)   Gul-E-Noor, F.; Jee, B.; Mendt, M.; Himsl, D.; Poeppl, A.; Hartmann, M.; Haase, J.; Krautscheid, H.; Bertmer, M. *J. Phys. Chem. C* **2012**, *116*, 20866-20873.

(15)   Dawson, D. M.; Jamieson, L. E.; Mohideen, M. I. H.; McKinlay, A. C.; Smellie, I. A.; Cadou, R.; Keddie, N. S.; Morris, R. E.; Ashbrook, S. E. *Phys. Chem. Chem. Phys.* **2013**, *15*, 919-929.

(16)   Lin, L.-C.; Kim, J.; Kong, X.; Scott, E.; McDonald, T. M.; Long, J. R.; Reimer, J. A.; Smit, B. *Angew. Chem., Int. Ed.* **2013**, *52*, 4410-4413.

(17)   Mazaj, M.; Mali, G.; Rangus, M.; Žunkovič, E.; Kaučič, V.; Logar, N. Z. *J. Phys. Chem. C* **2013**, *117*, 7552-7564.

(18)   Kong, X.; Deng, H.; Yan, F.; Kim, J.; Swisher, J. A.; Smit, B.; Yaghi, O. M.; Reimer, J. A. *Science* **2013**, *341*, 882-885.

(19)   Rossini, A. J.; Zagdoun, A.; Lelli, M.; Canivet, J.; Aguado, S.; Ouari, O.; Tordo, P.; Rosay, M.; Maas, W. E.; Copéret, C.; Farrusseng, D.; Emsley, L.; Lesage, A. *Angew. Chem., Int. Ed.* **2012**, *51*, 123-127.

(20)   Uemura, T.; Horike, S.; Kitagawa, K.; Mizuno, M.; Endo, K.; Bracco, S.; Comotti, A.; Sozzani, P.; Nagaoka, M.; Kitagawa, S. *J. Am. Chem. Soc.* **2008**, *130*, 6781-6788.

(21)   Shustova, N. B.; Ong, T.-C.; Cozzolino, A. F.; Michaelis, V. K.; Griffin, R. G.; Dinca, M. *J. Am. Chem. Soc.* **2012**, *134*, 15061-15070.

(22)   Vukotic, V. N.; Harris, K. J.; Zhu, K.; Schurko, R. W.; Loeb, S. J. *Nat. Chem.* **2012**, *4*, 456-460.

(23)   Rives, S.; Jobic, H.; Kolokolov, D. I.; Gabrienko, A. A.; Stepanov, A. G.; Ke, Y.; Frick, B.; Devic, T.; Férey, G.; Maurin, G. *J. Phys. Chem. C* **2013**, *117*, 6293-6302.

(24)   Loiseau, T.; Serre, C.; Huguenard, C.; Fink, G.; Taulelle, F.; Henry, M.; Bataille, T.; Férey, G. *Chem. Eur. J.* **2004**, *10*, 1373-1382.

(25)   Loiseau, T.; Lecroq, L.; Volkringer, C.; Marrot, J.; Férey, G.; Haouas, M.; Taulelle, F.; Bourrelly, S.; Llewellyn, P. L.; Latroche, M. *J. Am. Chem. Soc.* **2006**, *128*, 10223-10230.

(26)   Jiang, Y.; Huang, J.; Marx, S.; Kleist, W.; Hunger, M.; Baiker, A. *J. Phys. Chem. Lett.* **2010**, *1*, 2886-2890.

(27)   Mowat, J. P. S.; Miller, S. R.; Slawin, A. M. Z.; Seymour, V. R.; Ashbrook, S. E.; Wright, P. A. *Microporous Mesoporous Mater.* **2011**, *142*, 322-333.

(28)   Hajjar, R.; Volkringer, C.; Loiseau, T.; Guillou, N.; Marrot, J.; Férey, G.; Margiolaki, I.; Fink, G.; Morais, C.; Taulelle, F. *Chem. Mater.* **2011**, *23*, 39-47.

(29)   Xu, J.; Terskikh, V. V.; Huang, Y. *J. Phys. Chem. Lett.* **2013**, *4*, 7-11.

(30)   Schnell, I.; Spiess, H. W. *J. Magn. Reson.* **2001**, *151*, 153-227.

(31)   Samoson, A.; Tuherm, T.; Gan, Z. *Solid State Nucl. Magn. Reson.* **2001**, *20*, 130-136.

(32)   Lewandowski, J. R.; Dumez, J.-N.; Akbey, U.; Lange, S.; Emsley, L.; Oschkinat, H. *J. Phys. Chem. Lett.* **2011**, *2*, 2205-2211.

(33)   Brown, S. P. *Solid State Nucl. Magn. Reson.* **2012**, *41*, 1-27.

(34)   Reif, B. *J. Magn. Reson.* **2012**, *216*, 1-12.

(35)   Hodgkinson, P. *Annu. Rep. NMR Spectrosc.* **2011**, *72*, 185-223.

(36)   Rood, J. A.; Noll, B. C.; Henderson, K. W. *Inorg. Chem.* **2006**, *45*, 5521-5528.

(37)   Leung, E.; Mueller, U.; Cox, G. *WO 2010106121 A1*, BASF SE, Germany, WO, **2010**, p. 12.

(38)   Available through Sigma-Aldrich, catalogue search. Access date: Sept. 12, 2013.

(39)   Feike, M.; Demco, D. E.; Graf, R.; Gottwald, J.; Hafner, S.; Spiess, H. W. *J. Magn. Reson., Ser. A* **1996**, *122*, 214-221.

(40)   van Rossum, B. J.; Foerster, H.; de Groot, H. J. M. *J. Magn. Reson.* **1997**, *124*, 516-519.

(41)   Charpentier, T. *Solid State Nucl. Magn. Reson.* **2011**, *40*, 1-20.

(42) Bonhomme, C.; Gervais, C.; Babonneau, F.; Coelho, C.; Pourpoint, F.; Azais, T.; Ashbrook, S. E.; Griffin, J. M.; Yates, J. R.; Mauri, F.; Pickard, C. J. *Chem. Rev.* **2012**, *112*, 5733-5779.

(43) Hu, J. Z.; Wang, W.; Liu, F.; Solum, M. S.; Alderman, D. W.; Pugmire, R. J.; Grant, D. M. *J. Magn. Reson., Ser. A* **1995**, *113*, 210-222.

(44) Kunwar, A. C.; Turner, G. L.; Oldfield, E. *J. Magn. Reson.* **1986**, *69*, 124-127.

(45) Feike, M.; Graf, R.; Schnell, I.; Jaeger, C.; Spiess, H. W. *J. Am. Chem. Soc.* **1996**, *118*, 9631-9634.

(46) Bennett, A. E.; Rienstra, C. M.; Auger, M.; Lakshmi, K. V.; Griffin, R. G. *J. Chem. Phys.* **1995**, *103*, 6951-6958.

(47) Herzfeld, J.; Berger, A. E. *J. Chem. Phys.* **1980**, *73*, 6021-6030.

(48) Frydman, L.; Harwood, J. S. *J. Am. Chem. Soc.* **1995**, *117*, 5367-5368.

(49) Gan, Z.; Kwak, H.-T. *J. Magn. Reson.* **2004**, *168*, 346-351.

(50) Amoureux, J. P.; Delevoye, L.; Steuernagel, S.; Gan, Z.; Ganapathy, S.; Montagne, L. *J. Magn. Reson.* **2005**, *172*, 268-278.

(51) Kemp, T. F.; Smith, M. E. *Solid State Nucl. Magn. Reson.* **2009**, *35*, 243-252.

(52) Davis, J. H.; Jeffrey, K. R.; Bloom, M.; Valic, M. I.; Higgs, T. P. *Chem. Phys. Lett.* **1976**, *42*, 390-394.

(53) Salager, E.; Day, G. M.; Stein, R. S.; Pickard, C. J.; Elena, B.; Emsley, L. *J. Am. Chem. Soc.* **2010**, *132*, 2564-2566.

(54) Cahill, L. S.; Hanna, J. V.; Wong, A.; Freitas, J. C. C.; Yates, J. R.; Harris, R. K.; Smith, M. E. *Chem. Eur. J.* **2009**, *15*, 9785-9798.

(55) Brunner, E.; Freude, D.; Gerstein, B. C.; Pfeifer, H. *J. Magn. Reson.* **1990**, *90*, 90-99.

(56) Fulmer, G. R.; Miller, A. J. M.; Sherden, N. H.; Gottlieb, H. E.; Nudelman, A.; Stoltz, B. M.; Bercaw, J. E.; Goldberg, K. I. *Organometallics* **2010**, *29*, 2176-2179.

(57) Wagner, G.; Pardi, A.; Wuethrich, K. *J. Am. Chem. Soc.* **1983**, *105*, 5948-5949.

(58) *CRC Handbook of Chemistry and Physics*, *Internet Version 2005*, <http://www.hbcpnetbase.com>, CRC Press: Boca Raton, FL, **2005**.

(59) Hallock, K. J.; Lee, D. K.; Ramamoorthy, A. *J. Chem. Phys.* **2000**, *113*, 11187-11193.

(60) Bielecki, A.; Kolbert, A. C.; Levitt, M. H. *Chem. Phys. Lett.* **1989**, *155*, 341-346.

(61) Brouwer, D. H. *J. Am. Chem. Soc.* **2008**, *130*, 6306-6307.

(62) Harper, J. K.; Iuliucci, R.; Gruber, M.; Kalakewich, K. *CrystEngComm* **2013**, doi: 10.1039/c3ce40108a.

(63)   Brouwer, D. H.; Alavi, S.; Ripmeester, J. A. *Phys. Chem. Chem. Phys.* **2008**, *10*, 3857-3860.

(64)   Strub, H.; Beeler, A. J.; Grant, D. M.; Michl, J.; Cutts, P. W.; Zilm, K. W. *J. Am. Chem. Soc.* **1983**, *105*, 3333-3334.

(65)   Willans, M. J.; Schurko, R. W. *J. Phys. Chem. B* **2003**, *107*, 5144-5161.

(66)   Wittebort, R. J.; Olejniczak, E. T.; Griffin, R. G. *J. Chem. Phys.* **1987**, *86*, 5411-5420.

(67)   Larsen, F. H. *Annu. Rep. NMR Spectrosc.* **2010**, *71*, 103-137.

(68)   Brunner, E. *J. Chem. Soc., Faraday Trans.* **1990**, *86*, 3957-3960.

(69)   Harris, R. K.; Becker, E. D.; Cabral De Menezes, S. M.; Goodfellow, R.; Granger, P. *Pure Appl. Chem.* **2001**, *73*, 1795-1818.

(70)   Pyykkö, P. *Mol. Phys.* **2008**, *106*, 1965-1974.

4.6 Appendix

Section A1: Powder XRD and TGA Results
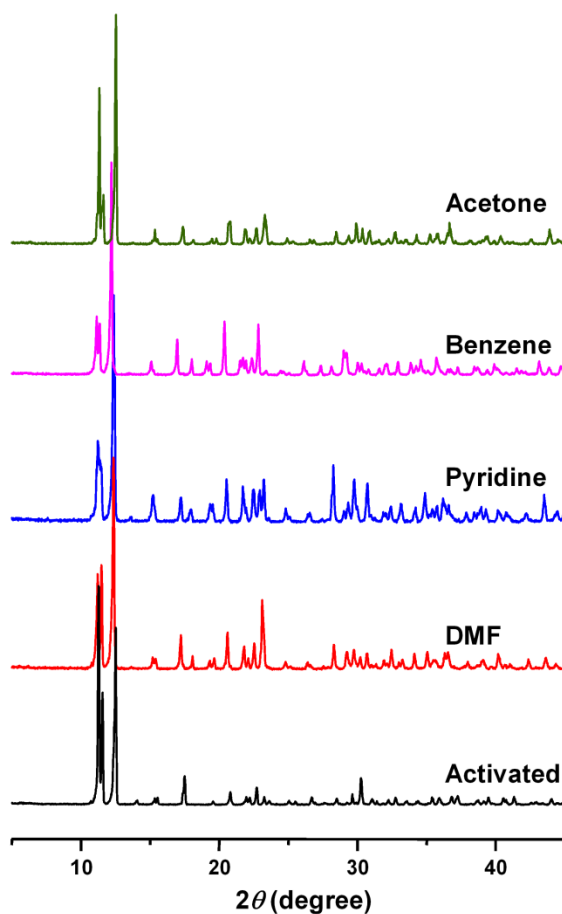
Figure 4-A1: Powder XRD patterns of microporous α-Mg$_3$(H/DCOO)$_6$ samples.

Table 4-A1: Crystallographic data of microporous α-Mg$_3$(H/DCOO)$_6$ samples.

Sample	activated		DMF		benzene		pyridine
	SC-XRD[a]	PXRD	SC-XRD[a]	PXRD	SC-XRD[a]	PXRD	PXRD
T (K)	100	293	100	293	100	293	293
a (Å)	11.324	11.375	11.4007	11.367	11.3762	11.423	11.468
b (Å)	9.847	9.911	9.9047	9.988	9.9831	10.093	10.032
c (Å)	14.623	14.618	14.5357	14.853	15.0358	15.148	14.884
α (°)	90	90	90	90	90	90	90
β (°)	91.150	91.34	91.317	91.51	91.203	91.11	90.91
γ (°)	90	90	90	90	90	90	90
V (Å^3)	1630.2	1648	1640.94	1686	1707.2	1746	1712

a: From the literature.[36]
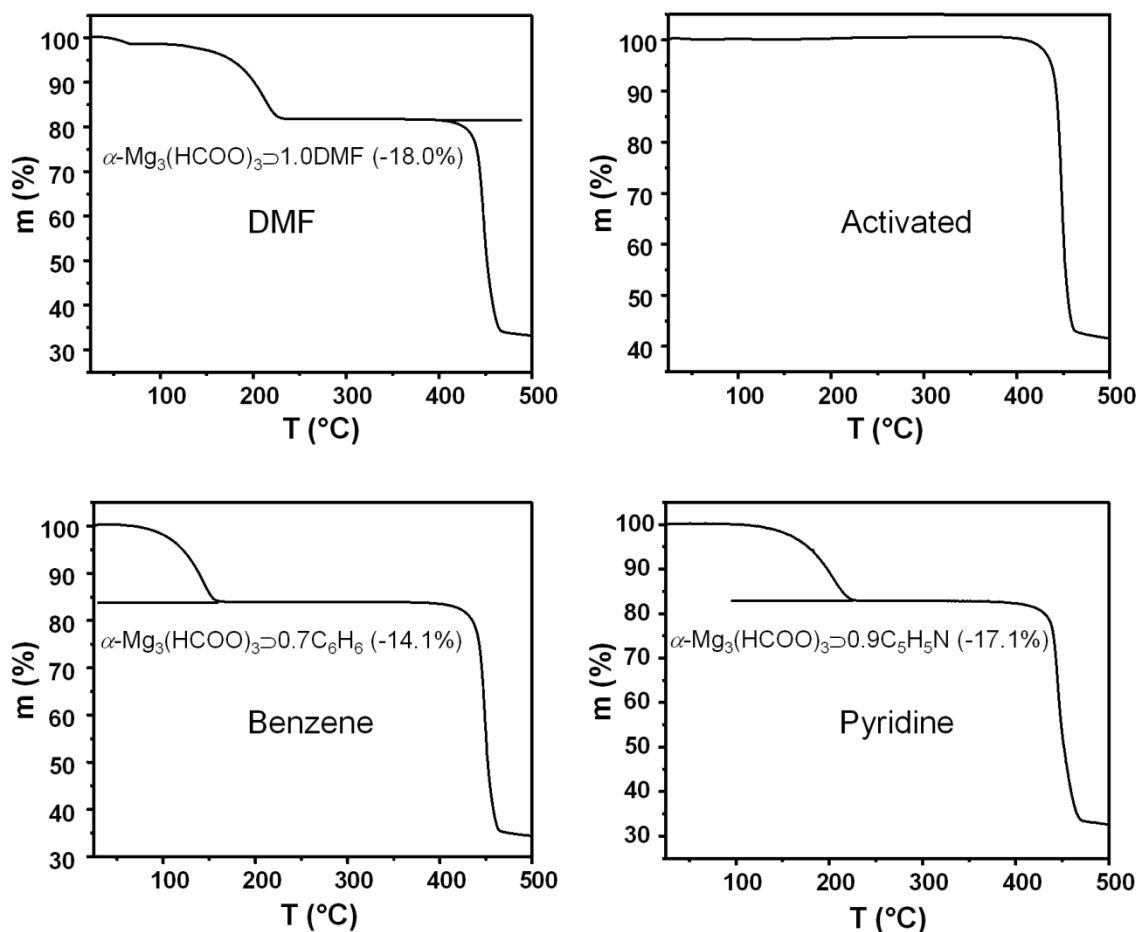
Figure 4-A2: TGA traces of microporous α-Mg$_3$(HCOO)$_6$ samples.

Section A2: SSNMR Characterizations

Table 4-A2: SSNMR experimental conditions.

Experiment	Number of scans	Pulse delay (s)
^{1}H static	32	2
^{1}H 18 kHz MAS	16	2
^{1}H 62.5 kHz MAS	8	120
^{1}H-^{1}H BABA DQ	16 × 128	2
^{1}H→^{13}C 18 kHz CPMAS	256	3
^{1}H→^{13}C FSLG-HETCOR	256 × 64	3
^{13}C PHORMAT	256 × 96	2
^{2}H static	3600	2
^{25}Mg 5 kHz MAS	2024	1
^{25}Mg SPAM-3QMAS	3200 × 48	1

Section A3: H–C Bond Lengths Before and After H-Optimization

Table 4-A3: H–C bond lengths before and after H-optimization.

Phase	Bond	Bond length (Å)	
		Before H-optimization	After H-optimization
activated	H1–C1	0.930	1.111
	H2–C2	0.930	1.109
	H3–C3	0.930	1.104
	H4–C4	0.930	1.104
	H5–C5	0.930	1.106
	H6–C6	0.930	1.114
DMF	H1–C1	0.930	1.109
	H2–C2	0.930	1.106
	H3–C3	0.930	1.106
	H4–C4	0.930	1.106
	H5–C5	0.930	1.107
	H6–C6	0.930	1.107
benzene	H1–C1	0.930	1.108
	H2–C2	0.930	1.108
	H3–C3	0.930	1.105
	H4–C4	0.930	1.108
	H5–C5	0.930	1.104
	H6–C6	0.930	1.110

Section A4: The Shortest Distances between Two Protons

The shortest internuclear distances between two protons were measured on the H-optimized structures.

Table 4-A4: The shortest distances between two protons.

Activated Phase

H site	Shortest distance between two protons (Å)					
	−H1	−H2	−H3	−H4	−H5	−H6
H1	6.712	5.609	3.598	3.515	3.931	3.354
H2	5.609	2.742	5.104	3.581	3.711	3.445
H3	3.598	5.104	4.035	4.621	3.830	3.701
H4	3.515	3.581	4.621	6.637	3.150	4.278
H5	3.931	3.711	3.830	3.150	5.869	3.768
H6	3.354	3.445	3.701	4.278	3.768	7.801

DMF Phase

H site	Shortest distance between two protons (Å)					
	−H1	−H2	−H3	−H4	−H5	−H6
H1	6.650	5.592	3.426	3.665	3.900	3.250
H2	5.592	2.763	5.325	3.646	3.707	3.530
H3	3.426	5.325	4.270	4.373	3.653	3.729
H4	3.665	3.646	4.373	6.595	3.050	3.949
H5	3.900	3.707	3.653	3.050	5.870	3.865
H6	3.250	3.530	3.729	3.949	3.865	7.070

Benzene Phase

H site	Shortest distance between two protons (Å)					
	−H1	−H2	−H3	−H4	−H5	−H6
H1	7.098	5.363	3.493	3.504	3.781	3.324
H2	5.363	3.341	5.540	3.711	3.547	3.422
H3	3.493	5.540	4.345	4.638	3.828	3.635
H4	3.504	3.711	4.638	6.694	3.499	3.927
H5	3.781	3.547	3.828	3.499	5.727	4.077
H6	3.324	3.422	3.635	3.927	4.077	7.095

Acetone Phase

H site	Shortest distance between two protons (Å)					
	−H1	−H2	−H3	−H4	−H5	−H6
H1	6.980	5.548	3.535	3.488	3.971	3.311
H2	5.548	2.805	5.217	3.589	3.567	3.542
H3	3.535	5.217	4.068	4.587	3.703	3.688
H4	3.488	3.589	4.587	6.611	3.125	4.124
H5	3.971	3.567	3.703	3.125	5.888	3.872
H6	3.311	3.542	3.688	4.124	3.872	7.196

Section A5: The Relationship between DQ Correlations and ^{1}H–^{1}H Distances

The distances were taken from Section A4.

Table 4-A5: Observed DQ correlations and the corresponding ^{1}H–^{1}H distances.

Activated Phase

τ_{exc} (μs)	DQ correlation	Distance (Å)
55.6	H1–H3	3.598
	H1–H4	3.515
	H1–H6	3.354
	H2–H2	2.742
	H2–H4	3.581
	H2–H5	3.711
	H2–H6	3.445
	H3–H5	3.830
	H3–H6	3.701
	H4–H5	3.150
	H5–H6	3.768
111.1	H1–H2	5.609
	H2–H3	5.104
	H3–H3	4.035
	H3–H4	4.621
	H4–H6	4.278
	H5–H5	5.869
Not observed	H1–H1	6.712
	H4–H4	6.637
	H6–H6	7.801
N.A.[a]	H1–H5	3.931

a: The DQ correlation of two overlapping peaks (along the SQ dimension) is not available.

DMF Phase

τ_{exc} (μs)	DQ correlation	Distance (Å)
55.6	H1–H3	3.426
	H1–H4	3.665
	H1–H6	3.250
	H2–H2	2.763
	H2–H4	3.646
	H3–H5	3.653
	H4–H5	3.050
111.1	H1–H5	3.900
	H2–H5	3.707
	H3–H6	3.729
	H4–H6	3.949
	H5–H6	3.865
166.7	H3–H3	4.270
	H3–H4	4.373
Not observed	H1–H1	6.650
	H1–H2	5.592
	H2–H3	5.325
	H4–H4	6.595
	H5–H5	5.870
	H6–H6	7.070
N.A.[a]	H2–H6	3.530

a: The DQ correlation of two overlapping peaks (along the SQ dimension) is not available.

Benzene Phase

τ_{exc} (μs)	DQ correlation	Distance (Å)
55.6	H1–H3	3.493
	H1–H4	3.504
	H1–H5	3.781
	H1–H6	3.324
	H2–H2	3.341
	H2–H4	3.711
	H2–H5	3.547
	H2–H6	3.422
	H3–H5	3.828
	H3–H6	3.635
	H4–H6	3.927
	H5–H6	4.077
111.1	H1–H2	5.363
	H3–H3	4.345
	H3–H4	4.638
166.7	H2–H3	5.540
Not observed	H1–H1	7.098
	H4–H4	6.694
	H5–H5	5.727
	H6–H6	7.095
N.A.[a]	H4–H5	3.499

a: The DQ correlation of two overlapping peaks (along the SQ dimension) is not available.

Chapter 5

5 Capturing the Guest Dynamics in Metal–Organic Frameworks CPO-27-M (M = Mg, Zn, Ni, Co) by ^{2}H Solid-State NMR

5.1 Introduction
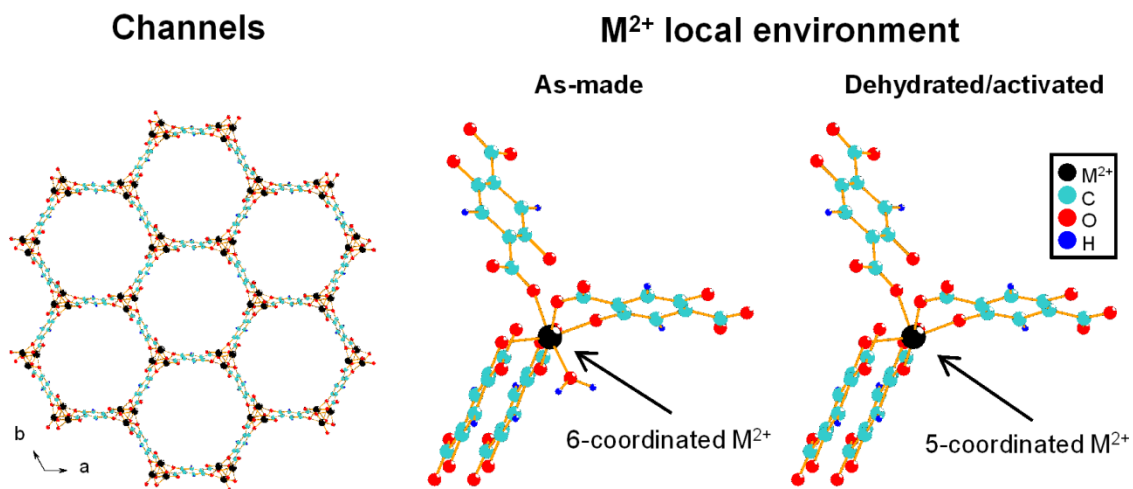
Figure 5-1: Left: The channels of dehydrated CPO-27-M. Right: The local environments of M^{2+} in as-made and dehydrated (activated) CPO-27-M.

The discovery of the extended family of metal–organic frameworks (MOFs) in recent years has opened up great opportunities for the development of gas separation and storage materials as well as sensors.[1] As novel inorganic–organic hybrid porous materials, MOFs often possess very large surface areas, giving rise to high gas storage capacity, and channels and cavities that allow selective inclusion of guest molecules according to their sizes and polarities. In particular, MOFs with coordinately unsaturated metal sites, such as CPO-27-M[2-5] series (M = Mg, Zn, Ni, Co, also named as M-MOF-74[6] or M/DOBDC[7,8], DOBDC = 2,5-dioxido-1,4-benzenedicarboxylate), have shown much improved guest adsorption and selectivity[8-22] compared to those of classical MOFs (that only consist of fully coordinated metal sites). As Figure 5-1 illustrates, the structure of as-made CPO-27-M[2] consists of one-dimensional honeycomb channels with a diameter of ~ 11 Å, formed by the interconnecting threefold helical chains of edge-sharing MO_6 units. In each MO_6,

five of the six oxygens belong to four DOBDC linkers, and the remaining oxygen is from a water molecule directly bound to the M^{2+} center. This water molecule can be removed upon dehydration. The coordination site vacated by activation is known to be the preferential adsorption site for various guest molecules,[15-23] and the strong interaction between them is considered to be responsible for good guest selectivity and large maximum uptake. In addition, the adsorption behaviors of CPO-27-M are found to be highly dependent on the metal centers,[8,11-15,20] emphasizing the fundamental importance of obtaining molecular-level knowledge on how the guest molecules interact with the exposed metal centers.

The discussion of the guest-metal interactions in CPO-27-M has been based on diffraction-based techniques,[15-19] IR and Raman spectroscopy,[19,21-23] thermodynamic data such as adsorption isotherms,[4,8,10-16,19-21] and theoretical modeling.[11,14,18,21,22,24-32] Due to the difficulty of obtaining suitable single crystals for X-ray diffraction, the framework structures of CPO-27-M samples were typically determined from more limited powder X-ray and neutron diffraction data.[2-5,15-19] It is even more challenging to obtain the molecular-level details about the guest molecules by diffraction-based techniques since the guest molecules are often disordered and/or undergoing rapid motions. IR and Raman spectroscopy can be utilized to probe the binding of guest molecules but the strong background signals from the MOF itself usually dominate the spectrum, making the analysis of weak adsorbate signals rather difficult. Thermodynamic data, as the macroscopic properties of interfaces, provide the information on the binding strengths but not the binding mechanisms. The results from theoretical modeling, on the other hand, have to be validated and refined by experimental observations. Solid-state NMR (SSNMR) spectroscopy is a method complementary to diffraction-based techniques because it is sensitive to local ordering and geometries. A previous study has demonstrated the power of solid-state ^{25}Mg NMR as a sensitive probe of adsorbing guest molecules on the Mg center in CPO-27-Mg.[33] The dehydration of CPO-27-Mg induces the local Mg structure change from a perfectly ordered to disordered environment, although long-range ordering of the framework remains. The disordering of local Mg environment persists if the sample is partially rehydrated or loaded with volatile organic compounds (VOCs). The local ordering can only be completely restored if enough water

is available.[33] Two recent reports[34,35] presented variable-temperature (VT) ^{13}C NMR spectra, relaxation measurements, and computer simulation of CO_2 adsorbed inside CPO-27-Mg. One of the most striking observations is that they found the CO_2 dynamics above 150 K should be interpreted as the rapid hopping between neighboring Mg centers[35] rather than the localized uniaxial rotation.[34]

Solid-state ^2H NMR has been extensively used to follow the guest dynamics occurring inside of the porous materials.[36-43] When the motion of a ^2H-enriched molecule is constrained, *e.g.*, by guest-metal interactions in CPO-27-M, the ^2H static NMR pattern is broad and should not display the narrow line expected for isotropic motion (random tumbling). The observed ^2H line shape can be simulated using a proper dynamic model, considering the possible interactions between the guest molecule and the host framework as well as their geometries. The proposed dynamic model can be further confirmed by acquiring ^2H NMR spectra at various temperatures, since the ^2H line shape is very sensitive to the motion with the rate constant between 10^3 and 10^7 s^{-1} (*i.e.*, the intermediate regime).[44,45] Fitting the experimental ^2H line shape in the intermediate regime allows one to obtain the activation energy of the motion. In the current work, ^2H static NMR experiments over a broad temperature range from 133 to 293 K of four guest molecules, D_2O, CD_3CN, acetone-d_6, and C_6D_6, adsorbed in CPO-27-Mg and CPO-27-Zn were performed. D_2O was studied because trace amount of water can significantly influence the adsorption performance for other guest molecules.[46,47] CH_3CN, acetone and benzene are common VOCs and consist of several prototypical functional groups that can potentially interact with the exposed metal sites: cyano, carbonyl, and π-electrons. For CPO-27-Ni and CPO-27-Co, only the preliminary results of C_6D_6-loaded samples were shown, due to complications resulting from the presence of paramagnetic Ni^{2+} and Co^{2+} ions.

5.2   Experimental Section

5.2.1   Sample Preparation

As-made CPO-27-M (M = Mg, Zn, Co and Ni) samples were prepared following the procedures modified from those reported in literature.[2-5]

CPO-27-Mg ([Mg$_2$(C$_8$H$_2$O$_6$)(H$_2$O)$_2$]·8H$_2$O): 0.75 mmol 2,5-dioxido-1,4-benzenedicarboxylic acid (H$_4$DOBDC, Sigma-Aldrich, 98%) was dissolved in 10 mL tetrahydrofuran (THF, reagent grade, Caledon) in a Teflon-lined inlet of an autoclave (23 mL). An aqueous sodium hydroxide solution (3 mL, 1 M) was added to this solution. 1.5 mmol magnesium nitrate hexahydrate (Mg(NO$_3$)$_2$·6H$_2$O, Sigma-Aldrich, 99%) was first dissolved in 5 mL deionized water and then added to the Teflon inlet while stirring, upon which a yellow precipitate formed. The autoclave was sealed and the mixture was reacting at 110 °C for 3 d. The resulting light yellow powder was filtered, repeatedly washed with THF, and dried at room temperature (yield: 75% based on Mg).

CPO-27-Zn ([Zn$_2$(C$_8$H$_2$O$_6$)(H$_2$O)$_2$]·8H$_2$O): 0.75 mmol H$_4$DOBDC was dissolved in 10 mL THF in a Teflon-lined inlet of an autoclave (23 mL). An aqueous sodium hydroxide solution (3 mL, 1 M) was added to this solution while stirring. 1.65 mmol zinc nitrate hexahydrate (Zn(NO$_3$)$_2$·6H$_2$O, Sigma-Aldrich, 98%) was dissolved in 5 mL deionized water and added to the Teflon inlet. After 1 hour vigorous stirring, the autoclave was sealed and the mixture was reacting at 110 °C for 3 d. The resulting yellow-green powder was filtered, repeatedly washed with THF, and dried at room temperature (yield: 80% based on Zn).

CPO-27-Co ([Co$_2$(C$_8$H$_2$O$_6$)(H$_2$O)$_2$]·8H$_2$O): 0.75 mmol H$_4$DOBDC was dissolved in 10 mL THF in a Teflon-lined inlet of an autoclave (23 mL). 1.5 mmol cobalt(II) acetate tetrahydrate (Co(CH$_3$COO)$_2$·4H$_2$O, Sigma-Aldrich, 98%) was dissolved in 5 mL deionized water and added to the Teflon inlet. After 1 hour stirring, the autoclave was sealed and the mixture was reacting at 110 °C for 3 d. The resulting red-orange powder was filtered, repeatedly washed with THF, and dried at room temperature (yield: 75% based on Co).

CPO-27-Ni ([Ni$_2$(C$_8$H$_2$O$_6$)(H$_2$O)$_2$]·8H$_2$O): 0.75 mmol H$_4$DOBDC was dissolved in 10 mL THF in a Teflon-lined inlet of an autoclave (23 mL). 1.5 mmol nickel(II) acetate tetrahydrate (Ni(CH$_3$COO)$_2$·4H$_2$O, Sigma-Aldrich, 98%) was dissolved in 5 mL deionized water and added to the Teflon inlet. After 1 hour stirring, the autoclave was sealed and the mixture was reacting at 110 °C for 3 d. The resulting ochre powder was

filtered, repeatedly washed with THF, and dried at room temperature (yield: 73% based on Ni).

In order to prepare dehydrated (activated) samples, as-made CPO-27-Mg was pre-exchanged with fresh methanol several times. After that, ~0.1 g methanol-exchanged sample was added into a glass tube, inserted into a Schlenk tube, and then activated under dynamic vacuum at 523 K for 6 h. The mass of dehydrated CPO-27-Mg was accurately determined and precisely measured volume of deuterated guest molecule was injected into the glass tube containing the dehydrated samples. The tube was flame sealed and placed in an oven at 383 K overnight, allowing the guest molecules to disperse uniformly throughout the sample. Prior to ^{2}H SSNMR experiments, guest-loaded samples were tightly packed into 5 mm o.d. glass tubes in a glove box and sealed with multi-layers of Teflon tape. The packed samples were under N_2 protection during all NMR experiments. The ^{2}H NMR patterns did not show any significant change after storing the packed samples in a dessicator for six months. Guest-loaded CPO-27-Zn, Co, and Ni samples were obtained in a similar way but using a lower activation temperature (423 K) and without methanol pre-exchange. Theoretical loading amount was calculated according to the ratio of guest molecules to metal centers.

The identity and crystallinity of CPO-27-M samples were examined by powder X-ray diffraction. PXRD patterns (Figure 5-A1, appendix) were recorded on a Rigaku diffractometer using Co Kα radiation (λ = 1.7902 Å). Samples were scanned at 5° $\leqslant$ 2θ $\leqslant$ 45° at a scan rate of 10°/min with a step-size of 0.02°.

The guest contents of CPO-27-M samples were checked by thermogravimetric analysis (TGA). The samples were heated under N_2 atmosphere on a Mettler Toledo TGA/DTA851e instrument from 25 to 500 °C at a constant heating rate of 10 °C/min.

5.2.2   NMR Characterization

The ^{2}H static SSNMR spectra of guest-loaded CPO-27-M samples were measured on a Varian Infinity Plus 400 WB spectrometer at 61.3 MHz at a magnetic field of 9.4 T using a horizontal 5 mm static probe and exorcycled quadrupole echo sequence.[48] The

90° pulse of ^{2}H was 3.6 μs and the interpulse delay τ was set to be 30 μs. The chemical shift of ^{2}H was referenced to D_2O at 4.8 ppm, relative to neat $(CD_3)_4Si$. The pulse delay of ^{2}H was between 0.5 and 2 s and the number of scans was between 2048 and 24576.

To capture all dynamic features of the system, variable-temperature (VT) ^{2}H SSNMR experiments were performed from 133 to 293 K. The sample temperature was controlled by a Varian variable-temperature unit. The samples were kept at least 10 min at a given temperature to ensure that thermal equilibrium was reached before acquiring the NMR signal.

The line-broadening of ^{2}H ($I = 1$) SSNMR spectroscopy is dominated by the first-order quadrupolar interaction between the nuclear quadrupole moment and the electric field gradient (EFG), denoted by the EFG tensor with three nonzero principle components V_{XX}, V_{YY}, V_{ZZ}.[49] The three components are ordered such that $|V_{XX}| \leq |V_{YY}| \leq |V_{ZZ}|$, and they satisfy $V_{XX} + V_{YY} + V_{ZZ} = 0$. Two parameters are typically reported,

$$C_Q = (eQV_{ZZ})/h \qquad \textbf{(Equation 5-1)}$$

$$\eta_Q = (V_{XX} - V_{YY})/V_{ZZ} \qquad \textbf{(Equation 5-2)}$$

where C_Q is the nuclear quadrupolar coupling constant in Hz and η_Q is the asymmetry parameter. For static C–D or O–D bonds, the largest component of the EFG tensor, V_{ZZ}, is typically along the bond direction. The other two components are equal and perpendicular to the bonds (*i.e.*, axial symmetric, $\eta_Q = 0$). Any motion that causes a reorientation of the EFG tensor can result in changes in the ^{2}H static line shape. The ^{2}H NMR spectrum looks identical to that under the static condition if the reorientation is slower than 10^3 s^{-1} (the slow-limit regime). When the rate constant increases, the line shape evolves gradually between 10^3 and 10^7 s^{-1} (the intermediate regime) until at about 10^7 s^{-1} or faster (the fast-limit regime) the line shape can be described by an averaged effective tensor. In this work, the motion is described in terms of sets of successive rotations.[50] The first set, $\Omega_j^{(1)} = (\alpha_j^{(1)}, \beta_j^{(1)}, \gamma_j^{(1)})$, rotates the principle axis system of the EFG tensor into coincidence with an intermediate jump frame, where (α, β, γ) is Euler angles in Rose convention.[51] N_1 such rotations can be defined, $j = 1, 2, \ldots, N_1$. The

second set, $\Omega_k^{(2)} = (\alpha_k^{(2)}, \beta_k^{(2)}, \gamma_k^{(2)})$, can be then specified to rotate the intermediate jump axes into any of N_2 different orientations with respect to a crystal-fixed reference frame.

^{2}H NMR patterns were simulated using EXPRESS package[50] in MATLAB and QuadFit software.[52] The former was used to obtain the motionally averaged ^{2}H EFG parameters, including C_Q and η_Q, as well as the ^{2}H line shape in the intermediate regime; whereas the latter was used to simulate the ^{2}H line shape when different types of motions coexisted. The η_Q values of static C–D and O–D bonds were assumed to be zero.

5.3 Results and Discussion

5.3.1 Dynamic Models
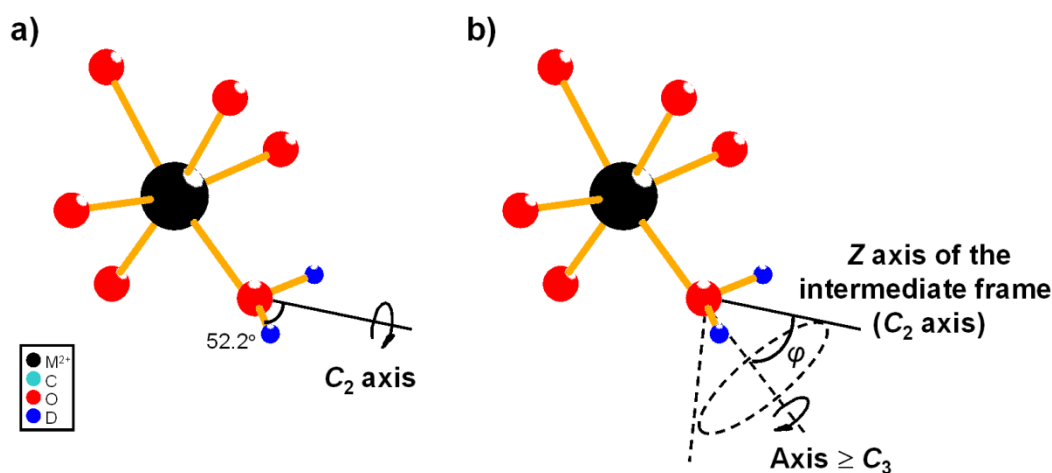
Figure 5-2: Schematic illustration of guest dynamics using D_2O adsorbed on CPO-27-M as an example: (a) π flip-flop of D_2O about its C_2 axis (*i.e.*, internal motion) followed by (b) uniaxial rotation of the whole D_2O molecule (*i.e.*, external motion). φ is the angle between the Z axis of the intermediate frame (C_2 axis of D_2O) and the rotation axis.

Thermal motions of guest molecules can be classified into two groups: motions that occur inside of a single molecule ("internal motions"), and motions of the molecule as a whole ("external motions"). As shown in Figure 5-2, π (180°) flip-flop of D_2O about its C_2 axis is a good example of internal motions while the uniaxial rotation of the whole D_2O molecule is external motion. The two types of motions often occur simultaneously

but internal motions generally have much smaller activation energy and therefore persist even if all external motions have been quenched at low temperature. Internal motions are determined by the geometry of guest molecules. In this work, possible internal motions include π flip-flop of D_2O about its C_2 axis (hereafter referred to as "π flip-flop"), rotation of $-CD_3$ group of CD_3CN or acetone-d_6 about its C_3 axis (hereafter referred to as "C_3"), and in-plane rotation of C_6D_6 about its C_6 axis (hereafter referred to as "C_6"). For external motions, two dynamic models are proposed: the above-mentioned uniaxial rotation and the non-localized multiple-site hopping.

5.3.1.1　Uniaxial Rotation

It has been demonstrated in previous studies that the exposed metal centers of CPO-27-M are the preferential binding sites.[15-23] The strengths of binding, characterized by the heat of adsorption, are particularly large (> 40 kJ·mol^{-1}) for some guest molecules. Strong chemical bonding between guest molecules and metal centers is suggested in such cases. Therefore, an intuitive idea of external motions is that the guest molecule can be strongly bound to a M^{2+} ion and undergoing rapid uniaxial rotation as a whole about a fixed rotational angle φ (Figure 5-2b).

5.3.1.2　Multiple-Site Hopping

In the multiple-site hopping model, the guest molecule is not bound to a specific M^{2+} ion and hence is allowed to hop rapidly between different metal ions of CPO-27-M. During such non-localized hopping, the angle between the Z axis of the intermediate frame and the crystallographic c axis, θ, is constant. As Figure 5-3a illustrates, there are six M^{2+} chains within a single channel and the M^{2+} ions in each chain are related to each other by the translation along the c axis. The hopping between different metal centers can be divided into two types: exchange between different M^{2+} chains, and translation along the M^{2+} chains. Only the first type causes the change of ^2H line shape since the second one has no effect on the orientation of the EFG tensors. Therefore, it seems that the hopping of guest molecules in three dimensions is equivalent to the hopping between six M^{2+} ions in the single a,b plane. Due to shorter diffusion lengths, the hopping between two neighboring M^{2+} ions is much more favorable. As a result, there are only five

possible hopping motions: two-site, three-site, four-site, five-site, and six-site hopping. The six-site hopping can be conveniently visualized as a circular rotation of the whole molecule on a cone with the cone angle θ; whereas the other four motions occur on an arc with the angle of 60°, 120°, 180° and 240°, respectively (Figure 5-3b). The five hopping motions have different effects on the ^2H line shapes in the fast-limit regime (Figure 5-3c), among which only the six-site hopping results in a typical Pake doublet.
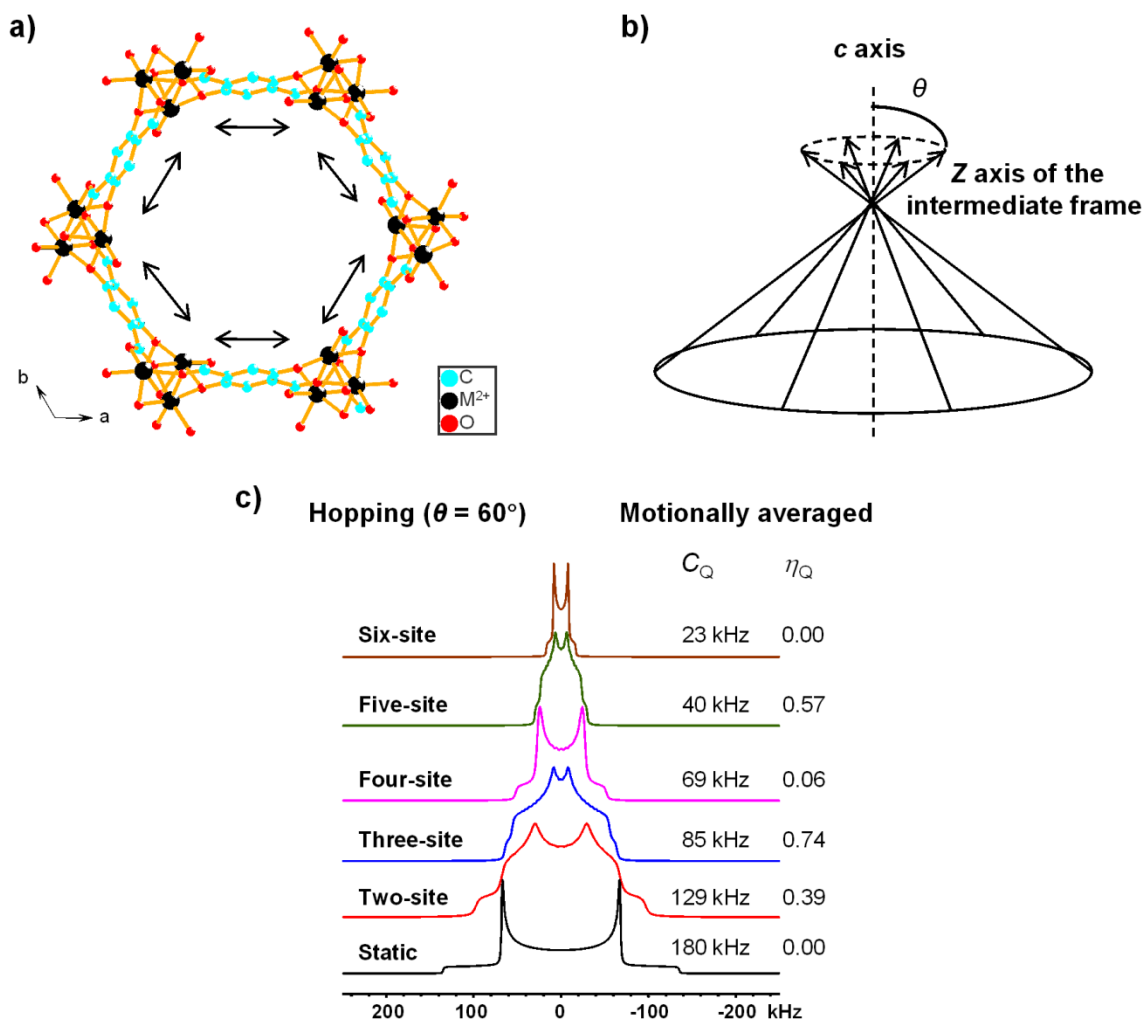
Figure 5-3: (a) A brief schematic illustration of the non-localized multiple-site hopping on the *a,b* plane. (b) In the language of NMR, the hopping of a guest molecule between different M^{2+} ions in the *a,b* plane is equivalent to motions occurring on the base of a cone with the cone angle of θ. (c) Analytical simulations (performed using EXPRESS package) of ^2H static powder patterns of multiple-site hopping in the fast-limit regime.

5.3.2   D$_2$O in CPO-27-M

As an ever-present component of many gas mixtures, water plays an important role in the guest adsorption. There is a significant loss of the adsorption capacity when activated CPO-27-M is exposed to the humid atmosphere (namely "water effect").[46,47] The strong water–metal interaction has been suggested to be responsible for such "water effect". However, it is challenging to characterize this interaction, in particular at low water coverage, since water molecules are usually disordered and/or undergoing rapid motions. ^{2}H SSNMR spectroscopy is therefore very suitable to provide the molecular-level information about this "water effect".
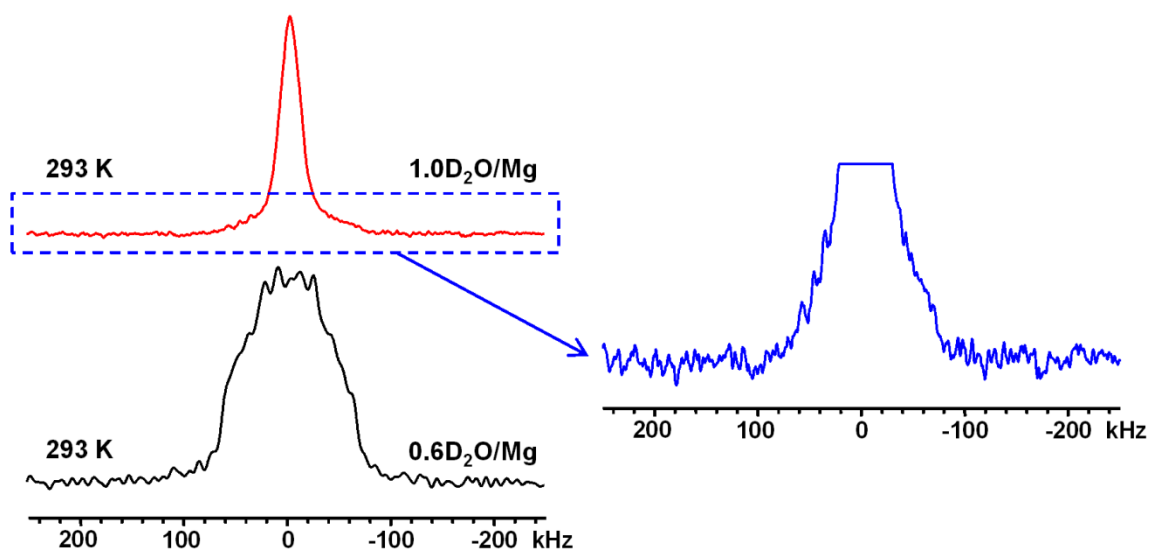
Figure 5-4: Experimental ^{2}H static spectra of D$_2$O in CPO-27-Mg at 293 K as a function of loading.

The ^{2}H static spectra of D$_2$O in CPO-27-Mg at 293 K as a function of loading are shown in Figure 5-4. At a low loading of 0.6D$_2$O/Mg, the ^{2}H spectrum exhibits a single, broad pattern with a nonzero η_Q ~ 0.8, which is a line shape typical of fast π flip-flop about a C_2 symmetry axis. According to the model shown in Figure 5-2a, where all D$_2$O molecules are bound to Mg^{2+} ions and flipping rapidly about the sector of the D–O–D angle (104.5°, gas phase[53]), the experimental line shape can be simulated using the C_Q of 195 kHz for static O–D bond, agreeing well with those observed in various hydrates of inorganic compounds.[54] The above-mentioned "water effect" is therefore due to the fact

that some Mg^{2+} ions have been covered by strongly bound water molecules and therefore are not accessible any more for other guest molecules. When the loading is increased to $1.0D_2O$ per Mg^{2+}, however, there are at least two components in the ^2H spectrum. The broad feature has a line width comparable to the pattern of $0.6D_2O/Mg$, indicating some D_2O are still strongly bound. The center component, exhibiting a Lorentzian line shape with a full-width at half-height (FWHH) of ~ 24 kHz, is likely due to the disordered D_2O that only weakly interact with Mg^{2+} ions. The motions of such D_2O are less constrained, giving rise to a sharp and featureless profile. The direct observation of two types of D_2O molecules confirms a previous ^{25}Mg SSNMR study[33] that the water molecules seem not to be homogenously distributed within the channels, even though in principle every Mg^{2+} should adsorb one water molecule. The water initially coordinated to Mg^{2+} ions (*i.e.*, the broad component) interact with the water molecules subsequently entering the channels (*i.e.*, the narrow component), probably via hydrogen bonding, leaving a significant amount of five-coordinated Mg unaffected, and resulting in an obvious loss of observed ^{25}Mg intensity (*i.e.*, typically six-coordinated Mg) compared to the as-made sample.

In order to obtain more details on the nature of motion, variable temperature (VT) ^2H SSNMR experiments were performed on the $0.6D_2O/Mg$ sample. The acquired ^2H SSNMR spectra are shown in Figure 5-5. The ^2H line shape starts to evolve below 193 K and two horns with a splitting of ~ 150 kHz emerge at 173 K. The two horns become more evident at 153 K. The observed ^2H line shapes of the $0.6D_2O/Mg$ sample at 173 K and 153 K are typical of π flip-flop of D_2O in the intermediate regime.
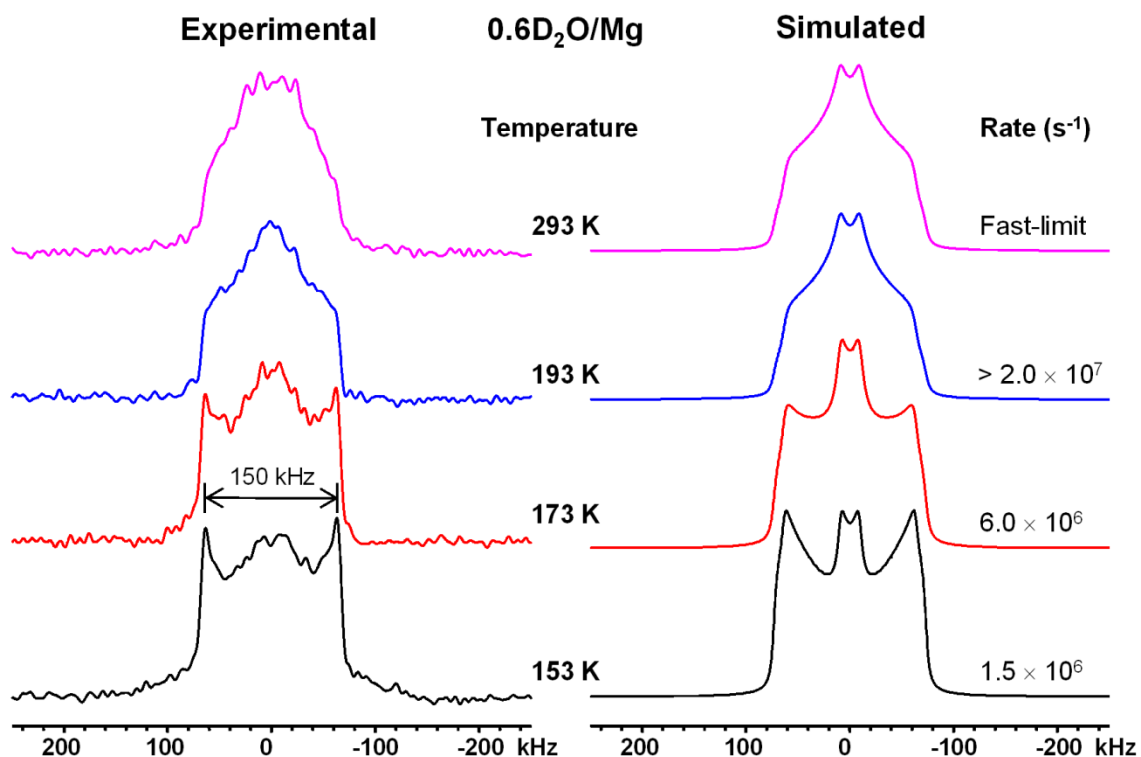
Figure 5-5: Experimental and simulated ^{2}H static spectra of the 0.6D$_2$O/Mg sample as a function of temperature. The dynamic model for simulation: π flip-flop of D$_2$O about its C_2 axis.

As Figure 5-6a illustrates, the ^{2}H static spectrum of the 0.6D$_2$O/Zn sample at 293 K looks distinct from that of the 0.6D$_2$O/Mg sample but similar to that of the 1.0D$_2$O/Mg sample, consistent with the fact that the "water effect" is dependent on the nature of metal ions.[46] The ^{2}H spectrum of 0.6D$_2$O/Zn sample also consists of a broad feature, which is identified as π flip-flop of the bound D$_2$O, and a sharp Lorentzian-type peak with a FWHH of ~ 12 kHz, which is attributed to the D$_2$O that are not strongly bound to Zn^{2+}. The center peak of the 0.6D$_2$O/Zn sample is even sharper than that of the 1.0D$_2$O/Mg sample, implying much higher mobility of D$_2$O in CPO-27-Zn. Moreover, the existence of large amounts of unbound D$_2$O, at a low loading of 0.6D$_2$O/Zn, also indicates that the five-coordinated Zn^{2+} of activated CPO-27-Zn has a lower affinity to H$_2$O than the five-coordinated Mg^{2+} of activated CPO-27-Mg, agreeing with the reported thermodynamic data and theoretical modeling results: From TGA results, it was determined that water in CPO-27-Mg were evacuated at a higher temperature than those in CPO-27-Zn.[2,3] In

addition, the calculated hydration energy of five-coordinated Mg^{2+} to six-coordinated Mg^{2+} (-102.6 kJ·mol^{-1}) is higher than the energy for Zn^{2+} (-91.2 kJ·mol^{-1}).[55] The ^2H spectrum of the 2.0D$_2$O/Zn sample at 293 K is unsurprisingly overwhelmed by a very sharp Lorentzian pattern with a FWHH of only ~ 3 kHz, illustrating that most D$_2$O molecules are undergoing rapid isotropic tumbling within the channels.
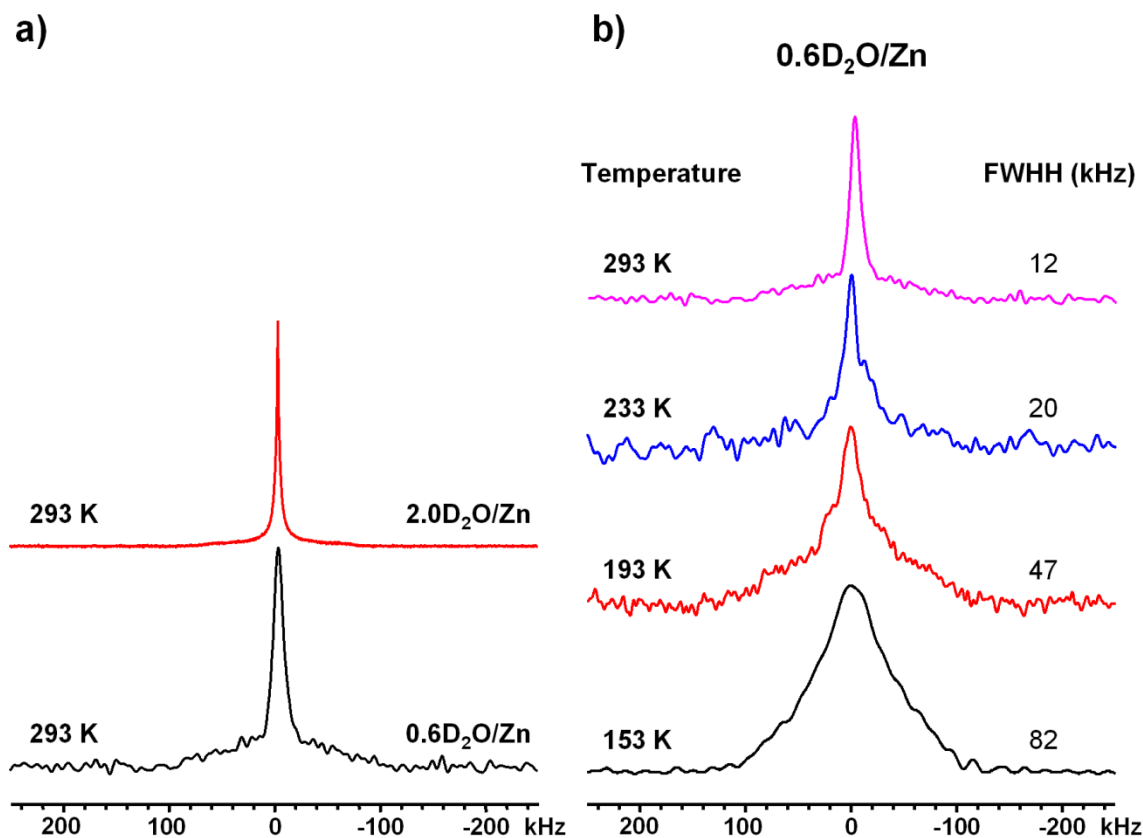
Figure 5-6: Experimental ^2H static spectra of (a) D$_2$O in CPO-27-Zn at 293 K as a function of loading, and (b) the 0.6D$_2$O/Zn sample as a function of temperature.

The VT ^2H static spectra of the 0.6D$_2$O/Zn sample are shown in Figure 5-6b. The ^2H spectra always consist of a broad component and a narrow center component. When the temperature drops, it seems that the unbound D$_2$O molecules (*i.e.*, the narrow component) are gradually converted to the bound D$_2$O molecules (*i.e.*, the broad component), but never completed even at 153 K, which is the lowest temperature measured, implying a weaker interaction between D$_2$O and exposed Zn^{2+} than Mg^{2+}.

5.3.3   CD$_3$CN in CPO-27-M
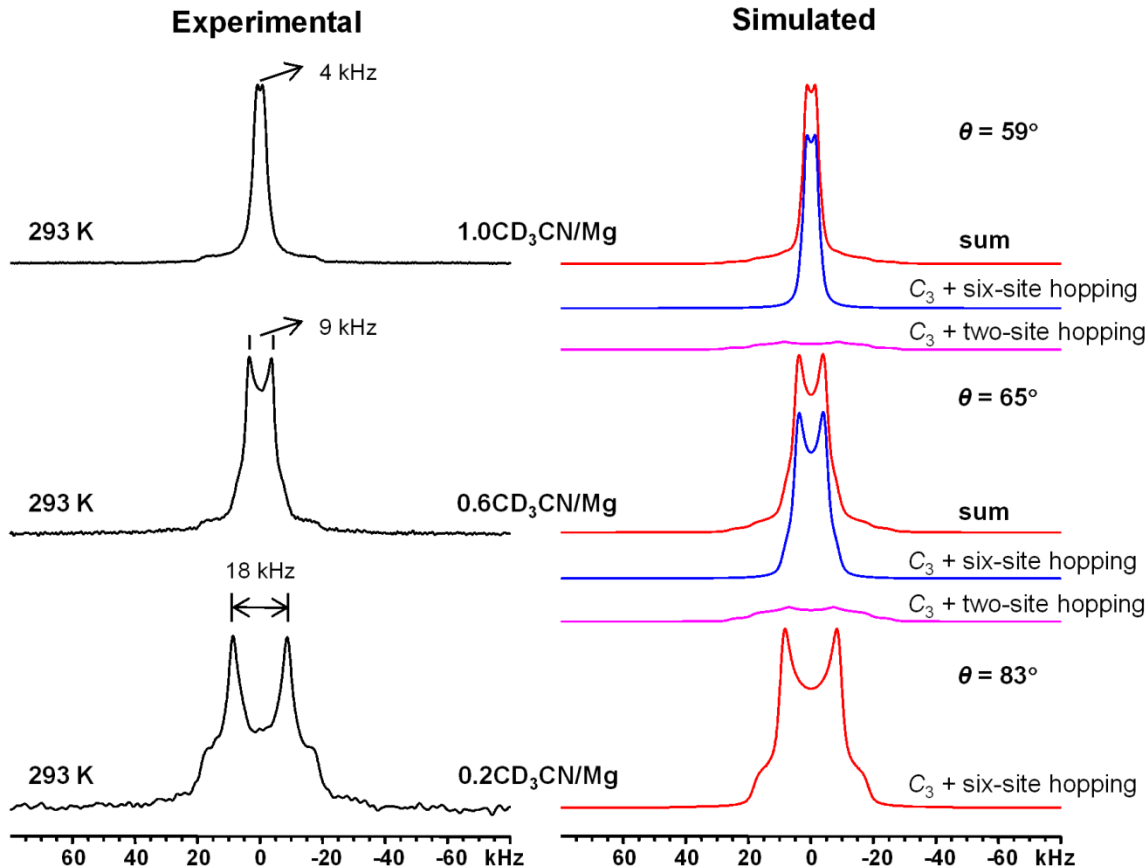
Figure 5-7: Experimental and simulated ^{2}H static spectra of CD$_3$CN in CPO-27-Mg at 293 K as a function of loading. The dynamic models for simulation: rotation of methyl C–D about its C_3 axis followed by non-localized six-site (or two-site) hopping motions.

Many toxic volatile organic compounds (VOCs) such as pesticides contain cyano groups. CH$_3$CN serves as an interesting model of these VOCs. Furthermore, CH$_3$CN is a Lewis base which can interact with exposed metal centers (Lewis acids) of CPO-27-M. The ^{2}H static spectra of CD$_3$CN in CPO-27-Mg at 293 K as a function of loading are shown in Figure 5-7. At a low loading of 0.2CD$_3$CN/Mg, the ^{2}H spectrum exhibits a typical Pake doublet with the horn separation of ~ 18 kHz, corresponding to a C_Q of 24 kHz. This C_Q value is significantly smaller than the common C_Q values for the internal motion of –CD$_3$ group in CD$_3$CN (~ 50 kHz[54,56,57]), when it is rotating rapidly about its fixed C_3 axis. Therefore, there must be additional reorientation of the whole CD$_3$CN molecule (external motion) occurring simultaneously, further narrowing the spectrum.

When more CD_3CN molecules are adsorbed, the ^2H spectra become narrower and are the superimposition of two components: a broad component with a non-zero η_Q, and a center narrow Pake doublet. It is worth mentioning that the horn separation of the Pake doublet decreases when the loading increases, from ~ 18 kHz in the $0.2CD_3CN/Mg$ sample and ~ 9 kHz in the $0.6CD_3CN/Mg$ sample, to ~ 4 kHz in the $1.0CD_3CN/Mg$ sample, the origin of which is discussed as follow.
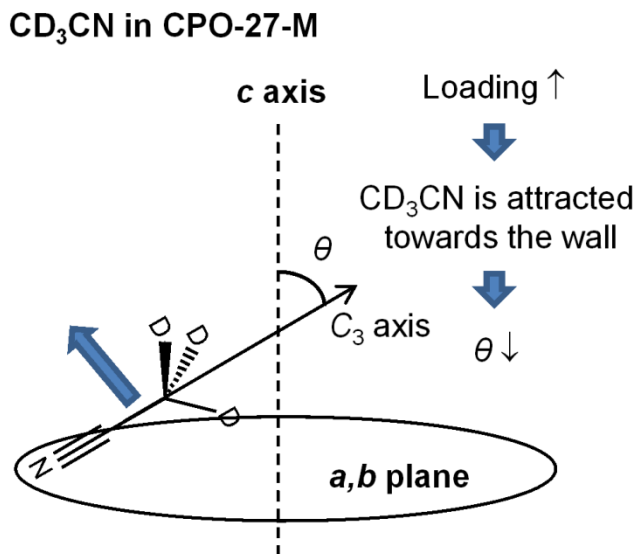
Figure 5-8: Schematic illustration of the local geometry of CD_3CN adsorbed in CPO-27-M as a function of loading.

Both uniaxial rotation and multiple-site hopping models can be used to simulate the external motion of CD_3CN in CPO-27-Mg. However, to exhibit the Pake doublet, a motion with a C_3 or higher axial symmetry is required. As previous literatures described, the uniaxial rotation of guest molecules is virtually unfavorable for CPO-27-M since the chemical environment around M^{2+} is not strictly axially symmetric and the "cone" for uniaxial rotation is not of constant free energy.[32,35] The non-localized six-site hopping model has to be used, in which the whole CD_3CN molecules are hopping between six sites in the a,b plane (Figure 5-3). At higher loading, the channels of CPO-27-Mg become more crowded. As a result, the enhanced repulsive forces between neighboring CD_3CN molecules cause them to stay apart along the channel from each other, giving rise to a smaller angle (θ) between the C_3 axis of $-CD_3$ group (the Z axis of the intermediate

frame) and the c axis (Figure 5-8), agreeing well with the above-mentioned experimental observations. Another reason to use the multiple-site hopping model is that the broad component can be fitted reasonably well with a two-site hopping model using the same θ.
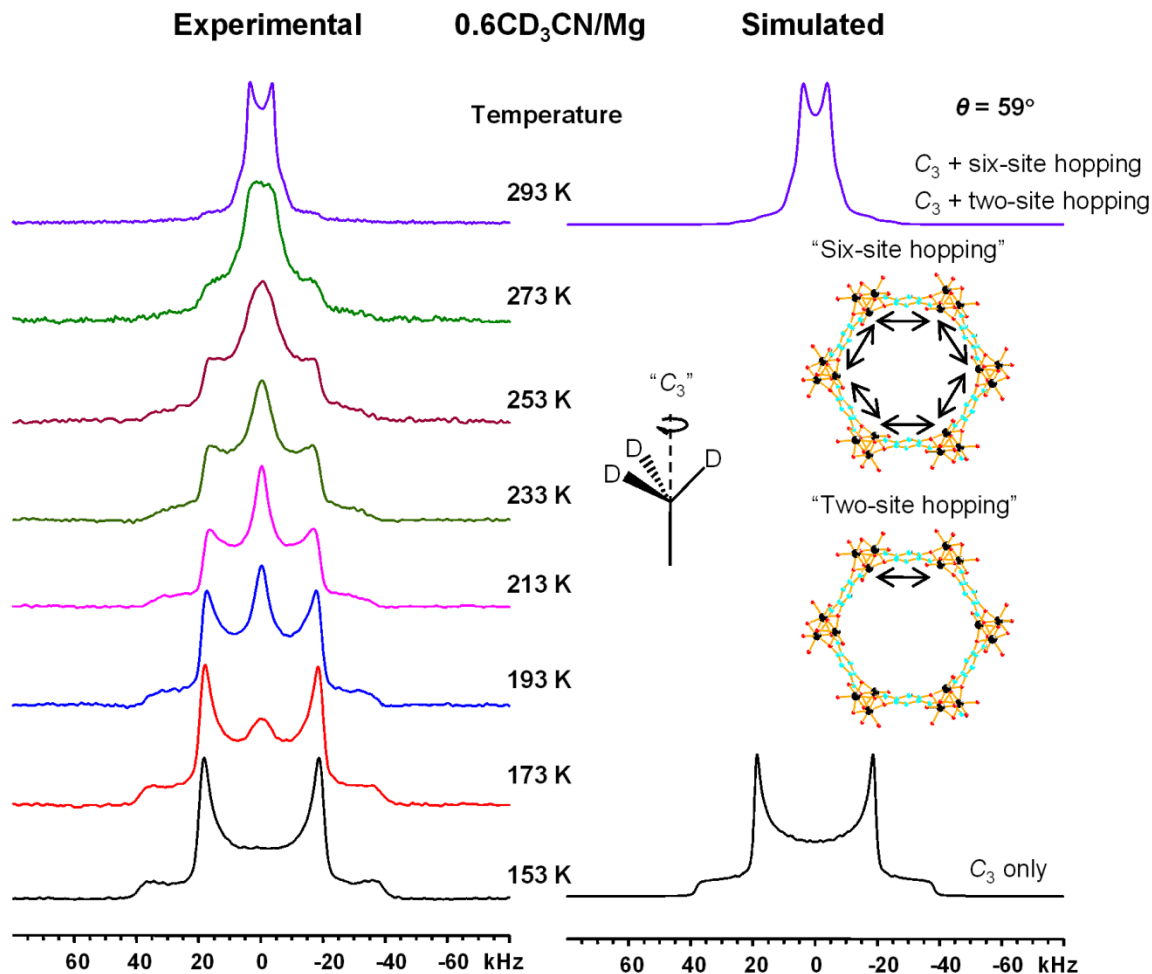
Figure 5-9: Experimental ^{2}H static spectra of the 0.6CD$_3$CN/Mg sample as a function of temperature. The dynamic models for simulation: rotation of methyl C–^{2}H about its C_3 axis followed by non-localized six-site (or two-site) hopping motions.

In order to determine the accurate value of θ, the ^{2}H EFG parameters of static C–D bond in methyl groups have to be established. ^{2}H static spectra of the 0.6CD$_3$CN/Mg sample over a broad temperature range, from 293 to 153K, are shown in Figure 5-9. The center component gradually loses its Pake doublet-like feature at lower temperatures and eventually evolves into a Lorentzian peak (with approximately the same FWHH as the

center component at 293 K). At the same time, the broad component becomes more and more prominent and two new edges with the separation of ~ 78 kHz start to appear at 253 K, which are assigned to the CD$_3$CN that are not involved in the non-localized hopping (*i.e.*, they are strongly bound to Mg^{2+} ions). With sufficient cooling, the center Lorentzian component disappears and only the broad component is present at 153 K, which is a Pake doublet with a C_Q of 51 kHz. This C_Q value is typical of the internal motion of –CD$_3$, indicating that all non-localized hopping motions have been quenched. With a low activation energy, the internal motion of methyl group is still in the fast-limit regime even at the lowest temperature measured (153 K). The EFG parameters of the internal motion of –CD$_3$ group obtained from this experiment are used to simulate the ^{2}H spectra of other CPO-27-M samples loaded with CD$_3$CN and acetone-d$_6$. The accurate θ values of CD$_3$CN/Mg samples as a function of loading are therefore shown in Figure 5-7. It should be mentioned that the observed trend of change of ^{2}H spectra is inconsistent with what is expected for the six-site hopping (or any of the other multiple-site hopping models) on the single *a,b* plane (Figure 5-A2–A4). A possible reason for this is given as follow according to the crystal symmetry of CPO-27-M.
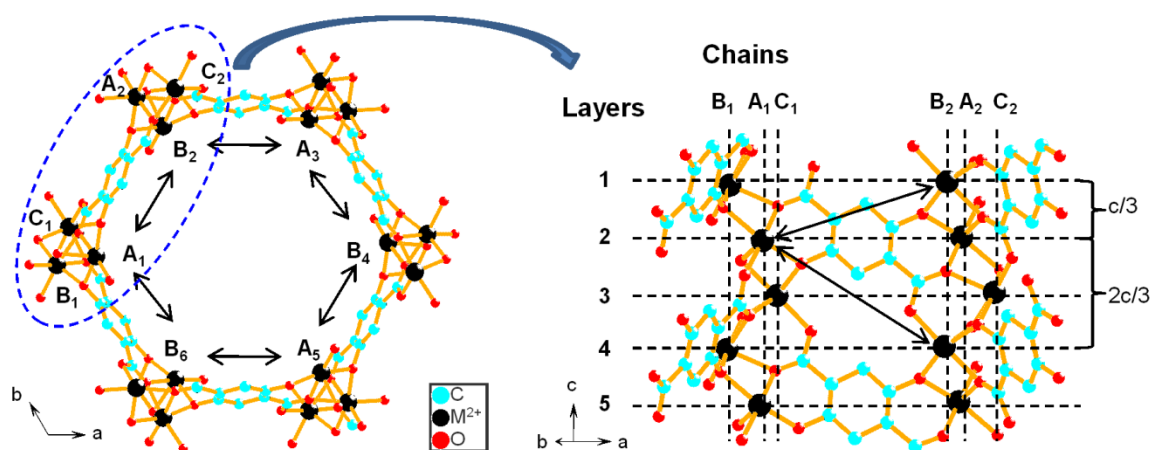
Figure 5-10: A detailed schematic illustration of the non-localized multiple-site hopping viewed along the *c* axis (left) and perpendicular to the *c* axis (right).

The isostructural CPO-27-M MOFs crystallize in the trigonal space group *R*-3 (No. 148).[2-5] As mentioned earlier, the one-dimensional channels of CPO-27-M are formed by the interconnection of edge-sharing MO$_6$ octahedra by DOBDC linkers. Figure

5-10 illustrates that the edge-sharing MO_6 octahedra consist of three types of M^{2+} chains along the c axis, labeled as chain A, chain B, and chain C, respectively, exposing to three different channels. The M^{2+} ions in the same chain are related to each other by a translation along the c axis while the M^{2+} ions in different chains are related to each other by a 3_1 screw axis. However, only two types of M^{2+} chains are accessible for each channel, *e.g.*, chain A and chain B. Within this channel, the M^{2+} ions in chain A_1 are related to the M^{2+} ions in chain A_3 and chain A_5 by a C_3 rotation axis; whereas the M^{2+} ions in chain A_1 are related to the M^{2+} ions in chain B_4 by an inversion center (same for A_3 and B_6, A_5 and B_2). Therefore, as Figure 5-10 shows, there are two possible paths for the "two-site" hopping (*e.g.*, $A_1 \leftrightarrow B_2$) if all translation motions (along the c axis) have been ignored: $A_1(2)$ (*i.e.*, the M^{2+} in chain A_1 and layer 2) $\leftrightarrow B_2(1)$, and $A_1(2) \leftrightarrow B_2(4)$, with diffusion lengths of 7.97 and 8.65 Å, respectively. In the fast-limit regime, the consequences of two motions are indistinguishable and both are equivalent to that of a "two-site" hopping on the single *a,b* plane, *i.e.*, yielding the identical line shape. Nevertheless, with different diffusion lengths, the two motions are expected to possess very similar, but unequal activation energies. Therefore, the rate constants of two motions are typically different at the same temperature and such difference becomes detectable when the motions enter the intermediate regime upon cooling (Figure 5-A2). The resulting ^2H NMR line shape must be a superimposition of two patterns. In addition, if translation motions are also taken into account, the "two-site" hopping is virtually an ensemble of a large number of closely related motions including $A_1(2) \leftrightarrow B_2(1)$, $A_1(2) \leftrightarrow B_2(4)$, $A_1(2) \leftrightarrow A_1(5) \leftrightarrow B_2(4)$, $A_1(2) \leftrightarrow B_2(4) \leftrightarrow B_2(1)$, *etc.*, with a certain distribution of activation energy. The observed ^2H spectrum hence must more or less display the features characteristic of systems with distributions. The scenario of guest dynamics in the intermediate regime becomes even more complicated for other "multiple-site" hopping motions due to much more possible diffusion paths, in particular for the "six-site" hopping. Under extreme conditions, the doublet-like features could completely disappear and only a featureless pattern could be observed, like the center component appeared in the ^2H spectra of the $0.6CD_3CN/Mg$ sample between 273 and 173 K. For this sample, all multiple-site hopping of CD_3CN have been quenched (*i.e.*, in the slow-limit regime) with sufficient cooling (153 K) and they become identical again.

Figure 5-11: Experimental and simulated ^{2}H static spectra of the 0.4CD$_3$CN/Zn sample as a function of temperature. The dynamic models for simulation: rotation of methyl C–^{2}H about its C_3 axis followed by non-localized six-site (or two-site) hopping motions.

The ^{2}H static spectrum of the 0.4CD$_3$CN/Zn sample at ambient temperature (Figure 5-11) exhibits a typical Pake doublet, which is very similar to that of the 0.2CD$_3$CN/Mg sample. Therefore, the motion of CD$_3$CN in CPO-27-Zn at 293 K is also the non-localized hopping between six sites. However, the VT ^{2}H NMR behavior of CD$_3$CN adsorbed on Zn^{2+} is distinct from what is observed for CD$_3$CN adsorbed on Mg^{2+}. Two shoulders arise below 273 K and the Pake doublet is eventually evolved into a

pattern with a C_Q of ~36 kHz and a nonzero η_Q of ~0.4 at 238 K. Spectral simulations reveal that it corresponds to a non-localized two-site hopping with θ of 62°, which is much smaller than the 83° at 293 K. It hence seems that the CD$_3$CN is attracted towards the walls at low temperatures, resulting in a smaller angle (θ) of the C_3 axis with respect to the c axis. Below 238 K, some CD$_3$CN molecules become localized (*i.e.*, not involved in the multiple-site hopping). The amount of localized CD$_3$CN increases when the temperature decreases and the non-localized two-site hopping finally freezes at 193 K. The internal motion of methyl group persists under all conditions.

Although very different VT ^{2}H NMR behaviors are observed in CD$_3$CN/Mg and CD$_3$CN/Zn samples, it is not straightforward to compare the relative binding strengths of CD$_3$CN on Mg^{2+} and Zn^{2+} based on the ^{2}H SSNMR data. There is an observable amount of CD$_3$CN hopping between two adjacent sites at 293 K for CD$_3$CN in CPO-27-Mg, which is a hint of stronger binding. However, the conversion from the non-localized to the localized CD$_3$CN for CPO-27-Mg completes at a significantly lower temperature than CPO-27-Zn (153 K compared to 193 K). More experiments are thus required to thoroughly understand the binding of CD$_3$CN.

5.3.4 Acetone-d$_6$ in CPO-27-M

Acetone is one of the most extensively used probe molecules for the measurement of the acidity for solid acid catalysts.[58] Moreover, acetone is a model compound for the large groups of carbonyl-containing compounds. The carbonyl group of acetone, acting as a Lewis base, can coordinate with the exposed metal centers of CPO-27-M. Figure 5-12 illustrates the ^{2}H static spectra of acetone-d$_6$ ((CD$_3$)$_2$CO) in CPO-27-Mg at 293 K as a function of loading. Like the samples loaded with CD$_3$CN (at high loading), there are also two components in the ^{2}H spectra: a broad component with a nonezero η_Q of ~ 0.5, and a narrow Pake doublet in the center. The broad component is assigned to the external motion of acetone molecules with symmetry lower than C_3. In literature, rapid π flip-flop of acetone about the C=O bond also yields a non-zero η_Q but this η_Q value (~ 0.7) is derived from the values in this work. Therefore, similar to CD$_3$CN/Mg samples, the broad component has to be attributed to the hopping of whole acetone between two neighboring

Mg^{2+} ions. The horn separation of the center component is significantly narrower than that of the internal motion of –CD_3 group, unambiguously implying an additional reorientation of the whole acetone molecules with high symmetry (*i.e.*, six-site hopping). It is worth mentioning that the horn separation enlarges with increasing loading for $(CD_3)_2CO/Mg$ samples, opposite to what is found for CD_3CN/Mg samples, the origin of which is provided in the next section.
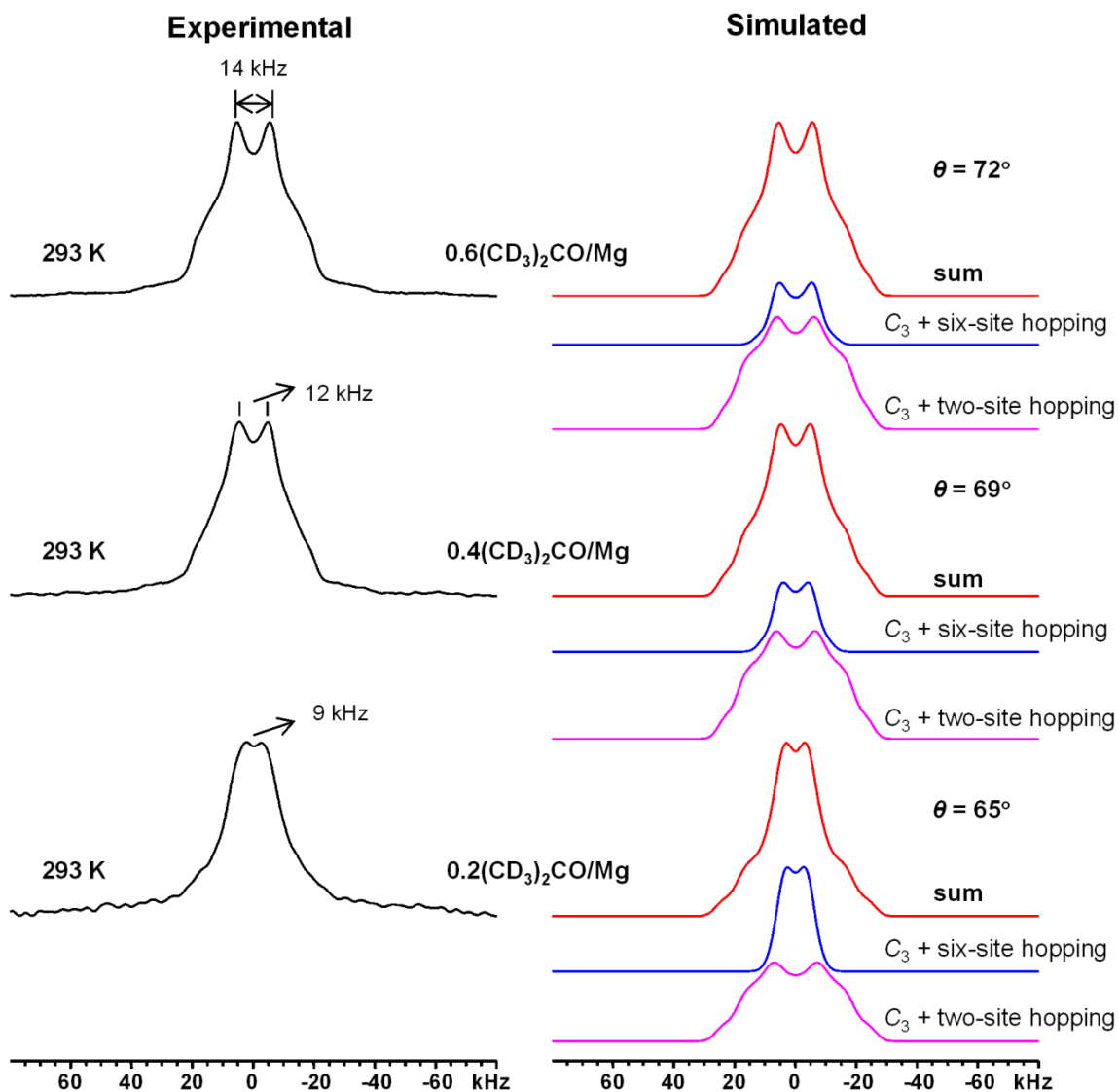
Figure 5-12: Experimental and simulated ^2H static spectra of acetone-d_6 in CPO-27-Mg at 293 K as a function of loading. The dynamic models for simulation: rotation of methyl C–^2H about its C_3 axis followed by non-localized six-site (or two-site) hopping motions.
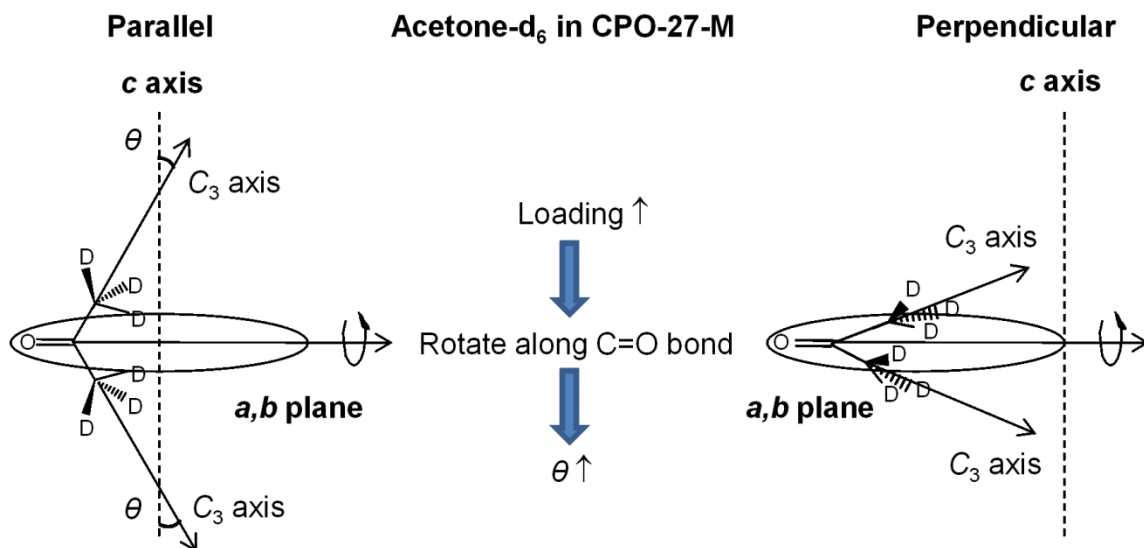
Figure 5-13: Schematic illustration of the local geometry of acetone-d_6 adsorbed in CPO-27-M as a function of loading.

Firstly, the ^{2}H spectra at 293 K imply that the two methyl groups of acetone must be equivalent (*i.e.*, they have identical θ, θ is the angle between the C_3 axis of the methyl group and the c axis, Figure 5-13): The two components of the ^{2}H spectra should be interpreted as acetone molecules have two distinct types of external motions (a two-site hopping and a six-site hopping), rather than that the two methyl groups of the same acetone reorientate in two different ways, since in principle their motions must possess the same type of symmetry (*i.e.*, both are axial symmetric or both are not axial symmetric). Therefore, the C=O bond of acetone must be in the *a,b* plane (Figure 5-13). The allowed range for θ thus varies between 32° (calculated from the C–C–C angle of acetone in gas phase,[53] 116°), in which the C–C–C plane is parallel to the c axis, and 90°, in which the C–C–C plane is perpendicular to the c axis. At a low loading, the C–C–C plane is expected to align approximately along the c axis because under such condition the two methyl groups of acetone are farthest away from the walls and minimize the repulsion forces between methyl groups and the walls. When more and more acetone is added, the repulsion forces between adjacent acetone molecules along the Mg^{2+} chains (*e.g.*, the two acetone molecules absorbed on $A_1(2)$ and $A_1(5)$, respectively, shown in Figure 5-10) cause the acetone to rotate with respect to the C=O bond, giving rise to a

larger θ. The second motion, corresponding to the broad feature, could be fitted as well with a two-site hopping of acetone using the same θ.
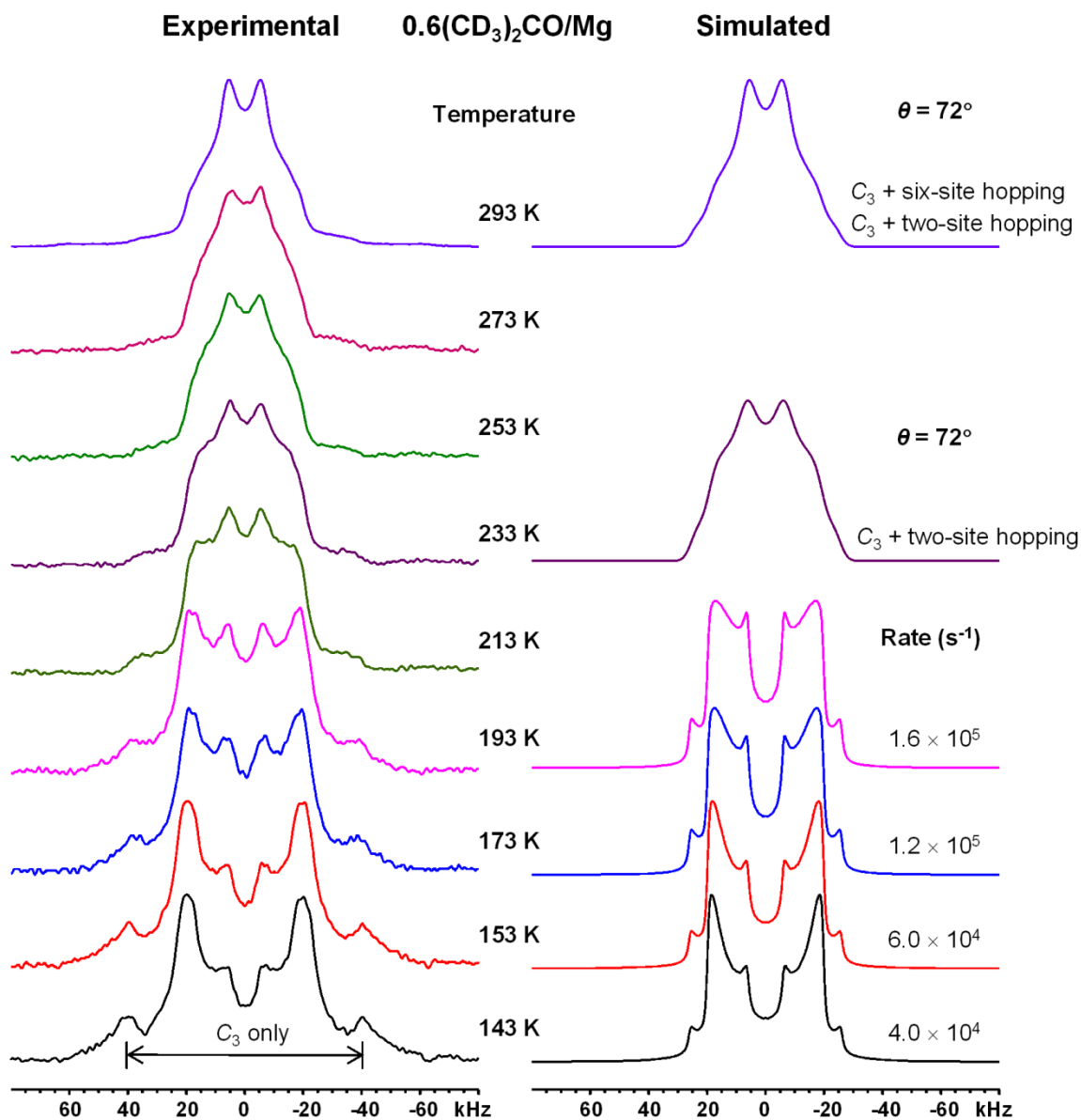
Figure 5-14: Experimental and simulated ^{2}H static spectra of the $0.6(CD_3)_2CO/Mg$ sample as a function of temperature. The dynamic models for simulation: rotation of methyl C–D about its C_3 axis followed by non-localized six-site (or two-site) hopping motions.
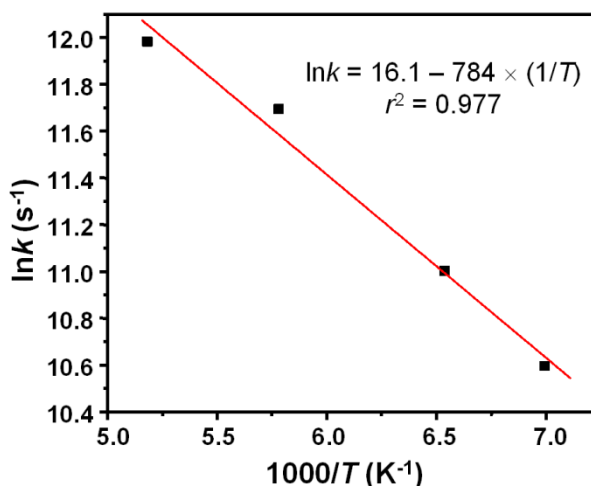
Figure 5-15: Arrhenius plot for the rate constant of the two-site hopping motion between 193 and 143 K.

The ^{2}H static spectra of the $0.6(CD_3)_2CO/Mg$ sample over the temperature range from 293 to 143 K are shown in Figure 5-14. The shoulders of the broad component become more and more prominent at lower temperatures. At 233 K, the six-site hopping motion disappears and only the two-site hopping motion persists. The conversion from the six-site hopping to the two-site hopping upon cooling is reasonable, since the six-site hopping has a much longer diffusion length and thus must have higher activation energy. When the temperature is further decreased, the ^{2}H spectra exhibit two noticeable changes: One is the emergence of two new edges at ~ ±40 kHz, corresponding to the $(CD_3)_2CO$ molecules that have been transformed into localized species;[59-62] and the other change is that the center component starts to display the line shape characteristic of the two-site hopping in the intermediate regime. The rate constant of the two-site hopping is hence determined by simulating the line shape of the center component. As Figure 5-15 shows, the temperature dependence of the rate constant between 193 and 143 K shows a typical Arrhenius dependence, with an activation energy $E = 6.5 \pm 0.6$ kJ·mol^{-1} and a pre-exponential factor of $k_0 = (9.8 \pm 0.1) \times 10^6$ s^{-1}. Since the activation energy for the non-localized two-site hopping is quite low, it seems that acetone only weakly interacts with Mg^{2+}. From a previous study, ^{25}Mg SSNMR data suggested there is a distribution of local Mg environments for CPO-27-Mg loaded with acetone (or CH_3CN), although powder XRD patterns indicates the long-range ordering of the framework is retained.[33] The

interaction between the oxygen of carbonyl group and Mg^{2+} is not strong enough to ensure all the adsorbed acetone molecules are perfectly ordered, *i.e.*, they have identical $Mg–OC(CH_3)_2$ distance. Instead, a distribution of the $Mg–OC(CH_3)_2$ distance from site to site is expected, giving rise to an asymmetric and featureless ^{25}Mg line shape characteristic of disordered systems. The same situation occurs for the CPO-27-Mg sample loaded with CH_3CN.
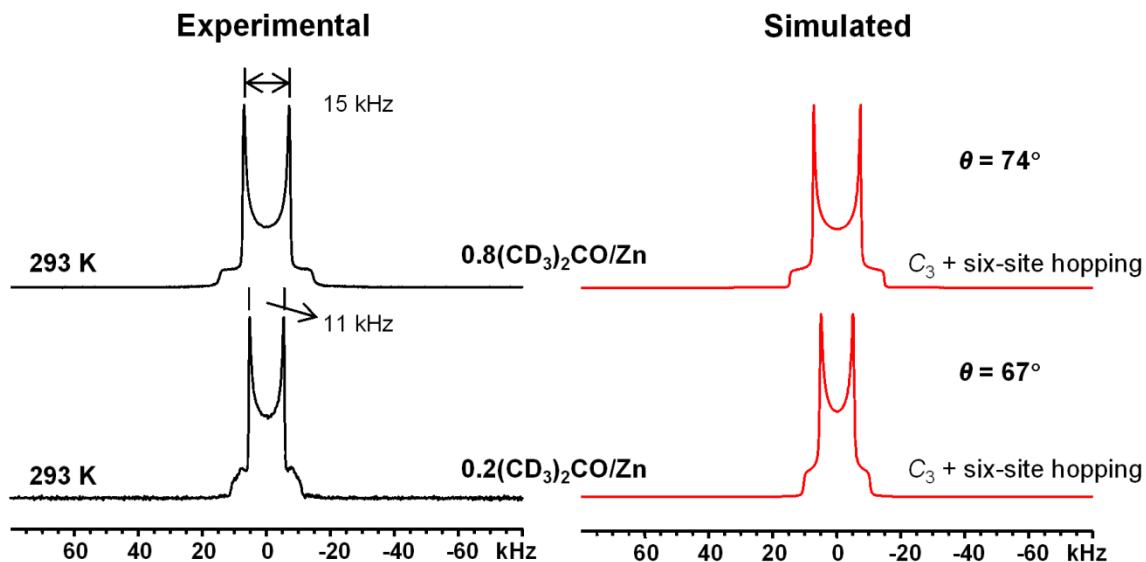
Figure 5-16: Experimental and simulated ^2H static spectra of acetone-d_6 in CPO-27-Zn at 293 K as a function of loading. The dynamic models for simulation: rotation of methyl C–D about its C_3 axis followed by non-localized six-site (or two-site) hopping motions of the whole molecule.

In sharp contrast to the CPO-27-Mg samples, the ^2H static spectra of the CPO-27-Zn samples loaded with acetone-d_6 at 293 K (Figure 5-17) only contain a Pake doublet even at a high loading of $0.8(CD_3)_2CO$ per Zn^{2+}, implying a six-site hopping motion for acetone. The absence of two-site hopping reveals that the acetone in CPO-27-Zn is more mobile than the acetone in CPO-27-Mg, *i.e.*, a weaker interaction exists between acetone and Zn^{2+} than ^{25}Mg. Thermodynamic data illustrate that more energy is required to break the $Mg^{2+}–OC(CH_3)_2$ bond (93.3 kJ·mol^{-1}) than the $Zn^{2+}–OC(CH_3)_2$ bond (72.8 kJ·mol^{-1})[63]. The horn separation enlarges with the increasing loading of $(CD_3)_2CO$ in CPO-27-Zn, similar to the $(CD_3)_2CO$/Mg samples.
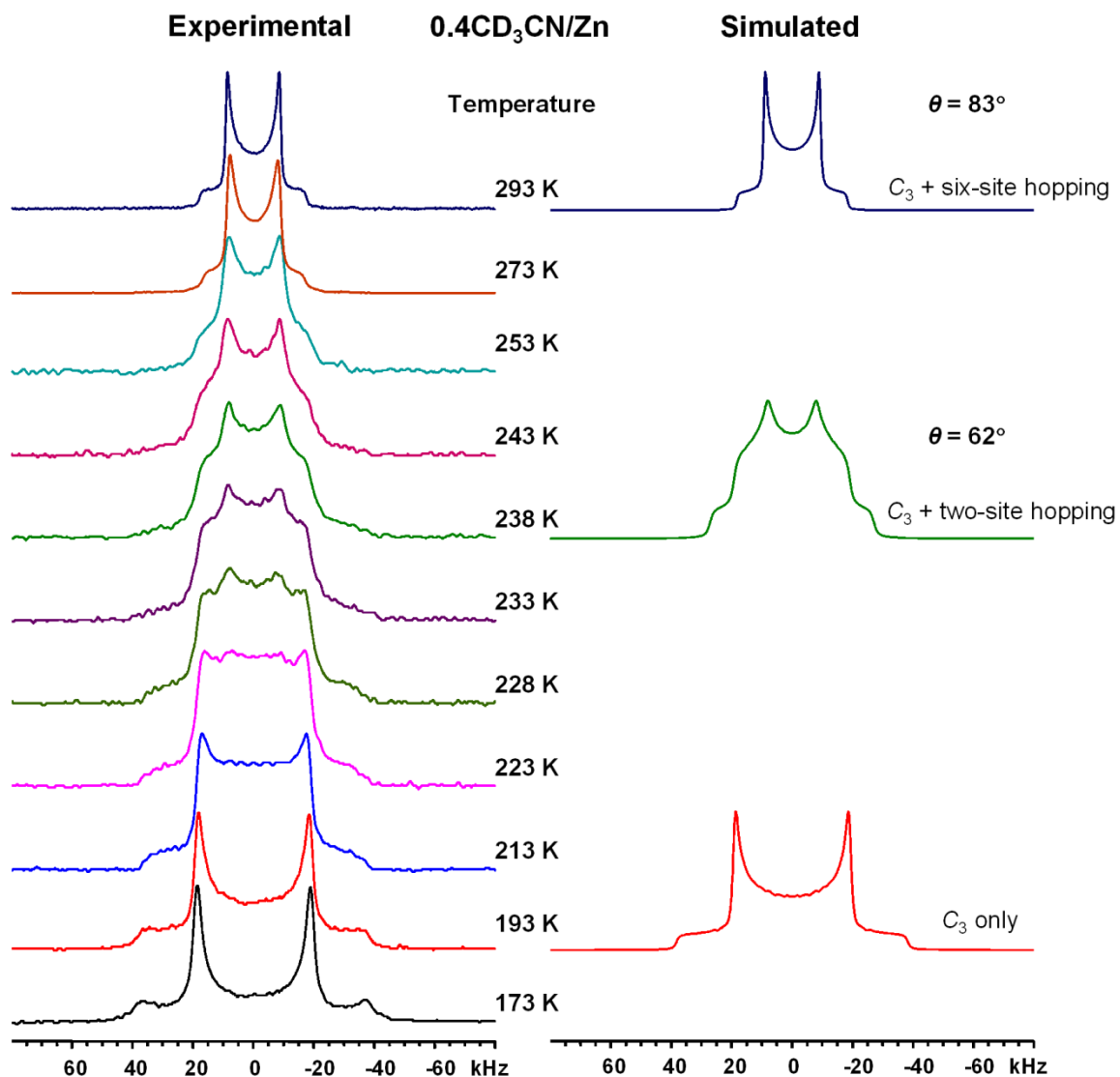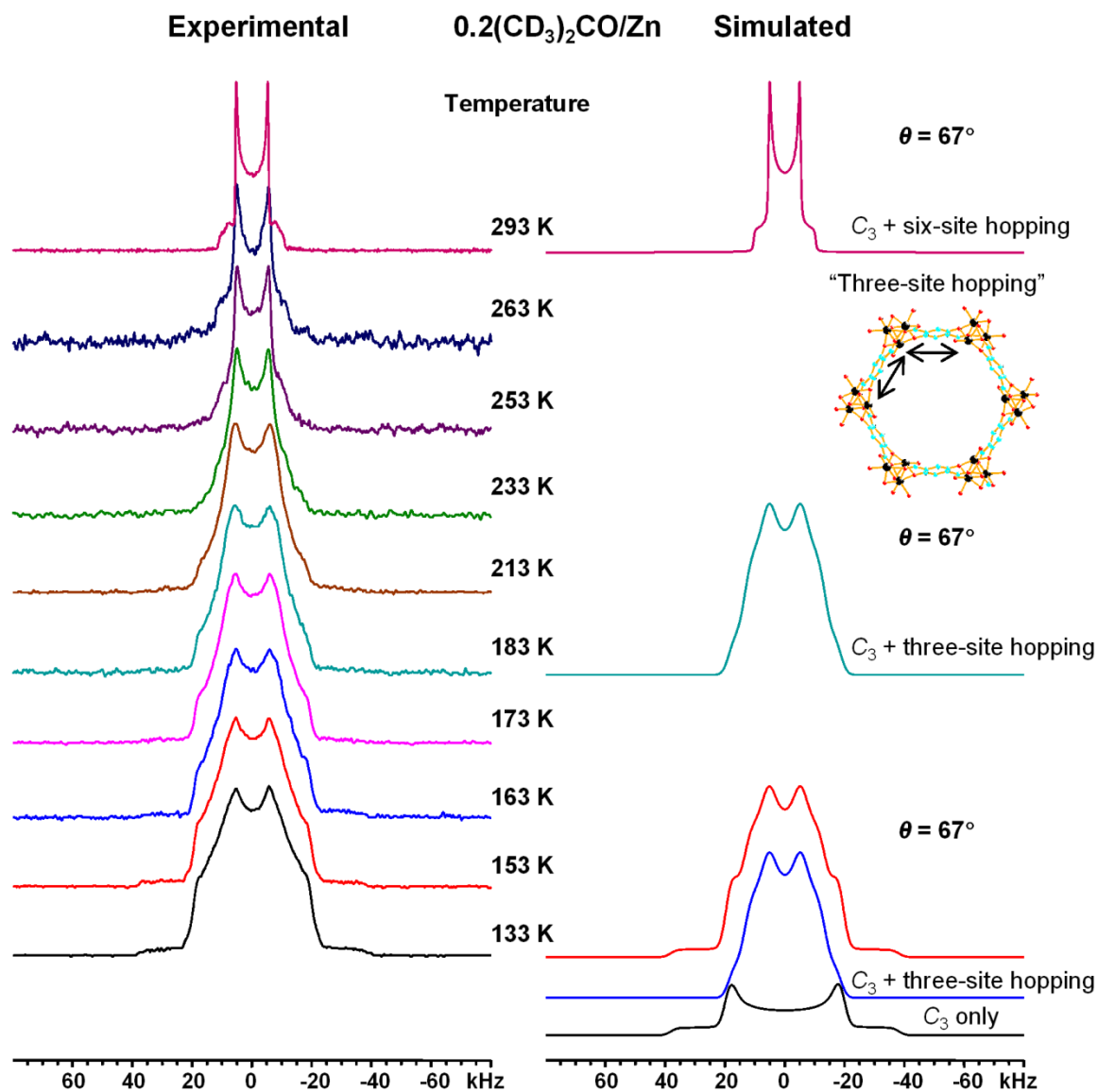
Figure 5-17: Experimental and simulated ^{2}H static spectra of the 0.2(CD$_3$)$_2$CO/Zn sample as a function of temperature. The dynamic models for simulation: rotation of methyl C–^{2}H about its C_3 axis followed by non-localized six-site (or three-site) hopping motions.

The VT ^{2}H NMR spectra of the 0.2(CD$_3$)$_2$CO/Zn sample are shown in Figure 5-17. A new broad component arises at about 253 K and the center Pake doublet is eventually converted to a pattern with a nonzero η_Q at 183 K. According to the C_Q (25 kHz) and η_Q (0.44) values, it is identified as the acetone that undergo rapid three-site hopping with the same θ (67°) as the six-site hopping at 293 K. The observation of the three-site hopping

in the $0.2(CD_3)_2CO/Zn$ sample, rather than the two-site hopping in the $0.2(CD_3)_2CO/Mg$ sample, again validates the higher mobility of acetone in CPO-27-Zn than CPO-27-Mg. With sufficient cooling, the two edges of the internal motion of methyl group become evident but the three-site hopping motion never stops even at the lowest temperature measured (133 K), further confirming that the interaction between acetone and Zn^{2+} is weaker than ^{25}Mg.

5.3.5 C_6D_6 in CPO-27-M

Although CPO-27-M MOFs have been demonstrated to be promising candidates for selective separation of alkenes from alkanes,[11,15,21] only limited information is known on the nature of the interactions between exposed metal centers and π systems. In CPO-27-M, benzene can interact with exposed M^{2+} ions in two different ways: The six $C^{\delta-}$–$H^{\delta+}$ bond dipoles of benzene combine to produce a region with negative electrostatic potential on the face of the π system. Electrostatic forces facilitate a natural attraction of cations to the surface of the π system, which is called the cation-π interaction.[64] The second type of interaction exists only for ions with unfilled d orbitals (Ni^{2+} or Co^{2+}),[15,21,23] which is a π-donation bond involving a process with donation of electrons from the filled π orbital of benzene to the unfilled d orbital of ions.

5.3.5.1   CPO-27-Mg and CPO-27-Zn

As Figure 5-18 illustrates, the ^2H static spectra of the $0.2C_6D_6/Mg$ sample at 293 K exhibits a Pake doublet with the C_Q of 20 kHz, which is much smaller than the typical C_Q value (~ 90 kHz^{36-38}) for in-plane rotation of benzene about its C_6 axis, implying the existence of additional external motion. When the sample is cooled down, the two horns of the Pake doublet gradually diminish and a Lorentzian pattern with FWHH of ~16 kHz emerges at 213 K. Two new horns are observed at ~ ±35 kHz at 203 K and become more and more prominent at lower temperatures, which are unambiguously assigned to the in-plane rotation of benzene. The center Lorentzian pattern eventually diminishes at 143 K. The C_Q of C–D bond in benzene, averaged by rapid in-plane rotation about its C_6 axis, is therefore C_Q = 92 kHz and η_Q = 0, agreeing well with the literature.[36-38] The external motion observed in the ^2H spectrum at 293 K is identified as the six-site hopping motion.

It is worth mentioning that the above-mentioned trend of change is similar to that of the center Pake doublet of the $0.6CD_3CN/Mg$ sample, implying the same origin.
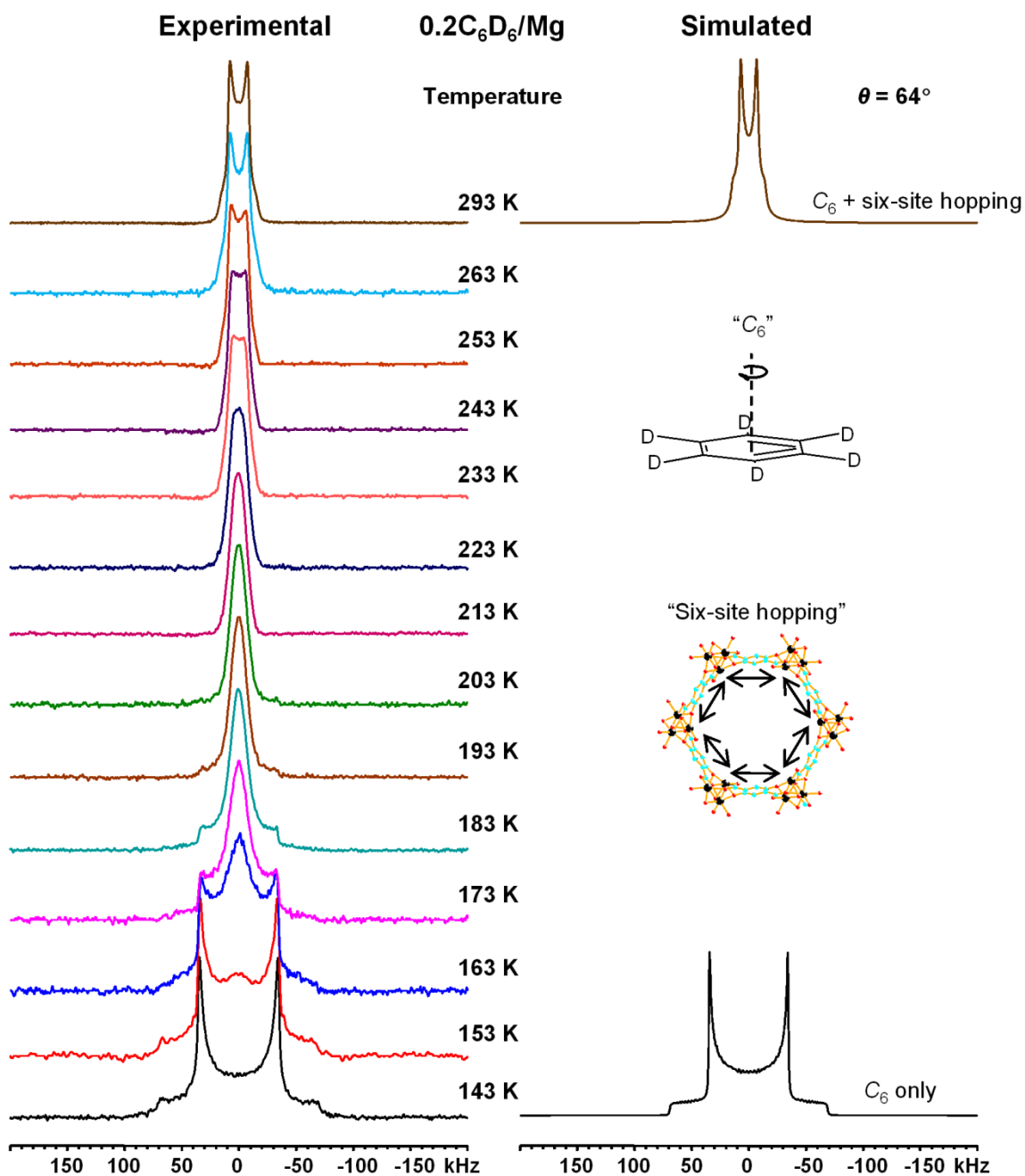
Figure 5-18: Experimental and simulated ^2H static spectra of the $0.2C_6D_6/Mg$ sample as a function of temperature. The dynamic models for simulation: in-plane rotation of benzene about its C_6 axis followed by non-localized six-site hopping.

The ^{2}H static spectra of C_6D_6 in CPO-27-Zn at 293 K as a function of loading are shown in Figure 5-19. At a low loading of $0.2C_6D_6$ per Zn^{2+}, the ^{2}H spectrum is a typical Pake doublet with the horn splitting of ~ 25 kHz, corresponding to the benzene molecules that are undergoing the rapid six-site hopping motion. When the loading is increased, at $0.6C_6D_6$ per Zn, the ^{2}H spectrum consists of a very sharp, solution-like NMR peak in the middle, and a broad component at the bottom. The former one is assigned to the benzene molecules that do not interact with Zn^{2+} ions and thus undergo rapid isotropic tumbling inside of the channels; whereas the latter one is due to the benzene molecules that have strong interactions with Zn^{2+} ions.
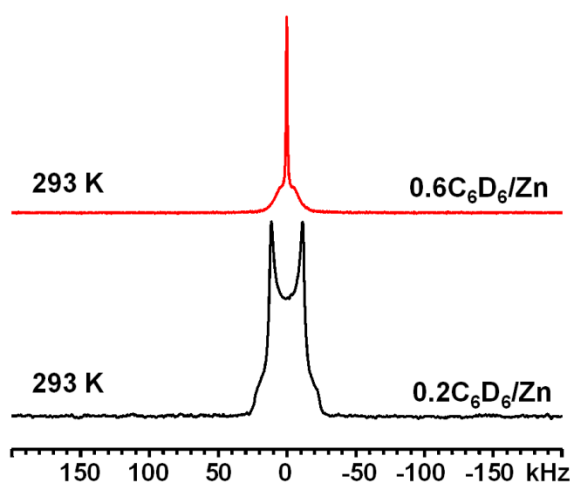
Figure 5-19: Experimental ^{2}H static spectra of C_6D_6 in CPO-27-Zn at 293 K as a function of loading.

As illustrated in Figure 5-20, the ^{2}H static spectrum of the $0.2C_6D_6$/Zn sample at 273 K consists of a new sharp feature in the middle, which looks like a Lorentzian pattern similar to what appeared in the VT ^{2}H spectra of the $0.2C_6D_6$/Mg sample. Below 273 K, the gap between the two horns of the Pake doublet is filled by this new feature. There is little change for the resulting "flat" top over a very broad temperature range, from 273 to 153 K. Although the flattening of two horns can be observed for certain types of motion in the intermediate regime (*e.g.*, the four-site hopping, Figure 5-A3), it should disappear immediately when the temperature is varied. Therefore, the "flat" top observed here is unlikely to be the result of a single motion. Lacking more experimental evidence, the

details about the origin of such feature are unavailable. At 153 K, two shoulders at ~ ±35 kHz and two edges at ~ ±70 kHz become evident, indicating some benzene molecules have attached to Zn^{2+} ions.
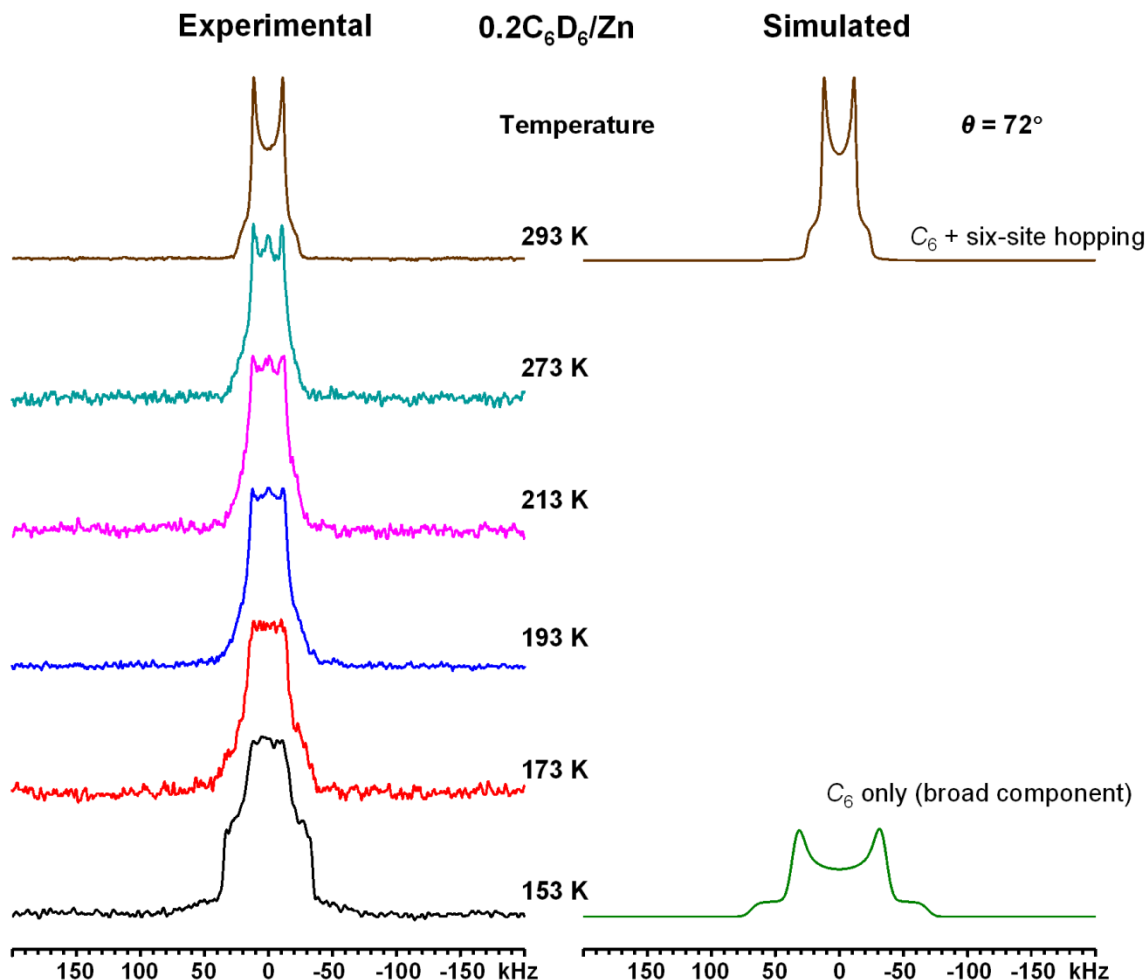
Figure 5-20: Experimental ^2H static spectra of the $0.2C_6D_6/Zn$ sample as a function of temperature. The dynamic models for simulation: in-plane rotation of benzene about its C_6 axis followed by non-localized six-site hopping.

5.3.5.2   CPO-27-Ni and CPO-27-Co

From the NMR point of view, the behaviors of CPO-27-Ni and CPO-27-Co, as paramagnetic solids, are distinct from those of diamagnetic solids (*e.g.*, CPO-27-Mg and CPO-27-Zn). The large magnetic moment of the unpaired electrons of paramagnetic ions such as Ni^{2+} ($S = 1$, S is the total spin of electrons) and Co^{2+} ($S = 3/2$) couples with the

magnetic moment of the nucleus of interest. Such interaction is formally equivalent to chemical shift anisotropy but quite comparable in magnitude to quadrupolar coupling.[65] Herein, the effects of paramagnetic centers are analyzed in the following way.[66]

The coupling between an electronic and a nuclear magnetic moment, treated similar to chemical shift anisotropy, consists of an isotropic interaction (the Fermi contact shift) and an anisotropic dipolar interaction (the dipolar or pseudocontact shift):

$$\delta_{hyp} = \delta_{con} + \delta_{dip}$$ (**Equation 5-3**)

where the hyperfine shift δ_{hyp} is the chemical shift due to the paramagnetic center, δ_{con} is the Fermi contact shift, and δ_{dip} is the dipolar shift. The two interactions differ in their mechanism. The former one is a through-bond effect, resulting from a spin delocalization of the unpaired electron. In the case of C_6D_6 in CPO-27-Ni (or CPO-27-Co), the unpaired d electrons of Ni^{2+} (or Co^{2+}) can enter the π^* orbital of benzene by back donation. As a consequence, significant Fermi contact spin density, $\rho_{\alpha\beta}$, can be found at the deuterium nuclei, inducing a large Fermi contact shift. The Fermi contact shift δ_{con} is proportional to $\rho_{\alpha\beta}$ and inversely proportional to the absolute temperature T:

$$\delta_{con} = m\frac{S+1}{T}\rho_{\alpha\beta}$$ (**Equation 5-4**)

where m is a collection of constants. Since $\rho_{\alpha\beta}$ can be either positive or negative, Fermi contact shifts have different signs: positive spin density corresponds to a downfield shift while negative spin density gives rise to an upfield shift.

Dipolar interaction, in contrast, is a through-space interaction proportional to $1/r^3$, where r is the distance from the nucleus studied to the unpaired electron. The line shape of the powder pattern is influenced by the anisotropic part of the dipolar interaction.

Under the experimental conditions applied, C_6D_6 molecules are undergoing rapid motions, which could not only average the quadrupolar interactions but also the electron-nucleus coupling. Only the averaged values of δ_{hyp} are reported in this chapter.
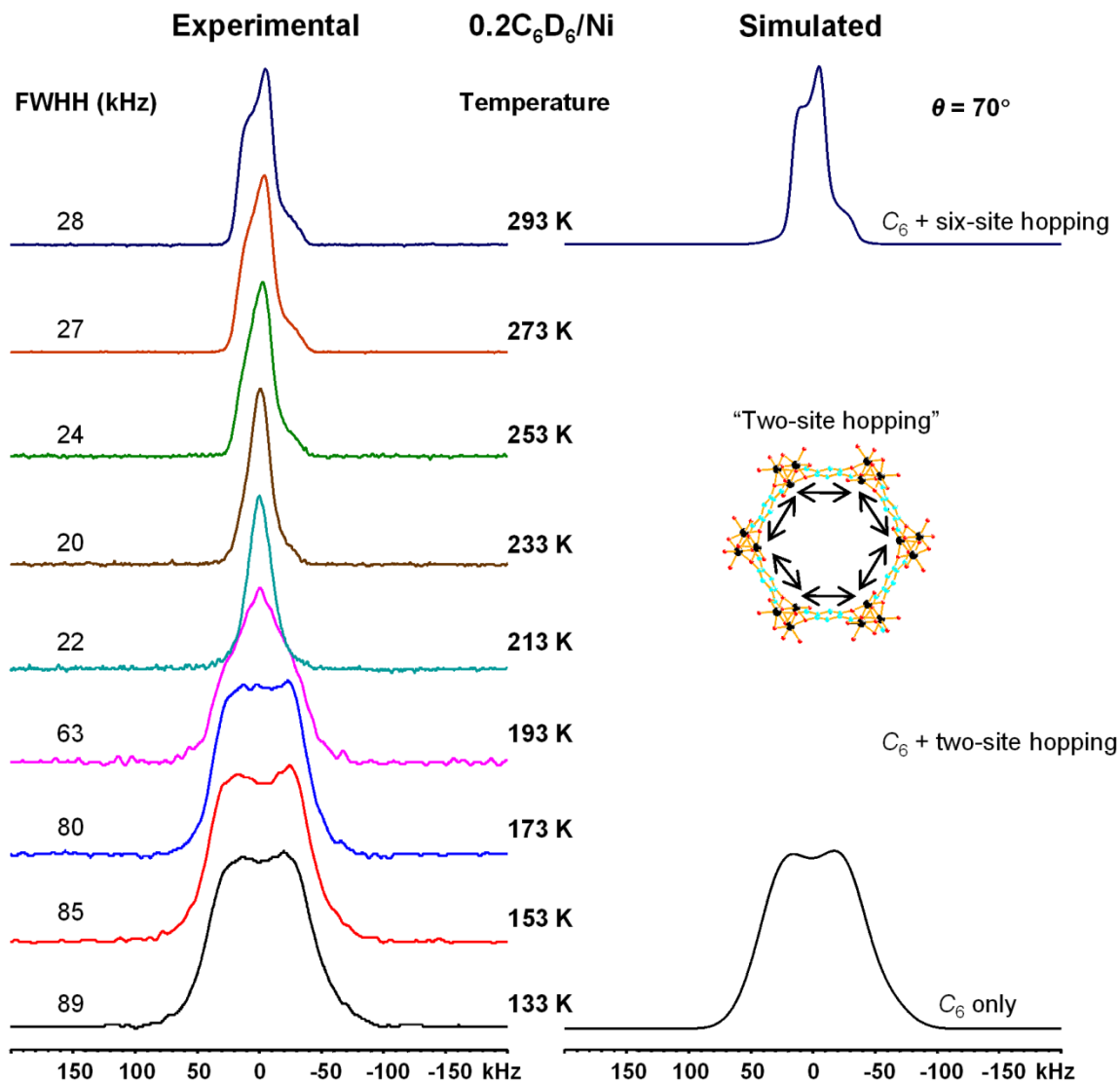
Figure 5-21: Experimental and simulated ^{2}H static spectra of the 0.2C$_6$D$_6$/Ni sample as a function of temperature. The dynamic models for simulation: in-plane rotation of benzene about its C_6 axis followed by non-localized six-site hopping.

The ^{2}H static spectra of the 0.2C$_6$D$_6$/Ni sample as a function of temperature are shown in Figure 5-21. The ^{2}H spectrum at ambient temperature (293 K) is significantly distorted by the strong coupling between the unpaired electrons of Ni^{2+} and the magnetic moment of ^{2}H, giving rise to an asymmetric pattern. Simulation of this spectrum yields a set of ^{2}H EFG parameters: $C_Q = 30$ kHz, $\eta_Q = 0$, and hyperfine shifts: $\delta_{iso} = -80$ ppm, $\Omega = 300$ ppm, $\kappa = 1$, $\alpha = 0°$, $\beta = 20°$, and $\gamma = 0°$, where α, β, γ are Euler angles between the

EFG and CSA tensors (herein hyperfine shifts are treated as chemical shifts) in Rose convention.[51] The small C_Q (= 30 kHz) and axial symmetric η_Q (= 0) and κ (= 1) values all indicate that C_6D_6 in CPO-27-Ni also experiences a rapid in-plane rotation about its C_6 axis followed by a non-localized hopping between six sites. The FWHH of the spectrum (28 kHz) is close to the C_Q obtained from spectral simulation, opening up the possibilities to use this value to estimate the C_Q when spectral simulation is not possible.

Upon cooling, the FWHH values of the ^{2}H spectra of the $0.2C_6D_6$/Ni sample change little between 293 and 213 K (Figure 5-21), illustrating that the six-site hopping motion still dominates over this temperature range. However, the ^{2}H spectrum at 193 K exhibits an isosceles triangle-like line shape with a markedly larger FWHH of about 63 kHz, distinct from the ^{2}H spectrum at 293 K. According to the FWHH, the spectrum is interpreted as the benzene molecules which are hopping between two adjacent sites (C_Q = 62 kHz and η_Q = 0.50 from EXPRESS simulation). The ^{2}H spectra become even broader (FWHH > 80 kHz) below 193 K. At the same time, two horns with the splitting of ~ 40 kHz emerge, although not obvious. The ^{2}H spectrum at 133 K can be fitted with a set of NMR parameters: C_Q = 92 kHz, η_Q = 0, δ_{iso} = -110 ppm, Ω = 200 ppm, κ = 1, α = 0°, β = 20°, and γ = 0°. The C_Q and η_Q values imply that all non-localized hopping motions have been quenched at 133 K. The only motion is in-plane rotation of benzene about its C_6 axis. There is a significant upfield shift (~ 30 ppm) of the ^{2}H isotropic hyperfine shift at 133 K compared to that at 293 K, indicating that the Fermi contact spin density, $\rho_{\alpha\beta}$, is negative at deuterium nuclei and gives rise to an upfield shift at lower temperatures (Equation 5-4). The effects from chemical shift interaction are negligible in paramagnetic systems because ^{2}H has a very narrow chemical shift range.

The ^{2}H static spectra of the $0.2C_6D_6$/Co sample as a function of temperature are shown in Figure 5-22. The paramagnetic effects of Co^{2+} are expected to be more obvious than those of Ni^{2+} because Co^{2+} has more unpaired electrons. It is confirmed by the fact that all ^{2}H spectra of the $0.2C_6D_6$/Co sample completely lose their features and only display profiles which are asymmetrically broadened along the upfield region. Without any spectral feature, no spectral simulation can be performed. However, as mentioned earlier, the FWHH of the ^{2}H spectrum is a good estimation of the C_Q. At 293 K, the

FWHH is about 26 kHz, corresponding to a rapid in-plane rotation of benzene about its C_6 axis followed by a non-localized six-site hopping. The ^{2}H spectra become broader and broader below 213 K. The FWHH reaches ~ 93 kHz at 133 K, under which all benzene molecules are bound to Co^{2+} ions and only in-plane rotation of benzene is allowed.
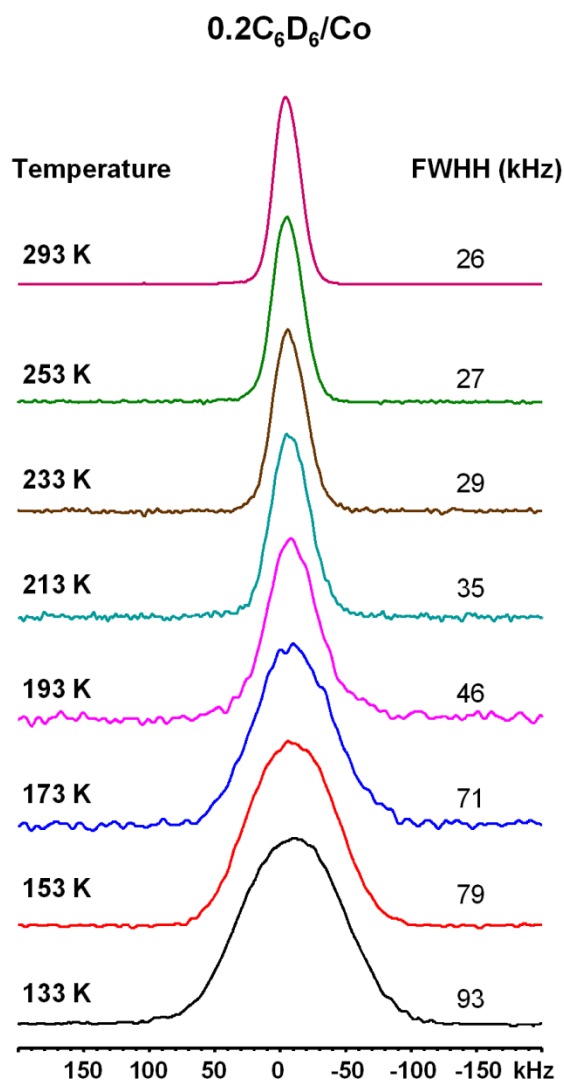
0.2C$_6$D$_6$/Co

Figure 5-22: Experimental ^{2}H static spectra of the 0.2C$_6$D$_6$/Co sample as a function of temperature.

According to the VT ^{2}H NMR data, most of the benzene molecules have been converted to bound species at 153 K except CPO-27-Zn, the relative binding strengths of benzene on exposed metal centers are therefore: $Mg^{2+} \approx Ni^{2+} \approx Co^{2+} > Zn^{2+}$. The cation-$\pi$

interaction increases when the charge density of the ion increases. Four ions have the same charge and almost identical ionic radii. However, the small electronegativity of Mg makes the Mg–O mainly ionic in nature; whereas there are more degrees of covalent bonding (*i.e.*, more charge delocalization) for other metals. Since Mg^{2+} has the highest charge density, it must possess the strongest cation-π interaction. For the other three metals, although Ni (and Co) has a larger electronegativity (and hence a weaker cation-π interaction), the binding strength is significantly enhanced by the formation of π-donation bond between benzene and Ni^{2+} (and Co^{2+}). The total binding strength of benzene on Ni^{2+} (and Co^{2+}) thus is stronger than Zn^{2+} and can be comparable to Mg^{2+}.

5.3.6   A Summary of Observed Motions

The ^2H NMR parameters obtained from spectral simulation (or estimated from the FWHH) are shown in Table 5-1. The corresponding motions are also described. The internal motions include: π flip-flop of D_2O about its C_2 axis ("π flip-flop", the D–O–D angle is 104.5°), rotation of $-CD_3$ group about its C_3 axis ("C_3"), and in-plane rotation of C_6D_6 about its C_6 axis ("C_6"). The external motions, which occur simultaneously with the internal motions, are non-localized multiple-site hopping motions ("six-site hopping", *etc.*). During hopping, the angle θ is constant. θ is the angle between the crystallographic c axis and the Z axis of the intermediate jump frame, which is the C_3 axis of $-CD_3$ group (for CD_3CN and actone-d_6) or the C_6 axis of C_6D_6.

Table 5-1: Simulated ^{2}H NMR parameters and motions.

Sample	T (K)	Motions	C_Q (kHz)	η_Q
0.6D$_2$O/Mg	293	π-flip flop	97.5	0.75
	153	π-flip flop (intermediate)	97.5	0.75
1.0D$_2$O/Mg	293	π-flip flop	N/A	N/A
		free tumbling	~ 24[a]	N/A
0.6D$_2$O/Zn	293	π-flip flop	N/A	N/A
		free tumbling	~ 12[a]	N/A
	153	π-flip flop and others	~ 82[a]	N/A
0.2CD$_3$CN/Mg	293	C_3 + six-site hopping (θ = 83°)	24	0
0.6CD$_3$CN/Mg	293	C_3 + six-site hopping (θ = 65°)	12	0
		C_3 + two-site hopping (θ = 65°)	35	0.45
	153	C_3	51	0
1.0CD$_3$CN/Mg	293	C_3 + six-site hopping (θ = 59°)	5	0
		C_3 + two-site hopping (θ = 59°)	37	0.38
0.4CD$_3$CN/Zn	293	C_3 + six-site hopping (θ = 83°)	24	0
	238	C_3 + two-site hopping (θ = 62°)	36	0.41
	193	C_3	51	0
0.2(CD$_3$)$_2$CO/Mg	293	C_3 + six-site hopping (θ = 65°)	12	0
		C_3 + two-site hopping (θ = 65°)	35	0.45
0.4(CD$_3$)$_2$CO/Mg	293	C_3 + six-site hopping (θ = 69°)	16	0
		C_3 + two-site hopping (θ = 69°)	34	0.49
0.6(CD$_3$)$_2$CO/Mg	293	C_3 + six-site hopping (θ = 72°)	18	0
		C_3 + two-site hopping (θ = 72°)	34	0.51
	233	C_3 + two-site hopping (θ = 72°)	34	0.51
	143	C_3 + two-site hopping (θ = 72°) (intermediate)	34	0.51
0.2(CD$_3$)$_2$CO/Zn	293	C_3 + six-site hopping (θ = 67°)	14	0
	183	C_3 + three-site hopping (θ = 67°)	25	0.44
	133	C_3 + three-site hopping (θ = 67°)	25	0.44
		C_3	51	0
0.8(CD$_3$)$_2$CO/Zn	293	C_3 + six-site hopping (θ = 74°)	20	0
0.2C$_6$D$_6$/Mg	293	C_6 + six-site hopping (θ = 64°)	20	0
	143	C_6	92	0
0.2C$_6$D$_6$/Zn	293	C_6 + six-site hopping (θ = 72°)	33	0
	153	C_6 and others	92	0
0.2C$_6$D$_6$/Ni	293[b]	C_6 + six-site hopping (θ = 70°)	30	0
	133[c]	C_6	92	0
0.2C$_6$D$_6$/Co	293	C_6 + six-site hopping	~ 26[a]	N/A
	133	C_6	~ 93[a]	N/A

a: Estimated from the FWHH. b: The hyperfine shift: δ_{iso} = -80 ppm, Ω = 300 ppm, κ =1, α = 0°, β = 20°, γ = 0°. c: The hyperfine shift: δ_{iso} = -110 ppm, Ω = 200 ppm, κ =1, α = 0°, β = 20°, γ = 0°.

5.4 Conclusions

In summary, the dynamics of four prototypical guest molecules (D_2O, CD_3CN, acetone-d_6, C_6D_6) in the isostructural CPO-27-M (M = Mg, Zn, Ni, Co) MOFs were examined by ^{2}H SSNMR experiments. The internal motion of guest molecules, including π flip-flop of D_2O about its C_2 axis, rotation of methyl group about its C_3 axis and in-plane rotation of C_6D_6 about its C_6 axis, persists over the whole temperature range studied. Additional reorientation of the whole molecule (external motion) is desirable for the simulation of ^{2}H spectra of CD_3CN, acetone-d_6 and C_6D_6 in CPO-27-M. Two models are employed to demonstrate the external motion: the uniaxial rotation, in which the guest molecules are strongly bound to metal centers; and the multiple-site hopping, in which the guest molecules are allowed to jump between neighboring metal centers. The ^{2}H NMR data imply that the external motion should be interpreted using the multiple-site hopping model rather than the uniaxial rotation model. Moreover, the validity of dynamic models has been checked by varying the loading as well as the temperature. Since the motions are constrained by the interactions between guest molecules and exposed metal centers, different guest molecules are expected to have distinct dynamic behaviors. The relative binding strengths of the same guest molecule on different metal centers are hence evaluated, which are clearly dependent on the nature of metal centers. For instance, the binding strengths of benzene on M^{2+} are: $Mg^{2+} \approx Ni^{2+} \approx Co^{2+} > Zn^{2+}$, due to both cation-$\pi$ and π-donation interactions. It should be highlighted the local Mg environments of CPO-27-Mg samples probed by a previous ^{25}Mg SSNMR study has been directly confirmed by the results of ^{2}H SSNMR experiments. The approaches and the results presented in this work are hoped to shed light on the future study of CPO-27-M and related materials: On one hand, molecular-level information is obtained to assist one to understand the "water effect". On the other hand, some insights into the nature of the interactions between several prototypical volatile organic compounds and metal centers are provided, which are both guest-specific and metal-specific, implying that CPO-27-M can be potentially used to selectively detect and capture a large variety of VOCs by using different metal centers.

5.5 References

(1)   Special issue for Metal–Organic Frameworks: Zhou, H.-C.; Long, J. R.; Yaghi, O. M. *Chem. Rev.* **2012**, *112*, 673-1268.

(2)   Dietzel, P. D. C.; Blom, R.; Fjellvåg, H. *Eur. J. Inorg. Chem.* **2008**, *2008*, 3624-3632.

(3)   Dietzel, P. D. C.; Johnsen, R. E.; Blom, R.; Fjellvåg, H. *Chem. Eur. J.* **2008**, *14*, 2389-2397.

(4)   Dietzel, P. D. C.; Panella, B.; Hirscher, M.; Blom, R.; Fjellvåg, H. *Chem. Commun.* **2006**, 959-961.

(5)   Dietzel, P. D. C.; Morita, Y.; Blom, R.; Fjellvåg, H. *Angew. Chem., Int. Ed.* **2005**, *44*, 6354-6358.

(6)   Rosi, N. L.; Kim, J.; Eddaoudi, M.; Chen, B.; O'Keeffe, M.; Yaghi, O. M. *J. Am. Chem. Soc.* **2005**, *127*, 1504-1518.

(7)   McDonald, T. M.; Lee, W. R.; Mason, J. A.; Wiers, B. M.; Hong, C. S.; Long, J. R. *J. Am. Chem. Soc.* **2012**, *134*, 7056-7065.

(8)   Caskey, S. R.; Wong-Foy, A. G.; Matzger, A. J. *J. Am. Chem. Soc.* **2008**, *130*, 10870-10871.

(9)   Yazaydin, A. O.; Snurr, R. Q.; Park, T.-H.; Koh, K.; Liu, J.; LeVan, M. D.; Benin, A. I.; Jakubczak, P.; Lanuza, M.; Galloway, D. B.; Low, J. J.; Willis, R. R. *J. Am. Chem. Soc.* **2009**, *131*, 18198-18199.

(10)   Britt, D.; Tranchemontagne, D.; Yaghi, O. M. *Proc. Natl. Acad. Sci. U. S. A.* **2008**, *105*, 11623-11627.

(11)   Bae, Y.-S.; Lee, C. Y.; Kim, K. C.; Farha, O. K.; Nickias, P.; Hupp, J. T.; Nguyen, S. T.; Snurr, R. Q. *Angew. Chem., Int. Ed.* **2012**, *51*, 1857-1860.

(12)   García, E. J.; Mowat, J. P. S.; Wright, P. A.; Pérez-Pellitero, J.; Jallut, C.; Pirngruber, G. D. *J. Phys. Chem. C* **2012**, *116*, 26636-26648.

(13)   Grant Glover, T.; Peterson, G. W.; Schindler, B. J.; Britt, D.; Yaghi, O. *Chem. Eng. Sci.* **2011**, 66, 163-170.

(14)   Zhou, W.; Wu, H.; Yildirim, T. *J. Am. Chem. Soc.* **2008**, *130*, 15268-15269.

(15)   Geier, S. J.; Mason, J. A.; Bloch, E. D.; Queen, W. L.; Hudson, M. R.; Brown, C. M.; Long, J. R. *Chem. Sci.* **2013**, *4*, 2054-2061.

(16)   Wu, H.; Zhou, W.; Yildirim, T. *J. Am. Chem. Soc.* **2009**, *131*, 4995-5000.

(17)   Queen, W. L.; Brown, C. M.; Britt, D. K.; Zajdel, P.; Hudson, M. R.; Yaghi, O. M. *J. Phys. Chem. C* **2011**, *115*, 24915-24919.

(18)   Wu, H.; Simmons, J. M.; Srinivas, G.; Zhou, W.; Yildirim, T. *J. Phys. Chem. Lett.* **2010**, *1*, 1946-1951.

(19)   Dietzel, P. D. C.; Johnsen, R. E.; Fjellvåg, H.; Bordiga, S.; Groppo, E.; Chavan, S.; Blom, R. *Chem. Commun.* **2008**, 5125-5127.

(20)   Dietzel, P. D. C.; Georgiev, P. A.; Eckert, J.; Blom, R.; Strässle, T.; Unruh, T. *Chem. Commun.* **2010**, *46*, 4962-4964.

(21)   Peralta, D.; Chaplais, G.; Simon-Masseron, A.; Barthelet, K.; Chizallet, C.; Quoineaud, A.-A.; Pirngruber, G. D. *J. Am. Chem. Soc.* **2012**, *134*, 8115-8126.

(22)   Valenzano, L.; Civalleri, B.; Chavan, S.; Palomino, G. T.; Arean, C. O.; Bordiga, S. *J. Phys. Chem. C* **2010**, *114*, 11185-11191.

(23)   Bonino, F.; Chavan, S.; Vitillo, J. G.; Groppo, E.; Agostini, G.; Lamberti, C.; Dietzel, P. D. C.; Prestipino, C.; Bordiga, S. *Chem. Mater.* **2008**, *20*, 4957-4968.

(24)   Valenzano, L.; Civalleri, B.; Sillar, K.; Sauer, J. *J. Phys. Chem. C* **2011**, *115*, 21777-21784.

(25)   Ding, L. F.; Yazaydin, A. O. *J. Phys. Chem. C* **2012**, *116*, 22987-22991.

(26)   Yu, K.; Kiesling, K.; Schmidt, J. R. *J. Phys. Chem. C* **2012**, *116*, 20480-20488.

(27)   Kong, L.; Román-Pérez, G.; Soler, J. M.; Langreth, D. C. *Phys. Rev. Lett.* **2009**, *103*, 096103/096101-096103/096104.

(28)   Krishna, R.; van Baten, J. M. *J. Phys. Chem. C* **2012**, *116*, 23556-23568.

(29)   Zeitler, T. R.; Allendorf, M. D.; Greathouse, J. A. *J. Phys. Chem. C* **2012**, *116*, 3492-3502.

(30)   Haldoupis, E.; Nair, S.; Sholl, D. S. *J. Am. Chem. Soc.* **2012**, *134*, 4313-4323.

(31)   Park, J.; Kim, H.; Han, S. S.; Jung, Y. *J. Phys. Chem. Lett.* **2012**, *3*, 826-829.

(32)   Lopez, M. G.; Canepa, P.; Thonhauser, T. *J. Chem. Phys.* **2013**, 138, 154704.

(33)   Xu, J.; Terskikh, V. V.; Huang, Y. *J. Phys. Chem. Lett.* **2013**, *4*, 7-11.

(34)   Kong, X.; Scott, E.; Ding, W.; Mason, J. A.; Long, J. R.; Reimer, J. A. *J. Am. Chem. Soc.* **2012**, *134*, 14341-14344.

(35)   Lin, L.-C.; Kim, J.; Kong, X.; Scott, E.; McDonald, T. M.; Long, J. R.; Reimer, J. A.; Smit, B. *Angew. Chem., Int. Ed.* **2013**, *52*, 4410-4413.

(36)   Shantz, D. F.; Lobo, R. F. *Top. Catal.* 1999, 9, 1-11.

(37)   Sutrisno, A.; Huang, Y. *Solid State Nucl. Magn. Reson.* **2013**, *49-50*, 1-11.

(38)   Hoffmann, H. C.; Debowski, M.; Mueller, P.; Paasch, S.; Senkovska, I.; Kaskel, S.; Brunner, E. *Materials* **2012**, *5*, 2537-2572.

(39)   Nishchenko, A. M.; Kolokolov, D. I.; Gabrienko, A. A.; Stepanov, A. G. *J. Phys. Chem. C* **2012**, *116*, 8956-8963.

(40)   Zhu, J.; Mosey, N.; Woo, T.; Huang, Y. *J. Phys. Chem. C.* **2007**, *111*, 13427-13436.

(41)   Gonzalez, J.; Devi, R. N.; Wright, P. A.; Tunstall, D. P.; Cox, P. A. *J. Phys. Chem. B* **2005**, *109*, 21700-21709.

(42)   Shustova, N. B.; Ong, T.-C.; Cozzolino, A. F.; Michaelis, V. K.; Griffin, R. G.; Dinca, M. *J. Am. Chem. Soc.* **2012**, *134*, 15061-15070.

(43)   Kolokolov, D. I.; Jobic, H.; Stepanov, A. G.; Ollivier, J.; Rives, S.; Maurin, G.; Devic, T.; Serre, C.; Ferey, G. *J. Phys. Chem. C* **2012**, *116*, 15093-15098.

(44)   Wittebort, R. J.; Olejniczak, E. T.; Griffin, R. G. *J. Chem. Phys.* **1987**, *86*, 5411-5420.

(45)   Larsen, F. H. *Annu. Rep. NMR Spectrosc.* **2010**, *71*, 103-137.

(46)   Kizzie, A. C.; Wong-Foy, A. G.; Matzger, A. J. *Langmuir* **2011**, *27*, 6368-6373.

(47)   Yu, J.; Balbuena, P. B. *J. Phys. Chem. C* **2013**, *117*, 3383-3388.

(48)   Antonijevic, S.; Wimperis, S. *J. Magn. Reson.* **2003**, *164*, 343-350.

(49)   MacKenzie, K. J. D.; Smith, M. E. *Multinuclear Solid-State NMR of Inorganic Materials*; 1st ed.; Pergamon: Oxford; New York, **2002**.

(50)   Vold, R. L.; Hoatson, G. L. *J. Magn. Reson.* **2009**, *198*, 57-72.

(51)   Rose, M. E. *Elementary Theory of Angular Momentum*; Wiley: New York, **1957**.

(52)   Kemp, T. F.; Smith, M. E. *Solid State Nucl. Magn. Reson.* **2009**, *35*, 243-252.

(53)   *CRC Handbook of Chemistry and Physics*, *Internet Version 2005*, <http://www.hbcpnetbase.com>, CRC Press: Boca Raton, FL, **2005**.

(54)   Chihara, H.; Nakamura, N. *Nuclear Quadrupole Resonance Data, LB New Series*; Springer: Berlin; Heidelberg, **1997**.

(55)   Pavlov, M.; Siegbahn, P. E. M.; Sandström, M. *J. Phys. Chem. A* **1998**, *102*, 219-228.

(56)   Suits, B. H.; Sepa, J.; Gorte, R. J.; White, D. *J. Phys. Chem. B* **2000**, *104*, 5124-5131.

(57)   Trout, B. L.; Suits, B. H.; Gorte, R. J.; White, D. *J. Phys. Chem. B* **2000**, *104*, 11734-11747.

(58)   Biaglow, A. I.; Gorte, R. J.; Kokotailo, G. T.; White, D. *J. Catal.* **1994**, *148*, 779-786.

(59)   Meirovitch, E.; Rananavare, S. B.; Freed, J. H. *J. Phys. Chem.* **1987**, *91*, 5014-5020.

(60)   Sidhu, P. S.; Bell, J.; Penner, G. H.; Jeffrey, K. R. *Can. J. Chem.* **1995**, *73*, 2196-2207.

(61)   Benevelli, F.; Kolodziejski, W.; Wozniak, K.; Klinowski, J. *Phys. Chem. Chem. Phys.* **2001**, *3*, 1762-1768.

(62)   Udachin, K. A.; Enright, G. D.; Ratcliffe, C. I.; Ripmeester, J. A. *ChemPhysChem* **2003**, *4*, 1059-1064.

(63)   Luo, Y.-R. *Comprehensive Handbook of Chemical Bond Energies*; CRC Press: Boca Raton, **2007**.

(64)   Ma, J. C.; Dougherty, D. A. *Chem. Rev.* **1997**, *97*, 1303-1324.

(65)   Nayeem, A.; Yesinowski, J. P. *J. Chem. Phys.* **1988**, *89*, 4600-4608.

(66)   Casabianca, L. B.; De Dios, A. C. *J. Chem. Phys.* **2008**, *128*, 052201.

5.6 Appendix

Section A1: Powder XRD Characterizations of CPO-27-M Samples
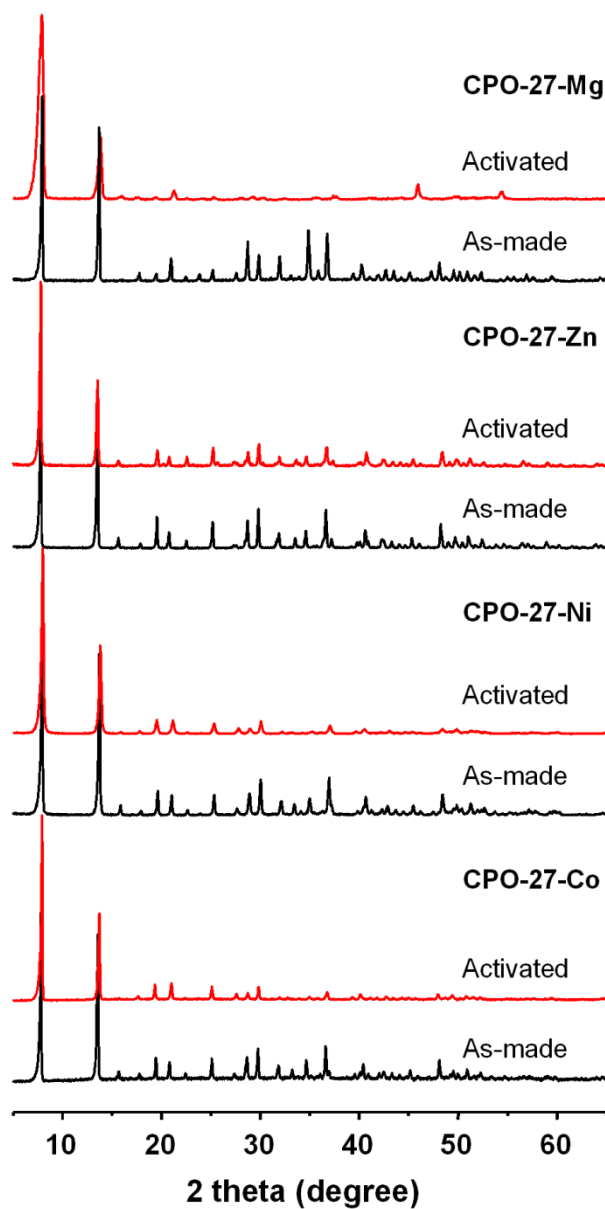
Figure 5-A1: Powder XRD patterns of as-made and activated CPO-27-M samples.

Section A2: Simulated ^{2}H NMR Spectra of the Two-Site Hopping Motions

ΔE = 24 kJ·mol^{-1}, k_0 = 1 × 10^{12} s^{-1} $\qquad$ ΔE = 22 kJ·mol^{-1}, k_0 = 1.2 × 10^{12} s^{-1}
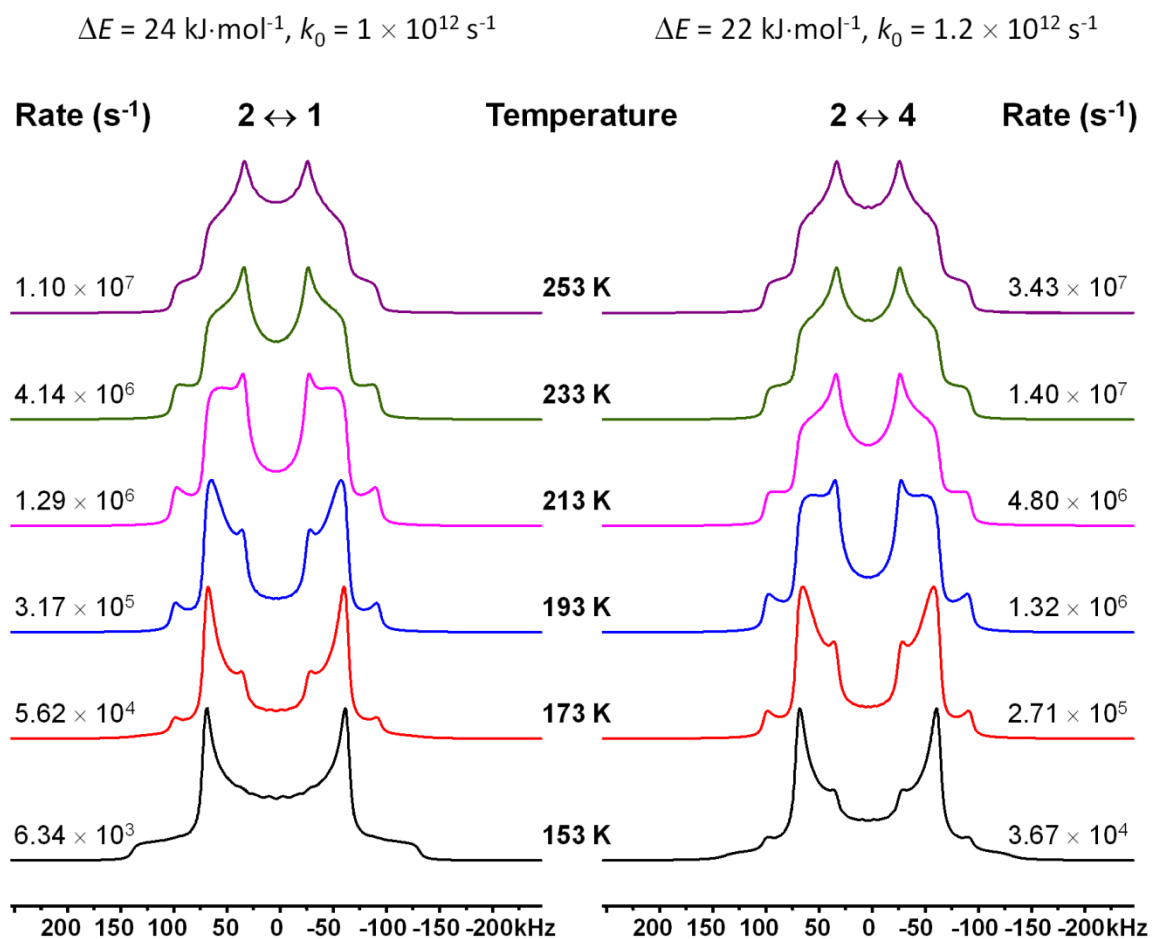
Figure 5-A2: Simulated variable temperature ^{2}H NMR spectra of two close-related two-site hopping motions (2 ↔ 1 and 2 ↔ 4 shown in Figure 5-3).

Section A3: Simulated ^{2}H NMR Spectra of the other Hopping Motions
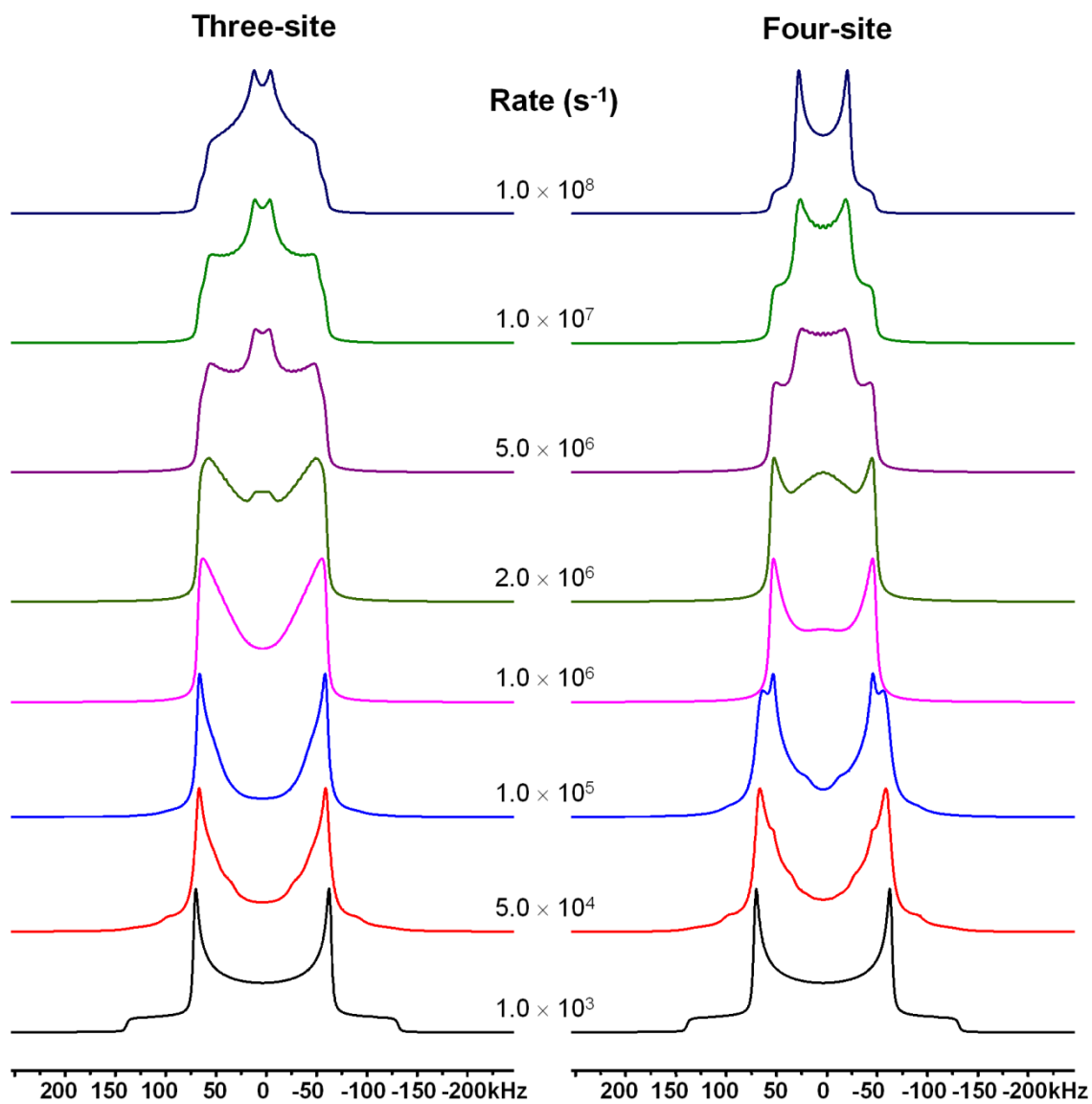
Figure 5-A3: Simulated variable temperature ^{2}H NMR spectra of three- and four- site (in the single *a,b* plane) hopping motions.
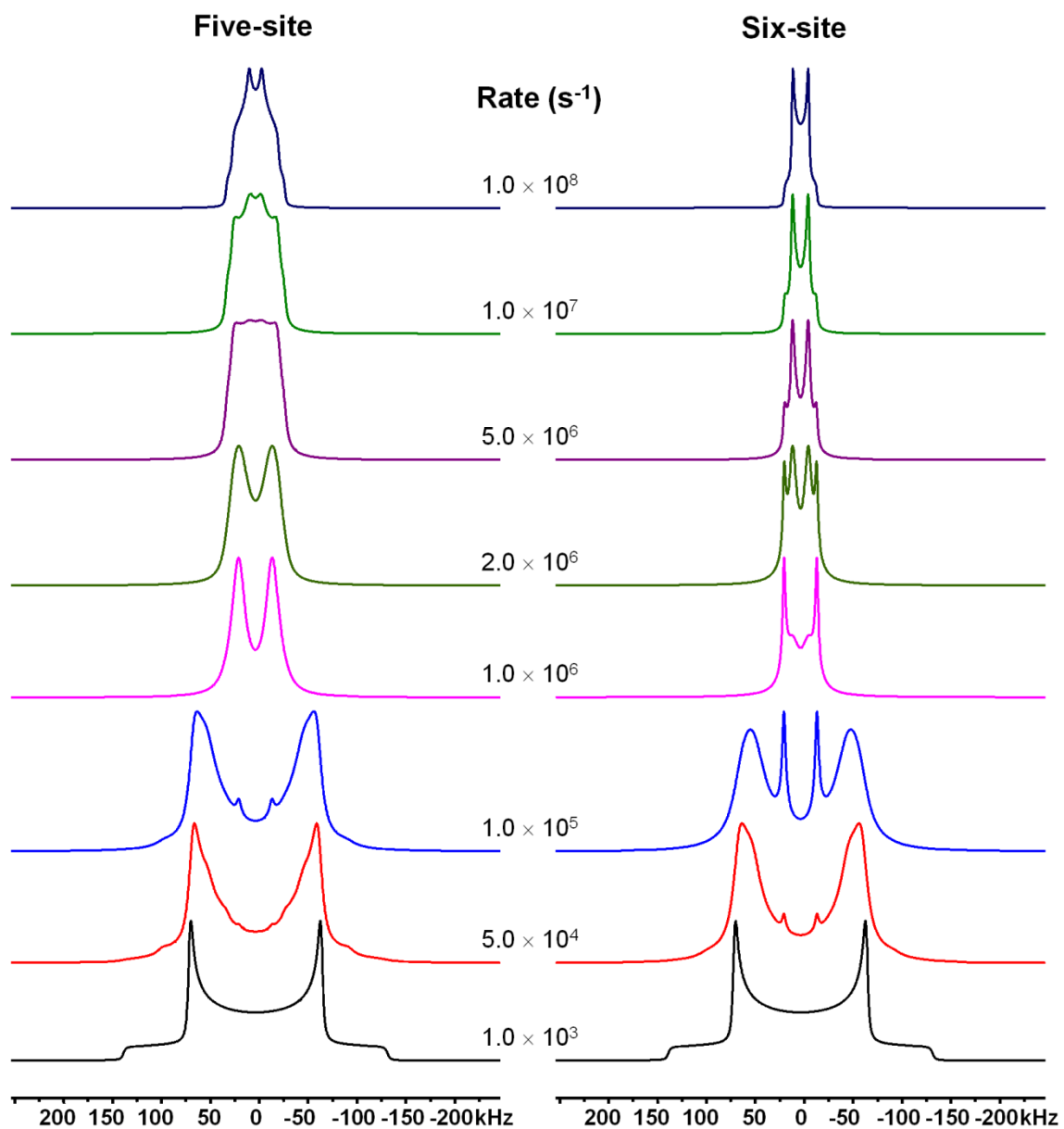
Figure 5-A4: Simulated variable temperature ^{2}H NMR spectra of five- and six- site (in the single *a*,*b* plane) hopping motions.

Chapter 6

6 Identification of Non-Equivalent Framework Oxygen Species in Metal–Organic Frameworks by ^{17}O Solid-State NMR[‡]

6.1 Introduction

One of the most exciting advances in the field of porous materials in recent years is the emergence of a family of hybrid inorganic-organic solids known as metal–organic frameworks (MOFs).[1] MOFs are prepared via self-assembly of metal cations with organic linkers to form 3D networks with many novel topologies. They usually have high thermal stability, permanent porosity, and exceptionally high surface areas, leading to many potentially important applications in areas such as ion-exchange, catalysis, molecular recognition, drug delivery and in particular gas separation and storage. Detailed structural characterization of these industrially relevant materials is essential because understanding the relationship between their properties and the structures allows one to develop new applications and improve the current performance. Although the structures of many MOFs can be determined by single crystal X-ray diffraction, a significant number of MOF structures have to be refined from more limited powder XRD data due to the lack of suitable single crystals. It is even worse for activated MOFs since activation (desolvation) may reduce the crystallinity. In such cases a reliable structure solution requires additional information from complementary techniques such as solid-state NMR (SSNMR) spectroscopy. Indeed, SSNMR experiments have been used extensively for MOF characterization.[2-3] ^{1}H and ^{13}C SSNMR spectroscopy has been routinely used for characterization of organic linkers.[4-8] ^{2}H NMR spectroscopy is employed to examine the flexibility of the framework and the dynamics of the guest species.[9-10] ^{129}Xe NMR spectroscopy has been utilized to study the porosity in the MOF frameworks.[11-13] Very recently, the utility of DNP (dynamic nuclear polarization)-enhanced ^{13}C and ^{15}N NMR

---

spectroscopy in MOF characterization has been reported.[14] SSNMR experiments of several metal centers such as ^{27}Al,[7,15,16] ^{45}Sc,[17] ^{71}Ga,[18] ^{25}Mg[19,20] and ^{67}Zn[21] has been employed to directly characterize the local structures around metal centers.

The oxygen present in various carboxylate ligands is a key constituent of many MOFs. The two oxygens of carboxylate groups often have different bonding modes.[22,23] Certain MOFs have water molecules directly bound to the metal center[23]. Some organic linkers have phenol groups and the phenol oxygen can bind to a metal ion upon deprotonation.[23] Ideally ^{17}O SSNMR spectroscopy should be utilized for identification of these different oxygen species because ^{17}O exhibits a large chemical shift range and is also sensitive to both the electric field gradient (EFG) and the chemical shielding (CS) tensors.[24-28] However, ^{17}O SSNMR work on MOFs has been very rare due to the very low natural abundance (0.037%) of ^{17}O.[29]

In the present work, we were able to directly synthesize two ^{17}O-enriched MOFs with ^{17}O-enriched water as the ^{17}O source, including microporous α-Mg$_3$(HCOO)$_6$[22] and CPO-27-Mg[23] (also known as Mg-MOF-74[30,31] or Mg/DOBDC[32], DOBDC = 2,5-dioxido-1,4-benzenedicarboxylate). The two MOFs are among the most important and frequently examined MOF systems with unique structure features. By acquiring ^{17}O SSNMR spectra at the magnetic field of 21.1 T, we were able to establish the spectral signatures of various non-equivalent framework oxygen species present in the above mentioned MOFs. Our research is also highlighted by the development of a facile approach to estimate the ^{17}O-enrichment degree by time-of-flight secondary ion mass spectrometry (TOF-SIMS).[33-35] The results will serve as a benchmark for characterizing not only the existing MOFs, but also the new MOF-based materials yet to come.

6.2 Experimental Section

6.2.1 Sample Preparation

A typical synthesis of as-made ^{17}O-enriched microporous α-Mg$_3$(HCOO)$_6$ involves mixing 3 mmol Mg(NO$_3$)$_2$·6H$_2$O (Sigma-Aldrich, 99%), 6 mmol formic acid (Alfa Aesar, 97%), 0.25 g ^{17}O-enriched H$_2$O (CortecNet, 41.8% ^{17}O atom) and 10 mL

N,N'-dimethylformamide (DMF, Reagent grade, Caledon) in a 23 mL Teflon-lined autoclave and then heated at 383 K for 2 days. The product was washed with DMF and recovered by vacuum filtration as a white powder. The as-made α-Mg$_3$(HCOO)$_6$ sample was activated under dynamic vacuum at 423 K for 1 d to obtain the activated sample.

^{17}O-enriched CPO-27-Mg was also synthesized solvothermally. Typically, 0.75 mmol 2,5-dioxido-1,4-benzenedicarboxylic acid (H$_4$DOBDC, Sigma-Aldrich, 98%) was first dissolved in a mixture of 0.25 g ^{17}O-enriched H$_2$O (CortecNet, 41.8% ^{17}O atom), 3 mL 1M NaOH(aq) and 10 mL tetrahydrofuran (THF, reagent grade, Caledon). The solution was then heated at 358 K for 12 h in a 23 mL Teflon-lined autoclave. This was followed by slowly adding 1.5 mmol Mg(NO$_3$)$_2$·6H$_2$O to the above solution. The resulting mixture was finally heated at 383 K for 3 days. The as-synthesized CPO-27-Mg was washed by THF and collected by vacuum filtration as a yellow powder. In order to obtain activated CPO-27-Mg, the as-made sample was pre-exchanged with fresh methanol three times and activated under dynamic vacuum at 623 K overnight. The sample was allowed to cool gradually to room temperature under vacuum and sealed in a glass tube.

The identity and phase purity of the ^{17}O-enriched MOFs were examined by powder XRD. Powder XRD patterns (Figure 6-A1, appendix) were recorded on a Rigaku diffractometer using Co Kα radiation (λ = 1.7902 Å). Samples were scanned at 5° ⩽ 2θ ⩽ 65° at a scan rate of 10°/min with a step-size of 0.02°.

To estimate the enrichment degrees of ^{17}O in the frameworks of microporous α-Mg$_3$(HCOO)$_6$ and CPO-27-Mg, time-of-flight secondary ion mass spectrometry (TOF-SIMS)[33] was applied by measuring the ratio of ^{17}O/^{16}O. TOF-SIMS is a surface sensitive analytical technique, which can accurately measure isotope ratios.[34,35] The MOF samples for TOF-SIMS measurement were prepared as follows: Activated MOF powders were pressed in between two silicon wafers (coated with an indium layer). The two wafers were then separated to expose a cross section of the pressed particles. An ION-TOF (Gmbh) TOF-SIMS IV equipped with a Bi cluster liquid metal ion source was used to determine the ratio of ^{17}O to ^{16}O. A 25 keV Bi^{3+} cluster primary pulsed ion beam (10 kHz,

pulse width < 2 ns, target current ~1 pA) was chosen to bombard the surface of the sample to generate secondary ions. Negative secondary ions were extracted from the sample surface, mass separated and their arrival times were detected via a reflection time-of-flight analyzer. The arrival times of ions were converted to mass/charge ratio (m/z) via calibration of $^1H^-$ and $^{12}C^-$. Secondary ion mass spectra were collected for 120 s at 128 × 128 pixels by rastering the Bi^{3+} ion beam over an area (500 μm × 500 μm) at three spots on each sample. The detailed procedures to estimate ^{17}O content by TOF-SIMS were shown in the Appendix. The $^{17}O/^{16}O$ isotope ratios were determined to be 8.2(2)% and 1.5(1)% for microporous α-Mg$_3$(HCOO)$_6$ and CPO-27-Mg, respectively.

6.2.2   NMR Characterizations and Theoretical Calculations

All ^{17}O SSNMR experiments at 21.1 T ($v_0(^{17}O)$ = 122.0 MHz) were conducted on a Bruker Avance II spectrometer at the National Ultrahigh-Field NMR Facility for Solids in Ottawa, Canada. The magic-angle spinning (MAS) spectra were acquired by using the 90°-τ-180° echo sequence[36] with a 4 mm H/X MAS Bruker probe. The samples were packed in ZrO$_2$ rotors for 12 and 18 kHz MAS experiment, respectively. The pulse delay was 2–5 s. The static ^{17}O SSNMR spectrum of as-made α-Mg$_3$(HCOO)$_6$ was also collected using the 90°-τ-90° echo sequence[36]. The ^{17}O chemical shifts were referenced to an external liquid sample of H$_2$O (δ_{iso} = 0 ppm). The liquid water sample was also used for rf power calibration. Typically, the non-selective 90° pulse length is 12 μs, corresponding to a central transition selective 90° pulse of 4 μs. Continuous-wave proton decoupling of a radio frequency field of 80 kHz was used in the static experiment. More detailed spectrometer conditions used in the SSNMR experiments are listed in Table 6-A1. For α-Mg$_3$(HCOO)$_6$ and CPO-27-Mg samples, ^{17}O SSNMR measurements were performed on both as-made and activated samples. Sample-packing was done in the atmospheric environment and no precaution was needed. However, in the case of the activated CPO-27-Mg sample, it had to be packed into an air-tight rotor in a glove box under nitrogen atmosphere to preventing sample from adsorbing water.

^{17}O NMR parameters, including quadrupolar coupling constant (C_Q), asymmetry parameter (η_Q) and isotropic chemical shift (δ_{iso}) were determined by simulations of ^{17}O

MAS spectra using the DMFIT program.[37] The experimental error for each measured parameter was determined by visual comparison of experimental spectra with simulations. The parameter of concern was varied bi-directionally starting from the best-fit value and all other parameters were kept constant, until noticeable differences between the spectra were observed.

^{17}O SSNMR spectra of the MOFs were also acquired at 9.4 T on a Varian Infinity Plus 400 WB ($v_0(^{17}O)$ = 54.2 MHz) spectrometer. A Varian Chemagnetics 5-mm HXY triple-tuned T3 MAS probe was utilized for all MAS experiments (90°-τ-90° echo with continuous-wave proton decoupling), spinning at 10 kHz. Detailed experimental conditions are listed in Table 6-A1 and the spectra are shown in Figure 6-A4. For microporous α-Mg$_3$(HCOO)$_6$, although ^{17}O signals were observed, the signals from different ^{17}O sites overlap with each other and with spinning sidebands as well due to the limitation of the spinning speed which can be achieved. For activated CPO-27-Mg, no signal was observed after 22 hours, which is consistent with the fact that this particular sample has much lower degree of ^{17}O-enrichment. Overall, the factors such as the low sensitivity and the larger quadrupolar broadening at lower field strength as well as the low spinning rates limited by the probe available to us make the ^{17}O spectra acquired at 9.4 T not suitable for analysis. Therefore, they will not be discussed further.

Gauge including projector augmented wave (GIPAW) quantum chemical calculations[38,39] of as-made and activated microporous α-Mg$_3$(HCOO)$_6$ phases were conducted using the CASTEP code (version 4.4, Accelrys Materials Studio). The NMR module was used to calculate the ^{17}O NMR parameters. Unit cell parameters and atomic coordinates were taken from the crystal structures of the MOFs examined.[22] As described in *Chapter 3*, the H positions of four samples were optimized prior to the NMR calculations. The unit cell parameters were not allowed to change since the unit cell dimensions are well defined from the powder XRD. The solvent DMF molecules were kept in the pores. The calculations were performed using ultra-soft pseudopotentials generated from the "on-the-fly" method implemented within the CASTEP. The Generalized Gradient Approximation (GGA) with Perdew, Burke and Ernzerhof (PBE) functional was used. The $C_Q(^{17}O)$ values were calculated from the EFG tensor produced

by the CASTEP calculation using $Q(^{17}O)$ = -2.558×10^{-30} m^2.[40] The isotropic chemical shift for ^{17}O was computed using the correlation δ_{iso} = 287.5 - σ_{iso} (all in ppm), where 287.5 ppm is the absolute shielding value of liquid H$_2$O (δ_{iso} = 0 ppm).[41]

Ab initio calculations of as-made and activated CPO-27-Mg were also performed using Gaussian 09 program[42] running on SHARCNET (www.sharcnet.ca). ^{17}O EFG tensors were calculated using hybrid DFT at B3LYP/6-31G** level, using the GIAO method. The model cluster used in the calculations was truncated from the periodic structures and terminated with H atoms.[23,43] The EFG tensor parameters were extracted from the oxygens surrounding the center Mg ion using the Gaussian output file by the EFGShield program.[44] To obtain the ^{17}O reference shielding, we first carried out geometry optimization on H$_2$O and then calculated its chemical shielding at B3LYP/6-31G** level.

6.3 Results and Discussion

As mentioned earlier, the major obstacle that prevents ^{17}O SSNMR spectroscopy from being used for MOF characterization is the extremely low natural abundance of ^{17}O (0.037%). ^{17}O isotopic enrichment is hence required, with the associated high cost. In this work, depending on the target MOF system, two strategies were used to cost-effectively prepare ^{17}O-enriched MOFs, which are briefly described below. More details are provided in the Experimental Section.

(1) A recent study reported that ^{17}O-enriched oxides can be economically prepared ionothermally with ionic liquid incorporating a trace amount of ^{17}O-enriched water as solvent.[45] Since many MOFs are synthesized using non-aqueous solvents in the presence of a very small amount of water, such situation can also be exploited for making ^{17}O-enriched MOFs effectively. Indeed, we prepared MOF microporous α-Mg$_3$(HCOO)$_6$, by directly reacting solid Mg(NO$_3$)$_2\cdot$6H$_2$O and formic acid in 10 mL DMF with only 0.25 mL ^{17}O-enriched water.

(2) The second method is similar to that used for incorporating ^{17}O into MOF-5.[29] It involves direct ^{17}O-exchange of carboxylate and phenol oxygens with ^{17}O-enriched

water in strong basic (NaOH) solution prior to the addition of metal ions. A similar approach was also used in this work to prepare ^{17}O-enriched CPO-27-Mg.

Estimation of the degree of ^{17}O-enrichment in MOFs was a challenging task as these MOFs do not dissolve in solvents. We established a protocol to evaluate ^{17}O-enrichment in MOFs by using time-of-flight secondary ion mass spectrometry (TOF-SIMS). The ^{17}O/^{16}O isotope ratios of the frameworks estimated for the two ^{17}O-enriched samples of α-Mg$_3$(HCOO)$_6$ and CPO-27-Mg are 8.2(2)% and 1.5(1)%, respectively. When comparing with the ^{17}O/^{16}O ratio of 0.0381% at natural abundance, the degrees of the enrichment are estimated at 215 and 39 times the natural abundance of ^{17}O for α-Mg$_3$(HCOO)$_6$ and CPO-27-Mg, respectively. See the Supporting Information for the detailed data analyses. The efficiency of ^{17}O-enrichment is then evaluated by comparing the measured ^{17}O/^{16}O ratio with the theoretical value, assuming ^{17}O atoms are homogeneously distributed in the reaction mixture.[45] However, whether the solvent is involved in the ^{17}O-exchange is very important for the calculation of theoretical ^{17}O-enrichment. In the current work, stable aprotic solvents (DMF and THF) and low temperature (383 K) conditions were used, implying that the solvents could be considered not to be involved in the ^{17}O-exchange. Therefore, the theoretical values of ^{17}O/^{16}O ratios are 8.9% for microporous α-Mg$_3$(HCOO)$_6$ and 2.9% for CPO-27-Mg, which are also the maximum ^{17}O-enrichment degrees that can be achieved since the incorporation of ^{17}O into the frameworks are usually incomplete. It is noteworthy that the measured ^{17}O/^{16}O ratio of α-Mg$_3$(HCOO)$_6$ is very close to the theoretical value, whereas it is only half for CPO-27-Mg. The observed difference in the efficiency of ^{17}O incorporation must be due to the difference in the reactivity of formic acid and 2,5-dioxido-1,4-benzenedicarboxylic acid with H$_2$^{17}O.

The ^{17}O magic-angle spinning (MAS) spectra of the above-prepared ^{17}O-enriched MOFs were acquired at a magnetic field of 21.1 T. The spectra are sensitive to the oxygen bonding mode to the metal center and can be used to distinguish chemically different oxygen species.

Microporous α-magnesium formate, α-Mg$_3$(HCOO)$_6$ represents the situation where one of the oxygen in carboxylate group is bonded to one metal centre (μ^1-O) and the other oxygen in the same –COO$^-$ group bound to two metal ions (μ^2-O). Microporous α-Mg$_3$(HCOO)$_6$ was first prepared by Rood and co-workers,[22] and is one of the successfully commercialized MOFs.[46-47] Its basic building unit is a MgO$_6$ octahedron with each Mg cation bound to six oxygens from six different formate anions (HCOO$^-$). The framework consists of corner- and edge-sharing MgO$_6$ octahedra with one dimensional channel systems (4.5×5.5 Å^2) along the b direction (Figure 6-1).
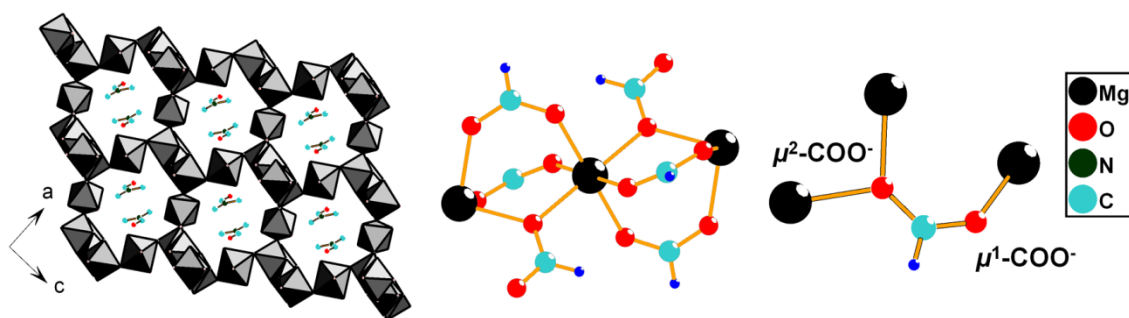
Figure 6-1: Illustrations of the framework with DMF (solvent) in the pore, Mg, and O environments of microporous α-Mg$_3$(HCOO)$_6$. The hydrogens of DMF are omitted for clarity.

The ^{17}O 18 kHz MAS spectrum of the as-made α-Mg$_3$(HCOO)$_6$ spun at 18 kHz was first acquired at the field strength of 21.1 T is shown in Figure 6-2a. It contains two separate resonances. The spectral simulations yielded the following NMR parameters (Table 6-1): site 1: C_Q = 6.8(3) MHz, η_Q = 0.80(10), δ_{iso} = 230(5) ppm; site 2: C_Q = 8.0(3) MHz, η_Q = 0.45(10), δ_{iso} = 289(5) ppm. The chemical shifts and the C_Q values are in the range of carboxylate oxygen reported in the literature.[25-26] Thus, the ^{17}O MAS spectrum clearly shows that there are at least two groups of non-equivalent oxygens from the formate anions. The crystal structure indicates that there are 12 non-equivalent oxygen sites.[22] They can be further divided into two groups based on their bonding modes. Six independent oxygens adopt μ^2-O bonding mode, while the other six crystallographically non-equivalent O sites adopt μ^1-O mode. It appears that the two observed resonances originate from μ^2-O and μ^1-O oxygens. To confirm this argument and further assign the

signals, GIPAW DFT calculations were carried out and the results (Table 6-A2) clearly show that six μ^2-oxygens have very similar EFG parameters and chemical shifts: C_Q = 5.98–6.80 MHz; η_Q = 0.80–0.99, δ_{iso} = 246.8–265.9 ppm and that the NMR parameters of the six μ^1-oxygens are akin to each other: C_Q = 7.94–8.03 MHz; η_Q = 0.26–0.31, δ_{iso} = 307.6–319.7 ppm. Thus, we can assign the signals at 230 and 289 ppm to the six μ^2- and the six μ^1-oxygens, respectively. This sample also illustrates why we had to carry out the MAS experiment at a very high magnetic field as it is evident from Figure 6-2 that the peaks due to different bonding modes are barely resolved even at 21.1 T. For each bonding mode, the local environments of six crystallographically non-equivalent oxygen sites are so close that we were not able to distinguish them further due to their very similar NMR parameters. To separate these sites with close environments, resolution-enhancement techniques including double-rotation (DOR),[48,49] multiple-quantum MAS (MQMAS),[50] and the satellite transition MAS (STMAS)[51] should be used. They can also be combined with sensitivity enhancement method such as DNP.[52]
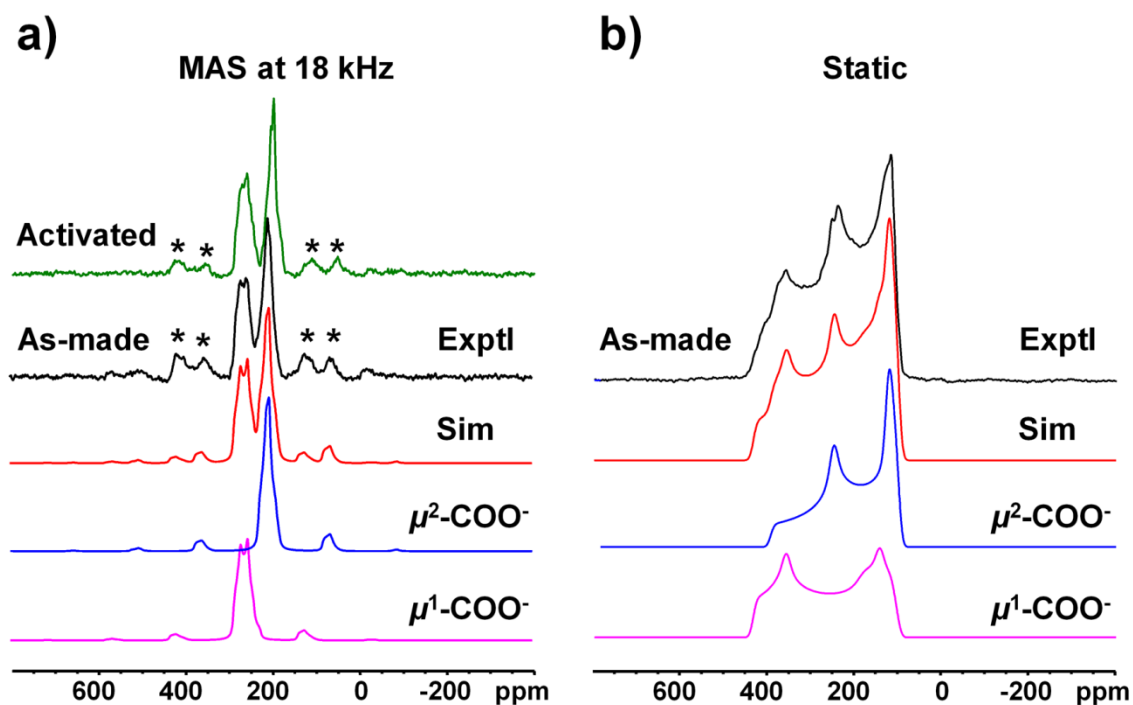
Figure 6-2: Experimental and simulated ^{17}O (a) MAS and (b) static SSNMR spectra of microporous α-Mg$_3$(HCOO)$_6$ at 21.1 T. *: spinning sidebands.

Table 6-1: Experimental ^{17}O NMR parameters of the MOF samples.

Sample	O site	C_Q (MHz)	η_Q	δ_{iso} (ppm)	Ω (ppm)	κ
α-Mg$_3$(HCOO)$_6$	μ^2–COO$^-$	6.8(3)	0.80(10)	230(5)	260(10)[a]	-0.4(1)[a]
	μ^1–COO$^-$	8.0(3)	0.45(10)	289(5)	220(10)[b]	0.5(1)[b]
CPO-27-Mg	Ph–O$^-$	9.1(3)	0.60(10)	87(10)		
	μ^2–COO$^-$	7.3(3)	0.10(10)	226(10)		
	μ^1–COO$^-$	7.1(3)	0.70(10)	251(10)		

a: The Euler angles between CSA tensors and EFG tensors are: $\alpha = 60°$, $\beta = 0°$, $\gamma = 30°$.

b: The Euler angles between CSA tensors and EFG tensors are: $\alpha = 10°$, $\beta = 10°$, $\gamma = 10°$.

The ^{17}O static spectrum of the as-made α-Mg$_3$(HCOO)$_6$ was also collected at 21.1 T (Figure 6-2b). The line shape simulated with the ^{17}O EFG parameters is distinct from the experimental line shape, indicating that the static pattern is broadened by CSA interactions as well. The ^{17}O CSA tensor parameters obtained from the static experiment are: $\Omega = 260(10)$ ppm, $\kappa = -0.4(1)$ for μ^2-oxygens and $\Omega = 220(10)$ ppm, $\kappa = 0.5(1)$ for μ^1-oxygens, respectively. As mentioned earlier, it is not possible to separate the CSA parameters for individual crystallographically non-equivalent O sites.

The ^{17}O 18 kHz MAS spectrum of the activated α-Mg$_3$(HCOO)$_6$ was acquired and shown in Figure 6-2a. It looks almost identical with the spectrum of the as-made sample, agreeing with the fact that the coordination modes of oxygens do not change after activation. The calculated ^{17}O NMR parameters are also similar to the values of the as-made sample (Table 6-A2).
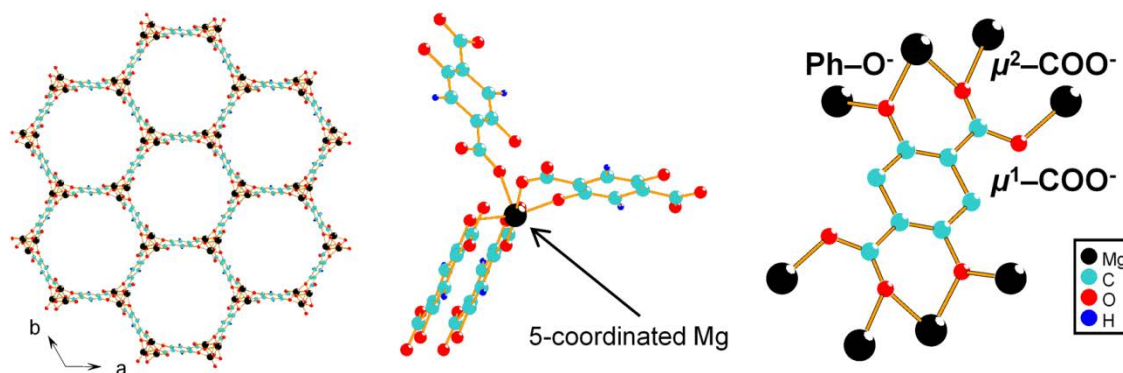
Figure 6-3: Illustrations of the framework, Mg and O environments of activated CPO-27-Mg.
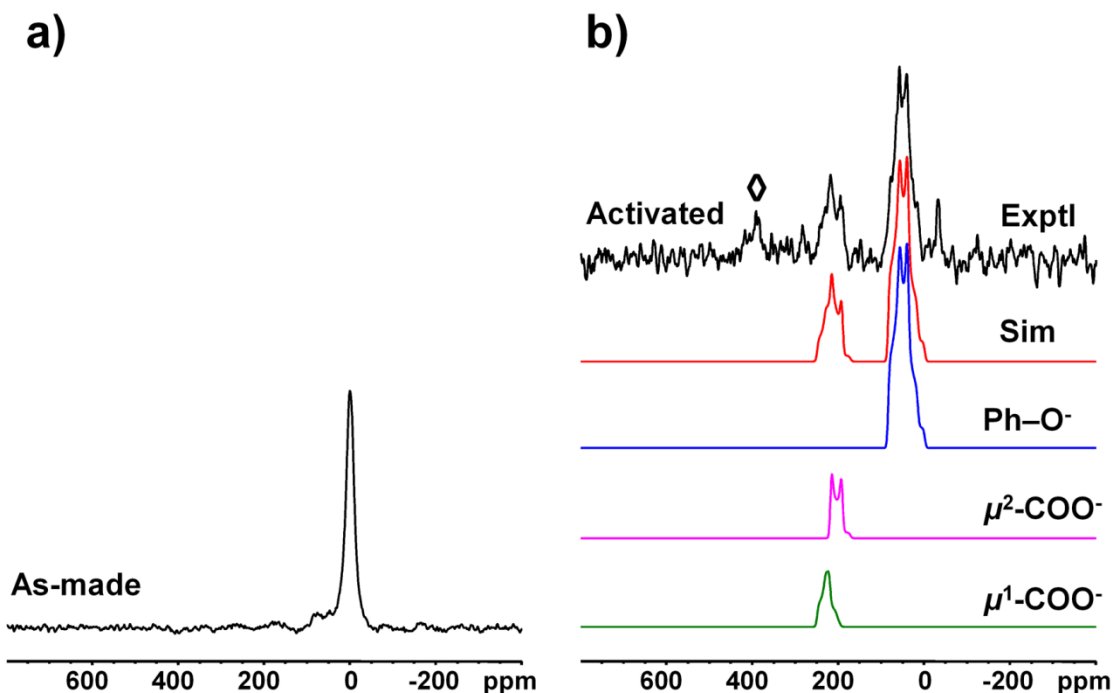
Figure 6-4: Experimental and simulated ^{17}O MAS SSNMR spectra of (a) as-made and (b) activated CPO-27-Mg at 21.1 T. ◊: ^{17}O background signal from ZrO_2 rotor. (Ref. 53)

CPO-27-Mg is another Mg-containing MOF with potential industrial applications due to its exceptional ability of adsorbing CO_2.[32] The precursor of the organic linker is 2,5-dioxido-1,4-benzenedicarboxylic acid which contains two phenol and two carboxylic groups. Upon deprotonation, oxygens from all four groups in the same linker are bound to the Mg atoms to form a honeycomb structure with a one-dimensional channel system (Figure 6-3). As-made phase contains MgO_6 octahedra with each metal ion bound to five oxygens from four 2,5-dioxido-1,4-benzenedicarboxylate (DOBDC) ligands.[23] The sixth coordination site is occupied by a water molecule, which can be removed upon dehydration. The ^{17}O 12 kHz MAS spectrum of as-made CPO-27-Mg is overwhelmingly dominated by a broad peak with Gaussian shape centered at around 0 ppm (Figure 6-4a). This very strong peak is due to the large amount of water molecules occluded inside of the channels. In order to clearly observe carboxylate and phenol oxygens, we examined the dehydrated phase. Its ^{17}O MAS spectrum is illustrated in Figure 6-4b, which contains

several resonances. The peak centered at around 80 ppm is due to the phenol oxygen bound to the Mg ions based on the shift value.[25-26] The signal at about 230 ppm is assigned to the framework carboxylate oxygen. We noticed that the intensity of the carboxylate oxygens is much weaker than that of the phenol oxygen. We further obtained a MAS spectrum by using a much longer pulse delay of 20 s (spectrum not shown) which indicates that the difference in intensity is not due to spin-lattice relaxation time (T_1). It is likely that during the synthesis, the phenol oxygen undergoes a much faster exchange with ^{17}O in water. There is a small sharp feature at about -20 ppm which might be due to the Mg–OH formed during the dehydration process.[54] The ^{17}O NMR parameters of dehydrated CPO-27-Mg simulated from the MAS spectrum are shown in Table 6-1. The peak assignment is also confirmed by our *ab initio* calculation results (Table 6-A3).

6.4 Conclusions

In this work, we successfully prepared two prototypical ^{17}O-enriched MOFs. Due to the diversity of MOF-based materials, different types of MOFs may require different isotopic enrichment methods to effectively incorporate ^{17}O from ^{17}O-enriched H_2O. Two synthetic strategies for ^{17}O-enrichment were discussed. Using these ^{17}O-enriched MOFs we were able to acquire ^{17}O SSNMR spectra at a magnetic field of 21.1 T. They provide distinct spectral signatures of various key oxygen species commonly existing in representative MOFs. We demonstrate that ^{17}O SSNMR spectroscopy can be used to differentiate chemically non-equivalent oxygens. The synthetic approaches for preparation of ^{17}O-enriched sample described in this paper are fairly simple and cost-effective. The ^{17}O-enrichment degrees were measured by using a facile approach of TOF-SIMS. It is hoped that this work will encourage other researchers to use ^{17}O SSNMR spectroscopy for MOF characterization.

6.5 References

(1)   Special issue for Metal–Organic Frameworks: Zhou, H.-C.; Long, J. R.; Yaghi, O. M. *Chem. Rev.* **2012**, *112*, 673-1268.

(2)   Sutrisno, A.; Huang, Y. *Solid State Nucl. Magn. Reson.* **2013**, *49-50*, 1-11.

(3)   Hoffmann, H. C.; Debowski, M.; Mueller, P.; Paasch, S.; Senkovska, I.; Kaskel, S.; Brunner, E. *Materials* **2012**, *5*, 2537-2572.

(4)   Dawson, D. M.; Jamieson, L. E.; Mohideen, M. I. H.; McKinlay, A. C.; Smellie, I. A.; Cadou, R.; Keddie, N. S.; Morris, R. E.; Ashbrook, S. E. *Phys. Chem. Chem. Phys.* **2013**, *15*, 919-929.

(5)   Besara, T.; Jain, P.; Dalal, N. S.; Kuhns, P. L.; Reyes, A. P.; Kroto, H. W.; Cheetham, A. K. *Proc. Natl. Acad. Sci. U. S. A.* **2011**, *108*, 6828-6832.

(6)   Gul-E-Noor, F.; Jee, B.; Mendt, M.; Himsl, D.; Poeppl, A.; Hartmann, M.; Haase, J.; Krautscheid, H.; Bertmer, M. *J. Phys. Chem. C* **2012**, *116*, 20866-20873.

(7)   Jiang, Y.; Huang, J.; Marx, S.; Kleist, W.; Hunger, M.; Baiker, A. *J. Phys. Chem. Lett.* **2010**, *1*, 2886-2890.

(8)   Devautour-Vinot, S.; Maurin, G.; Serre, C.; Horcajada, P.; Paula da Cunha, D.; Guillerm, V.; de Souza Costa, E.; Taulelle, F.; Martineau, C. *Chem. Mater.* **2012**, *24*, 2168-2177.

(9)   Kolokolov, D. I.; Stepanov, A. G.; Guillerm, V.; Serre, C.; Frick, B.; Jobic, H. *J. Phys. Chem. C* **2012**, *116*, 12131-12136.

(10)   Shustova, N. B.; Ong, T.-C.; Cozzolino, A. F.; Michaelis, V. K.; Griffin, R. G.; Dinca, M. *J. Am. Chem. Soc.* **2012**, 134, 15061-15070.

(11)   Pawsey, S.; Moudrakovski, I.; Ripmeester, J.; Wang, L.-Q.; Exarhos, G. J.; Rowsell, J. L. C.; Yaghi, O. M. *J. Phys. Chem. C* **2007**, *111*, 6060-6067.

(12)   Springuel-Huet, M.-A.; Nossov, A.; Adem, Z.; Guenneau, F.; Volkringer, C.; Loiseau, T.; Férey, G.; Gedeon, A. *J. Am. Chem. Soc.* **2010**, *132*, 11599-11607.

(13)   Ooms, K. J.; Wasylishen, R. E. *Microporous Mesoporous Mater.* **2007**, *103*, 341-351.

(14)   Rossini, A. J.; Zagdoun, A.; Lelli, M.; Canivet, J.; Aguado, S.; Ouari, O.; Tordo, P.; Rosay, M.; Maas, W. E.; Coperet, C.; Farrusseng, D.; Emsley, L.; Lesage, A. *Angew. Chem., Int. Ed.* **2012**, *51*, 123-127.

(15)   Loiseau, T.; Serre, C.; Huguenard, C.; Fink, G.; Taulelle, F.; Henry, M.; Bataille, T.; Férey, G. *Chem. Eur. J.* **2004**, *10*, 1373-1382.

(16)   Loiseau, T.; Lecroq, L.; Volkringer, C.; Marrot, J.; Ferey, G.; Haouas, M.; Taulelle, F.; Bourrelly, S.; Llewellyn, P. L.; Latroche, M. *J. Am. Chem. Soc.* **2006**, *128*, 10223-10230.

(17)   Mowat, J. P. S.; Miller, S. R.; Slawin, A. M. Z.; Seymour, V. R.; Ashbrook, S. E.; Wright, P. A. *Microporous Mesoporous Mater.* **2011**, *142*, 322-333.

(18)   Hajjar, R.; Volkringer, C.; Loiseau, T.; Guillou, N.; Marrot, J.; Ferey, G.; Margiolaki, I.; Fink, G.; Morais, C.; Taulelle, F. *Chem. Mater.* **2011**, *23*, 39-47.

(19)   Xu, J.; Terskikh, V. V.; Huang, Y. *J. Phys. Chem. Lett.* **2013**, *4*, 7-11.

(20)   Xu, J.; Terskikh, V. V.; Huang, Y. *Chem. Eur. J.* **2013**, *19*, 4432-4436.

(21)   Sutrisno, A.; Terskikh, V. V.; Shi, Q.; Song, Z.; Dong, J.; Ding, S. Y.; Wang, W.; Provost, B. R.; Daff, T. D.; Woo, T. K.; Huang, Y. *Chem. Eur. J.* **2012**, *18*, 12251-12259.

(22)   Rood, J. A.; Noll, B. C.; Henderson, K. W. *Inorg. Chem.* **2006**, *45*, 5521-5528.

(23)   Dietzel, P. D. C.; Blom, R.; Fjellvaag, H. *Eur. J. Inorg. Chem.* **2008**, *2008*, 3624-3632.

(24)   Ashbrook, S. E.; Smith, M. E. *Chem. Soc. Rev.* **2006**, *35*, 718-735.

(25)   Wu, G. *Prog. Nucl. Magn. Reson. Spectrosc.* **2008**, *52*, 118-169.

(26)   Gerothanassis, I. P. *Prog. Nucl. Magn. Reson. Spectrosc.* **2010**, *56*, 95-197.

(27)   Bonhomme, C.; Coelho, C.; Baccile, N.; Gervais, C.; Azais, T.; Babonneau, F. *Acc. Chem. Res.* **2007**, *40*, 738-746.

(28)   Yamada, K. *Annu. Rep. NMR Spectrosc.* **2010**, *70*, 115-158.

(29)   Mueller, M.; Hermes, S.; Kaehler, K.; van den Berg, M. W. E.; Muhler, M.; Fischer, R. A. *Chem. Mater.* **2008**, *20*, 4576-4587.

(30)   Rosi, N. L.; Kim, J.; Eddaoudi, M.; Chen, B.; O'Keeffe, M.; Yaghi, O. M. *J. Am. Chem. Soc.* **2005**, *127*, 1504-1518.

(31)   McDonald, T. M.; lee, W. R.; Mason, J. A.; Wiers, B. M.; Hong, C. S.; Long, J. R. *J. Am. Chem. Soc.* **2012**, *134*, 7056-7065.

(32)   Caskey, S. R.; Wong-Foy, A. G.; Matzger, A. J. *J. Am. Chem. Soc.* **2008**, *130*, 10870-10871.

(33)   Benninghoven, A. *Angew. Chem., Int. Ed.* **1994**, *33*, 1023-1043.

(34)   Stephan, T. *Planet. Space Sci.* **2001**, *49*, 859-906.

(35)   Ohlhausen, J. A.; Coker, E. N.; Ambrosini, A.; Miller, J. E. *Surf. Interface Anal.* **2013**, *45*, 320-323.

(36)   Kunwar, A. C.; Turner, G. L.; Oldfield, E. *J. Magn. Reson.* **1986**, *69*, 124-127.

(37)   Massiot, D.; Fayon, F.; Capron, M.; King, I.; Le Calve, S.; Alonso, B.; Durand, J.-O.; Bujoli, B.; Gan, Z.; Hoatson, G. *Magn. Reson. Chem.* **2002**, *40*, 70-76.

(38)   Charpentier, T. *Solid State Nucl. Magn. Reson.* **2011**, *40*, 1-20.

(39)   Bonhomme, C.; Gervais, C.; Babonneau, F.; Coelho, C.; Pourpoint, F.; Azais, T.; Ashbrook, S. E.; Griffin, J. M.; Yates, J. R.; Mauri, F.; Pickard, C. J. *Chem. Rev.* **2012**, *112*, 5733-5779.

(40)   Pyykkö, P. *Mol. Phys.* **2008**, *106*, 1965-1974.

(41)   Wasylishen, R. E.; Bryce, D. L. *J. Chem. Phys.* **2002**, *117*, 10061-10066.

(42)   Frisch, M. J. *Gaussian 09*, revision A.1; Gaussian, Inc.: Wallingford, CT, 2009.

(43)   Wu, H.; Zhou, W.; Yildirim, T. *J. Am. Chem. Soc.* **2009**, *131*, 4995-5000.

(44)   Adiga, S.; Aebi, D.; Bryce, D. L. *Can. J. Chem.* **2007**, *85*, 496-505.

(45) Griffin, J. M.; Clark, L.; Seymour, V. R.; Aldous, D. W.; Dawson, D. M.; Iuga, D.; Morris, R. E.; Ashbrook, S. E. *Chem. Sci.* **2012**, *3*, 2293-2300.

(46) Leung, E.; Mueller, U.; Cox, G.; Hoeffken, H. W. *WO 2009115513 A1*, BASF SE, Germany, WO, **2009**, p. 21.

(47) Leung, E.; Mueller, U.; Cox, G. *WO 2010106121 A1*, BASF SE, Germany, WO, **2010**, p. 12.

(48) Samoson, A.; Lippmaa, E.; Pines, A. *Mol. Phys.* **1988**, *65*, 1013-1018.

(49) Chmelka, B. F.; Mueller, K. T.; Pines, A.; Stebbins, J.; Wu, Y.; Zwanziger, J. W. *Nature* **1989**, *339*, 42-43.

(50) Frydman, L.; Harwood, J. S. *J. Am. Chem. Soc.* **1995**, *117*, 5367-5368.

(51) Gan, Z. H. *J. Am. Chem. Soc.* **2000**, *122*, 3242-3243.

(52) Blanc, F.; Sperrin, L.; Jefferson, D. A.; Pawsey, S.; Rosay, M.; Grey, C. P. *J. Am. Chem. Soc.* **2013**, *135*, 2975-2978.

(53) O'Dell, L. A.; Savin, S. L. P.; Chadwick, A. V.; Smith, M. E. *Faraday Discuss.* **2007**, *134*, 83-102.

(54) van Eck, E. R. H.; Smith, M. E. *J. Chem. Phys.* **1998**, *108*, 5904-5912.

6.6 Appendix

Section A1: Powder XRD Characterizations of CPO-27-Mg Samples
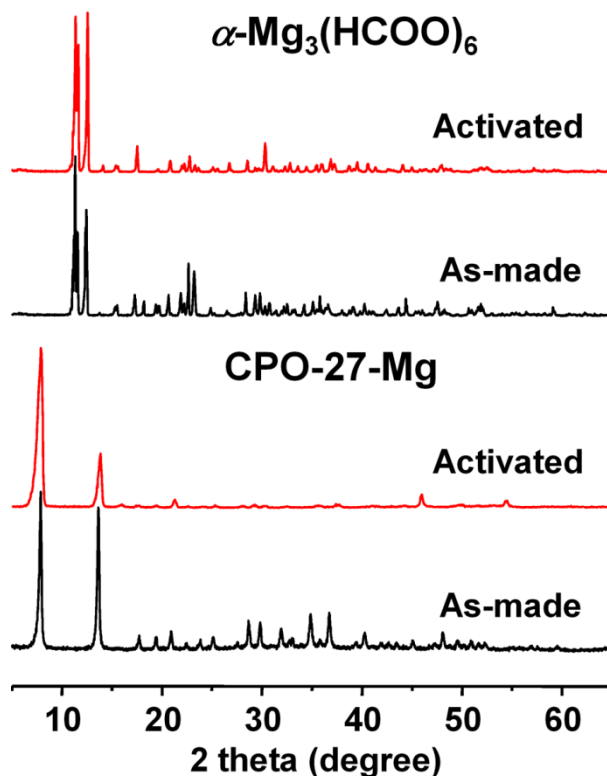
Figure 6-A1: Powder XRD patterns of [17]O-enriched MOF samples.

Section A2: The Procedures for Estimating [17]O-Enrichment by TOF-SIMS

In this work, we used the O_2^- isotope pattern to estimate [17]O-enrichment. At natural abundance, the relative intensities of the three peaks associated with O_2^- at m/z 32 ($^{16}O_2^-$), 33 ($^{16}O^{17}O^-$) and 34 ($^{16}O^{18}O^-$) are 99.525, 0.076 and 0.399%, respectively. Thus, at natural abundance, the ratio of $^{16}O^{18}O^-/^{16}O_2^-$ theoretically should be 0.401%. To check the viability of the TOF-SIMS approach, we first performed a control experiment where the ratio of $^{16}O^{18}O^-/^{16}O_2^-$ was directly measured on the α-Mg$_3$(HCOO)$_6$ which is not [17]O-labeled. Its mass spectrum is shown in Figure 6-A2. The measured $^{16}O^{18}O^-/^{16}O_2^-$ ratio is 0.418(68)%, which is consistent with the theoretical prediction.

We then proceeded to record the mass spectra of two [17]O-enriched samples (Figure 6-A2). Compared to the control experiment, the intensity of the peak at m/z 34 for [17]O-enriched samples increases significantly, which can be attributed to $^{17}O_2^-$. Upon removing the contribution (0.401%) from the natural abundance O_2^- isotopomer at m/z 34 (*i.e.*, $^{16}O^{18}O^-$), we obtain ratios of $^{17}O_2^-/^{16}O_2^-$ from the intensities of the peaks at m/z 32 and 34. Assuming $^{17}O_2^-/^{16}O_2^- = {}^{17}O/^{16}O$, the $^{17}O/^{16}O$ isotope ratios of the frameworks are therefore estimated at 8.2(2)% and 1.5(1)%, corresponding to 215 and 39 times the natural abundance of ^{17}O for the two [17]O-enriched samples of α-Mg$_3$(HCOO)$_6$ and CPO-27-Mg, respectively.
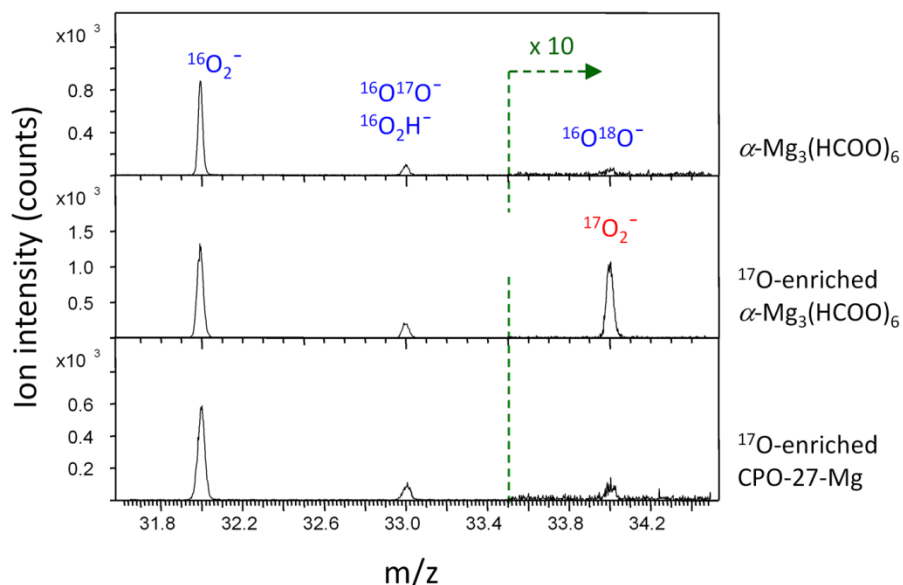
Figure 6-A2: Secondary ion mass spectra in O_2^- region for the MOF samples.

Oxygen-related ion images in Figure 6-A3a obtained on a crystal of control α-Mg$_3$(HCOO)$_6$ show the natural abundance of $^{18}O^-$ and $^{16}O^{18}O^-$ at m/z 18 and 34, respectively. With the [17]O-enrichment, as shown in Figure 6-A3b, the ion intensities at these two m/z positions increase significantly and are dominated by $^{17}OH^-$ and $^{17}O_2^-$, respectively. Also shown are the abundant O^- and OH^- ions. The ion image of MgO$_2$H$^-$ is included to represent magnesium in the two α-Mg$_3$(HCOO)$_6$ samples. It is also evident from the ion image that ^{17}O was incorporated into the crystals homogenously.

Field of view: 217.8 × 217.8 μm²

16O	16OH	18O	16O₂	16O18O	Mg16O₂H
tc:1.078e+6	tc:1.061e+6	tc:4.113e+3	tc:3.289e+4	tc:2.910e+2	tc:3.463e+4

Field of view: 121.1 × 121.1 μm²

16O	17O+16OH	17OH	16O₂	17O₂	Mg16O₂H
tc:1.540e+6	tc:1.403e+6	tc:1.208e+5	tc:4.431e+4	tc:3.779e+3	tc:3.165e+4
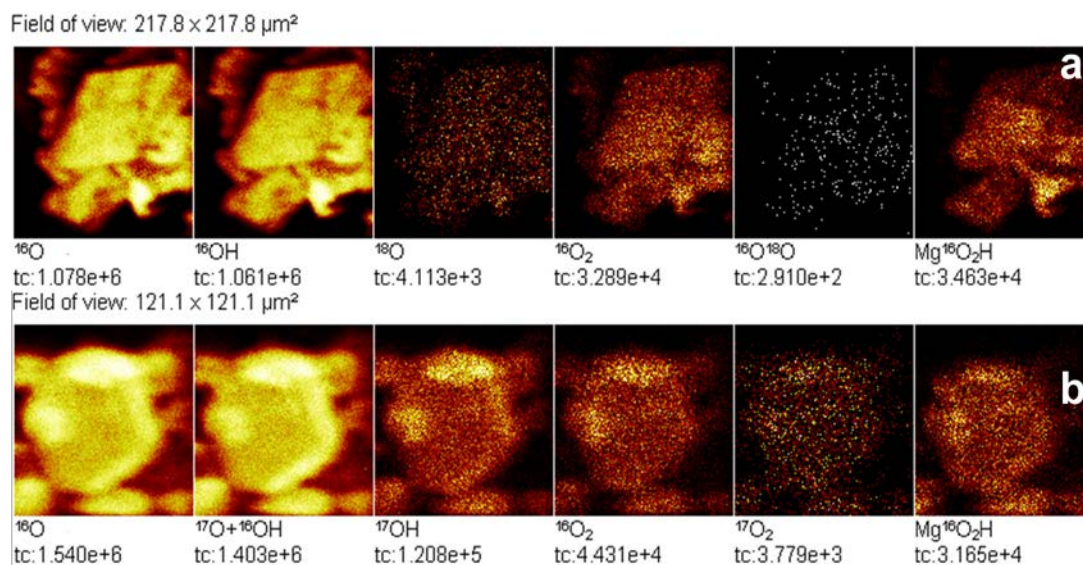
Figure 6-A3: Oxygen-related ion images obtained on a crystal on (a) the control and (b) the ^{17}O-enriched α-Mg$_3$(HCOO)$_6$. The peaks at m/z 18 and 34 in (a) are assigned to ^{18}O$^-$ and ^{16}O^{18}O$^-$, reflecting the natural abundance of the isotopes of O and O$_2$, respectively. The increased intensities observed at m/z 18 and 34 in (b) are attributed to the enriched ^{17}O as ^{17}OH$^-$ and ^{17}O$_2^-$, respectively.

Section A2: Solid-State NMR Characterizations

Table 6-A1: ^{17}O SSNMR measurement conditions.

Sample	Field (T)	v_{rot} (kHz)	90° pulse (μs)	Pulse delay (s)	Number of scan	Experiment time (h)
α-	21.1	18	4	5	3072	4.2
Mg$_3$(HCOO)$_6$	9.4	10	2.3	1	81920	22.2
CPO-27-Mg	21.1	12	4	2	28672	15.6
	9.4	10	2.3	1	81920	22.2
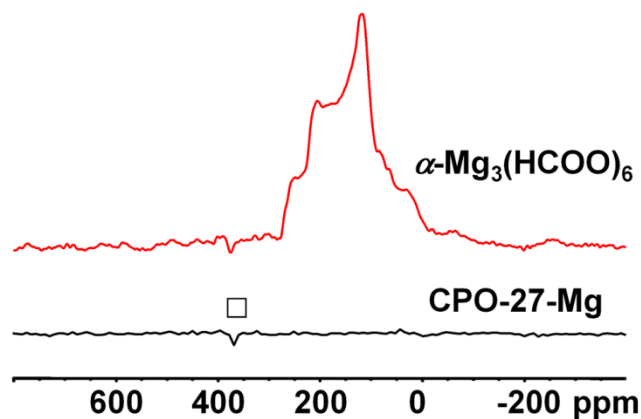
Figure 6-A4: ^{17}O MAS spectra of MOFs at 9.4 T. □: transmitter artifact.

Table 6-A2: ^{17}O NMR parameters of α-Mg$_3$(HCOO)$_6$ using the CASTEP code.

Sample	O site	O mode	$|C_Q|$ (MHz)	η_Q	δ_{iso} (ppm)
As-made	O1	μ^2–COO$^-$	6.80	0.80	257.3
	O3	μ^2–COO$^-$	6.30	0.97	246.8
	O5	μ^2–COO$^-$	6.12	0.96	257.8
	O7	μ^2–COO$^-$	6.67	0.86	265.9
	O9	μ^2–COO$^-$	5.98	0.99	251.8
	O11	μ^2–COO$^-$	6.26	0.92	257.1
	O2	μ^1–COO$^-$	8.02	0.26	319.7
	O4	μ^1–COO$^-$	7.94	0.30	308.3
	O6	μ^1–COO$^-$	7.88	0.31	307.6
	O8	μ^1–COO$^-$	7.97	0.30	308.1
	O10	μ^1–COO$^-$	8.03	0.29	310.7
	O12	μ^1–COO$^-$	7.97	0.29	309.8
Activated	O1	μ^2–COO$^-$	6.64	0.80	249.9
	O3	μ^2–COO$^-$	6.37	0.89	247.5
	O5	μ^2–COO$^-$	6.03	0.97	245.4
	O7	μ^2–COO$^-$	6.59	0.88	259.0
	O9	μ^2–COO$^-$	6.90	0.98	241.5
	O11	μ^2–COO$^-$	6.10	0.93	253.0
	O2	μ^1–COO$^-$	8.01	0.27	313.6
	O4	μ^1–COO$^-$	7.90	0.26	309.4
	O6	μ^1–COO$^-$	7.80	0.31	296.4
	O8	μ^1–COO$^-$	7.84	0.29	302.5
	O10	μ^1–COO$^-$	7.99	0.28	302.8
	O12	μ^1–COO$^-$	7.88	0.25	309.3

Table 6-A3: ^{17}O NMR parameters of CPO-27-Mg calculated using Gaussian 09.

Sample	O site	O mode	$|C_Q|$ (MHz)	η_Q	δ_{iso} (ppm)
As-made	O1	μ^1–COO$^-$	7.25	0.91	263.0
	O2	μ^2–COO$^-$	7.54	0.69	264.7
	O3	Ph–O$^-$	9.74	0.52	142.7
	O4	H_2O	10.81	0.59	-2.9
Activated	O1	μ^1–COO$^-$	6.86	0.96	228.8
	O2	μ^2–COO$^-$	6.88	0.90	186.5
	O3	Ph–O$^-$	8.45	0.66	79.8

Chapter 7

7 A Comprehensive Study of Microporous Titanosilicates by Multinuclear Solid-State NMR Spectroscopy

7.1 Introduction

A variety of titanosilicate-based materials are now being extensively studied due to their potential industrial importance in the areas of ion exchange,[1-4] catalysis,[5-8] and adsorption.[9,10] On one hand, medium-pore microporous titanosilicates, such as sitinakite[11] and GTS-1,[12-14] have been suggested as possible materials for the removal of radioactive $^{137}Cs^+$ and $^{90}Sr^{2+}$ from nuclear waste solutions because of their high ion selectivity and radiation stability. On the other hand, large-pore microporous titanosilicates are another type of materials that have also attracted tremendous attentions in the recent decades. A large number of studies have been devoted to two well-known members, ETS-4 and ETS-10,[15] owing to their large twelve-member rings (12-rings). The structures of microporous titanosilicates are distinct from classical aluminosilicate zeolites in terms of coordination environments of framework cations: they can posses 5- and/or 6-coordinated Ti^{4+} rather than the 4-coordinated Al^{3+} in zeolites.[16] Moreover, such TiO_5 and TiO_6 polyhedra can interconnect with each other, forming one-dimensional edge- or corner-shared chains or clusters,[11-14,16-19] whereas the direct Al–O–Al connectivity is strictly forbidden in zeolites. Such unique structural features of the frameworks are considered to be responsible for the novel properties of microporous titanosilicates.[1-10] Charge-balancing extra-framework counter cations, such as Na^+ and K^+, also play an important role in the properties of microporous titanosilicates.[9-14] Different cations have different affinity to the negatively charged framework, and the change of cation locations often leads to the transformation between different phases.[12-14,20,21]

Thorough structural characterization of microporous titanosilicates is therefore essential to understand the relationship between their structures and properties. However, for many microporous titanosilicates, it is difficult to obtain suitable crystals for single-crystal X-ray diffractions experiments. In such cases, their crystal structures are usually determined based on the more limited powder XRD data. The situation is even worse for

samples with nonstoichiometric compositions,[16] disordered extra-framework counter cations,[12] or disordered frameworks.[15] Solid-state nuclear magnetic resonance (SSNMR) spectroscopy, as a technique complementary to XRD, has widespread applications in the characterization of solid materials including both crystalline and disordered phases,[22] because it can capture the local structural information around the nucleus of interest. SSNMR spectroscopy is hence very suitable for the investigation of microporous titanosilicates: $^{47/49}$Ti SSNMR spectroscopy can be used to probe the coordination environment of Ti^{4+} cations inside of the framework; ^{23}Na and ^{39}K SSNMR spectroscopy allow one to study the extra-framework Na^+ and K^+ species; whereas ^{29}Si chemical shifts are very sensitive to the nearest-neighbor cations around 4-coordinated Si^{4+}.

Despite the importance of $^{47/49}$Ti and ^{39}K SSNMR spectroscopy, previous reports of microporous titanosilicates were mainly focused on ^{29}Si and ^{23}Na SSNMR spectroscopy.[13,16,18,20,23-34] $^{47/49}$Ti[35-49] and ^{39}K[50-56] SSNMR spectroscopy are very challenging at low magnetic fields since they are "unreceptive" quadrupolar nuclei (spin $I > 1/2$) with very low gyromagnetic ratios (γ). $^{47/49}$Ti also have low natural abundances (7.28% for ^{47}Ti and 5.51% for ^{49}Ti)[57] and large electric quadrupole moments (Q). The low gyromagnetic ratios as well as the low natural abundances lead to very low intrinsic detection sensitivities. Moreover, the observed NMR pattern of quadrupolar nuclei is typically from the central ($1/2 \leftrightarrow -1/2$) transition broadened by second-order quadrupolar interactions with non-spherical electric field gradients (EFG), whose width depends on a factor of $Q^2[I(I + 1) - 3/4]/\gamma[2I(2I - 1)]^2$.[58] Therefore, the low gyromagnetic ratios as well as the large quadrupole moments give rise to very broad spectra, making the spectral acquisition difficult. Furthermore, $^{47/49}$Ti NMR experiment is also hindered by the unique nuclear properties of titanium: the two NMR-active isotopes of titanium, ^{47}Ti ($I = 5/2$) and ^{49}Ti ($I = 7/2$), have very similar gyromagnetic ratios. The difference in Larmor frequencies for the two isotopes is only ~ 10 kHz even at a high magnetic field of 21.1 T.[57] Therefore, more often than not, both ^{47}Ti and ^{49}Ti resonances from the same site are observed in the same spectrum and usually overlapping, making the spectral interpretation complicated. However, with a smaller I and a larger Q ($Q(^{49}$Ti$)/Q(^{47}$Ti$) = 0.8179$),[59] the second-order quadrupolar broadening of ^{47}Ti is about 3.522 times larger

than that of ^{49}Ti. In the case of overlapping $^{47/49}$Ti spectra, the narrower and stronger component is due to ^{49}Ti while the broader and weaker component is attributed to ^{47}Ti. Nevertheless, recent advance of spectrometers with high magnetic fields has greatly facilitated NMR studies of such "unreceptive" quadrupolar nuclei,[56,60-64] by reducing the effects caused by second-order quadrupolar interaction and increasing the sensitivity since the second-order quadrupolar broadening is inversely proportional to the magnitude of external magnetic field. The sensitivity can be further enhanced by several techniques including Quadrupolar Carr-Purcell-Meiboom-Gill (QCPMG)[65] using the adiabatic wide-band uniform-rate smooth truncation (WURST) pulse[66] and related sequences.[67-71]

In this work, several prototypical titanosilicates including natisite,[72] AM-1,[73] AM-4,[17] sitinakite,[20] GTS-1,[12-14] ETS-4,[16] and ETS-10,[18,19] were studied by multinuclear (^{29}Si, $^{47/49}$Ti, ^{23}Na, and ^{39}K) solid-state NMR spectroscopy. In particular, natural abundance $^{47/49}$Ti spectra were acquired using quadrupolar echo and QCPMG sequences at a high magnetic field of 21.1 T. The WURST pulse was integrated to enhance the signal/noise (S/N) ratio and generates a more accurate line shape of broad $^{47/49}$Ti static spectra over standard excitation pulses. Samples were chosen because they possess several typical coordination environments of Ti^{4+} in titanosilicates: AM-1 and natisite are crystalline phases with 5-coordinated Ti^{4+}; AM-4, sitinakite and GTS-1 are crystalline phases as well but contain 6-coordinated Ti^{4+}; whereas ETS-4 (with both 5- and 6- coordinated Ti^{4+}) and ETS-10 (with 6-coordinated Ti^{4+}) have disordered frameworks. Both chemical shielding (CS) and EFG parameters of ^{49}Ti were extracted from the experimental spectra. Furthermore, ^{23}Na (at 9.4 T) and ^{39}K (natural abundance, at 21.1 T) SSNMR spectra also provide fruitful structural information on the extra-framework cations. First-principles calculations based on the Gauge Including Projector Augmented Wave (GIPAW) method using plane wave basis sets and periodic boundary conditions (the CASTEP code)[74,75] were performed as well to assist in the interpretation of experimental spectra.

7.2   Experimental Section

7.2.1   Sample Preparation

Titanosilicate samples were provided by Dr. Zhi Lin (University of Aveiro, Portugal). Natisite was synthesized as follow. 15.00 g of sodium silicate solution (27% m/m SiO_2, 8% m/m Na_2O, Merck), 11.90 g of NaOH and 2.70 g of anatase (98% m/m, Merck) were mixed well in Teflon-lined autoclaves and treated at 230 °C for 3 days under autogenous pressure without agitation. The product was filtered off, washed at room temperature with distilled water, and dried at 70 °C overnight. The syntheses of other materials were carried out under hydrothermal conditions according to procedures reported in literature for ETS-10,[2,76] ETS-4,[3] AM-1,[23] AM-4,[23] GTS-1,[2] and sitinakite.[77]

The identity and crystallinity of titanosilicate samples were confirmed by powder XRD experiments (Figure 7-A1, appendix). All measurements were conducted on a Rigaku rotating anode diffractometer using graphite-monochromated Co Kα radiation with a wavelength of 1.7902 Å. Experimental XRD patterns were recorded within the range between 5° and 65° in 2θ at a step size of 0.02°. Simulated powder XRD patterns were generated using the Mercury software. The Si/Ti ratios of ETS-4 and ETS-10, as well as the Na/K ratios of GTS-1 and ETS-10, were determined by Dr. Zhi Lin using energy dispersive X-ray spectroscopy (EDS). The water content of sitinakite was checked by thermogravimetric analysis (TGA). The sample was heated under N_2 atmosphere on a Mettler Toledo TGA/DTA851e instrument from 25 to 500 °C at a constant heating rate of 10 °C/min.

7.2.2   NMR Characterizations and Theoretical Calculations

7.2.2.1 $^{47/49}$Ti Measurements

Natural abundance $^{47/49}$Ti SSNMR spectra were acquired at 21.1 T on a Bruker Avance II spectrometer at the National Ultrahigh-Field NMR Facility for Solids in Ottawa, Canada. A 7 mm home-built single-channel wide-line NMR probe was tuned to ^{49}Ti with a Larmor frequency of 50.67 MHz. $^{47/49}$Ti static SSNMR spectra of natisite and AM-1 were acquired by using the adiabatic Wide-band Uniform-Rate Smooth Truncation

(WURST) echo sequence, where the WURST pulse can uniformly excite quadrupolar nuclei such as $^{47/49}$Ti across a broad bandwidth.[66] A pulse width of 50 μs and a sweep width of 1 MHz were used in the WURST pulse. An interpulse delay τ of 500 μs was used. The $^{47/49}$Ti static WURST-echo spectra were acquired using the WURST pulse sweeping from both low-to-high (LTH) and high-to-low (HTL) directions. The two spectra were then co-added to improve the signal-to-noise ratio (S/N) and the line shape. $^{47/49}$Ti static SSNMR spectra of AM-4, sitinakite, GTS-1, ETS-4 and ETS-10 were acquired by using the 90°-τ-90° quadruplar echo sequence.[78] A 90° pulse width of 9 μs, corresponding to a selective 90° pulse width of 1.8 μs for ^{49}Ti central transition, was measured on the concentrated Cp_2TiCl_2/CH_2Cl_2 solution, which is also a secondary standard sample. The observed $^{47/49}$Ti spectra were referenced against it by setting the ^{49}Ti resonance to -773 ppm relative to ^{49}Ti in neat, liquid $TiCl_4$. An interpulse delay τ of 50 μs was used. The echo was recorded prior to the echo maximum and shifted to ensure that the free induction decay (FID) used in Fourier transformation begins exactly at the echo maximum.

For natisite, AM-1, AM-4 and GTS-1, $^{47/49}$Ti static WURST Quadrupolar Carr-Purcell-Meiboom-Gill (QCPMG) spectra were also collected,[70] which could significantly increase the S/N of the spectra by yielding a series of narrow 'spikelets' whose manifold reproduce the SSNMR powder patterns. The enter duration of each echo was 290 μs. 128 echos were acquired with a spikelet separation of 2000 Hz. The WURST pulse width was set to 50 μs. The broad $^{47/49}$Ti spectra were acquired piecewise by gradually increasing the transmitter frequency. The offsets of the transmitter frequency were set as a multiple of spikelet separation to ensure that the spikelets can be added up for each sub-spectrum. The sub-spectra with different frequency offsets were co-added in frequency scale (Hz). The resulting spectrum was then treated and referenced as a single spectrum. The conditions of $^{47/49}$Ti SSNMR experiments are shown in Table 7-A1.

7.2.2.2 ^{39}K Measurements

Natural abundance ^{39}K SSNMR spectra of GTS-1 and ETS-10 were collected at 21.1 T (with a Larmor frequency of 41.99 MHz) using a 7 mm double-tuned H/X MAS

Bruker probe. Magic-angle spinning (MAS) experiments were conducted at a spinning speed of 5 kHz and using the rotor-synchronized 90°-τ-180° echo sequence[78] with the continuous-wave ^{1}H decoupling. The 90° pulse width of ^{39}K on 1M KCl (aq) solution (δ_{iso} = 0 ppm) was 12 μs, corresponding to a selective 90° pulse of 6 μs for ^{39}K central transition. The pulse delays are 1 and 5 s for GTS-1, and 2 s for ETS-10. 8192 scans were accumulated for GTS-1 while it was 22528 scans for ETS-10.

7.2.2.3 ^{29}Si Measurements

^{29}Si MAS SSNMR experiments were performed on a Varian Infinity Plus 400 WB spectrometer operating at 79.36 MHz at a magnetic field of 9.4 T using a 7.5 mm triple-tuned T3 MAS probe with a spinning speed of 5 kHz. All ^{29}Si MAS spectra were acquired using the one-pulse sequence with continuous-wave ^{1}H decoupling. The radio frequency field for ^{1}H decoupling was approximately 40 kHz. A 45° pulse (3 μs) of ^{29}Si and a pulse delay of 60 s were used. The ^{29}Si chemical shift was referenced against the downfield peak of tris(trimethylsilyl)silane (TTMSS) at -9.8 ppm relative to the peak in tetramethylsilane (TMS). The numbers of scans were varied from 84 to 128.

7.2.2.4 ^{23}Na Measurements

^{23}Na SSNMR experiments were carried out at 105.67 MHz at 9.4 T using a 3.2 mm double-tuned MAS probe. ^{23}Na MAS SSNMR spectra were acquired using the one-pulse sequence with a spinning speed of 20 kHz. A 30° pulse (0.3 μs) of ^{23}Na was used for titanosilicate samples, corresponding to a liquid 90° pulse of 1.8 μs measured on 1M NaCl (aq) solution (δ_{iso} = 0 ppm). Rotor-synchronized ^{23}Na 3QMAS spectra with a spinning rate of 20 kHz were acquired using the standard Z-filter MQMAS sequence.[79] The excitation, conversion and selection pulse widths of ^{23}Na were optimized to 2.86, 1.03 and 10.00 μs, respectively. FID signals were Fourier-transformed and sheared to obtain the separate F1 and F2 dimensions using the Varian Spinsight software. The conditions of ^{23}Na SSNMR experiments are shown in Table 7-A2. To ensure that the relative intensities of different Na$^+$ sites were accurate, the spin-lattice relaxation time (T_1) of ^{23}Na (Table 7-A2) were measured using the inversion-recovery 180°-τ-90° sequence.

The intensity-τ plots were fitted by a three-component equation using the Spinsight software.

$^{47/49}$Ti static SSNMR spectra were simulated using the Ti47-49 model integrated in the DMFIT package,[80] which could simultaneously produce both ^{47}Ti and ^{49}Ti patterns. ^{39}K and ^{23}Na MAS SSNMR spectra, as well as the extracted slices of 2D 3QMAS spectra, were simulated using the QuadFit package.[81] The experimental error for each measured parameter was estimated by visual comparison of experimental spectra with those simulated. The parameter of concern was varied bi-directionally starting from the best-fit value and keeping other parameters constant, until noticeable differences between the two spectra were observed.

7.2.2.5   First-Principle Calculations

Gauge Including Projector Augmented Wave (GIPAW) quantum chemical calculations were conducted using the CASTEP code (version 4.4, Accelrys Materials Studio), running on a HP xw4400 workstation with a single Intel dual-core 2.67 GHz processor and 8 GB DDR RAM. The NMR module was used to calculate the ^{49}Ti electric field gradient (EFG) tensors. Unit cell parameters and atomic coordinates were taken from their crystal structures.[11,14,17,72,73] The "missing" hydrogen atoms of AM-4 were added using the Mercury software without the reduction of the symmetry of the space group. For sitinakite, the H_2O and disordered Na2 site were removed prior to calculation. The calculations were performed using ultra-soft pseudopotentials generated from the "on-the-fly" method implemented within the CASTEP. The Generalized Gradient Approximation (GGA) with Perdew, Burke and Ernzerhof (PBE) functional was used. Various plane-wave cut-off energies (450, 500 and 550 eV for coarse, medium and fine basis set accuracy, respectively) were applied depending on the size of the unit cell. Full geometry optimizations were used prior to EFG predications for all samples. The CASTEP results without geometry optimizations or with partial optimizations (H only) were also performed for some samples for comparison purposes. The isotropic chemical shielding of ^{29}Si and ^{49}Ti, the chemical shielding anisotropy (CSA) tensor of ^{49}Ti, and the C_Q and η_Q values of ^{23}Na and ^{49}Ti were produced automatically by the CASTEP program.

The isotropic chemical shielding of ^{29}Si were converted to the isotropic chemical shifts using the relationships: $\delta_{iso}(^{29}\text{Si}) = 323.31 - \sigma_{iso}(^{29}\text{Si, CASTEP})$ (in ppm), where 323.31 ppm is the absolute isotropic ^{29}Si chemical shielding in the literature.[82]

7.3   Results and Discussion

7.3.1   Natisite
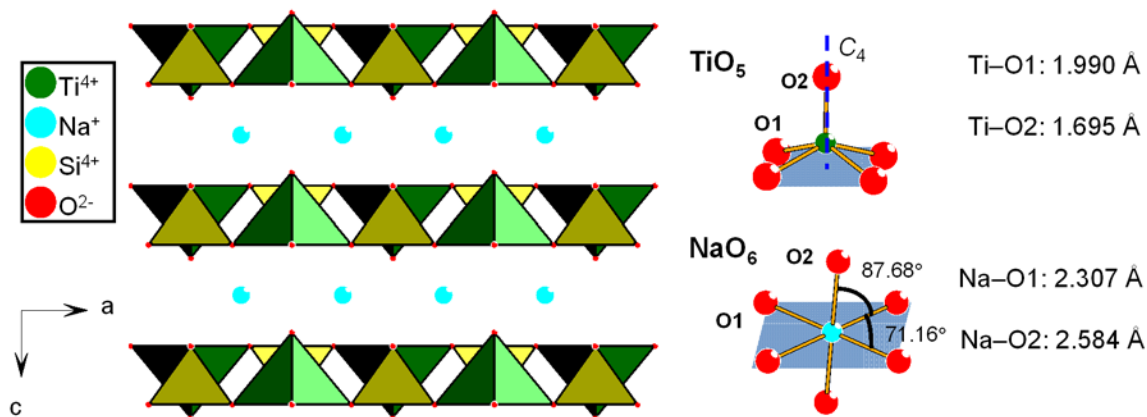
Figure 7-1: Left: the structure of natisite (Na–O bonds are omitted for clarity). Right: local environments of Ti^{4+} and Na^{+}. The atoms on the blue parallelograms are co-planar.

Previous single-crystal XRD data imply that natisite (Na$_2$TiOSiO$_4$ or Na$_2$TiSiO$_5$) crystallizes in the tetragonal $P4/nmm$ (No. 129) space group.[72] As Figure 7-1 shows, the crystal structure of natisite comprises anionic titanosilicate layers constructed by corner-sharing TiO$_5$ and SiO$_4$ units, which are separated by charge-balancing Na$^+$ cations. The single Ti^{4+} center is located inside of a square pyramid that consists of four basal O1 atoms and one apical O2 atom. The four basal O1 atoms are shared with four neighboring symmetry-related SiO$_4$ tetrahedra by a C_4 axis; whereas the apical O2 forms a terminal bond with Ti, which presents on both sides of the titanosilicate layer. The bond length between Ti and O2 (1.695 Å) is significantly shorter than those between Ti and O1 (1.990 Å), indicating that the former one is a Ti=O double bond, while the other four are Ti–O single bonds. Indeed, the high site symmetry of Ti (C_{4v}) suggests a zero asymmetry parameter (η_Q) of $^{47/49}$Ti SSNMR spectrum. The distorted square-pyramidal symmetry of Ti should result in a large quadrupolar coupling constant (C_Q). As mentioned earlier, all

SiO$_4$ units in natisite are crystallographically equivalent. Because all four oxygens bound to Si are shared by both Si and Ti, ^{29}Si SSNMR spectrum of natisite is expected to exhibit a single peak with the chemical shift typical of Si(4Ti) environment (*i.e.*, Si^{4+} connects to four Ti^{4+} via bridge O atoms). On the other hand, the single Na site of natisite is in a distorted octahedral geometry: Na and four nearest O atoms (O1) are co-planar while the other two O atoms (O2, related by an inversion center at Ti) are further away. The large deviation of Na–O distances (Na–O1: 2.307 Å and Na–O2: 2.584 Å) and O–Na–O angles (O1–Na–O1: 71.16° and O1–Na–O2: 87.68°) from the average values will yield a broad ^{23}Na SSNMR spectrum with a large C_Q and a non-zero η_Q.
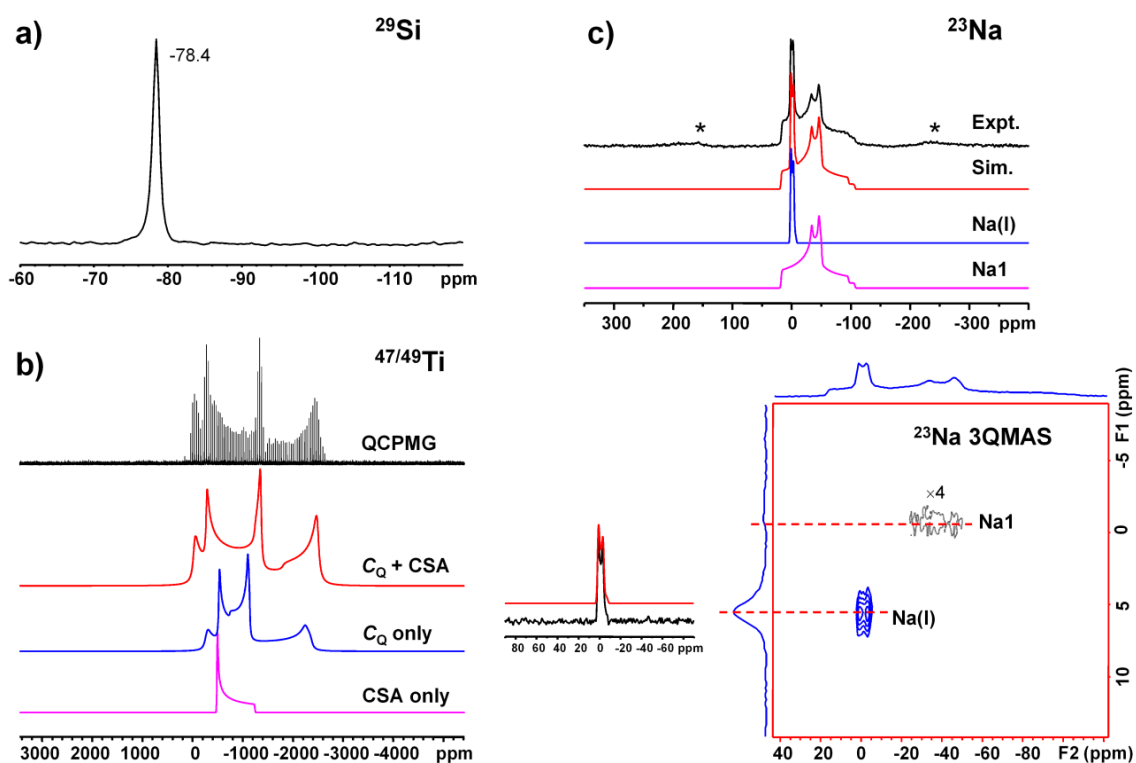
Figure 7-2: (a) ^{29}Si MAS spectrum of natisite at 9.4 T. (b) Experimental (QCPMG) and simulated natural abundance $^{47/49}$Ti static spectra of natisite at 21.1 T. (c) Experimental and simulated ^{23}Na MAS spectra of natisite at 9.4 T (top); ^{23}Na 2D 3QMAS spectrum of natisite at 9.4 T (bottom). The dashed lines corresponds to the slices taken for simulation (Na(I) only, since the signal of Na1 was too weak). The simulated ^{23}Na MAS spectrum was based on the parameters obtained from 3QMAS. *: spinning sidebands.

Although the ^{29}Si MAS SSNMR spectrum of natisite has been reported by Balmer and co-workers,[24] the S/N ratio was low and as many as four peaks were observed, at -61.7, -82.1, -89.1 and -93.6 ppm, respectively. They assigned the peak at -82.1 ppm to be the Si site of natisite and the other peaks to be impurities. In this work, a single sharp ^{29}Si resonance at -78.4 ppm is observed (Figure 7-2a), consistent with the fact that natisite only has one Si site. The ^{29}Si chemical shift is typical of Si sites in the Si(4Ti) local environments.[24,27] Therefore, it is likely that our sample has higher crystallinity and purity, giving rise to stronger ^{29}Si signal free of impurity peaks.

There is a previous $^{47/49}$Ti SSNMR study of natisite at a low magnetic field of 14.1 T.[47] However, the authors only reported the ^{49}Ti NMR parameters (C_Q = 18.2 MHz, η_Q = 0.00, and δ_{iso} = -673 ppm) without showing the NMR spectrum. Herein, natural abundance WURST-QCPMG $^{47/49}$Ti static spectrum of natisite at 21.1 T (Figure 7-2b) displays a stronger and narrower pattern from ~ -400 to ~ -1400 ppm superimposed on a weaker and broader pattern from ~ 0 to ~ -2600 ppm. The former one is assigned to the ^{49}Ti signal while the latter one is the ^{47}Ti signal. Both signals have the typical second-order quadrupolar line shapes of the center transition expected from a single Ti site with an axial symmetry $\geq C_3$ (*i.e.*, $\eta_Q = 0$), consistent with the proposed crystal structure from XRD data. However, as Figure 7-2b illustrates, the attempt to simulate the experimental $^{47/49}$Ti spectrum by only considering quadrupolar interaction was not successful and the contribution of chemical shielding anisotropy (CSA) has to be included in the simulation, which is also axial symmetric (*i.e.*, skew $\kappa = 1$). The resulting ^{49}Ti NMR parameters are: $C_Q(^{49}\text{Ti})$ = 10.7(2) MHz, $\eta_Q(^{49}\text{Ti})$ = 0.05(5), isotropic chemical shift $\delta_{iso}(^{49}\text{Ti})$ = -740(30) ppm, span $\Omega(^{49}\text{Ti})$ = 500(30) ppm, skew $\kappa(^{49}\text{Ti})$ = 1.0(1) and (α, β, γ) = (0°, 0°, 0°), where (α, β, γ) are Euler angles between EFG and CSA tensors in Rose convention.[83] Since the ^{47}Ti NMR parameters can be calculated from the ^{49}Ti NMR parameters using the nuclear quadrupole moment ratio and the gyromagenetic ratio difference between ^{47}Ti and ^{49}Ti, they are not shown in this work. The $C_Q(^{49}\text{Ti})$ value of natisite (10.7 MHz) is quite large for Ti-containing minerals but only moderately large for those with 5-coordinated Ti sites.[44] The $\delta_{iso}(^{49}\text{Ti})$ value is also in the normal range of Ti-containing minerals. It is noteworthy that the $C_Q(^{49}\text{Ti})$ value obtained in this work is derived from

that reported in the literature. The lower intrinsic sensitivity of $^{47/49}$Ti NMR at 14.1 T, resulting in a poorer spectral quality, might contribute to the large difference.

To the best of our knowledge, there is no previous ^{23}Na NMR study of natisite. ^{23}Na MAS spectrum of natisite at 9.4 T (Figure 7-2c) consists of two overlapping resonances: a narrow one at ~ 0 ppm and a very broad one from ~ 20 to ~ -110 ppm. To identify the two signals, ^{23}Na triple-quantum magic-angle spinning (3QMAS) experiment was performed, which removes the residual second-order quadrupolar broadening that is not averaged in conventional MAS experiments and thus allows a high spectral resolution along the high-resolution (F1) dimension.[84] Two signals, centered at -1 and 6 ppm along the F1 dimension, respectively, are clearly resolved in 2D ^{23}Na 3QMAS spectrum. The cross-section at -1 ppm corresponds to the broad resonance (very weak, not shown), while the one at 6 ppm corresponds to the narrow resonance. The ^{23}Na NMR parameters of the narrow resonance determined in the 3QMAS experiment, including C_Q, η_Q and δ_{iso}, are further refined by simulating the ^{23}Na MAS spectrum. However, the ^{23}Na NMR parameters of the broad resonance can only be determined in the MAS experiment. Since 3QMAS is not a quantitative technique, simulation of MAS spectrum also allows one to obtain correct relative intensities of different Na sites. The two sets of ^{23}Na NMR parameters are: $C_Q(^{23}$Na$) = 1.4(1)$ MHz, $\eta_Q(^{23}$Na$) = 0.0(1)$, $\delta_{iso}(^{23}$Na$) = 3.0(6)$ ppm for the narrow resonance, and $C_Q(^{23}$Na$) = 4.5(1)$ MHz, $\eta_Q(^{23}$Na$) = 0.8(1)$, $\delta_{iso}(^{23}$Na$) = 18.6(20)$ ppm for the broad resonance, respectively. The relative intensity of two resonances is 16% (the narrow resonance) to 84% (the broad resonance). Herein the broad resonance is assigned to the Na site resolved in the single-crystal XRD experiment (Na1, hereafter Na1 *etc.* is used to describe the Na sites determined from XRD data), because it has very high intensity and a large $C_Q(^{23}$Na$)$ due to the distorted coordination sphere of Na1. The narrow resonance (Na(I), hereafter Na(I) *etc.* is used to describe the Na sites that are not determined from XRD data but from ^{23}Na SSNMR results) may be owing to a small amount of sodium-rich impurities, which are unlikely associated with Si because no impurity peak was observed in the ^{29}Si MAS spectrum.

7.3.2 AM-1
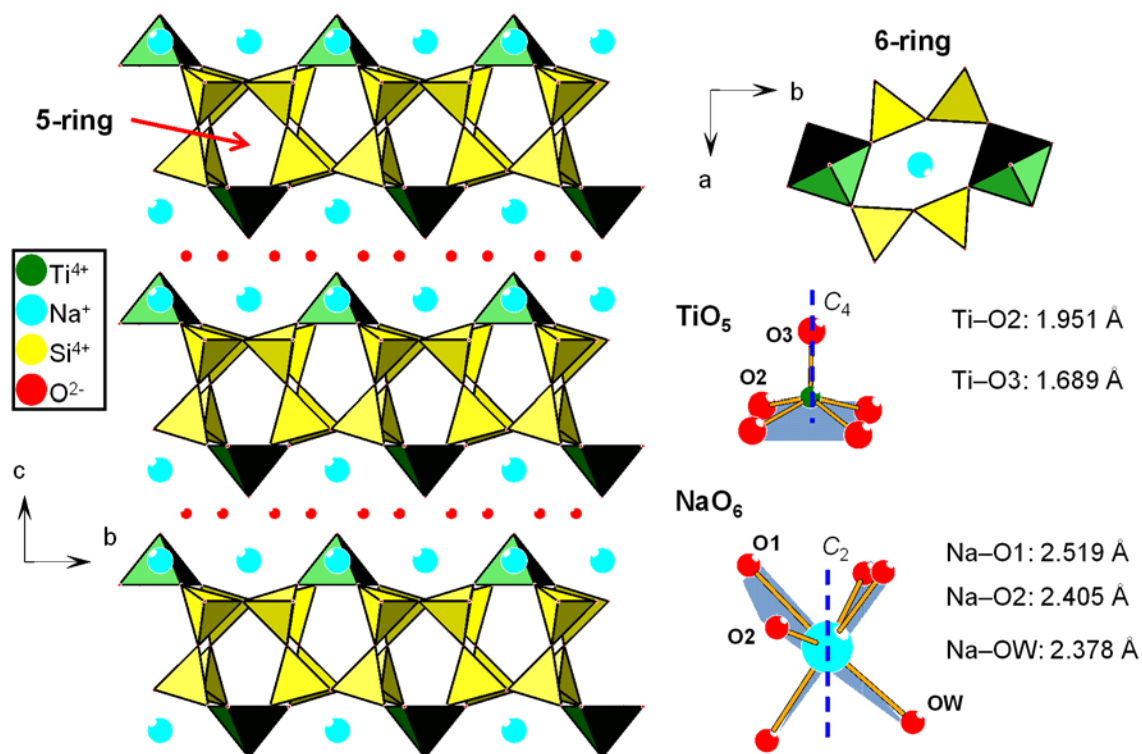
Figure 7-3: Left: the structure of AM-1 (The hydrogen atoms and Na–O bonds are omitted for clarity). Right: 6-rings and local environments of Ti^{4+} and Na^+. The atoms on the blue parallelograms are co-planar.

AM-1 ($Na_4Ti_2Si_8O_{22} \cdot 4H_2O$, also known as JDF-L1) is an unusual non-centrosymmetric layered titanosilicate crystallized in the tetragonal space group of $P42_12$ (No. 90),[73] which composes of $[Ti_2Si_8O_{22}]^{4-}$ layers along the a axis (Figure 7-3, left) with five-member rings (5-rings) built up of four SiO_4 tetrahedra and one TiO_5 square pyramid and 6-rings (Figure 7-3, right) built up of four SiO_4 tetrahedra and two TiO_5 units. 6-rings are along the c axis while 5-rings are along the a axis. Each TiO_5 unit connects to four symmetry-related SiO_4 tetrahedra by a C_4 rotation axis via corner-sharing basal O2 atoms. Therefore, TiO_5 units are isolated from each other with apex of TiO_5 pointing to the interlayer space. Unlike natisite, the apical O3 coordinates to no other atoms except Ti. The anionic charge of titanosilicate layers is balanced by the interlamellar Na^+ cations, located over the 6-rings, which effectively blocks the entrance to the intralamellar space. A layer of water molecules is sandwiched between two layers of Na^+ cations. The

coordination environment of the single Ti site of AM-1 (Figure 7-3, right) is similar to that of natisite, with four long Ti–O bonds (1.951 Å) and one short Ti=O bond (1.689 Å). The larger range of bond lengths between Ti and O of AM-1 will result in a larger $C_Q(^{49}\text{Ti})$ than natisite, and the high site symmetry of Ti (C_4) should give rise to a zero $\eta_Q(^{49}\text{Ti})$. However, the single Si site of AM-1 is in a Si(3Si, 1Ti) local environment and the ^{29}Si SSNMR peak should be more shielded than that of natisite. AM-1 has only one Na site in the octahedron geometry with a smaller range of Na–O bond lengths (Na–O1: 2.519 Å, Na–O2: 2.405 Å and Na–OW: 2.378 Å, respectively, where OW is the oxygen of water), implying AM-1 must have a smaller $C_Q(^{23}\text{Na})$ than natisite.
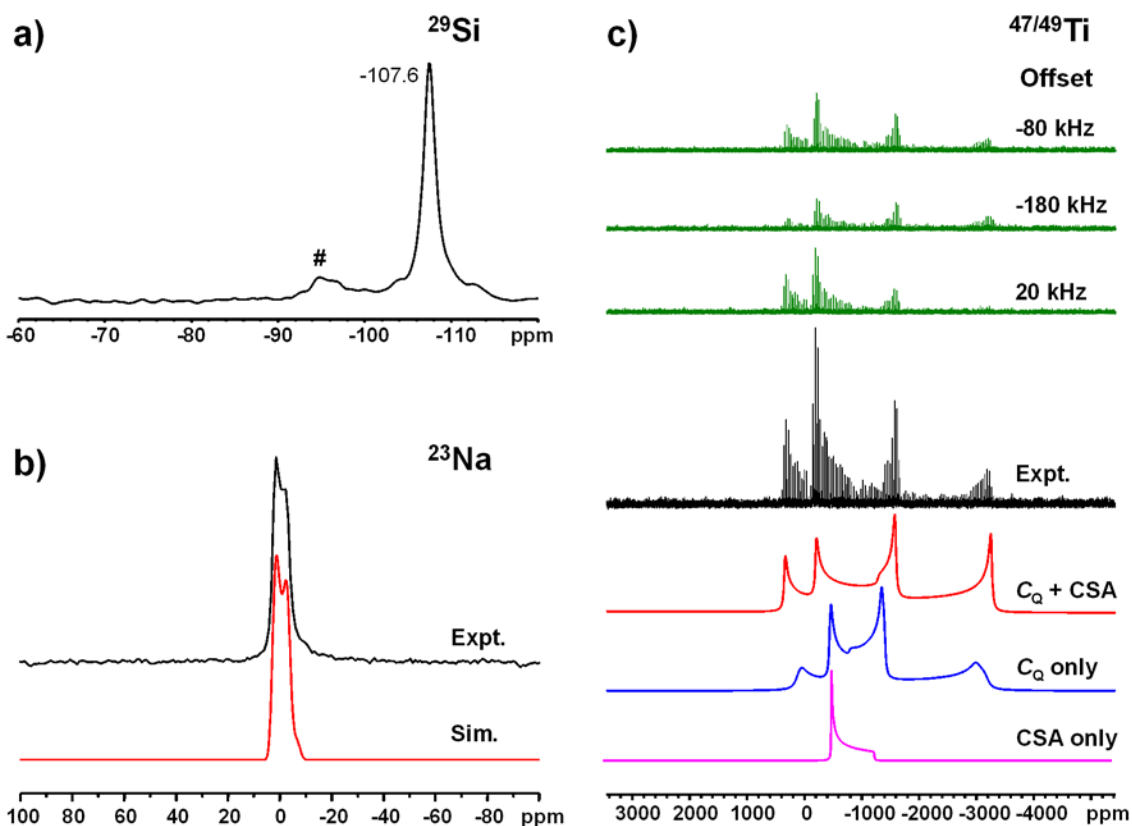
Figure 7-4: (a) ^{29}Si MAS SSNMR spectrum of AM-1 at 9.4 T. #: impurity. (b) Experimental and simulated ^{23}Na MAS SSNMR spectra of AM-1 at 9.4 T. (c) Experimental (QCPMG) and simulated natural abundance $^{47/49}\text{Ti}$ static SSNMR spectra of AM-1 at 21.1 T. The offset of the transmitter frequency is indicated on each sub-spectrum.

AM-1 has been previously studied by ^{29}Si and ^{23}Na SSNMR spectroscopy[23] but not by $^{47/49}$Ti SSNMR spectroscopy. ^{29}Si (Figure 7-4a) and ^{23}Na (Figure 7-4b) MAS spectra acquired in this work agree well with the reported spectra.[23] Natural abundance WURST-QCPMG $^{47/49}$Ti static spectrum of AM-1 at 21.1 T (Figure 7-4c) consists of a stronger and narrower ^{49}Ti pattern from ~ -200 to ~ -1700 ppm superimposed on a weaker and broader ^{47}Ti pattern from ~ 0 to ~ -2600 ppm. Similar to natisite, an axial symmetric CSA has to be included in the simulation. The resulting ^{49}Ti NMR parameters are: $C_Q(^{49}\text{Ti})$ = 13.4(2) MHz, $\eta_Q(^{49}\text{Ti})$ = 0.05(5), $\delta_{iso}(^{49}\text{Ti})$ = -783(30) ppm, $\Omega(^{49}\text{Ti})$ = 500(30) ppm, $\kappa(^{49}\text{Ti})$ = 1.0(1) and (α, β, γ) = (0°, 0°, 0°). The $C_Q(^{49}\text{Ti})$ value of AM-1 (13.4 MHz) is larger than that of natisite (10.7 MHz) due to a larger degree of distortion of TiO$_5$ unit. The observed η_Q and κ values are consistent with the high site symmetry of Ti (C_4). The $\delta_{iso}(^{49}\text{Ti})$ value is also in the normal range of Ti-containing minerals.

7.3.3   AM-4
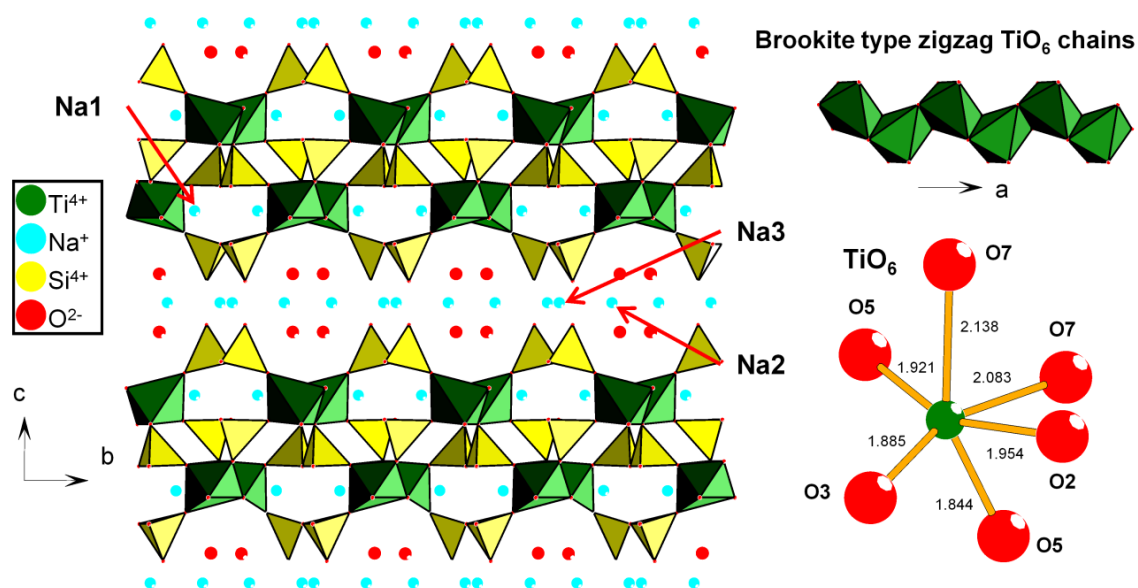
Figure 7-5: Left: the structure of AM-4 (left, the hydrogen atoms and Na–O bonds are omitted for clarity). Right: brookite-type zigzag TiO$_6$ chains and the local environment of Ti^{4+}. The Ti–O distances are shown in Å.

The space group of layered AM-4 (Na$_3$(Na,H)Ti$_2$O$_2$[Si$_2$O$_6$]$_2$·2H$_2$O) phase has been previously determined to be $A2/a$ (No. 15).[17] As Figure 7-5 shows, the structure is

built from interconnecting brookite-type TiO_6 octahedra[85] and SiO_4 octahedra, forming layers perpendicular to the *c* axis. Each layer can be viewed as a five-tier sandwich of SiO_4 : TiO_6 : SiO_4 : TiO_6 : SiO_4. TiO_6 octahedra link to each other by edge-sharing, forming brookite-type zigzag chains; while SiO_4 tetrahedra connect each other by corner-sharing, forming pyroxene-type chains. Both titanate and silicate chains run along the *a* axis and connect each other, forming the layers. Within the titanate chains the Ti is away from the center of octahedron due to the $Ti^{4+}\cdots Ti^{4+}$ cation repulsion, resulting in that Ti–O distances in the Ti octahedra vary in a wide range from 1.844 Å in Ti–O5 bond to 2.138 Å in Ti–O7 bond. The 1D pyroxene-type silicate chains in the surface and middle of layer are independent. There are three crystallographically distinct Na^+ cation sites in a ratio of 2Na1 : 1Na2 : 1Na3. Illustrated in Figure 7-5, Na1 exist in small cages within the layers. Na2 and water molecules are between the layers. However, the third Na (Na3) forms NaO_4 tetrahedron and these tetrahedra form a chain along the *a* axis via edge-sharing and interact with apexes of SiO_4 tetrahedra on the surface of layers.

As Figure 7-6a shows, ^{29}Si MAS spectrum of AM-4 at 9.4 T consists of a sharper resonance at -90.5 ppm and a broader resonance at -94.2 ppm. The two resonances are partially overlapped. Deconvolution of this spectrum yields an intensity ratio of 54% (-90.5 ppm) to 46% (-94.2 ppm), consist with the 1 : 1 ratio of two crystallographically distinct Si sites proposed by the crystal structure.[17] The ^{29}Si spectrum reported in the literature is slightly different from ours:[23] Three peaks were observed, two of which have approximately the same chemical shifts as ours while the third peak at -92.1 ppm was not observed in this work. The authors did not explain the origin of the third peak but it is likely due to some impurity. The next question to be addressed is the assignment of the two Si sites. As mentioned earlier, ^{29}Si chemical shifts are very sensitive to the nearest-neighbor cations around 4-coordinated Si^{4+}, *e.g.*, the ^{29}Si peak of natisite (-78.4 ppm) is more deshielded than that of AM-1 (-107.6 ppm) because the Si site of natisite is in a Si(4Ti) environment while it is Si(1Ti) for AM-1. Therefore, the peak at -90.5 ppm is assigned to Si1 and the one at -94.2 ppm is Si2 since Si1 is in a Si(3Ti) environment while Si2 is in a Si(1Ti) environment. The assignment is further examined by first-principle calculations of ^{29}Si chemical shifts, using GIPAW method implemented in the

CASTEP code, which has been proven to be a reliable method for spectral interpretation and assignment.[74,75] The calculation results (-91.64 ppm for Si1 and -95.26 ppm for Si2) confirm that Si1 is more deshielded compared to Si2.
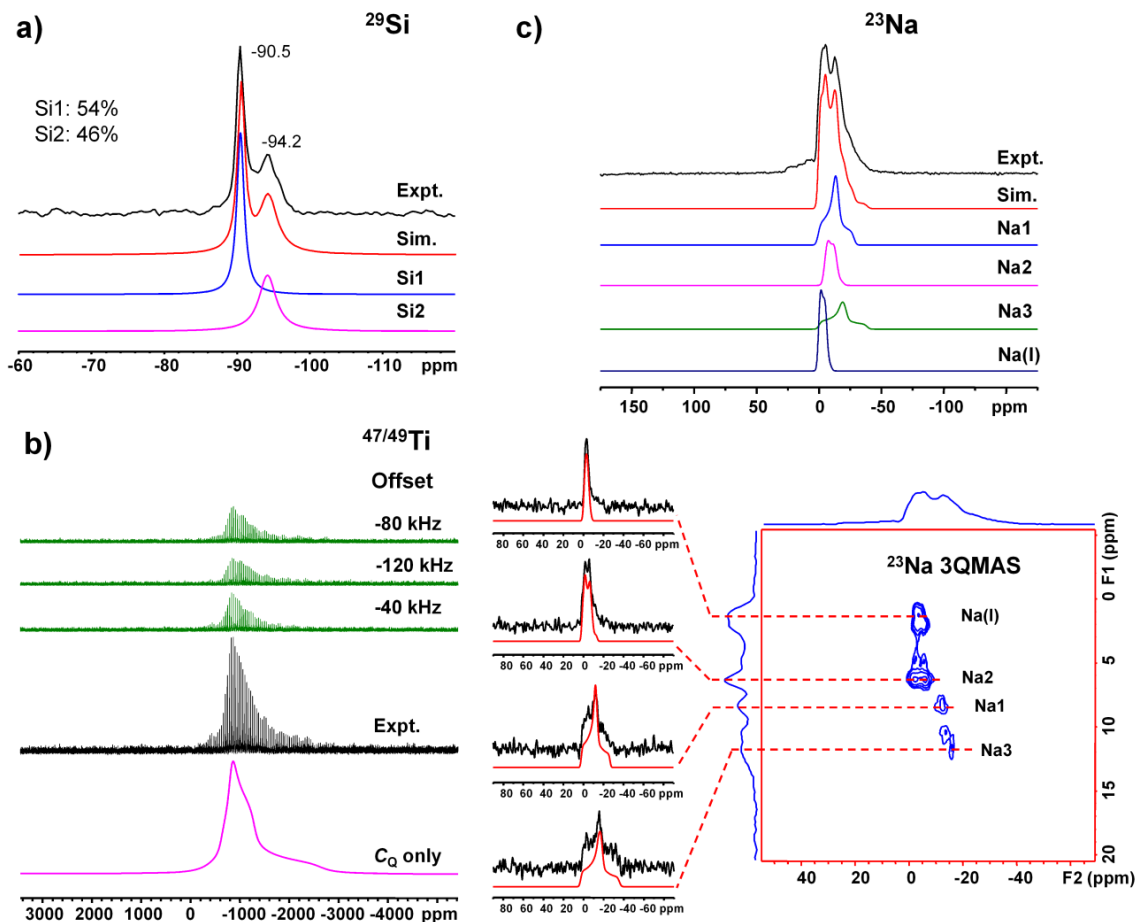
Figure 7-6: (a) Experimental and deconvoluted [29]Si MAS spectra of AM-4 at 9.4 T. (b) Experimental (QCPMG) and simulated natural abundance [47/49]Ti static spectra of AM-4 at 21.1 T. The offset of the transmitter frequency is indicated on each sub-spectrum. (c) Experimental and simulated [23]Na MAS spectra of AM-4 at 9.4 T (top); [23]Na 2D 3QMAS spectrum of AM-4 at 9.4 T (bottom). The simulated [23]Na MAS spectrum was based on the parameters obtained from 3QMAS.

There is no previous [47/49]Ti NMR study of AM-4. In sharp contrast to natisite and AM-1, natural abundance WURST-QCPMG [47/49]Ti static spectrum of AM-4 at 21.1 T exhibits a broad asymmetric profile centered at ~ -900 ppm. The line shape is somewhat

reminiscent to that of brookite,[43] consistent with the known structural similarity between the two compounds. Spectral simulation of AM-4 yields a set of [49]Ti NMR parameters: $C_Q(^{49}Ti) = 8.2(2)$ MHz, $\eta_Q(^{49}Ti) = 1.0(1)$, and $\delta_{iso}(^{49}Ti) = -850(30)$ ppm. The fact that the contribution of CSA can be neglected indicates that the [47/49]Ti static spectrum of AM-4 is mainly broadened by the second-order quadrupolar interaction. The $C_Q(^{49}Ti)$ of AM-4 is larger than that of brookite (6.7 MHz) due to a larger degree of distortion of TiO_6 unit: the Ti–O bond lengths of AM-4 vary from 1.844 to 2.138 Å while it is from 1.910 to 1.992 Å for brookite.[85] The non-zero η_Q is attributed to the low site symmetry of Ti (C_1). The $\delta_{iso}(^{49}Ti)$ of AM-4 is also close to that of brookite (-853 ppm).

Although both [23]Na MAS and 2D 3QMAS spectra of AM-4 have been reported in the literature,[23] no spectral simulation was performed. The spectra observed in this work (Figure 7-6c) are very similar to the reported spectra. Herein, simulations of four slices, taken from the cross-sections of peaks at 1, 6, 8, and 12 ppm along the F1 axis, respectively, are shown. Simulations of the other peaks along the F1 axis are not shown due to very low S/N and/or distorted line shapes. Each of the four slices can be fitted with a single resonance. [23]Na MAS spectrum simulated using these Na sites matches with the experimental spectrum reasonably well in the range between 0 and -30 ppm. However, there are only three crystallographic Na sites in AM-4. In this work, the Na sites corresponding to the peaks at 6, 8, and 12 ppm along the F1 axis are assigned to the three crystallographic Na sites based on 1) the intensity ratio (38% : 19% : 19%) is consistent with the 2 : 1: 1 ratio in the crystal structure; 2) their NMR parameters are comparable to the calculated values (Na1: $C_Q = 2.21$ MHz, $\eta_Q = 0.80$; Na2: $C_Q = 1.47$ MHz, $\eta_Q = 0.31$; and Na3: $C_Q = 3.90$ MHz, $\eta_Q = 0.88$). Therefore, Na1 has a set of NMR parameters: $C_Q(^{23}Na) = 2.1(1)$ MHz, $\eta_Q(^{23}Na) = 1.0(1)$, and $\delta_{iso}(^{23}Na) = 0.9(10)$ ppm. For the other two Na sites, Na2 has a smaller $C_Q(^{23}Na)$ than Na1: $C_Q(^{23}Na) = 1.7(1)$ MHz, $\eta_Q(^{23}Na) = 0.3(1)$, and $\delta_{iso}(^{23}Na) = -3.0(10)$ ppm; whereas Na3 has a $C_Q(^{23}Na)$ larger than Na1: $C_Q(^{23}Na) = 2.5(1)$ MHz, $\eta_Q(^{23}Na) = 0.9(1)$, and $\delta_{iso}(^{23}Na) = 0.3(10)$ ppm. The fourth Na site, which is not the crystallographic Na site of AM-4, has a set of ^{23}Na NMR parameters: $C_Q(^{23}Na) = 1.4(1)$ MHz, $\eta_Q(^{23}Na) = 0.1(1)$ and $\delta_{iso}(^{23}Na) = 1.3(10)$ ppm. The other peaks along the F1 axis may correspond to small amounts of sodium-rich impurities.

7.3.4   Sitinakite
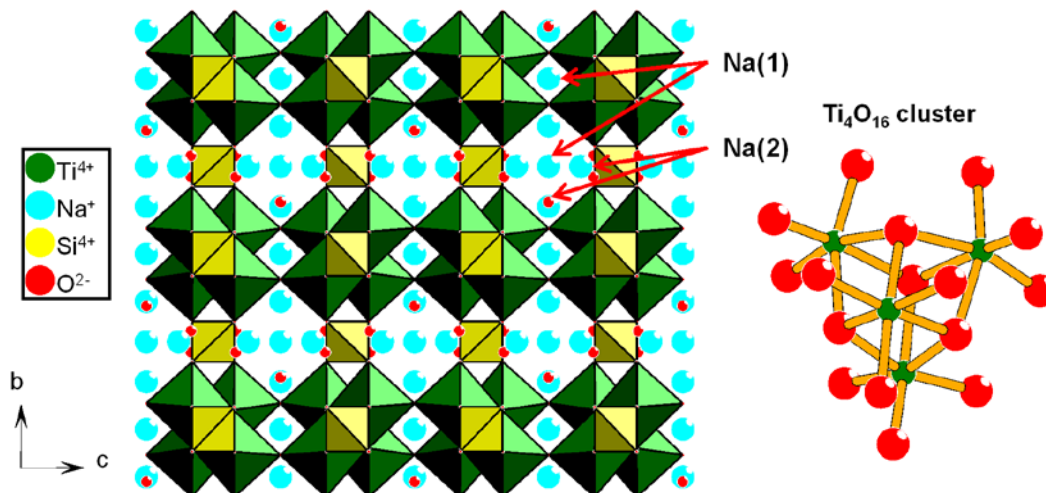
Figure 7-7: Left: the structure of sitinakite. The hydrogen atoms and Na–O bonds are omitted for clarity. Right: the structure of Ti_4O_{16} cluster.

Sitinakite ($Na_2Ti_2SiO_7 \cdot xH_2O$, x ~ 2.3 from TGA) is a microporous titanosilicate with only one 6-coordinated Ti site.[20] As Figure 7-7 shows, the most obvious structural feature of sitinakite is the cubane-like Ti_4O_{16} clusters, in which four TiO_6 octahedra link to each other by four 3-coordinated oxygens. The Ti_4O_{16} clusters then connect to each other by four bridging oxygens along the *c* axis; whereas in the other two dimensions, they are connected by tetrahedrally coordinated silicon atoms through oxygen, forming 3D framework. The 1D channels are along the *c* axis with 8-rings. There are two types of Na in sitinakite: One is located in the channels (exchangeable, referred to as Na(II)), while the other one is tightly coordinated by four oxygens of the Ti–O–Si framework and two water molecules (not exchangeable, namely Na(I)). The numbers of crystallographically distinct Na sites as well as their site occupancies, however, usually are not fixed because it has been demonstrated that sitinakite can undergo phase transformation when heated, dehydrated, or ion-exchanged without the alternation of the framework topology.[11,20] In such cases, the migrations of Na^+ cations in the channels (Na(II)) or water molecules are considered to be responsible to the phase transformation. The distortion degree of TiO_6 units indeed changes with different phases and even different temperatures. For instance, the Ti–O bond lengths of fully-hydrated sitinakite

vary between 1.832 and 2.073 Å at 20 K, and between 1.869 and 2.043 Å at 298 K.[20] Moreover, thermally- or dehydration- induced disorder within the structure of sitinakite were also described in literature,[20] which may result in a spectrum characteristic of disordered systems.
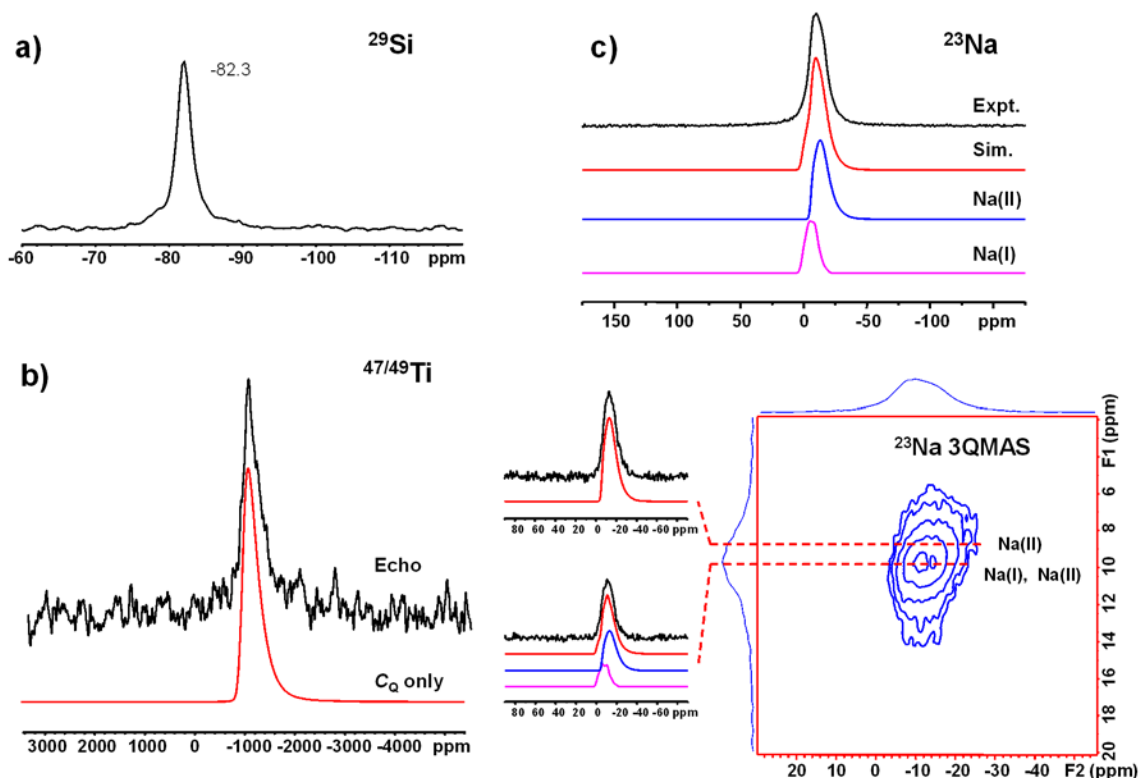
Figure 7-8: (a) Experimental ^{29}Si MAS SSNMR spectrum of sitinakite at 9.4 T. (b) Experimental (Echo) and simulated natural abundance [47/49]Ti static SSNMR spectra of sitinakite at 21.1 T. (c) Experimental and simulated ^{23}Na MAS SSNMR spectra of sitinakite at 9.4 T (top); [23]Na 2D 3QMAS spectrum of sitinakite at 9.4 T (bottom). The simulated [23]Na MAS spectrum was based on the parameters obtained from 3QMAS.

[29]Si MAS spectrum of sitinakite (Figure 7-8a) exhibits a sharp peak centered at -82.3 ppm, which is consistent with the literature value.[20,26] To the best of our knowledge, there is no previous [47/49]Ti NMR study of sitinakite. As Figure 7-8b shows, the disorder of the framework of sitinakite can be revealed by natural abundance [47/49]Ti static SSNMR experiments at 21.1 T. Distinct from natisite, AM-1 and AM-4, no signal can be acquired in the WURST-QCPMG experiment due to a very short spin-spin relaxation time (T_2) of

sitinakite. A short T_2 is often an indication of the local disorder around the observed nucleus. In principle, QCPMG experiment requires a sample with high crystallinity and thus a long T_2; whereas quadrupolar echo experiment can be applied to both disordered and crystalline systems, although it has lower sensitivity for crystalline systems compared to QCPMG experiment. Therefore, [47/49]Ti quadrupolar echo spectrum of sitinakite was acquired, which displays a narrow but featureless peak centered at ~ -900 ppm. This peak is asymmetrically broadened with a long tail at the low-frequency side, which is a hint of a distribution of [47/49]Ti NMR parameters due to a broad range of different Ti local environments. To extract the [47/49]Ti NMR parameters of sitinakite by spectral simulation, a Gaussian distribution model (in the QuadFit package)[81] was used on both C_Q and η_Q. The [49]Ti NMR parameters of sitinakite are established as: $C_Q(^{49}\text{Ti}) = 13 \pm 11$ MHz, $\eta_Q(^{49}\text{Ti}) = 0.85 \pm 0.15$, and $\delta_{\text{iso}}(^{49}\text{Ti}) = -850$ ppm.

Similar to the reported spectrum,[20] [23]Na MAS spectrum of sitinakite at 9.4 T (Figure 7-8c) exhibits a profile from ~ 10 to ~ -30 ppm, centered at ~ -9 ppm with a shoulder at ~ -13 ppm. However, no spectral simulation was performed in this literature. The fact that the observed spectrum cannot be fitted with a single resonance implies that there are at least two Na sites, agreeing well with the two types of Na^+ environments in sitinakite. [23]Na 3QMAS experiment was therefore performed to resolve the [23]Na peaks that are overlapping in the MAS spectrum. As Figure 7-8c illustrates, simulation of the slice taken from the cross-section of the shoulder at 9 ppm along the F1 axis gives rise to a single resonance. However, simulation of the slice corresponding to the cross-section at 10 ppm along the F1 axis yields another resonance with a more deshielded chemical shift. Using the NMR parameters obtained from 3QMAS, the [23]Na MAS spectrum can be simulated with two Na sites: Na(I): $C_Q(^{23}\text{Na}) = 1.9(1)$ MHz, $\eta_Q(^{23}\text{Na}) = 0.5(1)$, $\delta_{\text{iso}}(^{23}\text{Na}) = 0.4(10)$ ppm; and Na(II): $C_Q(^{23}\text{Na}) = 1.9 \pm 0.9$ MHz, $\eta_Q(^{23}\text{Na}) = 0.9 \pm 0.1$, $\delta_{\text{iso}}(^{23}\text{Na}) = 5.7$ ppm. As described in the literature,[20] Na(I) is tightly coordinated to the framework and ordered; whereas Na(II) is in the channels and can be disordered. Therefore, the latter Na site is assigned to Na(II) because it exhibits the line shape characteristic of disordered systems.

7.3.5   GTS-1
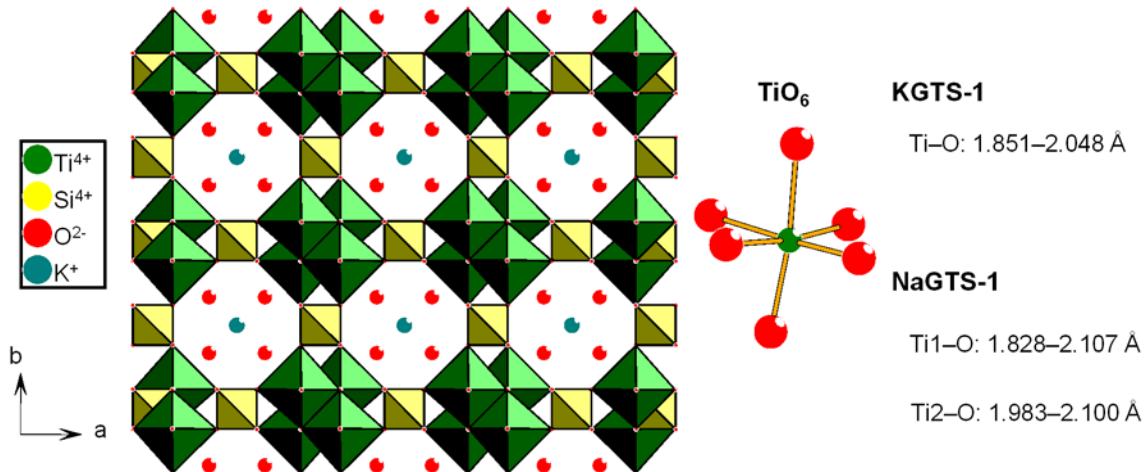
Figure 7-9: Left: the structure of KGTS-1. The hydrogen atoms and K–O bonds are omitted for clarity. Right: the local environment of Ti^{4+}. The Ti–O distances of two GTS-1 phases are shown in Å.

GTS-1 is a group of microporous titanosilicates with identical framework topology, isostructural to the mineral pharmacosiderite. The framework structure of GTS-1 (Figure 7-9) is very similar to sitinakite in that both structures are based on the interconnection of cubane-type Ti_4O_{16} clusters with isolated SiO_4 tetrahedra. The difference is that in GTS-1, Ti_4O_{16} clusters connect with SiO_4 in all three crystallographic directions, resulting in 3D channels with 8-ring windows. Similar to sitinakite, GTS-1 could undergo phase transformation as well without the alternation of the framework topology when heated or ion-exchanged.[12-14,21] The GTS-1 with K^+ as the counter cation (KGTS-1: $HK_3Ti_4O_4(SiO_4)_3 \cdot 4H_2O$) crystallizes in the cubic space group of *P*-43*m* (No. 215) and only has one Ti site (site symmetry: C_{3v}).[12] The single K^+ site is located in the center of channel, which is coordinated to four water molecules (K–O: 3.170 Å) and eight framework oxygens (K–O: 3.233 Å). It is worth mentioning that the water molecules are at tetrahedral corners and the symmetry at the oxygens is higher than C_{2v} (site symmetry: C_{3v}), indicating the water molecules must be disordered at ambient temperature. Because the K^+ directly coordinates to the framework, the disorder of water molecules must lead to the disorder of the framework. Moreover, the remaining proton of KGTS-1, **H**$K_3Ti_4O_4(SiO_4)_3 \cdot 4H_2O$, is not exchangeable. The position of this proton is not available

from the Rietveld refinement of the powder XRD pattern. However, previous study of the acid form of KGTS-1, $H_4Ti_4O_4(SiO_4)_3\cdot4H_2O$, suggests that the four protons are most likely to bound to the oxygens involved in interconnecting the Ti octahedra of the Ti_4O_{16} cluster. Therefore, it is likely that the proton of KGTS-1, **H**$K_3Ti_4O_4(SiO_4)_3\cdot4H_2O$, undergoes rapid exchange between the four oxygens, inducing the intrinsic disorder of the framework. The Na analog of KGTS-1, NaGTS-1 ($Na_4Ti_4O_4(SiO_4)_3\cdot6H_2O$), has a reduced crystal symmetry of *R3m* (No. 160, a subgroup of *P*-43*m*)[14] because Na$^+$ is too small to occupy the center of channel. The single Ti site of KGTS-1 now becomes two Ti sites with a ratio of 1 : 3 for NaGTS-1 and there is no proton bound to the Ti_4O_{16} clusters. The symmetry of Ti1 remains C_{3v}, the same as the Ti site of KGTS-1; whereas the symmetry of Ti2 is reduced to C_s. NaGTS-1 has two Na sites: one is four-coordinate (Na1, site symmetry: C_{3v}) and the other one is six-coordinate (Na2, site symmetry: C_s).
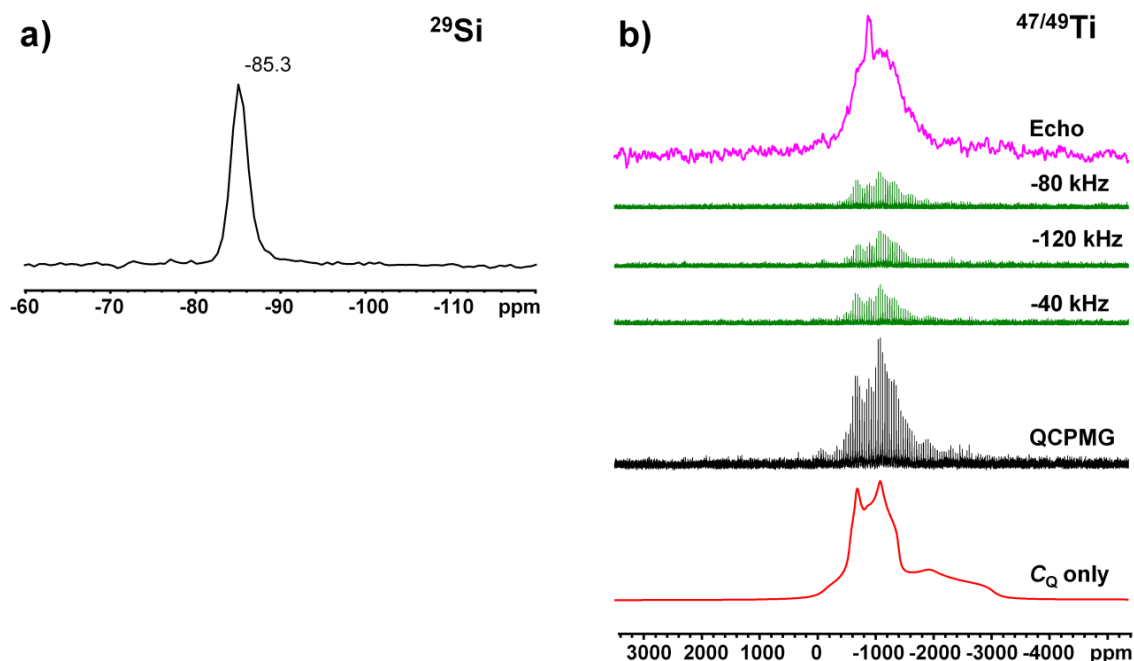

Figure 7-10: (a) Experimental ^{29}Si MAS SSNMR spectrum of GTS-1 at 9.4 T. (b) Experimental (Echo and QCPMG) and simulated natural abundance $^{47/49}$Ti static SSNMR spectra of GTS-1 at 21.1 T. The offset of the transmitter frequency is indicated on each sub-spectrum.

As Figure 7-A1 shows, powder XRD pattern indicates that this GTS-1 sample is virtually a mixture of KGTS-1 and NaGTS-1 (Na/K ~ 0.65 from EDS).[12,14] However, [29]Si MAS spectrum (Figure 7-10a) only consists of a single broad peak centered at -85.3 ppm, which is in the normal range of literature values.[26] The observation of a single peak rather than two illustrates that the local Si environments in two phases are very similar. Natural abundance [47/49]Ti static spectra of GTS-1 at 21.1 T are illustrated in Figure 7-10b. It is noteworthy that the spectra acquired using the QCPMG and quadrupolar echo techniques have close-related but different line shapes. The QCPMG spectrum consists of a narrower and stronger [49]Ti signal from ~ -400 to ~ -1400 ppm superimposed on a weaker and broader [47]Ti pattern from ~ 0 to ~ -3000 ppm, which are typical of a Ti site without axial symmetry. This site can only be Ti2 of NaGTS-1 since both the single Ti site of KGTS-1 and Ti1 of NaGTS-1 are axially symmetric. In sharp contrast, an additional narrow feature is observed in the echo spectrum centered at about -900 ppm, which is similar to the [47/49]Ti pattern of sitinakite. The narrow feature implies that the GTS-1 sample should contain some phases with a certain degree of disordering. As discussed earlier, the framework of KGTS-1 can be disordered due to either the disordered K^+ in the channel (which is directly bound to the framework oxygens) or the rapid exchange of proton among the four TiO_6 units in the Ti_4O_{16} clusters. Simulation of the QCPMG spectrum yields a set of [49]Ti NMR parameters for Ti2 of NaGTS-1: $C_Q(^{49}Ti) = 11.0(5)$ MHz, $\eta_Q(^{49}Ti) = 0.4(2)$, $\delta_{iso}(^{49}Ti) = -900(40)$ ppm. The effects of CSA interaction can be neglected in the simulation. Ti1 is not observed because it has a very large $C_Q(^{49}Ti)$, giving rise to a pattern too broad to be measured even at 21.1 T: the coordination sphere of Ti1 has a significantly larger degree of distortion (Ti1–O bond lengths: 1.828–2.107 Å) than that of Ti2 (Ti2–O bond lengths: 1.983–2.100 Å). Such prediction is further validated by the fact that the calculated $C_Q(^{49}Ti)$ of Ti1 (39.25 MHz) is much larger compared to Ti2 (10.13 MHz).
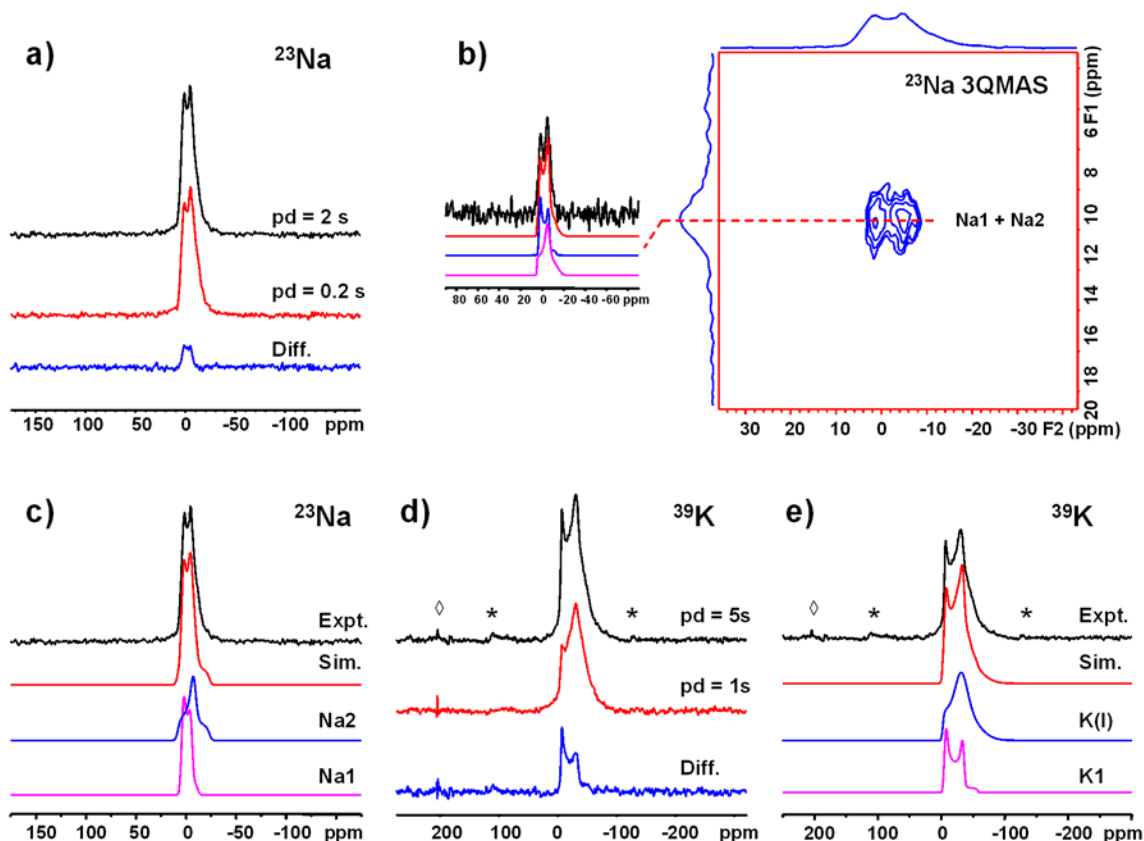
Figure 7-11: (a) ^{23}Na MAS SSNMR spectra of GTS-1 at 9.4 T as a function of pulse delay (pd). (b) ^{23}Na 3QMAS spectrum of GTS-1 at 9.4 T (bottom). The dashed lines correspond to the slices taken for simulation. (c) Experimental and simulated ^{23}Na MAS SSNMR spectra of GTS-1 at 9.4 T (pd = 2 s). The simulated ^{23}Na MAS spectrum was based on the difference spectrum of (a). (d) Natural abundance ^{39}K MAS SSNMR spectra of GTS-1 at 21.1 T as a function of pulse delay (pd). (e) Experimental and simulated natural abundance ^{39}K MAS SSNMR spectra of GTS-1 at 21.1 T. The simulated ^{39}K MAS spectrum was based on the parameters obtained from the difference spectrum of (d). *: spinning sidebands. ◊: transmitter artifact.

The local environments of Na$^+$ were studied by ^{23}Na SSNMR spectroscopy at 9.4 T. At first glance, ^{23}Na MAS spectrum of GTS-1 (Figure 7-11a) only displays a single resonance with two horns typical of patterns broadened by second-order quadrupolar interactions. However, the intensity of the right horn is even greater than that of the left horn, which is abnormal for MAS spectra of quadrupolar nuclei. Moreover, the observation of single ^{23}Na resonance is inconsistent with the crystal structure of NaGTS-

1. Therefore, ^{23}Na 3QMAS experiment was carried out to examine if there are actually two ^{23}Na resonances. Unfortunately, the slice extracted from the cross-section of the single peak along the F1 axis looks almost identical with the MAS spectrum (Figure 7-11b). Nevertheless, further investigation of MAS spectra as a function of pulse delay (Figure 7-11a) does confirm the existence of two ^{23}Na resonances: The first one has an axial symmetric quadrupolar line shape ($\eta_Q \approx 0$) with a relatively long spin-lattice relaxation time T_1, while the second one does not have an axial symmetry ($\eta_Q \approx 1$). The observed $\eta_Q(^{23}$Na) values agrees with the crystal structure of NaGTS-1, in which Na1 has a C_{3v} site symmetry while Na2 has a C_s site symmetry. The fact that the former one (Na1) has a long T_1 is indicative of high local ordering around this Na site. As shown in Figure 7-11c, using the ^{23}Na NMR parameters of Na1 obtained from the difference spectrum, the parameters of Na2 could also be determined: Na1: $C_Q(^{23}$Na) = 1.8(1) MHz, $\eta_Q(^{23}$Na) = 0.1(1), $\delta_{iso}(^{23}$Na) = 6.0(10) ppm; and Na2: $C_Q(^{23}$Na) = 2.2(1) MHz, $\eta_Q(^{23}$Na) = 1.0(1), $\delta_{iso}(^{23}$Na) = 8.3(10) ppm.

As mentioned earlier, although the sharp feature observed in the $^{47/49}$Ti echo spectrum has been assigned to the KGTS-1 phase, it is still not clear if the framework of KGTS-1 is disordered. Since K$^+$ is directly coordinated to the oxygens of TiO$_6$ in the framework, the disorder of K$^+$ must lead to the disorder of the framework as well. Herein, natural abundance ^{39}K MAS experiment of GTS-1 at 21.1 T was performed and the result is shown in Figure 7-11d. Interestingly, its line shape is similar to that of ^{23}Na MAS spectrum but the coexistence of two resonances is much more evident. Using the same approach shown in the former section, ^{39}K NMR parameters of two resonances are established: The one with an axial symmetry has $C_Q(^{39}$K) = 1.3(1) MHz, $\eta_Q(^{39}$K) = 0.1(1), $\delta_{iso}(^{39}$K) = 3(4) ppm; and the one without an axial symmetry has $C_Q(^{39}$K) = 1.3 ± 0.4 MHz, $\eta_Q(^{39}$K) = 0.9 ± 0.1, $\delta_{iso}(^{39}$K) = -2 ppm. The second K site is disordered due to the distribution of C_Q and η_Q. Direct observation of two ^{39}K resonances is somewhat striking since the crystal structure of KGTS-1 only consists one crystallographic K site. However, on one hand, the crystal structure of KGTS-1 was determined from the powder XRD data; on the other hand, the K cations of some KGTS-1 phase could be partially substituted by Na cations, resulting in a disorder of the K local environments. Such interpretation is

further verified by the measured short T_1 of this K site (K(I)), which is indicative of local disorder. The other site (K1) corresponds to the single crystallographic K site of KGTS-1 because of the high site symmetry and long T_1. Therefore, according to ^{39}K MAS experiments, disorder of the framework does exist in KGTS-1.

7.3.6 ETS-4
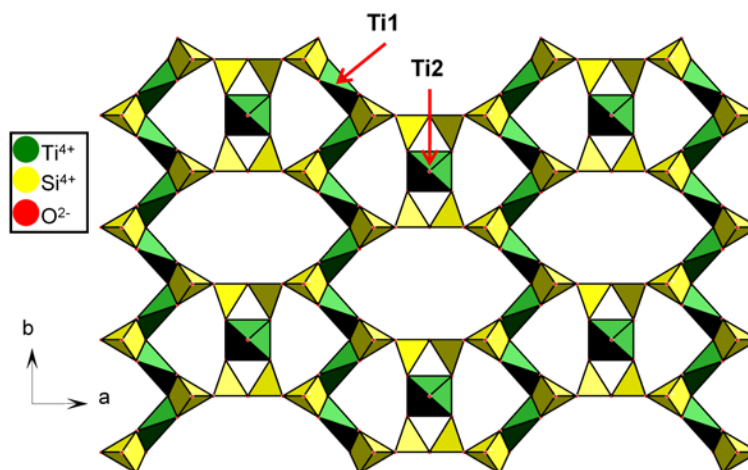
Figure 7-12: The structure of ETS-4. The hydrogen atoms and Na$^+$ cations are omitted for clarity.

As Figure 7-12 illustrates, the framework of ETS-4 ($Na_8(Ti_5H_2Si_{12}O_{39})\cdot(H_2O)_{8.45}$, Si/Ti ~ 2.1 from EDS) contains distorted octahedral TiO_6 chains, isolated square-pyramidal TiO_5 and tetrahedral SiO_4 units.[16] The TiO_6 octahedra (crystallographic Ti1 site) connect each other by sharing the opposite corner, forming –O–Ti–O–Ti–O– chains along the b axis, which is different from the edge-sharing brookite-type chains in AM-4. TiO_6 octahedra are very distorted, giving rise to O–Ti–O bond angles far from 90° (63–116°). The TiO_5 square-pyramids, which are the crystallographic Ti2 site, are surrounded by SiO_4 units. A striking structure feature of ETS-4 is that the interaction between neighboring TiO_5 pyramids is through water molecules, making them part of the structure. The anionic framework charges are compensated by extra-framework Na$^+$ cations (two Na sites: Na1 and Na2). Different from sitinakite and KGTS-1, whose frameworks are disordered due to the disordering of extra-framework species (counter cations and H_2O), the framework disorder of ETS-4 is intrinsic: 1) the 12-rings are only partially occupied

by TiO$_5$ units (occupancy: 0.25); 2) the orientation of TiO$_5$ units is random; and 3) water molecules mediating the interactions between neighboring TiO$_5$ units are also disordered. However, such disorder does not cause the termination of TiO$_6$ chain.
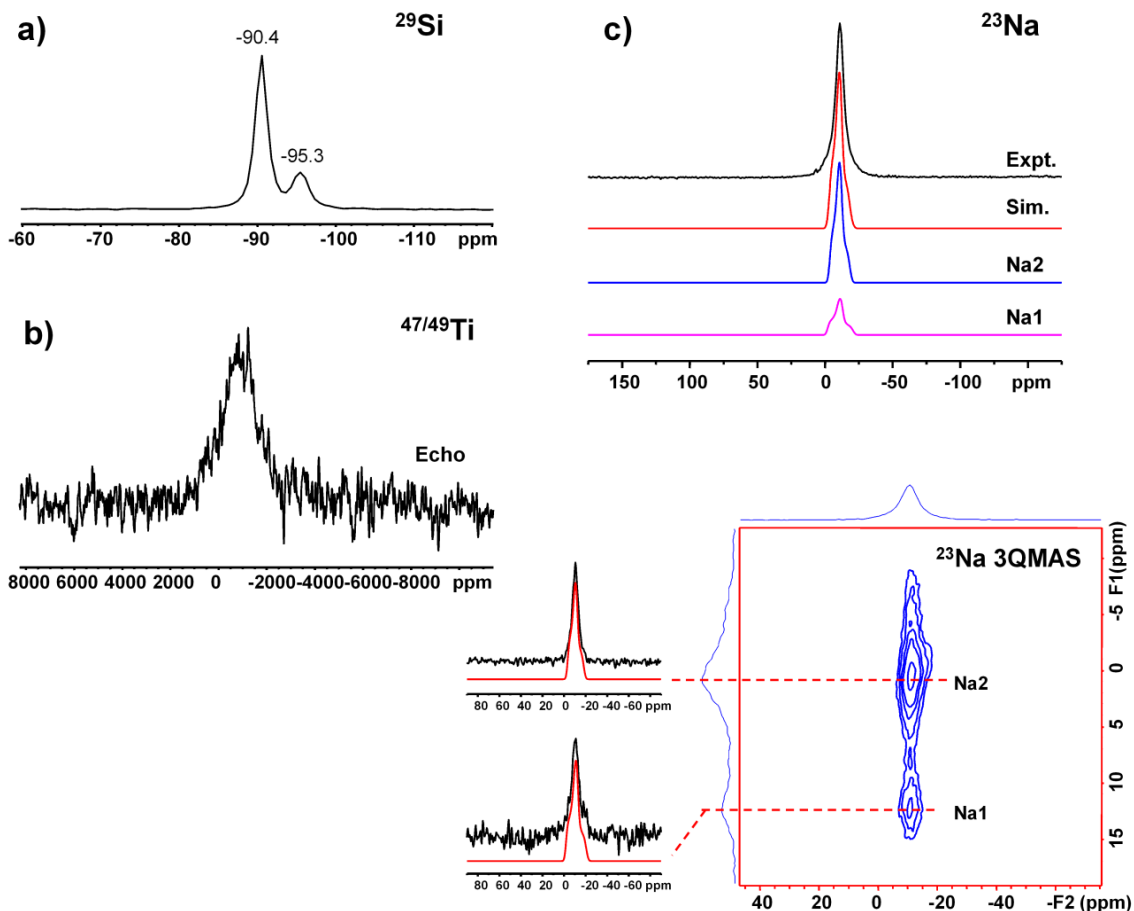
Figure 7-13: (a) Experimental ^{29}Si MAS SSNMR spectrum of ETS-4 at 9.4 T. (b) Experimental (Echo) natural abundance $^{47/49}$Ti static SSNMR spectrum of ETS-4 at 21.1 T. (c) Experimental and simulated ^{23}Na MAS SSNMR spectra of ETS-4 at 9.4 T (top); ^{23}Na 3QMAS spectrum of ETS-4 at 9.4 T (bottom). The dashed lines correspond to the slices taken for simulation. Simulated ^{23}Na MAS spectrum was based on the parameters obtained from 3QMAS.

Although ETS-4 has been extensively studied by ^{29}Si NMR experiments, it has never been characterized by $^{47/49}$Ti NMR. ^{29}Si MAS spectrum (Figure 7-13a) exhibits two peaks at -90.4 and -95.3 ppm, presenting the two Si local environments in ETS-4: Si(3Ti)

and Si(1Ti).[24,27] The acquisition of natural abundance $^{47/49}$Ti static echo spectrum of ETS-4 was very challenging even at 21.1 T. After performing the experiment for 16 h, the spectrum (Figure 7-13b) consists of a weak and very broad profile from ~ 900 to ~ -2600 ppm. However, the simulation and interpretation of $^{47/49}$Ti spectrum is rather difficult due to the poor S/N of the spectrum.

^{23}Na MAS spectrum of ETS-4 at 9.4 T only displays a sharp and featureless peak centered at -11 ppm (Figure 7-13c). However, two resonances along the F1 axis have been directly resolved in 2D ^{23}Na 3QMAS spectrum of ETS-4. Two sets of ^{23}Na NMR parameters were produced by spectral simulation: Na1 has $C_Q(^{23}$Na$)$ = 1.8(1) MHz, $\eta_Q(^{23}$Na$)$ = 0.8(1), $\delta_{iso}(^{23}$Na$)$ = -1.7(5) ppm; and Na2 has $C_Q(^{23}$Na$)$ = 1.6(1) MHz, $\eta_Q(^{23}$Na$)$ = 0.8(1), $\delta_{iso}(^{23}$Na$)$ = -3.4(5) ppm, consistent with the crystal structure of ETS-4. The two Na resonances are assigned based on the relative intensity, where the more abundant Na site is Na2.

7.3.7   ETS-10

Figure 7-14: The structure of ETS-10. The bridging O atoms are omitted to show the connectivity between Si/Si and Si/Ti. The distance a ≈ b causes the stacking defaults. The dashed line presents the TiO$_6$ chains. The five possible Na sites are also shown.

ETS-10 (($Na_{2-x}K_x$)$TiSi_5O_{13} \cdot 4H_2O$, Na/K ~ 4.5 and Si/Ti ~ 4.5 from EDS) is a large-pore microporous titanosilicate with a framework containing "TiO_2" rods (Figure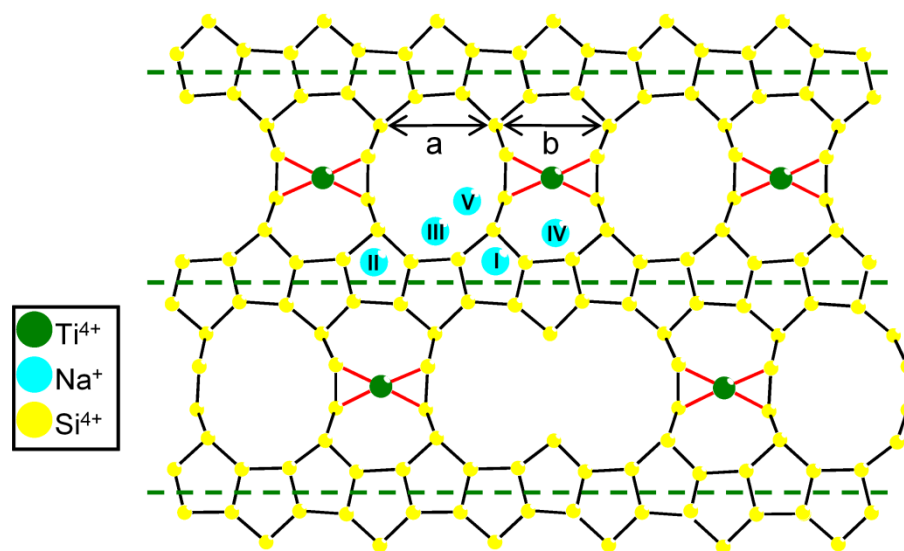 7-14), which extend along two orthogonal directions, surrounded by tetrahedral silicate units.[18,19] The pore structure consists of 12-, 7-, 5-, and 3-rings and has a 3D large-pore channel system, which makes it promising in many applications such as catalysis. The intrinsic disorder of the framework of ETS-10 arises from structural faulting that the alternating 12-rings filled with Ti and void can be broken by the voids. Therefore, it is possible to describe the structure (Figure 7-A2) in terms of an intergrowth of two ordered polymorphs with tetragonal (polymorph A) and monoclinic (polymorph B) symmetry, respectively.[18,19] Since ETS-10 contains corner-sharing TiO_6 octahedra and SiO_4 tetrahedra for every framework Ti, there is an associated -2 charge compensated by extra-framework cations, in this case, Na^+ and K^+ in channels. The location of Na sites were determined by lattice energy minimization calculations in the literature,[30] suggesting five possible Na sites in the structure (Figure 7-14): Na(I) and Na(II) is near the TiO_6 chains, close to the 5-ring apex on either side of the 12-ring; Na(III) is also near the TiO_6 chains but at the top (or bottom) of the 12-ring; whereas Na(IV) sits in the 12-ring filled with Ti (or 7-ring) between two orthogonal TiO_6 chains. Although there are many possibilities for the location of Na(V), all of which are in the 12-ring and thus have very similar energies. K^+ could, in principle, occupy all the above-mentioned five Na sites. However, previous studies show that Na(IV) and Na(V) are the most favored sites for K^+ substitution.[30,86]

Illustrated in Figure 7-15a, [29]Si MAS spectrum of ETS-10 consist of three peaks at -94.9, -96.9 and -104.3 ppm, respectively. According to the literature,[18] the former two are assigned to framework Si in the Si(1Ti) environment, while the latter one is assigned to Si in the Si(0Ti) environment. Although natural abundance [47/49]Ti static echo spectrum of ETS-10 has been reported by Nakata and co-workers,[41] it was recorded at a low magnetic field of 9.4 T and thus has a rather poor S/N. Moreover, no spectral simulation and interpretation were performed in this literature. [47/49]Ti spectrum of ETS-10 at 21.1 T (Figure 7-15b) has a much better S/N, which exhibits a typical quadrupolar pattern from ~ 1800 to ~ -4800 ppm, arising from a single Ti site. In this work, the spectrum can be

simulated reasonably well using a set of ^{49}Ti NMR parameters: $C_Q(^{49}\text{Ti}) = 16.5(20)$ MHz, $\eta_Q(^{49}\text{Ti}) = 0.85(10)$ and $\delta_{iso}(^{49}\text{Ti}) = -1100(50)$ ppm. The fact that the spectrum can be fitted using a single Ti site agrees with the crystal structure of ETS-10 that there is only one type of Ti environment: TiO_6 units that share their corners to form 1D chains (namely Ti(I)). The $C_Q(^{49}\text{Ti})$ of ETS-10 is quite large for 6-coordinated Ti,[44] confirming that the TiO_6 units is indeed highly distorted.

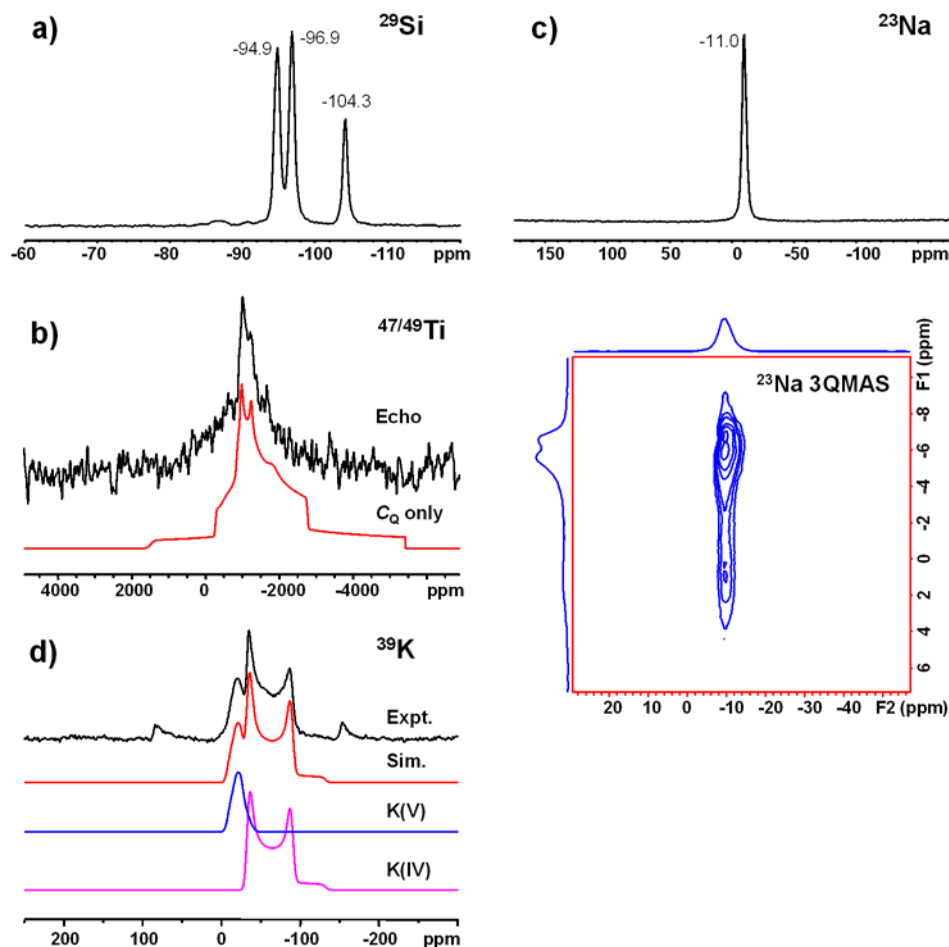**Figure 7-15:** (a) Experimental ^{29}Si MAS SSNMR spectrum of ETS-10 at 9.4 T. (b) Experimental (Echo) and simulated natural abundance $^{47/49}$Ti static SSNMR spectra of ETS-10 at 21.1 T. (c) Experimental ^{23}Na MAS SSNMR spectrum of ETS-10 at 9.4 T (top); ^{23}Na 3QMAS spectrum of ETS-4 at 9.4 T (bottom). (d) Experimental and simulated ^{39}K MAS SSNMR spectra of ETS-10 at 21.1 T. *: spinning sidebands.

The possible Na sites of ETS-10 have been studied in the literature,[29,30,33,86] demonstrating that the occupancy of these Na sites are determined by many parameters including the Ti/Si ratio, Na^+/K^+ ratio, and hydration degree. ^{23}Na MAS and 3QMAS spectra of ETS-10 (Figure 7-15d) are similar to those previously reported. It seems like all Na sites have very similar NMR parameters and it is not possible to resolve them by ^{23}Na NMR.

Natural abundance ^{39}K MAS spectrum of ETS-10 at 21.1 T (Figure 7-15d) clearly consists of two resonances: one is axial symmetric with NMR parameters of $C_Q(^{39}K) = 1.8(1)$ MHz, $\eta_Q(^{39}K) = 0.1(1)$ and $\delta_{iso}(^{39}K) = -18(4)$ ppm; whereas the other one is not axial symmetric with NMR parameters of $C_Q(^{39}K) = 0.95(10)$ MHz, $\eta_Q(^{39}K) = 0.6(1)$ and $\delta_{iso}(^{39}K) = -7(5)$ ppm. Observing two ^{39}K resonances rather than five is consistent with the literature that K^+ prefers to substituting Na^+ in Na(IV) and Na(V) among all five possible Na sites.[30,86] The former ^{39}K resonance is assigned to K^+ that occupies the Na(IV) site and the latter one is assigned to K^+ that occupies the Na(V) site (hereafter referred to as K(IV) and K(V), respectively). Since K(IV) is inside of 7-rings while K(V) is inside of 12-rings, the degree of distortion for the coordination sphere of K(IV) might be greater than K(V) due to stronger interactions between K^+ and the framework, giving rise to a larger C_Q. It is also worth mentioning that ^{39}K NMR is very sensitive to the local environment of counter cations, even though Na(IV) and Na(V) are not distinguishable by ^{23}Na NMR.

Table 7-1: Experimental ^{49}Ti NMR parameters.

Sample	Site	Coordination	C_Q [MHz]	η_Q	δ_{iso} [ppm]
natisite[a]	Ti1	5	10.7(1)	0.05(5)	-740(30)
AM-1[b]	Ti1	5	13.4(1)	0.05(5)	-783(30)
AM-4[c]	Ti1	6	8.2(2)	1.0(1)	-850(30)
sitinakite	Ti1	6	13 ± 11	0.85 ± 0.15	-850
NaGTS-1	Ti2	6	11.0(5)	0.4(2)	-900(40)
ETS-10	Ti(I)	6	16.5(20)	0.85(10)	-1100(50)

a: CSA: $\Omega = 500(30)$ ppm, $\kappa = 1.0(1)$, $(\alpha, \beta, \gamma) = (0°, 0°, 0°)$.

b: CSA: $\Omega = 500(30)$ ppm, $\kappa = 1.0(1)$, $(\alpha, \beta, \gamma) = (0°, 0°, 0°)$.

c: Gaussian distribution.

Experimental [49]Ti NMR parameters of titanosilicate samples studied in this work are shown in Table 7-1; while calculated ^{29}Si, ^{23}Na, and [49]Ti NMR parameters are shown in Table 7-A3–A5. The observed [47/49]Ti NMR parameters of titanosilicates can be related to their spectral features: For 5-coordinated Ti^{4+} (natisite and AM-1), it has a relatively large C_Q and a large CSA. For 6-coordinated Ti^{4+} in an edge-shared TiO_4 chain (AM-4), it has a small C_Q. For 6-coordinated Ti^{4+} in a corner-shared Ti_4O_{16} cluster (sitinakite and GTS-1), the local Ti environment can be disordered. For 6-coordinated Ti^{4+} in a corner-shared TiO_4 chain (ETS-10), it has a very large C_Q.

7.4   Conclusions

In this work, multinuclear SSNMR experiments, including [29]Si, ^{23}Na, [47/49]Ti, and [39]K NMR, were performed on several prototypical titanosilicates: natisite, AM-1, AM-4, sitinakite, GTS-1, ETS-4, and ETS-10. These samples were selected because they consist of several representative Ti local environments in titanosilicates: 5-coordinated Ti in the square-pyramidal geometry for natisite, AM-1, and ETS-4; edge-shared brookite-type TiO_6 chain for AM-4; cubane-type Ti_4O_{16} cluster for sitinakite and GTS-1; corner-shared TiO_6 chain for ETS-4 and ETS-10. Natural abundance [47/49]Ti SSNMR spectra acquired at 21.1 T imply that the observed spectral features can be directly related to these Ti local environments. This work is highlighted by the results from ^{29}Si, ^{23}Na, and [39]K SSNMR experiments as well: high-quality [29]Si MAS spectra without (or with very few) impurity peaks were collected, confirming the Si local environments proposed by crystal structures; whereas ^{23}Na and [39]K SSNMR experiments provide fruitful structure information about the counter cations, which are often disordered and thus are very difficult to be characterized by diffraction-based techniques such XRD. It should be pointed out that natural abundance [39]K SSNMR experiments were first carried out on titanosilicates, which has higher resolution than ^{23}Na SSNMR experiments. First-principles calculations of NMR parameters by the GIPAW method (the CASTEP code) also shed lights on the interpretation of ^{29}Si, ^{23}Na, and [47/49]Ti SSNMR spectra. It is hoped that the approach described and the results presented in this work can be used in the further investigation of titanosilicates with unknown or poorly demonstrated structures.

7.5 References

(1) Wang, L. M.; Chen, J.; Ewing, R. C. *Curr. Opin. Solid State Mater. Sci.* **2005**, *8*, 405-418.

(2) Lopes, C. B.; Coimbra, J.; Otero, M.; Pereira, E.; Duarte, A. C.; Lin, Z.; Rocha, J. *Quim. Nova* **2008**, *31*, 321-325.

(3) Lopes, C. B.; Lito, P. F.; Otero, M.; Lin, Z.; Rocha, J.; Silva, C. M.; Pereira, E.; Duarte, A. C. *Microporous Mesoporous Mater.* **2008**, *115*, 98-105.

(4) Popa, K.; Pavel, C. C. *Desalination* **2012**, *293*, 78-86.

(5) Murugavel, R.; Roesky, H. W. *Angew. Chem., Int. Ed.* **1997**, *36*, 477-479.

(6) Ratnasamy, P.; Srinivas, D.; Knoezinger, H. *Adv. Catal.* **2004**, *48*, 1-169.

(7) Uma, S.; Rodrigues, S.; Martyanov, I. N.; Klabunde, K. J. *Microporous Mesoporous Mater.* **2004**, *67*, 181-187.

(8) Dutta, P. K.; Severance, M. *J. Phys. Chem. Lett.* **2011**, *2*, 467-476.

(9) Kuznicki, S. M.; Bell, V. A.; Nair, S.; Hillhouse, H. W.; Jacubinas, R. M.; Braunbarth, C. M.; Toby, B. H.; Tsapatsis, M. *Nature* **2001**, *412*, 720-724.

(10) Rocha, J.; Anderson, M. W. *Eur. J. Inorg. Chem.* **2000**, 801-818.

(11) Poojary, D. M.; Cahill, R. A.; Clearfield, A. *Chem. Mater.* **1994**, *6*, 2364-2368.

(12) Behrens, E. A.; Poojary, D. M.; Clearfield, A. *Chem. Mater.* **1996**, *8*, 1236-1244.

(13) Poojary, D. M.; Bortun, A. I.; Bortun, L. N.; Clearfield, A. *Inorg. Chem.* **1996**, *35*, 6131-6139.

(14) Dadachov, M. S.; Harrison, W. T. A. *J. Solid State Chem.* **1997**, *134*, 409-415.

(15) Kuznicki, S. M. *US Patent 4,853,202*, **1989**.

(16) Cruciani, G.; De Luca, P.; Nastro, A.; Pattison, P. *Microporous Mesoporous Mater.* **1998**, *21*, 143-153.

(17) Dadachov, M. S.; Rocha, J.; Ferreira, A.; Lin, Z.; Anderson, M. W. *Chem. Commun.* **1997**, *1997*, 2371-2372.

(18) Anderson, M. W.; Terasaki, O.; Ohsuna, T.; Philippou, A.; MacKay, S. P.; Ferreira, A.; Rocha, J.; Lidin, S. *Nature* **1994**, *367*, 347-351.

(19) Anderson, M. W.; Terasaki, O.; Ohsuna, T.; Malley, P. J. O.; Philippou, A.; MacKay, S. P.; Ferreira, A.; Rocha, J.; Lidin, S. *Philos. Mag. B* **1995**, *71*, 813-841.

(20) Thorogood, G. J.; Kennedy, B. J.; Griffith, C. S.; Elcombe, M. M.; Avdeev, M.; Hanna, J. V.; Thorogood, S. K.; Luca, V. *Chem. Mater.* **2010**, *22*, 4222-4231.

(21) Ferdov, S. *Microporous Mesoporous Mater.* **2012**, *159*, 96-99.

(22)   MacKenzie, K. J. D.; Smith, M. E. *Multinuclear Solid-State NMR of Inorganic Materials*; 1st ed.; Pergamon: Oxford; New York, **2002**.

(23)   Lin, Z.; Rocha, J.; Brandao, P.; Ferreira, A.; Esculcas, A. P.; Pedrosa de Jesus, J. D.; Philippou, A.; Anderson, M. W. *J. Phys. Chem. B* **1997**, *101*, 7114-7120.

(24)   Balmer, M. L.; Bunker, B. C.; Wang, L. Q.; Peden, C. H. F.; Su, Y. *J. Phys. Chem. B* **1997**, *101*, 9170-9179.

(25)   Kostov-Kytin, V.; Mihailova, B.; Kalvachev, Y.; Tarassov, M. *Microporous Mesoporous Mater.* **2005**, *86*, 223-230.

(26)   Kostov-Kytin, V.; Nikolova, R.; Nakayama, N.; Simova, S.; Tzvetkova, P. C. *R. Acad. Bulg. Sci.* **2011**, *64*, 683-692.

(27)   Labouriau, A.; Higley, T. J.; Earl, W. L. *J. Phys. Chem. B* **1998**, *102*, 2897-2904.

(28)   Guo, M.; Feng, Z.; Li, G.; Hofmann, J. P.; Pidko, E. A.; Magusin, P. C. M. M.; Guo, Q.; Weckhuysen, B. M.; Hensen, E. J. M.; Fan, F.; Li, C. *Chem. Eur. J.* **2012**, *18*, 12078-12084.

(29)   Ganapathy, S.; Das, T. K.; Vetrivel, R.; Ray, S.; Sen, T.; Sivasanker, S.; Delevoye, L.; Fernandez, C.; Amoureux, J. P. *J. Am. Chem. Soc.* **1998**, *120*, 4752-4762.

(30)   Anderson, M. W.; Agger, J. R.; Luigi, D.-P.; Baggaley, A. K.; Rocha, J. *Phys. Chem. Chem. Phys.* **1999**, *1*, 2287-2292.

(31)   Pavel, C. C.; Vuono, D.; Catanzaro, L.; De Luca, P.; Bilba, N.; Nastro, A.; Nagy, J. B. *Microporous Mesoporous Mater.* **2002**, *56*, 227-239.

(32)   Yang, X.; Paillaud, J. L.; van Breukelen, H. F. W. J.; Kessler, H.; Duprey, E. *Microporous Mesoporous Mater.* **2001**, *46*, 1-11.

(33)   Southon, P. D.; Howe, R. F. *Chem. Mater.* **2002**, *14*, 4209-4218.

(34)   Zibrowius, B.; Weidenthaler, C.; Schmidt, W. *Phys. Chem. Chem. Phys.* **2003**, *5*, 773-777.

(35)   Kanert, O.; Kolem, H. *J. Phys. C: Solid State Phys.* **1988**, *21*, 3909-3916.

(36)   Dec, S. F.; Davis, M. F.; Maciel, G. E.; Bronnimann, C. E.; Fitzgerald, J. J.; Han, S. S. *Inorg. Chem.* **1993**, *32*, 955-959.

(37)   Tunstall, D. P.; Todd, J. R. M.; Arumugam, S.; Dai, G.; Dalton, M.; Edwards, P. P. *Phys. Rev. B: Condens. Matter* **1994**, *50*, 16541-16549.

(38)   MacKenzie, K. J. D.; Meinhold, R. H.; McGavin, D. G.; Ripmeester, J. A.; Moudrakovski, I. *Solid State Nucl. Magn. Reson.* **1995**, *4*, 193-201.

(39)   Labouriau, A.; Earl, W. L. *Chem. Phys. Lett.* **1997**, *270*, 278-284.

(40)   Bastow, T. J.; Gibson, M. A.; Forwood, C. T. *Solid State Nucl. Magn. Reson.* **1998**, *12*, 201-209.

(41)   Nakata, S.; Tanaka, Y.; Asaoka, S.; Nakamura, M. *J. Mol. Struct.* **1998**, *441*, 267-281.

(42)   Bastow, T. J.; Whitfield, H. J. *Chem. Mater.* **1999**, *11*, 3518-3520.

(43)   Bastow, T. J.; Doran, G.; Whitfield, H. J. *Chem. Mater.* **2000**, *12*, 436-439.

(44)   Padro, D.; Howes, A. P.; Smith, M. E.; Dupree, R. *Solid State Nucl. Magn. Reson.* **2000**, *15*, 231-236.

(45)   Gervais, C.; Smith, M. E.; Pottier, A.; Jolivet, J. P.; Babonneau, F. *Chem. Mater.* **2001**, *13*, 462-467.

(46)   Bastow, T. J.; Whitfield, H. J. *Solid State Commun.* **2001**, *117*, 483-488.

(47)   Padro, D.; Jennings, V.; Smith, M. E.; Hoppe, R.; Thomas, P. A.; Dupree, R. *J. Phys. Chem. B* **2002**, *106*, 13176-13185.

(48)   Ganapathy, S.; Gore, K. U.; Kumar, R.; Amoureux, J.-P. *Solid State Nucl. Magn. Reson.* **2003**, *24*, 184-195.

(49)   Gervais, C.; Veautier, D.; Smith, M. E.; Babonneau, F.; Belleville, P.; Sanchez, C. *Solid State Nucl. Magn. Reson.* **2004**, *26*, 147-152.

(50)   Lambert, J. F.; Prost, R.; Smith, M. E. *Clays Clay Miner.* **1992**, *40*, 253-261.

(51)   Krawietz, T. R.; Murray, D. K.; Haw, J. F. *J. Phys. Chem. A* **1998**, *102*, 8779-8785.

(52)   Thomas, P. A.; Baldwin, A.; Dupree, R.; Blaha, P.; Schwarz, K.; Samoson, A.; Gan, Z. H. *J. Phys. Chem. B* **2004**, *108*, 4324-4331.

(53)   Carroll, D. L.; Kemp, T. F.; Bastow, T. J.; Smith, M. E. *Solid State Nucl. Magn. Reson.* **2005**, *28*, 31-43.

(54)   Nielsen, U. G.; Majzlan, J.; Phillips, B.; Ziliox, M.; Grey, C. P. *Am. Mineral.* **2007**, *92*, 587-597.

(55)   Bowers, G. M.; Bish, D. L.; Kirkpatrick, R. J. *J. Phys. Chem. C* **2008**, *112*, 6430-6438.

(56)   Wu, G.; Zhu, J. *Prog. Nucl. Magn. Reson. Spectrosc.* **2012**, *61*, 1-70.

(57)   Harris, R. K.; Becker, E. D.; Cabral De Menezes, S. M.; Goodfellow, R.; Granger, P. *Pure Appl. Chem.* **2001**, *73*, 1795-1818.

(58)   Smith, M. E.; van Eck, E. R. H. *Prog. Nucl. Magn. Reson. Spectrosc.* **1999**, *34*, 159-201.

(59)   Pyykkö, P. *Mol. Phys.* **2008**, *106*, 1965-1974.

(60)   Zhu, J.; Trefiak, N.; Woo, T. K.; Huang, Y. *J. Phys. Chem. C* **2009**, *113*, 10029-10037.

(61)   Rossini, A. J.; Hung, I.; Schurko, R. W. *J. Phys. Chem. Lett.* 2010, 1, 2989-2998.

(62)   Stebbins, J. F.; Du, L.-S.; Kroeker, S.; Neuhoff, P.; Rice, D.; Frye, J.; Jakobsen, H. J. *Solid State Nucl. Magn. Reson.* **2002**, *21*, 105-115.

(63)   Duxson, P.; Provis, J. L.; Lukey, G. C.; van Deventer, J. S. J.; Separovic, F.; Gan, Z. H. *Ind. Eng. Chem. Res.* **2006**, *45*, 9208-9210.

(64)   Moudrakovski, I. L.; Ripmeester, J. A. *J. Phys. Chem. B* **2007**, *111*, 491-495.

(65)   Larsen, F. H.; Jakobsen, H. J.; Ellis, P. D.; Nielsen, N. C. *J. Phys. Chem. A* **1997**, *101*, 8597-8606

(66)   Kupce, E.; Freeman, R. *J. Magn. Reson., Ser. A* **1995**, *115*, 273-276.

(67)   Massiot, D.; Farnan, I.; Gautier, N.; Trumeau, D.; Trokiner, A.; Coutures, J. P. *Solid State Nucl. Magn. Reson.* **1995**, *4*, 241-248.

(68)   Brauniger, T.; Madhu, P. K.; Pampel, A.; Reichert, D. *Solid State Nucl. Magn. Reson.* **2004**, *26*, 114-120.

(69)   Larsen, F. H.; Farnan, I.; Lipton, A. S. *J. Magn. Reson.* **2006**, *178*, 228-236.

(70)   O'Dell, L. A.; Schurko, R. W. *Chem. Phys. Lett.* **2008**, *464*, 97-102.

(71)   Perras, F. A.; Viger-Gravel, J.; Burgess, K. M. N.; Bryce, D. L. *Solid State Nucl. Magn. Reson.* **2013**, *51-52*, 1-15.

(72)   Nyman, H.; O'Keeffe, M.; Bovin, J. O. *Acta Crystallogr., Sect. B* **1978**, *B34*, 905-906.

(73)   Ferdov, S.; Kolitsch, U.; Lengauer, C.; Tillmanns, E.; Lin, Z.; Sa Ferreira, R. A. *Acta Crystallogr., Sect. E* **2007**, *E63*, i186.

(74)   Charpentier, T. *Solid State Nucl. Magn. Reson.* **2011**, *40*, 1-20.

(75)   Bonhomme, C.; Gervais, C.; Babonneau, F.; Coelho, C.; Pourpoint, F.; Azais, T.; Ashbrook, S. E.; Griffin, J. M.; Yates, J. R.; Mauri, F.; Pickard, C. J. *Chem. Rev.* **2012**, *112*, 5733-5779.

(76)   Rocha, J.; Ferreira, A.; Lin, Z.; Anderson, M. W. *Microporous Mesoporous Mater.* **1998**, *23*, 253-263.

(77)   Ferdov, S.; Sa Ferreira, R. A.; Lin, Z. *J. Lumin.* **2008**, *128*, 1108-1112.

(78)   Kunwar, A. C.; Turner, G. L.; Oldfield, E. *J. Magn. Reson.* **1986**, *69*, 124-127.

(79)   Gan, Z.; Kwak, H.-T. *J. Magn. Reson.* **2004**, *168*, 346-351.

(80)   Massiot, D.; Fayon, F.; Capron, M.; King, I.; Le Calve, S.; Alonso, B.; Durand, J.-O.; Bujoli, B.; Gan, Z.; Hoatson, G. *Magn. Reson. Chem.* **2002**, *40*, 70-76.

(81)   Kemp, T. F.; Smith, M. E. *Solid State Nucl. Magn. Reson.* **2009**, *35*, 243-252.

(82)   Brouwer, D. H.; Moudrakovski, I. L.; Darton, R. J.; Morris, R. E. *Magn. Reson. Chem.* **2010**, *48*, S113-S121.

(83)   Rose, M. E. *Elementary Theory of Angular Momentum*; Wiley: New York, **1957**.

(84)   Frydman, L.; Harwood, J. S. *J. Am. Chem. Soc.* **1995**, *117*, 5367-5368.

(85)   Pauling, L.; Sturdivant, J. H. *Zeitschrift fuer Kristallographie, Kristallgeometrie, Kristallphysik, Kristallchemie* **1928**, *68*, 239-256.

(86)   Sankar, G.; Bell, R. G.; Thomas, J. M.; Anderson, M. W.; Wright, P. A.; Rocha, J. *J. Phys. Chem.* **1996**, *100*, 449-452.
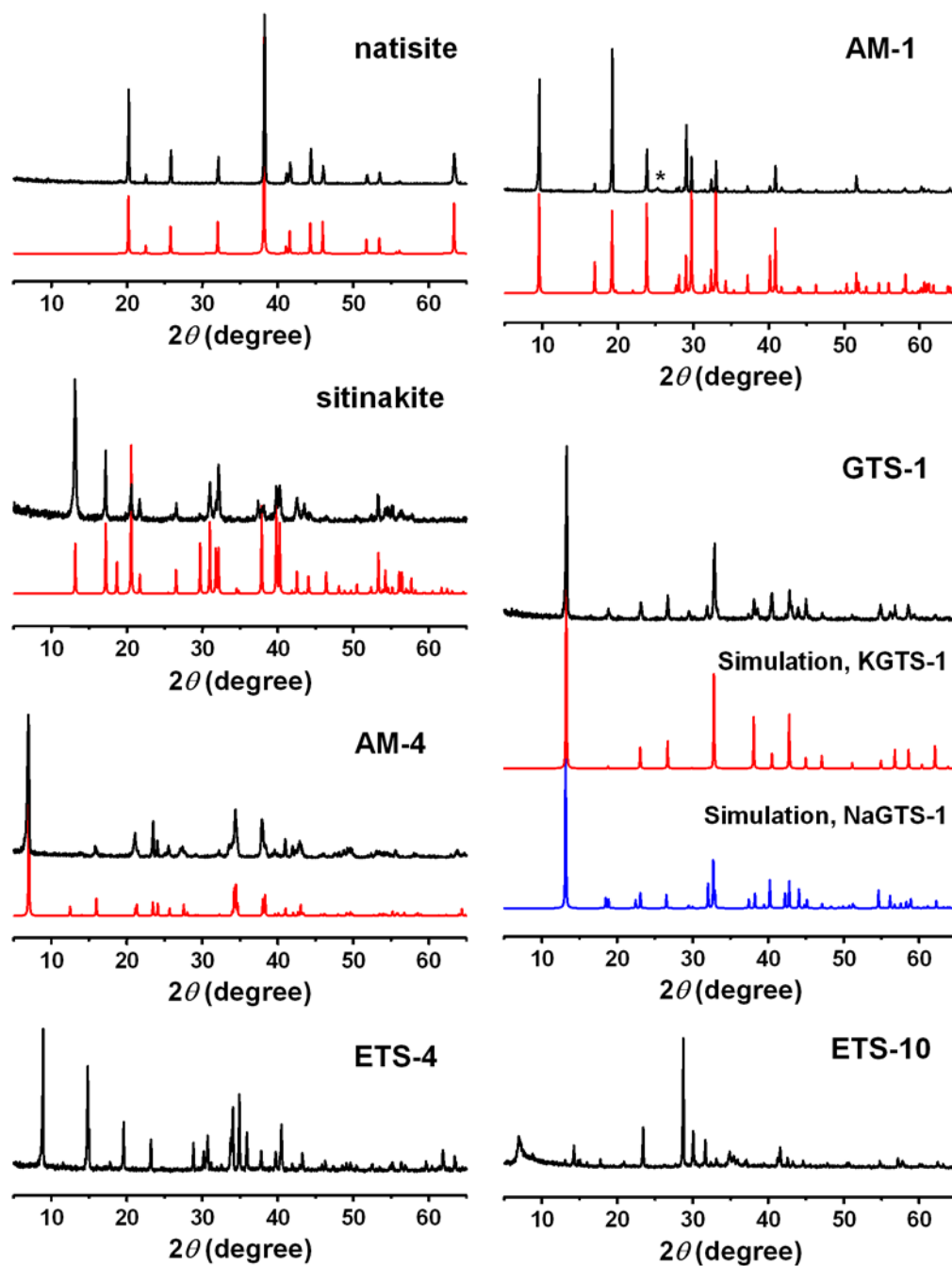
7.6 Appendix

Section A1: Powder XRD Patterns

Figure 7-A1: Powder XRD patterns of titanosilicates. *: impurity.

Section A2: Solid-State NMR Characterizations

Table 7-A1: $^{47/49}$Ti SSNMR measurement conditions.

Sample	Experiment	Pulse delay (s)	Number of scans
natisite	WURST-echo	0.5	32768 (LTH[a])
			32768 (HTL[b])
	WURST-QCPMG	1	2048 (-80 kHz[c])
AM-1	WURST-echo	0.5	49152 (LTH)
			49152 (HTL)
	WURST-QCPMG	0.5	8196 (-80 kHz)
			8196 (-120 kHz)
			8196 (-40 kHz)
AM-4	quadrupolar echo	0.5	49152
	WURST-QCPMG	0.5	8196 (-80 kHz)
			8196 (-120 kHz)
			8196 (-40 kHz)
sitinakite	quadrupolar echo	1	49152
GTS-1	quadrupolar echo	0.5	123904
	WURST-QCPMG	0.5	8196 (-80 kHz)
			8196 (-120 kHz)
			8196 (-40 kHz)
ETS-4	quadrupolar echo	0.5	118784
ETS-10	quadrupolar echo	1	49152

a: low-to-high direction for the WURST pulse.

b: high-to-low direction for the WURST pulse.

c: Increment (offset) of transmitter frequency.

Table 7-A2: ^{23}Na SSNMR measurement conditions.

Sample	Experiment	Pulse delay (s)	T_1 (s)	Number of scans
natisite	MAS	2	0.75	512
	3QMAS	2		312 × 64
AM-1	MAS	2	0.35	512
AM-4	MAS	2	0.16	1024
	3QMAS	2		312 × 64
GTS-1	MAS	0.2, 2	0.0012	512
	3QMAS	2		312 × 64
ETS-4	MAS	1	0.0013	1024
	3QMAS	0.5		1368 × 64
ETS-10	MAS	0.5	0.0074	1024
	3QMAS	0.5		600 × 128

Section A3: Calculated NMR Parameters

Table 7-A3: Calculated ^{29}Si NMR parameters

Sample	Site	Si environment	δ_{iso} [ppm]
natisite	Si1	Si(4Ti)	-78.84
AM-1	Si1	Si(1Ti)	-110.76
AM-4[a]	Si1	Si(3Ti)	-91.64
	Si2	Si(1Ti)	-95.26
sitinakite	Si1	Si(4Ti)	-69.92
NaGTS-1	Si1	Si(4Ti)	-79.51

a: The structure was not optimized.

Table 7-A4: Calculated ^{23}Na NMR parameters

Sample	Site	Coordination	C_Q [MHz]	η_Q
natisite	Na1	6	4.28	0.81
AM-1	Na1	6	1.75	0.22
AM-4	Na1	6	2.21	0.80
	Na2	6	1.47	0.31
	Na3	4	3.90	0.88
sitinakite	Na(I)	6	6.22	0.69
	Na(II)	6	4.98	0.53
NaGTS-1	Na1	4	1.92	0.00
	Na2	6	3.50	0.63

Table 7-A5: Calculated ^{49}Ti NMR parameters

Sample	Site	Coordination	C_Q [MHz]	η_Q	Ω [ppm]	κ
natisite	Ti1	5	9.88	0.00	644.94	-1.00
AM-1	Ti1	5	17.05	0.00	705.39	-1.00
AM-4	Ti1	6	11.13	0.92	127.35	0.55
sitinakite	Ti1	6	8.70	0.45	97.83	-0.68
NaGTS-1	Ti1	6	39.25	0.00	52.44	1.00
	Ti2	6	10.13	0.52	129.56	0.20

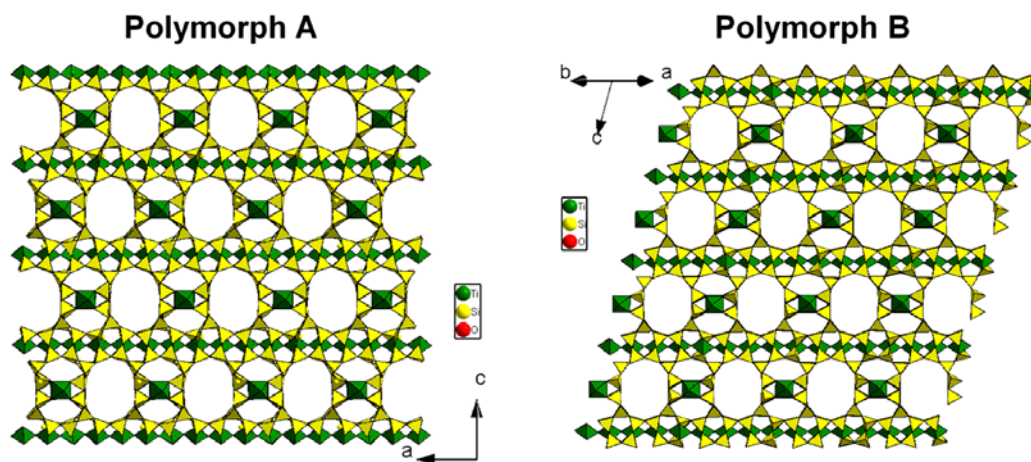Section A4: Two Polymorphs of ETS-10

Figure 7-A2: The structures of two polymorphs of ETS-10.

Chapter 8

8   Summary and Future Work

8.1   Summary

Microporous materials are important functional materials due to their promising properties such as large surface areas, selective adsorption, ion-exchange capacities, and catalysis activities. It is thus of fundamental importance to understand the relationships between the structures of microporous materials and their properties. In this thesis, two types of microporous materials, metal–organic frameworks (MOFs) and titanosilicates, were characterized by multinuclear solid-state NMR (SSNMR) spectroscopy combined with other techniques including theoretical calculations. It has been demonstrated that 1) the acquisition of unreceptive quadrupolar nuclei (^{25}Mg, ^{39}K, and $^{47/49}$Ti) is feasible at a high magnetic field of 21.1 T; 2) ultrahigh-resolution ^{1}H SSNMR spectra in MOFs can be obtained under favorable conditions; 3) ^{17}O can be efficiently incorporated into the framework of MOFs; 4) variable temperature (VT) ^{2}H SSNMR spectroscopy allows us to monitor the dynamic behaviors of guest molecules in CPO-27-M (M = Mg, Zn, Ni, Co); 5) theoretical calculations using CASTEP and Gaussian programs are valuable in spectral assignment and interpretation.

In *Chapter 2*, the local Mg environments and rehydration/adsorption probes of an important Mg-containing MOF, CPO-27-Mg, were probed by natural abundance ^{25}Mg SSNMR spectroscopy at 21.1 T. Upon removal of the water molecule bound to the Mg, the local Mg structure changes from a perfectly ordered to a disordered environment, although long-range ordering of the framework remains. A large amount of ^{25}Mg spins become NMR invisible due to the large C_Q resulting from the distorted square-pyramid geometry. The Mg disordering persists if the sample is only partially rehydrated. The local ordering can only be resorted completely if enough water is available. For the CPO-27-Mg loaded with organics, the ^{25}Mg environments are also disordered. The origins of the disordering are discussed based on both NMR data and computational modeling.

Chapter 3 describes that the multiple (four) non-equivalent Mg sites of another representative MOF, microporous α-$Mg_3(HCOO)_6$, can be directly differentiated by performing natural abundance ^{25}Mg 3QMAS SSNMR experiments at 21.1 T. The ability to acquire high-quality two-dimensional ^{25}Mg spectra at natural abundance is important since the cost of isotopic enrichment can be prohibitively high. The capability of differentiating multiple Mg sites with very similar local Mg environments is critical because it allows one to directly compare the NMR spectra with the X-ray determined structure.

As shown in *Chapter 4*, ultrahigh-resolution ^1H and ^{13}C SSNMR spectra can be collected in MOFs. Multiple (six) crystallographically non-equivalent, but chemically equivalent H (and C) sites of microporous α-$Mg_3(HCOO)_6$, can be differentiated by ^1H (and ^{13}C) SSNMR experiments. Like fingerprints, ^1H and ^{13}C spectra are very sensitive to the guest molecules included inside of the channels. Among the interesting results, the ability of achieving ultrahigh-resolution for ^1H NMR in solids by the combination of ultrafast MAS (62.5 kHz), isotopic (^2H) dilution, and ultrahigh magnetic field (21.1 T) is of particular importance because the structural information from ^1H SSNMR experiments complements that from single-crystal XRD which is incapable of accurately locating hydrogens. This work is also highlighted by the identification of weak C–H$\cdots$O and C–H$\cdots$N hydrogen bonds by ^1H SSNMR spectroscopy. The aromatic current effect was observed in the benzene sample as well.

The dynamic behavior of several prototypical guest molecules inside of CPO-27-M (M = Mg, Zn, Ni, Co) was exmained in *Chapter 5*. The internal motion of guest molecules, including π flip-flop of D_2O about its C_2 axis, rotation of methyl group about its C_3 axis and in-plane rotation of C_6D_6 about its C_6 axis, persists over the whole temperature range studied. Additional reorientation of the whole molecule (external motion) is desirable for the simulation of ^2H spectra of CD_3CN, acetone-d_6 and C_6D_6 in CPO-27-M. The ^2H NMR data imply that the external motion should be interpreted using the multiple-site hopping model, in which the guest molecules are allowed to jump between neighboring metal centers. Since the motions are constrained by the interactions between guest molecules and exposed metal centers, different guest molecules are

expected to possess distinct dynamic behaviors. The relative binding strengths of the same guest molecule on different metal centers are hence evaluated. The results indicate that the dynamic behavior is clearly dependent on the nature of metal centers. For instance, the relative binding strengths of benzene on M^{2+} are: $Mg^{2+} \approx Ni^{2+} \approx Co^{2+} > Zn^{2+}$, due to both cation-$\pi$ and π-donation interactions.

^{17}O-enriched CPO-27-Mg and α-Mg$_3$(HCOO)$_6$ were prepared (*Chapter 6*). Due to the diversity of MOF-based materials, different types of MOFs may require different isotopic enrichment methods to effectively incorporate ^{17}O from ^{17}O-enriched H$_2$O. Two synthetic strategies for ^{17}O-enrichment were developed. Using these ^{17}O-enriched MOFs ^{17}O SSNMR spectra can be collected at 21.1 T. They provide distinct spectral signatures of several key oxygen species commonly existing in MOFs. The results reveal that ^{17}O SSNMR spectroscopy can be used to differentiate chemically non-equivalent oxygens. The synthetic approaches for preparation of ^{17}O-enriched sample described in this thesis are fairly simple and cost-effective. The ^{17}O-enrichment was measured by a facile approach using TOF-SIMS.

Chapter 7 consists of a comprehensive study of titanosilicates by multinuclear SSNMR spectroscopy. Natural abundance NMR spectra of unreceptive quadrupolar nuclei, $^{47/49}$Ti and ^{39}K, were acquired at 21.1 T. $^{47/49}$Ti SSNMR spectroscopy provide insights into the coordination environments of Ti inside the framework, whereas ^{39}K SSNMR spectroscopy allows one to directly probe the local environment of extra-framework cations in titanosilicates. ^{29}Si and ^{23}Na SSNMR spectra were also collected and interpreted based on the crystal structure.

8.2 Suggestions for Future Work

1. It is hoped that the approach described and the results presented in this thesis will encourage future SSNMR studies of the unreceptive quadrupolar nuclei such as ^{25}Mg, ^{39}K, $^{47/49}$Ti, ^{43}Ca, ^{91}Zr, ^{135}Ba and ^{137}Ba in other microporous materials. The low intrinsic sensitivity of such nuclei can be effectively alleviated by performing SSNMR experiments at a high magnetic field of 21.1 T. The signal-to-noise ratio can be further improved by sensitivity enhance techniques including the QCPMG sequence.

2. We feel that ultrahigh-resolution ^{1}H SSNMR spectra of other MOF systems can also be acquired using the strategy described in *Chapter 4*. Guest-framework interactions such as weak hydrogen bond can be unraveled by ^{1}H SSNMR spectroscopy.

3. *Chapter 5* is mainly focused on the ^{2}H SSNMR study of diamagnetic samples (CPO-27-Mg and CPO-27-Zn). Since paramagnetic effects are anisotropic, they provide additional structural information about the guest molecules. Detailed analysis of the ^{2}H spectra of paramagnetic samples (CPO-27-Ni and CPO-27-Co) is required.

4. The methods for preparing ^{17}O-enriched CPO-27-Mg and α-Mg$_3$(HCOO)$_6$ can be applied to other MOF systems.

5. The results in this thesis imply that the structures of materials with unknown or poorly described structures can also be studied by multinuclear SSNMR spectroscopy in tandem with theoretical calculations.

Appendices: Copyright Permission

Copyright Clearance Center **RightsLink®**   Home   Account Info   Help

WILEY

Title: Resolving Multiple Non-equivalent Metal Sites in Magnesium–Containing Metal–Organic Frameworks by Natural Abundance 25Mg Solid-State NMR Spectroscopy

Author: Jun Xu,Victor V. Terskikh,Yining Huang

Publication: Chemistry - A European Journal

Publisher: John Wiley and Sons

Date: Feb 28, 2013

Copyright © 2013 WILEY-VCH Verlag GmbH & Co. KGaA, Weinheim

Logged in as:
Jun Xu
Account #:
3000694986

LOGOUT

Order Completed

Thank you very much for your order.

This is a License Agreement between Jun Xu ("You") and John Wiley and Sons ("John Wiley and Sons"). The license consists of your order details, the terms and conditions provided by John Wiley and Sons, and the payment terms and conditions.

Get the printable license.

License Number	3251550577589
License date	Oct 17, 2013
Licensed content publisher	John Wiley and Sons
Licensed content publication	Chemistry - A European Journal
Licensed content title	Resolving Multiple Non-equivalent Metal Sites in Magnesium-Containing Metal–Organic Frameworks by Natural Abundance 25Mg Solid-State NMR Spectroscopy
Licensed copyright line	Copyright © 2013 WILEY-VCH Verlag GmbH & Co. KGaA, Weinheim
Licensed content author	Jun Xu,Victor V. Terskikh,Yining Huang
Licensed content date	Feb 28, 2013
Start page	4432
End page	4436
Type of use	Dissertation/Thesis
Requestor type	Author of this Wiley article
Format	Print and electronic
Portion	Full article
Will you be translating?	No
Total	0.00 USD

ORDER MORE...   CLOSE WINDOW

Copyright Clearance Center

RightsLink®

ACS Publications
High quality. High impact.

Title: Identification of Nonequivalent Framework Oxygen Species in Metal–Organic Frameworks by 17O Solid-State NMR

Author: Peng He, Jun Xu, Victor V. Terskikh, Andre Sutrisno, Heng-Yong Nie, and Yining Huang

Publication: The Journal of Physical Chemistry C

Publisher: American Chemical Society

Date: Aug 1, 2013

Copyright © 2013, American Chemical Society

PERMISSION/LICENSE IS GRANTED FOR YOUR ORDER AT NO CHARGE

This type of permission/license, instead of the standard Terms & Conditions, is sent to you because no fee is being charged for your order. Please note the following:

- Permission is granted for your request in both print and electronic formats, and translations.
- If figures and/or tables were requested, they may be adapted or used in part.
- Please print this page for your records and send a copy of it to your publisher/graduate school.
- Appropriate credit for the requested material should be given as follows: "Reprinted (adapted) with permission from (COMPLETE REFERENCE CITATION). Copyright (YEAR) American Chemical Society." Insert appropriate information in place of the capitalized words.
- One-time permission is granted only for the use specified in your request. No additional uses are granted (such as derivative works or other editions). For any other uses, please submit a new request.

BACK   CLOSE WINDOW

Curriculum Vitae

Name:	Jun Xu
Post-secondary Education and Degrees:	Peking University Beijing, China 2004-2008 B.Sc. (Honors in Chemistry) The University of Western Ontario London, Ontario, Canada 2008-2013 Ph.D. candidate (Inorganic Chemistry)
Honours and Awards:	Wusi Scholarship (Peking University) 2007 Western Graduate Research Scholarship (UWO) 2008-2013 International Graduate Student Scholarship (UWO) 2008-2013
Related Work Experience	Undergraduate Research Assistant Peking University 2006-2008 Teaching Assistant The University of Western Ontario 2008-2013 Research Assistant The University of Western Ontario 2008-2013

Publications:

1. Li, L.-L; Sun, H.; Fang, C.-J.; Xu, J.; Jin, J.-Y.; Yan, C.-H. Optical Sensors based on Functionalized Mesoporous Silica SBA-15 for the Detection of Multianalytes (H^+ and Cu^{2+}) in Water. *J. Mater. Chem.*, **2007**, *17*, 4492-4498.
2. Li, Z.-X.; Li, L.-L.; Yuan, Q.; Feng, W.; Xu, J.; Sun, L.-D.; Song, W.-G.; Yan, C.-H. Sustainable and Facile Route to Nearly Monodisperse Spherical Aggregates of CeO_2 Nanocrystals with Ionic Liquids and Their Catalytic Activities for CO Oxidation. *J. Phys. Chem. C*, **2008**, *112*, 18405-18411.
3. Li, L.-L.; Xu, J.; Yuan, Q.; Li, Z.-X.; Song, W.-G.; Yan, C.-H. Facile Synthesis of Macrocellular Mesoporous Foamlike Ce-Sn Mixed Oxides with a Nanocrystalline

Framework by Using Triblock Copolymer as the Single Template. *Small*, **2009**, *5*, 2730-2737.

4. Sutrisno, A.; Liu, L.; Xu, J.; Huang, Y. Natural Abundance Solid-State ^{67}Zn NMR Characterization of Microporous Zinc Phosphites and Zinc Phosphates at Ultrahigh Magnetic Field. *Phys. Chem. Chem. Phys.*, **2011**, *13*, 16606-16617.

5. Xu, J.; Terskikh, V. V.; Huang, Y. ^{25}Mg Solid-State NMR: A Sensitive Probe of Adsorbing Guest Molecules on a Metal Center in Metal-Organic Framework CPO-27-Mg. *J. Phys. Chem. Lett.*, **2013**, *4*, 7-11.

6. Xu, J.; Terskikh, V. V.; Huang, Y. Resolving Multiple Non-equivalent Metal Sites in Magnesium-Containing Metal-Organic Frameworks by Natural Abundance ^{25}Mg Solid-State NMR Spectroscopy. *Chem. Eur. J.*, **2013**, *19*, 4432-4436. **Cover Article for Issue 14, 2013**.

7. Hu, Y.; Liu, Z.; Xu, J.; Huang, Y.; Song, Y. Evidence of Pressure Enhanced CO_2 storage in ZIF-8 Probed by FTIR Spectroscopy. *J. Am. Chem. Soc*, **2013**, *135*, 9287-9290.

8. He, P.; Xu, J.; Terskikh, V. V.; Sutrisno, A.; Nie, H.-Y.; Huang, Y. Identification of Nonequivalent Framework Oxygen Species in Metal-Organic Frameworks by ^{17}O Solid-State NMR. *J. Phys. Chem. C*, **2013**, *117*, 16953-16960. **Cover Article for Issue 33, 2013**.

9. Huang, Y.; Xu, J.; Gul-E-Noor, F.; He, P. Recent Solid-State NMR Studies of Quadrupolar Nuclei in Metal-Organic Frameworks. In *Metal-Organic Framework Materials*, John Wiley & Sons, submitted.

Presentations:

1. (Poster) Xu, J.; Huang, Y. "A Solid-State NMR Study of the Formation of AlPO$_4$-5 under Ionothermal Conditions". 93th Canadian Society for Chemistry Conference, May 29-June 2, 2010, Toronto, Canada.

2. (Poster) Xu, J.; Huang, Y. "An Investigation of the Formation of Microporous Materials, AlPO$_4$-11, under Ionothermal Conditions". 94th Canadian Society for Chemistry Conference, June 6-10, 2011, Montreal, Canada.

3. (Poster) Xu, J.; Sutrisno, A.; Terskikh, V. V.; Huang, Y. "Solid-State NMR Characterization of Metal-Organic Frameworks at Ultrahigh Magnetic Field of 21.1 T". EUROMAR 2012, July 1-5, 2012, Dublin, Ireland.

4. (Poster) Xu, J.; Sinelnikov, R.; Huang, Y. "Capturing the Guest Dynamics in Metal-Organic Frameworks CPO-27-M (M = Mg, Zn) by ^{2}H Solid-State NMR". 96th Canadian Society for Chemistry Conference, May 26-May 30, 2013, Quebec City, Canada.

5. (Oral) Xu, J.; Terskikh, V. V.; Huang, Y. "Determining the Number of Non-equivalent Sites for Each Element in MOF α-Mg$_3$(HCOO)$_6$ by Multinuclear Solid-State NMR at 21.1 T". 8th Annual Solid-State NMR Workshop, National Ultrahigh-Field NMR Facility for Solids, May 26, 2013, Quebec City, Canada. **Invited talk**.

6. (Poster) Xu, J.; Sinelnikov, R.; Huang, Y. "Capturing the Guest Dynamics in Metal-Organic Frameworks CPO-27-M (M = Mg, Zn, Ni, Co) by Variable-Temperature ^{2}H Solid-State NMR". 26th MOOT NMR Symposium, Oct 26-27, 2013, Kingston, Canada.